Elektronische Zustände in Typ-III-Halbleiterheterostrukturen

Dissertation zur Erlangung des
naturwissenschaftlichen Doktorgrades der
Bayerischen Julius-Maximilians-Universität Würzburg

vorgelegt von

Volker Latussek

aus

Hamm in Westfalen

Würzburg 2004

Eingereicht am: 27. Dezember 2004

bei der Fakultät für Physik und Astronomie

1. Gutachter: Prof. Dr. Gottfried Landwehr

2. Gutachter: Prof. Dr. Edwin Batke

der Dissertation

1. Prüfer: Prof. Dr. Edwin Batke

2. Prüfer: Prof. Dr. Haye Hinrichsen

der mündlichen Prüfung

Tag der mündlichen Prüfung: 27. September 2005

Doktorurkunde ausgehändigt am: . . . .

Inhaltsverzeichnis

Kapitel 1

Einleitung

Seit 1988 werden mit dem Verfahren der Molekularstrahlepitaxie (MBE: Molecular Beam Epitaxy) am Physikalischen Institut der Universität Würzburg Halbleiterheterostrukturen aus dem Halbleitermaterialsystem $Hg_{1-x}Cd_xTe$ hergestellt. Diese quecksilberhaltige Legierung ist ein II-VI-Verbindungshalbleiter und zeichnet sich durch eine legierungs- und temperaturabhängige fundamentale Energielücke aus. Die Bandstruktur ist je nach Temperatur und Legierungsfaktor x einerseits halbleitend, anderseits aber halbmetallisch. Die schmallückigen $Hg_{1-x}Cd_xTe$-Legierungen werden als Infrarotdetektoren eingesetzt.

Mit dem Verfahren der Molekularstrahlepitaxie ist es möglich Bandstrukturen mit spezifischen Eigenschaften herzustellen (band structure engineering). Unter diesen neuen Materialien stellen die Typ-III-Übergitter eine besondere Klasse dar. Bei diesen zweidimensionalen Materialstrukturen wird eine nur wenige Atomlagen dicke Schicht von 30 Å bis 100 Å aus dem Halbmetall HgTe, dem Trogmaterial, in eine Legierung aus $Hg_{1-x}Cd_xTe$, dem Barrierenmaterial, eingebettet und zu einem Übergitter aufgebaut.

Zweidimensionale Typ-III-Halbleiterheterostrukturen, wie die HgTe-$Hg_{1-x}Cd_xTe$-Quantentrogstrukturen und HgTe-$Hg_{1-x}Cd_xTe$-Übergitter, sind von fundamentalen Interesse zum Verständnis von elektronischen Zuständen komplexer Bandstrukturen und zweidimensionaler Ladungsträgersysteme.

Darüber hinaus werden HgTe-$Hg_{1-x}Cd_xTe$-Übergitter in der Sensorik als Infrarotdektoren eingesetzt, deren cut-off-Wellenlänge prozessgesteuert in der Molekularstrahlepitaxie über die Trogbreite, der Schichtdicke des HgTe, eingestellt werden kann.

Je nach verwendeten Barrierenmaterial $Hg_{1-x}Cd_xTe$ und Temperatur besitzen die Übergitterstrukturen mit großen Barrierenschichtdicken, das sind die Quantentrogstrukturen, in Abhängigkeit von der Trogbreite, für niedrige Trogbreiten eine normal halbleitende Subbandstruktur, während sich für größere Trogbreiten eine invertiert halbleitende Subbandstruktur einstellt. In der invertiert halbleitenden Subbandstruktur ist ein indirekter Halbleiter realisierbar. Bei Strukturen mit dünnen Barrierenschichtdicken ist die Minibanddispersion stark ausgeprägt und es kann sich zusätzlich eine halbmetallische Subbandstruktur ausbilden.

Diese speziellen Eigenschaften sind einzigartig und kennzeichnen die komplexe Bandstruktur von Typ-III-Heterostrukturen.

Erst die genaue Kenntnis und ein vertieftes Verständnis der komplexen Bandstruktur erlaubt die Interpretation von Ergebnissen aus (magneto)-optischen Untersuchungen der elektronischen Eigenschaften von Typ-III-Halbleiterheterostrukturen.

Die Berechnung der elektronischen Zustände in den HgTe-Hg$_{1-x}$Cd$_x$Te-Übergitter wurde in der vorliegenden Arbeit in der Envelopefunktionsnäherung durchgeführt.

Seit drei Jahrzehnten wird die Envelopefunktionennäherung (EFA: Envelope Function Approximation) sehr erfolgreich bei der Interpretation der experimentellen Ergebnisse von (magneto)-optischen Untersuchungen an Halbleiterheterostrukturen eingesetzt. Der Erfolg basiert auf der effektiven Beschreibung der quantisierten, elektronischen Zustände an Halbleitergrenzflächen, in Quantentrögen und Übergittern und der Einzigartigkeit, zur Berechnung der experimentellen Ergebnisse, die Abhängigkeit von äußeren Parametern, wie der Temperatur und des hydrostatischen Druckes, aber auch eines elektrischen und magnetischen Feldes, wie auch von freien Ladungsträgern, ein zu arbeiten. Die sehr gute quantitative Übereinstimmung der theoretischen Berechnungen in der Envelopefunktionennäherung und vieler experimenteller Messergebnisse an Halbleiterheterostrukturen baut auf der quantitativen Bestimmung der relevanten Bandstrukturparameter in der $\mathbf{k} \cdot \mathbf{p}$-Störungstheorie zur Beschreibung der elektronischen Eigenschaften der beteiligten Volumenhalbleiter auf.

In Kapitel 1 der vorliegenden Arbeit wird daher zunächst das Bandstrukturmodell des Volumenmaterials Hg$_{1-x}$Cd$_x$Te vorgestellt und daraus die Eigenwertgleichung des Hamilton-Operators in der Envelopefunktionennäherung abgeleitet. Danach wird das Lösungsverfahren, die Matrixmethode, zur Berechnung der Eigenwerte und Eigenfunktionen beschrieben und auf die Berechnung der elektronischen Subbandzustände der Typ-III-Hg$_{1-x}$Cd$_x$Te-Übergitter angewendet. Es folgt eine Diskussion der grundlegenden Eigenschaften der komplexen Bandstruktur in den verschiedenen Regimen der Typ-III-Halbleiterheterostrukturen und der charakteristischen Wellenfunktionen, den Grenzflächenzuständen.

An Ende dieses Kapitels wird die Berechnung des Absorptionskoeffizienten hergeleitet und die grundlegenden Eigenschaften der Diplomatrixelemente zur Charakterisierung der optischen Eigenschaften von HgTe-Hg$_{1-x}$Cd$_x$Te-Übergitter exemplarisch vorgestellt.

In Kapitel 2 sind die wesentlichen Ergebnisse aus dem Vergleich von Infrarotabsorptionsmessungen an HgTe-Hg$_{1-x}$Cd$_x$Te-Übergitter mit den berechneten Absorptionskoeffizienten zusammengestellt.

Kapitel 2

Elektronische Zustände in Typ-III-Halbleiterheterostrukturen

In diesem Kapitel werden die Grundlagen zur Berechnung der elektronischen Zustände in Halbleiterheterostrukturen im Rahmen der Envelopefunktionennäherung (EFA) kurz skizziert. Die Envelopefunktionennäherung wird sich bei der Berechnung von Infrarotabsorptionsspektren der experimentell untersuchten zweidimensionlen HgTe-Hg$_{1-x}$Cd$_x$Te-Heterostrukturen als sehr erfolgreich erweisen. Die Bandstrukturen der beteiligten Volumenmaterialien, des Halbmetalls HgTe und der Legierung Hg$_{1-x}$Cd$_x$Te, können dabei einheitlich im Kane-Modell beschrieben werden.

2.1 Die Envelopefunktionennäherung

Die Envelopefunktionennäherung stellt eine Erweiterung der $\mathbf{k} \cdot \mathbf{p}$-Störungstheorie dar, die eine bewährte Methode zur Berechnung von elektronischen Zuständen von Volumenhalbleitern ist.

Die grundlegende Idee der Envelopenfunktionennäherung ist die Folgende: Die Wellenfunktion des betrachteten Hamilton-Operators wird nach einem vollständigen Satz von Blochfunktionen $u_n(\mathbf{r})$ z. B. im Zentrum der Brillouin-Zone bei $\mathbf{k} = 0$ entwickelt:

$$\Psi(\mathbf{r}) = \sum_n F_n(\mathbf{r}) \, u_n(\mathbf{r}), \qquad (2.1)$$

mit den Envelopefunktionen $F_n(\mathbf{r})$. Unter der Annahme der Translationsinvarianz in der Ebene senkrecht zur Wachtumsrichtung z der Quantentrog- und Übergitterstrukturen liefert der folgende Seperationsansatz für die Envelopefunktionen $F_n(\mathbf{r})$ die Lösung

$$F_n(\mathbf{r}) = \exp[i(k_x x + k_y y)] \, f_n(z), \qquad (2.2)$$

mit den Wellenvektorkomponenten k_x und k_y .

Die Envelopefunktionen und die Energien in der Umgebung von $\mathbf{k} = 0$ werden im Rahmen der $\mathbf{k} \cdot \mathbf{p}$ Theorie durch Lösung von gekoppelten Differentialgleichungen 2. Ordnung berechnet.

$$\sum_{n'} H_{nn'} f_{n'}(z) =$$

$$\sum_{n'} \left(\sum_{\alpha,\beta}^{x,y,z} k_\alpha D_{nn'}^{\alpha\beta} k_\beta + \sum_\alpha^{x,y,z} P_{nn'}^\alpha k_\alpha + E_{n'}(z)\delta_{nn'} \right) f_{n'}(z) = E \cdot f_n(z) \tag{2.3}$$

mit n and n' den Summationsindizes der Blochfunktionen, $E_{n'}(z)$ sind die Bandkantenenergien. Die Dipolmatrixelemente $P_{nn'}^\alpha$ beschreiben die Kopplung zwischen den n and n' Bändern exakt, während die $D_{nn'}^{\alpha\beta}$ die Kopplung an die entfernten Bänder in Störungsrechnung 2. Ordnung berücksichtigen.

Das zugrundeliegende Bandstrukturmodell, das Kane-Modell, zur Beschreibung der Zustände eines schmallückigen Halbleiters im Γ-Punkt der Brillouin-Zone bei $\mathbf{k} = 0$ trägt der starken Kopplung zwischen dem Leitungs- (Γ_6) und den Valenzbändern (Γ_8, Γ_7) Rechnung und ist in Abbildung (2.1) für das Trogmaterial, das Halbmetall HgTe und das Barrierenmaterial $Hg_{0.32}Cd_{0.68}Te$ der untersuchten (001)-HgTe-$Hg_{1-x}Cd_xTe$-Übergitter gezeigt.
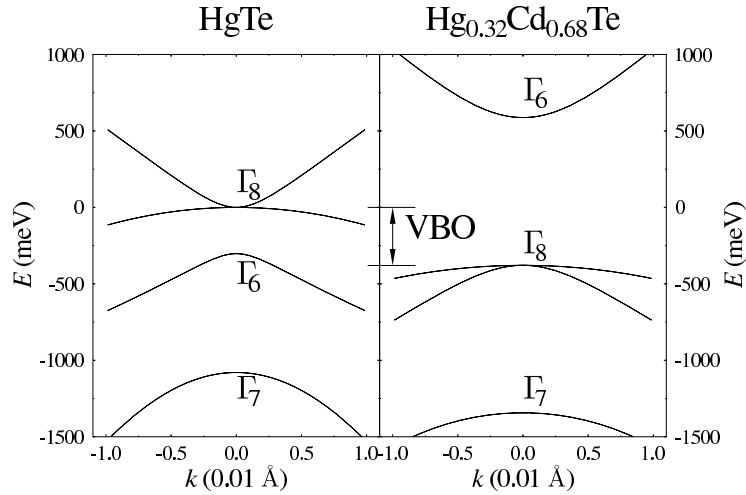
Abbildung 2.1: Bandstruktur von HgTe und $Hg_{1-x}Cd_xTe$ im Kane-Modell [2]. Die jeweils spinentarteten Bänder sind nach ihrer Symmetrie bezeichnet: Γ_6, Γ_7 und Γ_8. Zusätzlich eingetragen ist der für die Heterostrukturen charakteristische Valenzbandoffset (VBO).

Die, dem Kane-Modell zugrundliegende, Basis von 8 symmetrieangepassten Blochfunktionen, Γ_6, Γ_7 and Γ_8, lautet [2]:

$$
\begin{aligned}
u_1(\mathbf{r}) = |\Gamma_6, +1/2\rangle &= S\uparrow \\
u_2(\mathbf{r}) = |\Gamma_6, -1/2\rangle &= S\downarrow \\
u_3(\mathbf{r}) = |\Gamma_8, +3/2\rangle &= (1/\sqrt{2})(X + iY)\uparrow \\
u_4(\mathbf{r}) = |\Gamma_8, +1/2\rangle &= (1/\sqrt{6})[(X + iY)\downarrow - 2Z\uparrow] \\
u_5(\mathbf{r}) = |\Gamma_8, -1/2\rangle &= -(1/\sqrt{6})[(X - iY)\uparrow + 2Z\downarrow]
\end{aligned}
\tag{2.4}
$$

$$
\begin{aligned}
u_6(\mathbf{r}) = |\Gamma_8, -3/2\rangle &= -(1/\sqrt{2})(X - iY)\downarrow \\
u_7(\mathbf{r}) = |\Gamma_7, +1/2\rangle &= (1/\sqrt{3})[(X + iY)\downarrow + Z\uparrow] \\
u_8(\mathbf{r}) = |\Gamma_7, -1/2\rangle &= (1/\sqrt{3})[(X - iY)\uparrow - Z\downarrow],
\end{aligned}
$$

mit dem Gesamtdrehimpuls $j = 1/2$ für Γ_6, Γ_7 und $j = 3/2$ für Γ_8.

Der Hamilton-Operator $H_{nn'}$ in Gl. (2.3) für eine zweidimensionale Heterostruktur und [001]-Wachstumsrichtung stellt sich in der gewählten Basis der 8 Blochfunktionen nunmehr wie folgt dar[3]:

$$
H = \begin{pmatrix}
T & 0 & -\frac{1}{\sqrt{2}}Pk_+ & \sqrt{\frac{2}{3}}Pk_z & \frac{1}{\sqrt{6}}Pk_- & 0 & -\frac{1}{\sqrt{3}}Pk_z & -\frac{1}{\sqrt{3}}Pk_- \\
0 & T & 0 & -\frac{1}{\sqrt{6}}Pk_+ & \sqrt{\frac{2}{3}}Pk_z & \frac{1}{\sqrt{2}}Pk_- & -\frac{1}{\sqrt{3}}Pk_+ & \frac{1}{\sqrt{3}}Pk_z \\
-\frac{1}{\sqrt{2}}k_-P & 0 & U+V & -\bar{S}_- & R & 0 & \frac{1}{\sqrt{2}}\bar{S}_- & -\sqrt{2}R \\
\sqrt{\frac{2}{3}}k_zP & -\frac{1}{\sqrt{6}}k_-P & -\bar{S}_-^\dagger & U-V & C & R & \sqrt{2}V & -\sqrt{\frac{3}{2}}\tilde{S}_- \\
\frac{1}{\sqrt{6}}k_+P & \sqrt{\frac{2}{3}}k_zP & R^\dagger & C^\dagger & U-V & \bar{S}_+^\dagger & -\sqrt{\frac{3}{2}}\tilde{S}_+ & -\sqrt{2}V \\
0 & \frac{1}{\sqrt{2}}k_+P & 0 & R^\dagger & \bar{S}_+ & U+V & \sqrt{2}R^\dagger & \frac{1}{\sqrt{2}}\bar{S}_+ \\
-\frac{1}{\sqrt{3}}k_zP & -\frac{1}{\sqrt{3}}k_-P & \frac{1}{\sqrt{2}}\bar{S}_-^\dagger & \sqrt{2}V & -\sqrt{\frac{3}{2}}\tilde{S}_+^\dagger & \sqrt{2}R & U-\Delta & C \\
-\frac{1}{\sqrt{3}}k_+P & \frac{1}{\sqrt{3}}k_zP & -\sqrt{2}R^\dagger & -\sqrt{\frac{3}{2}}\tilde{S}_-^\dagger & -\sqrt{2}V & \frac{1}{\sqrt{2}}\bar{S}_+^\dagger & C^\dagger & U-\Delta
\end{pmatrix}
$$

mit den üblichen Abkürzungen:

$$
\begin{aligned}
k_\parallel^2 &= k_x^2 + k_y^2, \quad k_\pm = k_x \pm ik_y, \quad k_z = -i\partial/\partial z, \\
T &= E_c(z) + \frac{\hbar^2}{2m_0}\left((2F+1)k_\parallel^2 + k_z(2F+1)k_z\right), \\
U &= E_v(z) - \frac{\hbar^2}{2m_0}\left(\gamma_1 k_\parallel^2 + k_z\gamma_1 k_z\right), \\
V &= -\frac{\hbar^2}{2m_0}\left(\gamma_2 k_\parallel^2 - 2k_z\gamma_2 k_z\right), \\
R &= -\frac{\hbar^2}{2m_0}\left(\sqrt{3}\mu k_+^2 - \sqrt{3}\bar{\gamma}k_-^2\right), \\
\bar{S}_\pm &= -\frac{\hbar^2}{2m_0}\sqrt{3}k_\pm\left(\{\gamma_3, k_z\} + [\kappa, k_z]\right), \\
\tilde{S}_\pm &= -\frac{\hbar^2}{2m_0}\sqrt{3}k_\pm\left(\{\gamma_3, k_z\} - \frac{1}{3}[\kappa, k_z]\right), \\
C &= \frac{\hbar^2}{m_0}k_-[\kappa, k_z].
\end{aligned}
\tag{2.5}
$$

$[A, B] = AB - BA$ ist der Kommutator und $\{A, B\} = AB + BA$ der Anti-Kommutator der Operatoren A und B, P ist das Kane-Dipolmatrixelement, $E_c(z)$ (Leitungsband) und $E_v(z)$

(Valenzband) beschreibt die räumliche Variation der Bandkanten in Wachstumsrichtung der zweidimensionalen Heterostruktur, Δ ist die Energieaufspaltung auf Grund der Spin-Bahn-Wechselwirkung und γ_1, γ_2, γ_3, κ und F beschreiben die Fernbandanteile und μ und $\bar{\gamma}$ die aus Symmetrie-Argumenten sinnvollen Abkürzungen $\mu = (\gamma_3 - \gamma_2)/2$ und $\bar{\gamma} = (\gamma_3 + \gamma_2)/2$. Die Terme mit kubischer Symmetrie im Hamilton-Operator sind proportional zu μ (warping). Im Fall $\mu = 0$ ist der Hamilton-Operator axial-symmetrisch. Die Effekte der Inversions-Asymmetrie sind im $Hg_{1-x}Cd_xTe$ sehr klein und werden vernachlässigt [2].

Die Erweiterung auf eine beliebige Wachstumsrichtung [hkl] ist allein aus Symmetrieüberlegungen ableitbar und ist bei Novik *et. al.* [3] für die [kkl]-Richtung angegeben.

Die Berechnung der elektronischen Zustände in Halbleiterheterostrukturen führt nach Gl. (2.3) und Gl. (2.5) auf ein System von 8 gekoppelten Differentialgleichungen 2. Ordnung, das im Folgenden mit der Matrixmethode gelöst wird.

2.2 Die Matrixmethode

Die Berechnung der einzelnen Envelopefunktionen aus Gl. (2.3), das sind die normierbaren Eigenfunktionen zum Eigenwert E, die sogenannten Subbandfunktionen, zur zugehörigen Subbandenergie, wird zurückgeführt auf die Berechnung von Matrixelementen in der Matrixdarstellung des Hamilton-Operators Anhang [B]. Hierzu wird jede Komponente der Envelopefunktion $f_n(z)$ nach einem vollständigen, im Allgemeinen nicht-orthogonalen, Funktionensystem $\{g_i(z)\}$ entwickelt:

$$f_n(z) = \sum_i a_n^i \, g_i(z), \quad i = 0, 1, 2, \ldots \tag{2.6}$$

wobei die $g_i(z)$ auf das zu berechnende Heterostruktursystem angepasst werden [Seite 54] und [2]. Die Entwicklung in Gl. (2.6) führt auf eine Matrixdarstellung des Eigenwertproblems. Die numerische Diagonalisierung liefert neben den Eigenwerten, die Komponenten der Eigenvektoren, die a_n^i. Die daraus berechneten Subbandfunktionen erfüllen automatisch die Übergangsbedingungen (boundary conditions) [3].

Die Matrixmethode ist bei Latussek, Bangert und Landwehr im Detail beschrieben [Anhang B]. Das dort beschriebene Funktionensystem wurde zunächst durch die Eigenfunktionen eines Quantentroges ersetzt [5] und auf die Berechnung der Valenzbandstruktur einer GaAs-GaAlAs-Quantentrogstruktur angewendet [Seite 196ff].

Die Matrixmethode wurde erstmals vom Autor um die Klasse der nicht-orthogonalen Funktionensysteme $g_i(z)$ erweitert und auf das Kane-Modell zur Berechnung der Bandstruktur von Typ-III-Halbleiterheterostrukturen angewendet.

Auf Grund der schlechten Konvergenz bei der Berechnung der Grenzflächenzustände in Typ-III-Quantentrogstrukturen wurde ein neues Funktionensystem konstruiert [2], welches für sämtliche untersuchten Heterostrukturen – vom P-Typ-Inversionskanal in Germanium-Bikristallen, über GaAs-GaAlAs-Quantentrogstrukturen bis hin zu Typ-III-Übergittern – die erforderliche Konvergenz zeigt.

$z(\text{Å})$	F_1	F_2	F_3	F_4
		Exakte Envelopefunktion [5]		
0	7.481×10^{-2}	0	-1.016×10^{-1}	0
25	5.085×10^{-2}	1.634×10^{-2}	-7.229×10^{-2}	4.745×10^{-2}
50	7.697×10^{-3}	1.405×10^{-2}	-2.005×10^{-2}	3.077×10^{-2}
75	-1.553×10^{-3}	3.614×10^{-3}	-1.948×10^{-3}	3.797×10^{-3}
100	-6.114×10^{-4}	6.768×10^{-4}	-6.837×10^{-5}	3.306×10^{-4}
		Matrixmethode: 20(8)		
0	7.480×10^{-2}	0	-1.016×10^{-1}	0
25	5.086×10^{-2}	1.634×10^{-2}	-7.230×10^{-2}	4.745×10^{-2}
50	7.697×10^{-3}	1.405×10^{-2}	-2.005×10^{-2}	3.077×10^{-2}
75	-1.553×10^{-3}	3.615×10^{-3}	-1.948×10^{-3}	3.797×10^{-3}
100	-6.115×10^{-4}	6.767×10^{-4}	-6.809×10^{-5}	3.310×10^{-4}
		Matrixmethode: 12(6)		
0	7.453×10^{-2}	0	-1.012×10^{-1}	0
25	5.118×10^{-2}	1.634×10^{-2}	-7.270×10^{-2}	4.717×10^{-2}
50	7.638×10^{-3}	1.405×10^{-2}	-2.013×10^{-2}	3.069×10^{-2}
75	-1.967×10^{-3}	3.645×10^{-3}	-1.613×10^{-3}	3.649×10^{-3}
100	-3.483×10^{-4}	5.866×10^{-4}	-3.264×10^{-4}	3.682×10^{-4}
		Integralmethode [6]: 81 Gitterpunkte		
0	7.480×10^{-2}	9.296×10^{-4}	-1.016×10^{-1}	6.842×10^{-4}
25	5.084×10^{-2}	1.633×10^{-2}	-7.227×10^{-2}	4.740×10^{-2}
50	7.680×10^{-3}	1.400×10^{-2}	-2.004×10^{-2}	3.066×10^{-2}
75	-1.530×10^{-3}	3.619×10^{-3}	-1.955×10^{-3}	3.809×10^{-3}
100	-6.116×10^{-4}	6.772×10^{-4}	-6.850×10^{-5}	3.317×10^{-4}

Tabelle 2.1: Envelopefunktion des obersten Subbands (H1) für $k_\parallel = 0.04\,\text{Å}^{-1}$ in $\langle 10 \rangle$ Richtung eines $100\,\text{Å}$ GaAs-Ga$_{0.79}$Al$_{0.21}$As-Quantentroges. Die exakte Envelopefunktion von Andreani, Pasquarello und Bassani [5] wird mit dem numerischen Ergebnis aus der Matrixmethode für 20(8) und 12(6) Entwicklungsfunktionen je Spinorkomponente verglichen. Zusätzlich ist das numerische Resultat der Integralmethode von Winkler und Rössler [6] eingetragen. Der Ursprung der z–Achse ist in der Mitte des Quantentroges.

Die Genauigkeit der Matrixmethode oder allgemeiner von Variationsmethoden wird am besten durch den Vergleich mit exakten Lösungsverfahren überprüft. Als ein überzeugender Test zur Genauigkeit numerischer Resultate der Methode dient ein Vergleich mit exakten Ergebnissen aus Subbandrechnungen einer GaAs-Ga$_{1-x}$Al$_x$As-Heterostruktur von Andreani, Pasquarello und Bassani [5]. Die Subbänder und deren Envelopefunktionen der Vergleichsstruktur, einem un-

dotierten 100 Å GaAs-Ga$_{0.79}$Al$_{0.21}$As-Quantentrog, lösen das Eigenwertproblem der sogenannten 4×4-Luttinger-Matrix mit dem Rechteckpotential der Valenzbandoberkante. In Tabelle (2.1) sind die Zahlenwerte der vierkomponentigen Envelopefunktion $\underline{\mathbf{F}}(z)$ für das oberste Subband (H1), dem Grundzustand des schweren Loches, mit k$_{\parallel} = \sqrt{k_x^2 + k_y^2} = 0.04\,$Å^{-1} in der $\langle 10 \rangle$ Richtung eingetragen. Die Matrixmethode 20(8) mit der Entwicklung der Envelopefunktion nach 20 Basisfunktionen, davon 8 in der GaAs-Schicht, für jede Spinorkomponente zeigt eine hervorragende Übereinstimmung mit dem exakten Ergebnis [1]. Dies gilt auch außerhalb des Quantentroges, wo die Amplitude der Envelopefunktion [2] sehr klein ist. Um die rasche Konvergenz der Matrixmethode zu illustrieren wurde die Entwicklung der Envelopefunktion nach 12 Basisfunktionen in die Tabelle aufgenommen.

Aus dem Vergleich mit der Integralmethode von Winkler und Rössler [6], bei der die zugrundeliegenden Basisfunktionen ebene Wellen sind, wird deutlich, dass bei entsprechender Genauigkeit 81 Entwicklungsfunktionen pro Spinorkomponente benötigt werden, also viermal soviele wie bei der Matrixmethode [3].

Bevor nun die Ergebnisse der Berechnungen für die interessanten Anwendungen der Matrixmethode, den quecksilberhaltigen II–VI–Heterostukturen kommen, einige Bemerkungen zur Flexibilität und Leistungsfähigkeit der Methode. Die Matrixmethode wurde ursprünglich zur Berechnung der Envelopefunktion elektronischer Zustände in Halbleiterübergitter entwickelt, mit dem Separationsansatz der Envelopefunktion $\underline{\mathbf{F}}(\mathbf{r}) = e^{i\,q \cdot z} \left[e^{i\,\mathbf{k} \cdot \mathbf{r}}\, \underline{\mathbf{F}}(z) \right]$. Zudem wurden die Legendrepolynome als Grundlage des Konstruktionsprinzips der Basisfunktionen gewählt [2]. Zur Berechnung der erforderlichen Matrixelemente wird auf den Anhang [A] verwiesen.

Die hohe Genauigkeit der Ergebnisse in dem vorangehenden Beispiel einer Quantentrogstruktur zeigt deutlich, dass eine einheitliche Beschreibung von Subbandzuständen in Heterostrukturen gefunden ist. Der isolierte Quantentrog wird hier über ein Übergitter $d_I(d_{II})$ approximiert, das aus einer 100(200) Å GaAs(Ga$_{0.79}$Al$_{0.21}$As) Schichtfolge besteht. Für die Auswertung der Subbandzustände wurde $\mathbf{k} = (k_{\parallel}, q)$ zu $(0.04, 0)\,$Å^{-1} gewählt. Die Bandbreite des (H1)–Minibands, das ist die Differenz der Energieeigenwerte $E(\mathbf{k})$ zwischen dem Zentrum $(0,0)$ und dem Rand $(0, \pi/(d_I + d_{II}))$ der ersten Brillouin-Zone des Übergitters, ist für die angegebene Dicke d_{II} der Ga$_{0.79}$Al$_{0.21}$As Schicht kleiner als der absolute Fehler in der Berechnung der Eigenwerte (s. Fußnote 1). Die Breite der Minibänder ist somit ein Maß für die Kopplung der einzelnen Quantentröge in Vielfachquantentrogstrukturen.

Aus der hohen Genauigkeit der Matrixmethode bei sehr kleiner Amplitude der Envelopefunktion ergibt sich die Anwendung auf die Berechnung von resonanten Subbandzuständen in Tunnelstrukturen [10],[11].

---

[1] Der absolute Fehler in den Energieeigenwerten der gebundenen Zustände ist kleiner als 10^{-3}meV.

[2] Die Normierung der Envelopefunktion ist so gewählt, dass für z in Ångstrom gilt: $\int \sum_i |F_i(z)|^2\, \mathrm{d}z = 1$.

[3] Dies erfordert die Diagonalisierung einer $4 \times 81 = 324$ dimensionalen Matrix für jeden $\mathbf{k}$–Punkt. Dabei ist das numerische Diagonalisierungsverfahren ein n^3–Algorithmus [8],[9], d. h. verringert man die Anzahl n der Basisfunktionen auf 1/4, so wird der Rechenaufwand auf 1/64 reduziert.
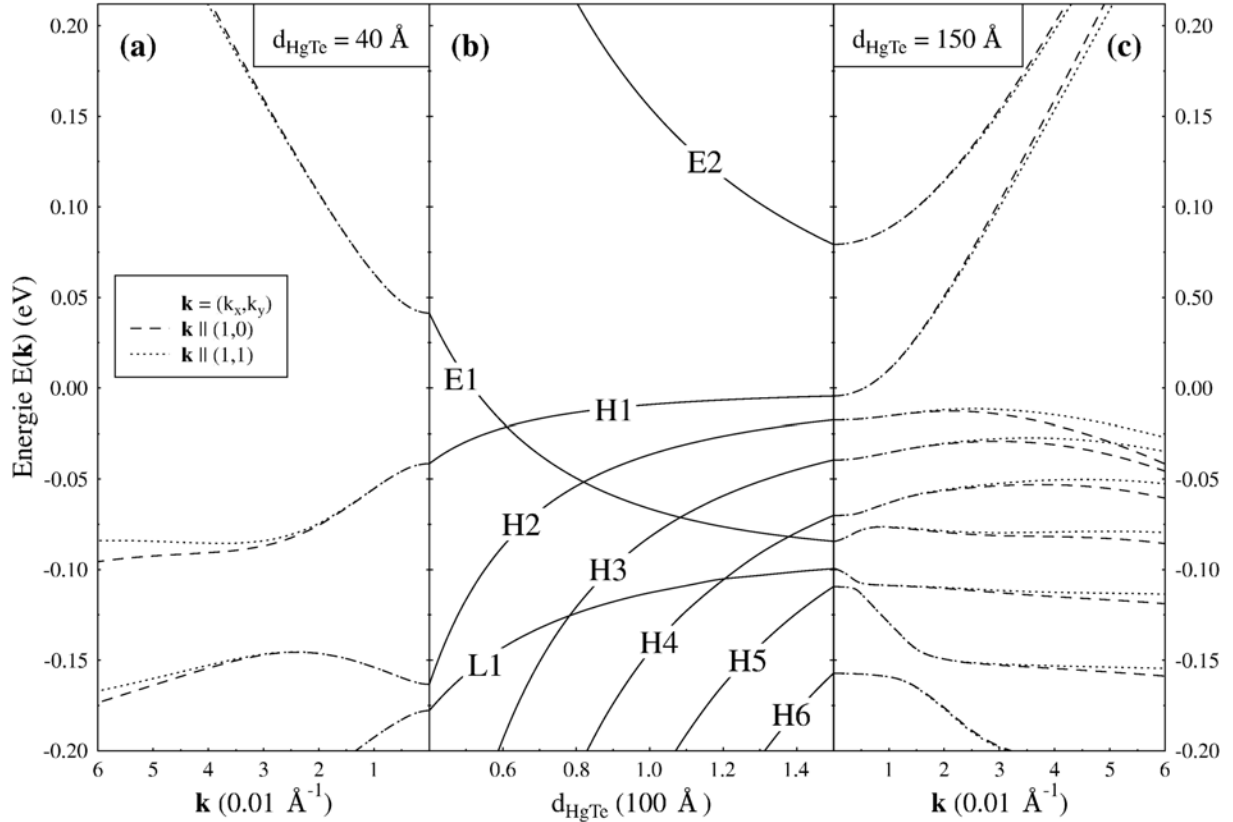
Abbildung 2.2: (a) Bandstruktur eines 40 Å-HgTe-Hg$_{0.32}$Cd$_{0.68}$Te-Quantentroges. (b) Verlauf der Subbandkanten als Funktion der Trogbreite. (c) Bandstruktur eines 150 Å-HgTe-Hg$_{0.32}$Cd$_{0.68}$Te-Quantentroges. Der Nullpunkt der Energieskala fällt mit der Valenzbandoberkante Γ_8 von HgTe zusammen.

2.3 Die Berechnung der Subbandstruktur von HgTe-Hg$_{1-x}$Cd$_x$-Te-Heterostrukturen

Der spezielle Bandkantenverlauf von Typ-III-Heterostrukturen führt zu einer starken Kopplung von Zuständen mit unterschiedlicher Symmetrie. Die elektronischen Eigenschaften von HgTe-Hg$_{1-x}$Cd$_x$Te-Heterostrukturen werden dabei durch die komplexe Bandstruktur der beteiligten Volumenhalbleiter bestimmt.

In Abbildung (2.2) sind die Subbandenergien eines HgTe-Hg$_{0.32}$Cd$_{0.68}$Te-Quantentroges in Abhängigkeit von der sogenannten Trogbreite, der Dicke der HgTe-Schicht, aufgetragen (b). Zusätzlich sind für eine Trogbreite von 40 Å (a) und 150 Å (c) die Bandstrukturen $E(\mathbf{k})$ senkrecht zur Wachstumsrichtung (Quantisierungsachse) eingezeichnet. Die Bandstruktur des 40 Å-Quantentroges wird als normal halbleitende Bandstruktur bezeichnet. Das Leitungsband ist ein E1-Subband, energetisch getrennt durch eine Energielücke von dem Valenzband, einem H1-Subband. Sowohl E1 als auch H1 sind auf Grund der starken Kopplung der Bänder untereinander stark nichtparabolisch (a). Mit zunehmender Trogbreite rutscht das E1-Subband energetisch in den Bereich der H-Subbänder. Da die H-Zustände vom E1-Zustand bei $\mathbf{k} = 0$ entkoppelt sind,

schneiden sich die Subbandkanten in Abbildung (2.2) (b). Oberhalb des Schnittpunktes bei ca. 60 Å ist das H1-Band das Leitungsband mit einer elektronenartigen Subbanddispersion (c) und das E1-Band bildet das Valenzband mit einer lochartigen Dispersion. Die Bandstruktur heißt invertiert halbleitend. Für den 150 Å-Quantentrog bildet sich eine indirekte Energielücke aus. Das Maximum des Valenzbandes, welches durch den H2-Zustand gebildet wird, liegt bei endlichem Wellenvektor $\mathbf{k}$. Das Leitungsband wird wie bei den invertiert halbleitenden Bandstrukturen aus dem H1-Band gebildet. Das E1-Band liegt für den 150 Å-Quantentrog energetisch unterhalb des H4-Bandes und läuft mit zunehmender Trogbreite auf den L1-Zustand zu.

Der L1-Zustand wird bei normal halbleitenden Bandstrukturen als leichter Loch-Zustand bezeichnet, mit Γ_8-Symmetrie. In Typ-III-Heterostrukturen bildet der L1-Zustand zusammen mit dem E1-Zustand, sofern dieser energetisch unterhalb der Valenzbandkante von HgTe liegt – das gilt für Trogbreiten ab ca. 60 Å – die sogenannten Grenzflächenzustände aus.

Die Berechnung der Bandstrukturen von HgTe-Hg$_{1-x}$Cd$_x$Te-Übergittern erfolgt analog zur Beschreibung auf Seite [12] und führt in den Typ-III-Heterostrukturen zu drei unterschiedlichen Klassen von Übergittern. Diese werden charakterisiert nach der Dispersion in Wachstumsrichtung, der Minibanddispersion und sind in Abbildung (2.3) schematisch zusammengefasst,
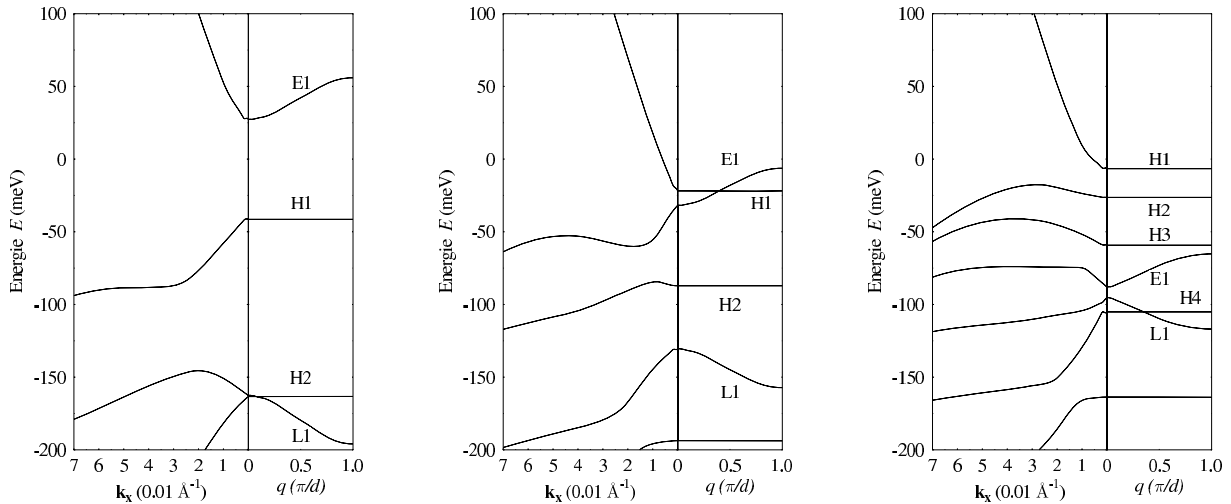
Abbildung 2.3: Bandstruktur eines normal halbleitenden (links), eines semimetallischen (mitte) und eines invertiert halbleitenden (rechts) HgTe-Hg$_{1-x}$Cd$_x$Te-Übergitters [2].

Die unterschiedlichen Regime der Bandstruktur, normal halbleitend, semimetallisch und invertiert halbleitend, können auch in einem einzigen HgTe-Hg$_{1-x}$Cd$_x$Te-Übergitter in Abhängigkeit der Temperatur eingestellt werden, [Seite 106].

2.4 Die Grenzflächenzustände

Die Bezeichnungen der Zustände, H1, H2, ..., L1, E1 und E2 in Abbildung (2.2) klassifizieren die Subbänder nach ihren Blochkomponenten aus Gl. (2.4). Die Bezeichnung für die schweren Loch-Zustände ist sinnvoll, da diese Zustände bei $\mathbf{k} = 0$ entkoppelt sind und die Envelopefunktion nur
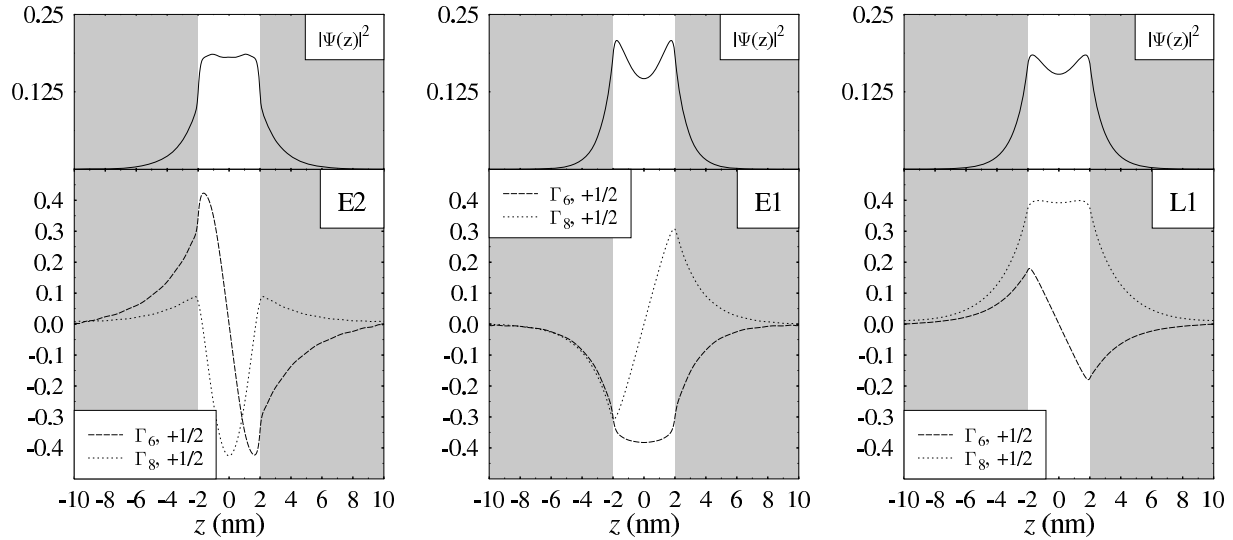
Abbildung 2.4: Envelopefunktionen E2, E1 und L1 eines $40\,\text{Å}$ HgTe-$\text{Hg}_{0.32}\text{Cd}_{0.68}$Te-Quantentroges. Zusätzlich ist im oberen Teil die Aufenthaltswahrscheinlichkeit gezeigt [2].
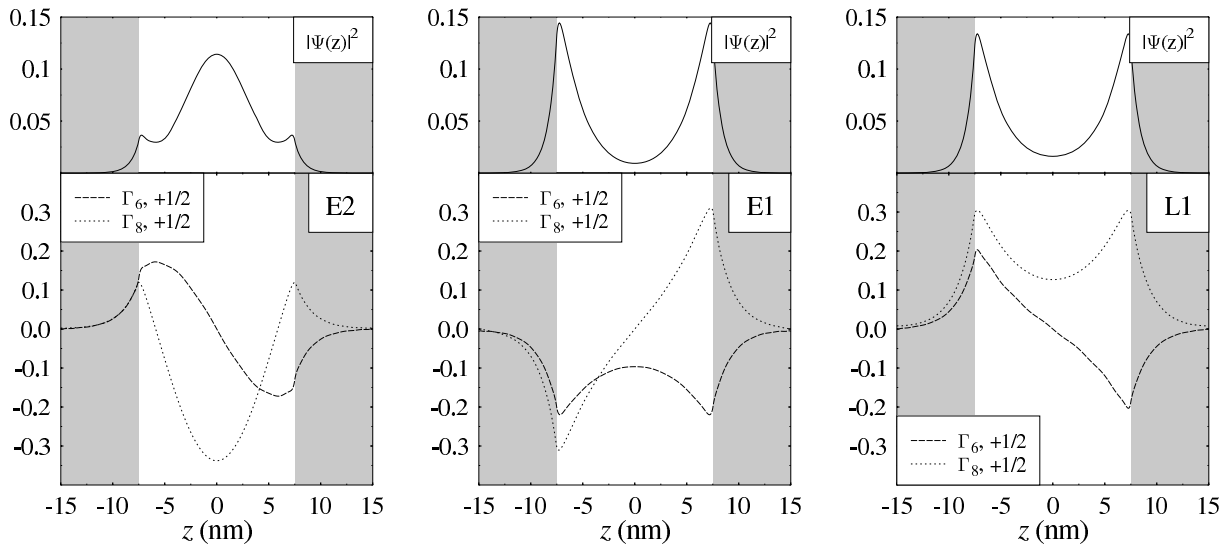
Abbildung 2.5: Envelopefunktionen E2, E1 und L1 eines $150\,\text{Å}$ HgTe-$\text{Hg}_{0.32}\text{Cd}_{0.68}$Te-Quantentroges. Zusätzlich ist im oberen Teil die Aufenthaltswahrscheinlichkeit gezeigt [2].

eine Komponente enthält, wobei H1 den Grundzustand bezeichnet mit einer Envelopefunktion ohne Knoten und Hi entsprechend mit $i-1$ Knoten und $i=1,2,\dots$. Alle anderen Lösungen des Kane-Modells weisen auf Grund der starken Kopplung eine große Mischung der Blochfunktionen auf, sodass die Klassifizierung nach der Blochkomponente mit der kleinsten Knotenzahl $i-1$ der Envelopefunktion vorgenommen wird [2].

In Abbildung (2.4) sind die Envelopefunktionen E2, E1 und L1 eines $40\,\text{Å}$-HgTe-$\text{Hg}_{0.32}\text{Cd}_{0.68}$Te-Quantentroges zusammen mit der Summe der Betragsquadrate der einzelnen Envelopefunktionen, das ist auf Grund der Orthogonalität der Blochfunktionen, die Aufenthaltswahrschein-

lichkeit der gesamten Wellenfunktion $\psi(\mathbf{r})$, eingetragen. Der Übersichtlichkeit wegen wurde auf die Γ_7-Komponente verzichtet, deren Beitrag in Systemen mit großer Spin-Bahnaufspaltung Δ vernachlässigbar ist [2]. In Abbildung (2.4) wird deutlich wie stark die einzelnen Blochkomponenten der Envelopefunktion koppeln und zur Envelopefunktion beitragen.

In Abbildung (2.5) sind die Zustände gleicher Klassifikation für einen 150 Å HgTe-Hg$_{0.32}$Cd$_{0.68}$Te-Quantentrog entsprechend aufgetragen. Aufgrund der erhöhten Aufenthaltswahrscheinlichkeit an der Grenzfläche von HgTe und Hg$_{1-x}$Cd$_x$Te werden die Zustände E1 und L1 Grenzflächenzustände genannt.

2.5   Die Berechnung des optischen Absorptionskoeffizienten

Der optische Absorptionskoeffizient wird bestimmt durch die komplexe dielektrische Funktion $\epsilon(\omega)$ und ist gegeben durch:

$$\alpha(\omega) = \frac{\omega}{c} \frac{\sqrt{2}\epsilon_2(\omega)}{\sqrt{\epsilon_1(\omega) + |\epsilon(\omega)|}} \tag{2.7}$$

mit $\epsilon(\omega) = \epsilon_1(\omega) + \mathrm{i}\epsilon_2(\omega)$. Die Dielekterische Funktion $\epsilon(\omega)$ wird mit Hilfe der Kubo-Formel für die dynamische Leitfähigkeit $\sigma(\omega)$ berechnet, wobei sich zunächst der Zusammenhang wie folgt darstellt:

$$\epsilon(\omega) = \epsilon_R(\omega) + \mathrm{i}\frac{\sigma(\omega)}{\omega\epsilon_0} \tag{2.8}$$

In Gleichung 2.8 ist $\epsilon_R(\omega)$ der Beitrag des Gitters und aller energetisch entfernter Dipolübergänge enthalten und ist im Bereich der untersuchten Absorptionsspektren konstant, Seite [143].

$$
\begin{aligned}
\sigma(\omega) &= \frac{e^2}{V} \int_0^\infty \mathrm{e}^{-\mathrm{i}\omega t}\mathrm{d}t \int_0^\beta \mathrm{d}\lambda\, \mathrm{Sp}[\rho v(\mathrm{i}\hbar\lambda)v(t)] \\
&= \pi\frac{e^2}{V\omega} \sum_{\alpha,\beta} |v_{\alpha\beta}|^2 \delta(\hbar\omega + \hbar\omega_{\alpha\beta}(f_\alpha - f_\beta)) \\
&\quad + \mathrm{i}\frac{e^2\hbar}{V} \sum_{\alpha,\beta} |v_{\alpha\beta}|^2 \frac{1}{\hbar\omega_{\alpha\beta}} \frac{(f_\alpha - f_\beta)}{\hbar\omega + \hbar\omega_{\alpha\beta}}
\end{aligned}
$$

Hier steht α und β für den Summenindex über alle Subbandzustände $F_\alpha = F_n(\mathbf{k})(z)$ mit der Energie $E_\alpha = E_n(\mathbf{k})$, $\hbar\omega_{\alpha\beta} = E_\alpha - E_\beta$ und f ist die Fermi-Funktion. Der Dipoloperator zur Berechnung der optischen Übergänge ist im $\mathbf{k} \cdot \mathbf{p}$-Bandstrukturschema durch den Geschwindigkeitsoperator gegeben

$$\mathbf{v} = \frac{1}{\hbar}\frac{\partial H}{\partial \mathbf{k}}. \tag{2.9}$$
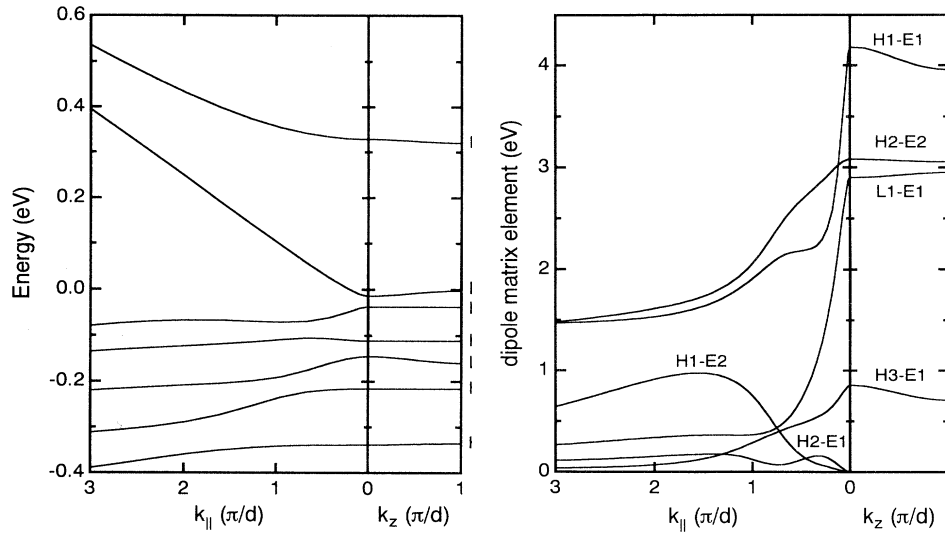
Abbildung 2.6: Normal halbleitende Bandstruktur (links) eines HgTe-Hg$_{0.32}$Cd$_{0.68}$Te-Übergitters und einige berechnete Dipolübergänge (rechts) als Funktion des Wellenvektors **k** .

Der Hamilton-Operator H ist gegeben durch Gl. (2.5).

In Abbildung (2.6) ist die normal halbleitende Bandstruktur (links) eines HgTe-Hg$_{0.32}$Cd$_{0.68}$Te-Übergitters, Seite [110] und die Dipolmatrixelemente (rechts) einiger ausgewählter Übergänge gezeigt. Die Dipolmatrixelemente sind nur schwach veränderlich mit der Minibanddispersion k_z, während in der Ebene senkrecht dazu, die Dipolmatrixelemente sehr stark von dem Wellenvektor $k_{\parallel}$ abhängen. Manche Übergänge, die symmetriebedingt bei $k_{\parallel} = 0$ verboten sind, schalten auf Grund der Mischung der Zustände mit endlichem $k_{\parallel}$ ein.

Weitere Beispiele für die **k**-Abhängigkeit der Dipolmatrixelemente, die erstmals vom Autor für Typ-III-Halbleiterheterostrukturen im Kane-Modell ausgerechnet wurden, sind auf den Seiten [91] und [143] diskutiert.

Im nächsten Kapitel wird der experimentell bestimmte Absorptionskoeffizient α mittels Infrarot-Fourier-Transmissionsspektroskopie mit den berechneten Absorptionskoeffizienten verglichen. Es zeigt sich, dass die gemessenen Dipolübergänge im untersuchten Energiebereich den Vorhersagen der Bandstrukturrechnung quantitativ zugeordnet werden können.

Kapitel 3

Optische Eigenschaften von Typ-III-Halbleiterheterostrukturen

In diesem Kapitel werden die wesentlichen Ergebnisse aus dem Vergleich der berechneten Absorptionskoeffizienten von HgTe-Hg$_{1-x}$Cd$_x$Te-Übergitter mit denen aus Infrarotabsorptionsexperimenten zusammengefasst. Es zeigt sich, dass auf Grund der quantitativen Übereinstimmung, die gemessenen Intersubbandübergänge zugeordnet und aus den berechneten Bandstrukturen eindeutig identifiziert werden können.

Darüber hinaus stellt der Vergleich unter Beweis, dass auch für die hier untersuchten Typ-III-Halbleiterheterostrukturen die Envelopefunktionennäherung eine leistungsfähige Methode zur Berechnung von elektronischen Zuständen komplexer Bandstrukturen darstellt.

Die Berechnungen von Landau-Zuständen zum Verständnis der magneto-optischen Messdaten und der Magneto-Transportuntersuchungen an dotierten HgTe-Hg$_{1-x}$Cd$_x$Te-Quantentrogstrukturen führt über die Untersuchungen in diesem Kapitel hinaus und wurde von Pfeuffer-Jeschke [2], auf der Grundlage der hier vorgestellten Arbeiten und in Anlehnung an die Arbeiten des Autors zu IV-IV-Halbleiterheterostrukturen im Anhang [B], sehr erfolgreich durchgeführt.

3.1 Der optische Absorptionskoeffizient von HgTe-Hg$_{1-x}$Cd$_x$Te-Übergittern

Das Infrarotspektrum des Absorptionskoeffizienten $\alpha(\omega)$ zeigt bei normal halbleitenden HgTe-Hg$_{1-x}$Cd$_x$Te-Übergittern im untersuchten Frequenzbereich des nahen und mittleren Infrarot zwei charakteristische Absorptionskanten, die den Dipolübergängen H1-E1 und L1-E1 der zugehörigen Energien der Subbandfunktionen H1, L1 und E1 zugeordnet werden können. Diese eindeutige Zuordnung erfolgt nicht allein auf Grund der energetischen Lage, sondern vielmehr aus der exzellenten Übereinstimmung der absoluten Höhe der Absorptionskanten, die sich bei der Berechnung des Absorptionskoeffizienten allein aus der zugrundegelegten Bandstruktur für Hg$_{1-x}$Cd$_x$Te und den daraus berechneten Dipolmatrixelementen ergeben.
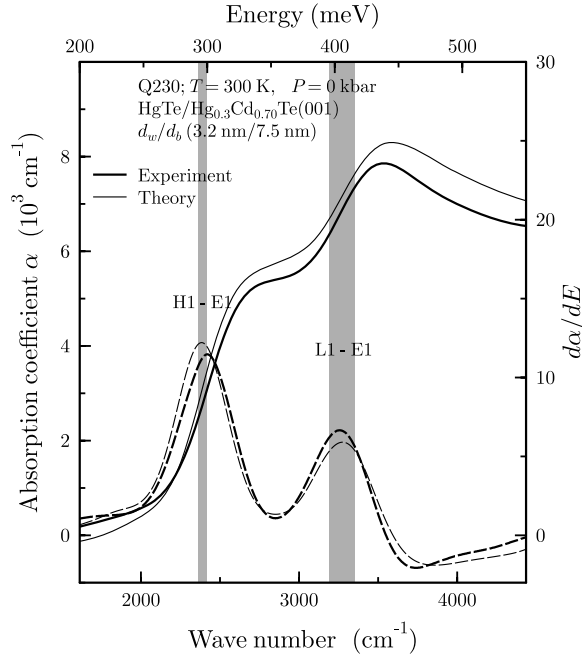
Abbildung 3.1: Absorptionskoeffizient als Funktion der Wellenzahl für ein HgTe-Hg$_{0,3}$Cd$_{0,7}$Te-Übergitter. Die Dicke der HgTe-Schicht ist dabei mit d_w und die der Hg$_{1-x}$Cd$_x$Te-Schicht mit d_b bezeichnet. Die Energien der Intersubbandübergänge fallen mit den Maxima der Ableitung zusammen. Die Breite der berechneten Minibänder bei $k_\parallel = 0$ ist grau gezeichnet [4].

Die energetische Lage des Übergangs H1-E1 hingegen wird im Wesentlichen durch die Dicke der HgTe-Schicht und die Energiedifferenz zwischen H1 und L1 durch den Valenzbandoffset zwischen HgTe und Hg$_{1-x}$Cd$_x$Te bestimmt. In Abbildung (3.1) sind die beiden Absorptionskanten exemplarisch für ein HgTe-Hg$_{0,3}$Cd$_{0,7}$Te-Übergitter mit 100 Perioden gezeigt [4]. Die HgTe-Schichtdicke d_w mit $d_w = 32$ Å und die Hg$_{1-x}$Cd$_x$Te-Schichtdicke d_b mit $d_b = 75$ Å sind mittels Röntgendiffraktometrie bestimmt.

Den Absorptionskanten in der Transmission T sind in der Infrarot-Fourier-Spektroskopie bei den Probendicken d mit $d \approx 1$ μm geometrische Interferenzeffekte überlagert, Seite [107], die selbst mit einer aufwendigen Kramers-Kronig-Transformation nicht vollständig unterdrückt werden können. Die genaue energetische Lage und Form der Absorptionskanten kann jedoch mittels eines Doppelexperiments bestimmt werden. Dazu wird die Transmission T für zwei leicht unterschiedliche Temperaturen gemessen. Es gilt in sehr guter Näherung [Seite 77]:

$$\frac{\Delta T}{T} \approx d\Delta\alpha. \tag{3.1}$$

Gleichung (3.1) besagt, dass die Änderung des Absorptionskoeffizienten $\Delta\alpha$ mit der Temperatur direkt aus dem Verhältnis der entsprechenden Transmissionspektren bestimmt werden kann. Dabei können die relevanten Übergangsenergien der Minibanddispersion (grau) in Abbildung (3.1) direkt den Maxima von $\Delta\alpha$ zugeordnet werden. Dieses Verfahren wurde sehr erfolgreich auf die Infrarotabsorptionsexperimente zur Bestimmung der hydrostatischen Deformationspoten-
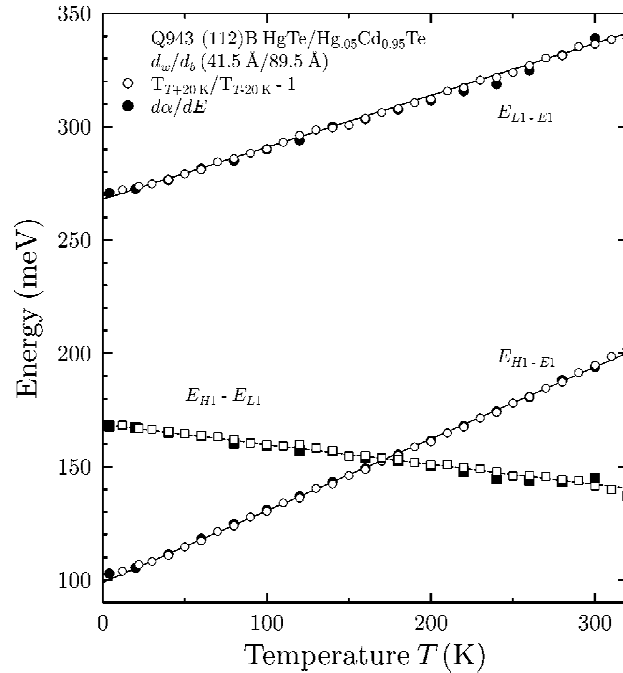
Abbildung 3.2: Experimentell bestimmte Energien der Dipolübergänge H1-E1 und L1-E1 als Funktion der Temperatur für ein (112)B-HgTe-$Hg_{0.05}Cd_{0.95}$-Übergitter. Das Verhalten legt den linearen Temperaturkoeffizienten $\Delta E_{E_1-L_1}/\Delta T$ fest.

ziale von HgTe angewendet, Seite [25] und [70].

3.2 Die Temperaturabhängigkeit des Valenzbandoffsets

Erst die systematischen Untersuchungen der Transmissionsspektren an vielen (001) und (112)B orientierten HgTe-$Hg_{1-x}Cd_x$-Übergittern in sämtlichen Regimen der komplexen Bandstruktur, von der normal halbleitenden bis hin zu den invertiert halbleitenden Strukturen, erlauben die quantitative Bestimmung des Valenzbandoffsets Λ zwischen HgTe und $Hg_{1-x}Cd_x$Te und darüber hinaus dessen Temperaturabhängigkeit.

Diese systematischen Untersuchungen sind in Würzburg möglich, da die Proben mit dem Verfahren der Molekularstrahlepitaxie kontrolliert und nach Wunsch hergestellt werden können.

Die absolute Größe des Valenzbandoffsets bei tiefen Temperaturen wurde nach langjähriger kontroverser Diskussion 1995 erstmals von Truchsess *et. al.* [Seite 107ff], aus magneto-optischen Daten und dem Vergleich mit den vorliegenden Bandstrukturrechnungen des Autors in dem heute gültigen Energiebereich von $\Lambda = (570 \pm 40)$ meV bestimmt.

Die systematischen Untersuchungen von Becker *et. al.*, Seite [76ff] und [87ff], ermöglichten darüber hinaus auch die Temperaturabhängigkeit des Valenzbandoffsets zu bestimmen.

Die Absorptionskanten verschieben mit zunehmender Temperatur zu höheren Energien. Die Differenz der gemessenen Dipolübergänge H1-E1 und L1-E1 verschiebt dabei im untersuchten
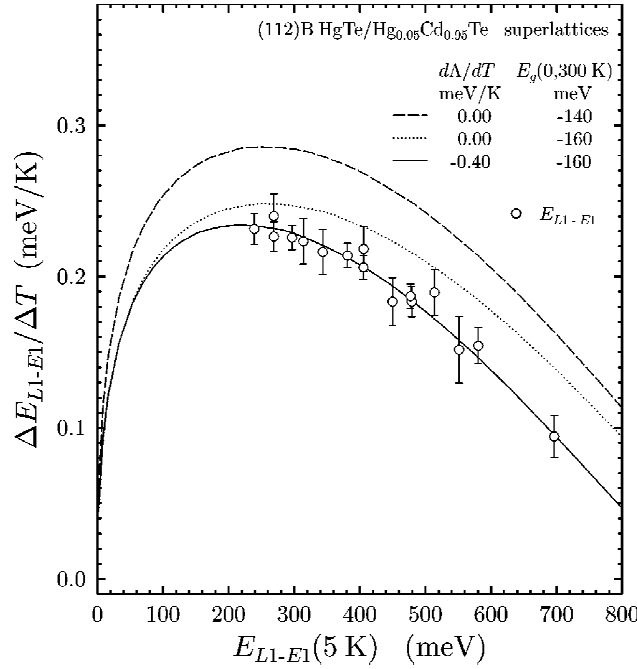
Abbildung 3.3: Experimentell bestimmte lineare Temperaturkoeffizienten als Funktion der Differenz der gemessenen Dipolübergangsenergien bei $T = 5\,\mathrm{K}$ für 13 verschiedene (112)B-HgTe-Hg$_{0.05}$Cd$_{0.95}$-Übergitter mit normal halbleitender Bandstruktur. Die Anpassung an die berechneten Bandstrukturen legt die Temperaturabhängigkeit des Valenzbandoffsets und der negativen Energielücke von HgTe fest (duchgezogene Linie).

Temperaturbereich linear zu niedrigen Energien mit $\Delta E_{E_1-L_1}/\Delta T$. Dieses Verhalten ist in Abbildung (3.2) exemplarisch für ein (112)B-HgTe-Hg$_{0.05}$Cd$_{0.95}$-Übergitter gezeigt.

Dieses gemessene Temperaturverhalten rechtfertig die systematische Betrachtung zu dem linearen Temperaturkoeffizienten $\Delta E_{E_1-L_1}/\Delta T$.

In Abbildung (3.3) ist die Temperaturabhängigkeit des energetischen Abstandes der Absorptionskanten, der lineare Temperaturkoeffizient $\Delta E_{E_1-L_1}/\Delta T$ als Funktion des Abstandes selbst für 13 verschiedene HgTe-Hg$_{1-x}$Cd$_x$-Übergitter aufgetragen.

Die berechnete lineare Temperaturkoeffizient für die beteiligten Subbänder E1 und L1 wird lediglich durch zwei Parameter bestimmt. Das sind der lineare Temperaturkoeffizient des Valenzbandoffsets $\frac{\mathrm{d}\Lambda}{\mathrm{d}T}$ und die Temperaturabhängigkeit der negativen Energielücke von HgTe, $E_g(0,T)$.

Nach der Methode der kleinsten Quadrate zur Anpassung der jeweils 13 berechneten Bandstrukturen an die Messergebnisse ergibt sich für die beiden zu bestimmenden Parameter:

$$\frac{\mathrm{d}\Lambda}{\mathrm{d}T} = (-0,40 \pm 0,04)\,\frac{\mathrm{meV}}{\mathrm{K}} \tag{3.2}$$

und

$$E_g(0, 300\,\text{K}) = (-160 \pm 2)\ \text{meV}. \tag{3.3}$$

Die Ergebnisse sind in Abbildung (3.3) eingetragen und wurden durch systematische Untersuchungen an invertiert halbleitenden HgTe-Hg$_{1-x}$Cd$_x$Te-Übergittern bestätigt [Seite 87ff].

Das Ergebnis aus Gl. (3.3) wurde in die empirische Beziehung der Energielücke von Hg$_{1-x}$Cd$_x$Te, $E_g(x, T)$, aufgenommen [Seite 78]:

$$
\begin{aligned}
E_g(x, T) \;=\;& -303(1-x) + 1606x - 132x(1-x) \\
& +0.1\,T^2 \frac{4.95(1-x) + 3.25x - 3.93x(1-x)}{T + 11(1-x) + 78.7x}\,.
\end{aligned}
$$

3.3 Deformationspotenziale des Halbmetalls HgTe

Die hydrostatischen Deformationspotenziale des Leitungsbandes C und des Valenzbandes a sind wichtige Parameter für die Bestimmung von Verspannungseffekten in Halbleiterheterostrukturen, sie sind aber experimentell nicht direkt zugänglich. Die Differenz $C - a$ hingegen kann aus der Druckabhängigkeit der Energielücke und experimentell aus der Verschiebung der Exzitonenabsorption oder Photolumineszenz in Abhängigkeit des hydrostatischen Druckes bestimmt werden. Diese experimentellen Methoden schlagen bei einem Halbmetall wie HgTe fehl.

Es ist in der vorliegenden Arbeit gelungen aus dem Vergleich der Bandstrukturberechnungen in Abhängigkeit des hydrostatischen Druckes P, die Druckexperimente an HgTe-Hg$_{1-x}$Cd$_x$Te-Übergittern einheitlich zu beschreiben und die Differenz $C - a$ der hydrostatischen Deformationspotenziale von HgTe zu bestimmen.

Die quantitative Beschreibung der optischen Eigenschaften von Halbleiterheterostrukturen aus dem Ansatz, bekannte Volumeneigenschaften ergeben neue und maßgeschneiderte Heterostruktureigenschaften, läßt somit auch den Umkehrschluss zu: Aus bekannten Heterostruktureigenschaften werden unbekannte Volumeneigenschaften bestimmt.

Allgemein werden Verspannungseffekte durch den Formalismus von Bir und Pikus beschrieben, wobei Terme proportional zum Verspannungstensor ϵ in den Hamilton-Operator aus Gl. (2.5) hinzuaddiert werden: $H_{nn'} + H_{nn'}^{BP}$. Der Bir-Pikus-Hamilton-Operator H^{BP} wird formal durch folgende Substitution der Matrixelemente in Gl. (2.5) aufgestellt:

$$k_i k_j \rightarrow \epsilon_{ij}. \tag{3.4}$$

Die Komponenten des Verspannungstensors ϵ_{ij} transformieren wie das Produkt der Wellenvektorkomponenten $k_i k_j$. Die Bandstrukturparameter in Gl. (2.5) werden formal durch die Deformationspotenziale ersetzt:

$$\frac{\hbar^2}{2m_0}(2F + 1) \;\rightarrow\; C,$$

$$
\begin{aligned}
\frac{\hbar^2}{m_0}\gamma_1 &\rightarrow -2a, \\
\frac{\hbar^2}{m_0}\gamma_2 &\rightarrow -b, \\
\frac{\hbar^2}{m_0}\gamma_3 &\rightarrow -\frac{1}{\sqrt{3}}d,
\end{aligned}
\tag{3.5}
$$

mit den bereits eingeführten hydrostatischen Deformationspotenzialen C und a und den uniaxialen Deformationspotenzialen b and d.

Der Bir-Pikus-Hamilton-Operator für eine [001]-Halbleiterheterostruktur ergibt sich mit der beschriebenen Substitution der Matixelemente aus Gl. (2.5) zu [3]:

$$
H^{BP} = \begin{pmatrix}
T_\epsilon & 0 & 0 & 0 & 0 & 0 & 0 & 0 \\
0 & T_\epsilon & 0 & 0 & 0 & 0 & 0 & 0 \\
0 & 0 & U_\epsilon + V_\epsilon & S_\epsilon & R_\epsilon & 0 & -\frac{1}{\sqrt{2}}S_\epsilon & -\sqrt{2}R_\epsilon \\
0 & 0 & S_\epsilon^\dagger & U_\epsilon - V_\epsilon & 0 & R_\epsilon & \sqrt{2}V_\epsilon & \sqrt{\frac{3}{2}}S_\epsilon \\
0 & 0 & R_\epsilon^\dagger & 0 & U_\epsilon - V_\epsilon & -S_\epsilon & \sqrt{\frac{3}{2}}S_\epsilon^\dagger & -\sqrt{2}V_\epsilon \\
0 & 0 & 0 & R_\epsilon^\dagger & -S_\epsilon^\dagger & U_\epsilon + V_\epsilon & \sqrt{2}R_\epsilon^\dagger & -\frac{1}{\sqrt{2}}S_\epsilon^\dagger \\
0 & 0 & -\frac{1}{\sqrt{2}}S_\epsilon^\dagger & \sqrt{2}V_\epsilon & \sqrt{\frac{3}{2}}S_\epsilon & \sqrt{2}R_\epsilon & U_\epsilon & 0 \\
0 & 0 & -\sqrt{2}R_\epsilon^\dagger & \sqrt{\frac{3}{2}}S_\epsilon^\dagger & -\sqrt{2}V_\epsilon & -\frac{1}{\sqrt{2}}S_\epsilon & 0 & U_\epsilon
\end{pmatrix}
$$

mit

$$
\begin{aligned}
T_\epsilon &= C \operatorname{Sp}(\epsilon), \\
U_\epsilon &= a \operatorname{Sp}(\epsilon), \\
V_\epsilon &= \frac{1}{2}b(\epsilon_{xx} + \epsilon_{yy} - 2\epsilon_{zz}), \\
S_\epsilon &= -d(\epsilon_{xz} - i\epsilon_{yz}), \\
R_\epsilon &= -\frac{\sqrt{3}}{2}b(\epsilon_{xx} - \epsilon_{yy}) + id\epsilon_{xy}
\end{aligned}
\tag{3.6}
$$

und der üblichen Abkürzung: $\operatorname{Sp}(\epsilon) = \epsilon_{xx} + \epsilon_{yy} + \epsilon_{zz}$.

Das vorgestellte Verfahren zur Aufstellung des Bir-Pikus-Hamilton-Operators kann aus den entsprechenden Symmetrie-Überlegungen für eine beliebige Richtung [hkl] verallgemeinert werden und ist für die häufig untersuchten [112]-Heterostrukturen für [kkl] bei Pfeuffer-Jeschke [2] angegeben.

Die Effekte einer uniaxialen Verspannung sind in den untersuchten HgTe-Hg$_{1-x}$Cd$_x$Te-Übergittern auf Grund der sehr guten Gitteranpassung vernachlässigbar, sodass die Terme proportional zu den uniaxialen Deformationspotenzialen b und d in Gl. (3.6) verschwinden. Die Bir-Pikus-Hamilton-Matrix H^{BP} ist bei einer hydrostatischen Deformation diagonal und enthält nur noch Elemente, die proportional zur Spur des Verspannungstensors $\operatorname{Sp}(\epsilon)$ ist.
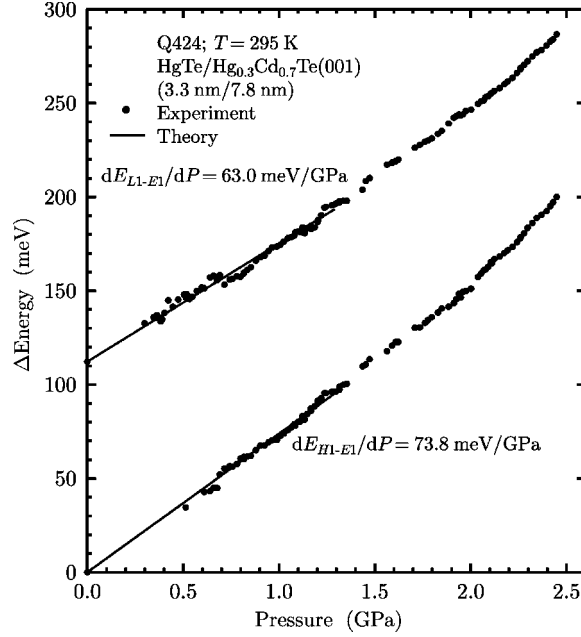
Abbildung 3.4: Druckabhängigkeit der Intersubbandübergänge H1-E1 und L1-E1 für ein HgTe-$\mathrm{Hg_{0.3}Cd_{0.7}Te}$-Übergitter mit einer Trogbreite von 33 Å (HgTe) und einer Barrierenbreite 78 Å ($\mathrm{Hg_{0.3}Cd_{0.7}Te}$).

Die Abhängigkeit von ϵ vom hydrostatischen Druck P ist dabei über die Zustandsgleichung von Murnaghan gegeben:

$$\mathrm{Sp}(\epsilon) = -1 + (1 + \frac{B_1}{B_0}P)^{-1/B_1}, \tag{3.7}$$

mit dem Bulkmodul $B(P) = B_0 + B_1 P$. Die Werte von B_0 und B_1 sind aus röntgen-kristallographischen Experimenten an HgTe und CdTe bekannt, und werden für $\mathrm{Hg_{1-x}Cd_xTe}$ linear interpoliert [4]. Die Ergebnisse der Druckexperimente an zwei HgTe-$\mathrm{Hg_{0.3}Cd_{0.7}Te}$- Übergittern sind in [4] und Seite [68ff] zusammengestellt.

Der Vergleich der experimentell beobachteten Verschiebung der Intersubbandübergänge H1-E1 und L1-E1 mit den Berechnungen des druckabhängigen Absorptionskoeffizienten liefert:

$$C - a = (3,69 \pm 0,10) \text{ eV}. \tag{3.8}$$

Aus der Verringerung der energetischen Aufspaltung von L1 und H1 mit ansteigendem hydrostatischen Druck wird die Druckabhängigkeit des Valenzbandoffsets Λ bestimmt zu:

$$\frac{\mathrm{d}\Lambda}{\mathrm{d}P} = (-25 \pm 2) \frac{\mathrm{meV}}{\mathrm{GPa}}. \tag{3.9}$$

Die Druckabhängigkeit des Heterostrukturparameters Λ kann auf Grund der praktisch gleichen Werte für die Bulkmoduln $B(P)$ von HgTe und CdTe auf die Differenz der Deformationspotenziale $a^{\mathrm{HgTe}} - a^{\mathrm{CdTe}}$ zurückgeführt werden. Es gilt:
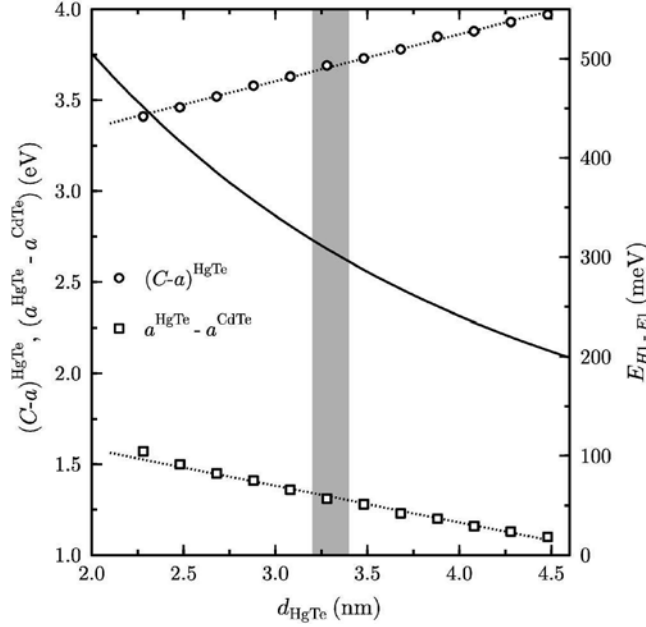
Abbildung 3.5: Werte von $C - a$ und $a^{\text{HgTe}} - a^{\text{CdTe}}$ als Funktion der HgTe-Schichtdicke d_{HgTe} die notwendig sind, um die experimentell bestimmte Druckabhängigkeit der Intersubbandübergänge eines HgTe-Hg$_{0.3}$Cd$_{0.7}$Te-Übergitters zu reproduzieren.

$$a^{\text{HgTe}} - a^{\text{CdTe}} \approx -B_0^{\text{CdTe}}\frac{\text{d}\Lambda}{\text{d}P} \qquad (3.10)$$

und hieraus mit $B_0 = 42,5$ GPa der Wert für

$$a^{\text{HgTe}} - a^{\text{CdTe}} = (1,31 \pm 0,10) \text{ eV}. \qquad (3.11)$$

Die Aussage „Aus bekannten Heterostruktureigenschaften werden unbekannte Volumenparameter abgeleitet", wird aber erst dann überzeugend und als Untersuchungsmethode zuverlässig, wenn die Bestimmung der Volumenparameter, hier die Deformationspotenziale, nur schwach von den Heterostrukturparametern abhängen. Das ist vor allem die Schichtdicke des zu untersuchenden Volumenmaterials, hier des Halbmetalls HgTe.

In Abbildung (3.5) sind die berechneten Werte für die hydrostatischen Deformationspotenziale von HgTe $C - a$ und $a^{\text{HgTe}} - a^{\text{CdTe}}$ um die experimentell bestimmten Intersubbandübergangsenergien zu reproduzieren, als Funktion der Dicke der HgTe-Schicht d_{HgTe} aufgetragen. Eine Unsicherheit in der Schichtdicke von ± 5 Å, also weit oberhalb der experimentellen Genauigkeit von röntgen-diffraktometrischen Untersuchungen, liefert lediglich einen Fehler in der Bestimmung der Deformationspotenziale von $\pm 0,10$ eV. Dies bestätigt in beeindruckender Weise die getroffene Aussage.

Kapitel 4

Zusammenfassung

Seit drei Jahrzehnten wird die Envelopefunktionennäherung (EFA) sehr erfolgreich bei der Interpretation der experimentellen Ergebnisse von (magneto)-optischen Untersuchungen an Halbleiterheterostrukturen eingesetzt. Der Erfolg basiert auf der effektiven Beschreibung der quantisierten elektronischen Zustände an Halbleitergrenzflächen, in Quantentrögen und Übergittern und der Einzigartigkeit, zur Berechnung der experimentellen Ergebnisse, die Abhängigkeit von äußeren Parametern, wie der Temperatur und des hydrostatischen Druckes, aber auch eines elektrischen und magnetischen Feldes, wie auch von freien Ladungsträgern, ein zu arbeiten. Die sehr gute quantitative Übereinstimmung der theoretischen Berechnungen in der Envelopefunktionennäherung und vieler experimenteller Messergebnisse an Halbleiterheterostrukturen baut auf der quantitativen Bestimmung der relevanten Bandstrukturparameter in der $\mathbf{k} \cdot \mathbf{p}$-Störungstheorie zur Beschreibung der elektronischen Eigenschaften der beteiligten Volumenhalbleiter auf.

Zum Verständnis vieler Experimente an Volumenhalbleitern ist es dabei nicht notwendig, die Bandstruktur in der gesamten Brillouin-Zone zu kennen, sondern lediglich in der Umgebung der relevanten Bandextrema. Bei den vorliegenden Experimenten an den II-VI-Halbleitermaterialien, HgTe und CdTe, die in der Zinkblendestruktur kristallisieren, ist dies – wie bei den III-V-Halbleitermaterialien, GaAs und GaAlAs – der Γ-Punkt, im Zentrum der Brillouin-Zone und dessen Bandextrema, dem Minimum des Leitungsbandes Γ_6 und dem Maximum des Valenzbandes Γ_8.

Seit 1988 werden mit dem Verfahren der Molekularstrahlepitaxie (MBE) am Physikalischen Institut der Universität Würzburg Halbleiterheterostrukturen aus dem Halbleitermaterialsystem $Hg_{1-x}Cd_xTe$ hergestellt. Mit diesem Verfahren ist es möglich, Bandstrukturen mit spezifischen Eigenschaften herzustellen (band structure engineering). Unter diesen neuen Materialien stellen die Typ-III-Übergitter eine besondere Klasse dar. Bei diesen Materialstrukturen wird eine nur wenige Atomlagen dicke Schicht von 30 Å bis 100 Å aus dem Halbmetall HgTe in eine Legierung aus $Hg_{1-x}Cd_xTe$ eingebettet und zu einem Übergitter aufgebaut. Das gezielte Wachstum im MBE-Verfahren ermöglicht nun die Variation der Bandstruktur und damit die optische Absorption im infraroten Spektralbereich.

Aus den Berechnungen der Bandstruktur dieser Typ-III-Übergitter in der Envelopefunktionsnäherung und der entsprechenden Absorptionsspektren im Vergleich zu den experimentellen Ergeb-

nissen der Infrarot-Fourier-Spektroskopie und der röntgen-diffraktometrischen Bestimmung der HgTe-Schichtdicke, ist es erstmals gelungen, den charakteristischen Strukturparameter, den Valenzbandoffset Λ sehr genau zu bestimmen und darüber hinaus dessen Temperaturabhängigkeit anzugeben: $\Lambda(T) = (570 - 0,40\,T/\text{K})\,\text{meV}$.

Die Strukturen in den Absorptionsspektren können quantitativ den Dipolübergängen der beteiligten Subbänder der Typ-III-Übergitter zugeordnet werden. Insbesondere können die Grenzflächenzustände identifiziert werden.

Die quantitative Beschreibung der optischen Eigenschaften von Halbleiterheterostrukturen aus dem Ansatz, bekannte Volumeneigenschaften ergeben neue und maßgeschneiderte Heterostruktureigenschaften, läßt auch den Umkehrschluss zu: Aus bekannten Heterostruktureigenschaften werden unbekannte Volumeneigenschaften bestimmt. Aus diesem neuen Ansatz heraus wurden erstmals Druckexperimente an Typ-III-Übergitter durchgeführt und daraus die Differenz der hydrostatischen Deformationspotenziale $C - a$ von HgTe sehr genau zu $(-3,69 \pm 0,10)\,\text{eV}$ bestimmt.

Die Berechnung der elektronischen Zustände in Heterostrukturen wurde in der Envelopefunktionsnäherung durchgeführt und als numerisches Eigenwertproblem über die Matrixmethode formuliert, einem Variationsverfahren, in dem die einzelnen Komponenten der Envelopefunktionen nach einem vollständigen Funktionensystem entwickelt werden.

Auf Grund der schlechten Konvergenz bei der Berechnung der Grenzflächenzustände in Typ-III-Quantentrogstrukturen wurde ein neues Funktionensystem konstruiert, welches für sämtliche, untersuchten Heterostrukturen – vom P-Typ-Inversionskanal in Germanium-Bikristallen, über GaAs-GaAlAs-Quantentrogstrukturen bis hin zu Typ-III-Übergittern – die erforderliche Konvergenz zeigt. Die einzelnen Komponenten der Envelopefunktionen werden durch sehr wenige, 10 - 20, Basisfunktionen sehr genau approximiert. Pfeuffer-Jeschke [1] konnte so die elektronischen Zustände im Magnetfeld, die Landau-Zustände, für Typ-III-Halbleiterheterostrukturen selbstkonsistent berechnen.

[1] A. Pfeuffer-Jeschke, Dissertation, Physikalisches Institut der Univerität Würzburg, (2000)

4.1   Electron states in type III semiconductor heterostructures

For three decades the envelope function approximation (EFA) has been very successful in the interpretation of experimental results of magneto-transport and optical investigations of semi-conducting heterostructures. Its success is based on the ability to describe the quantized electron states in semiconductor interfaces, quantum wells and superlattices combined with its unique ability to include the influence of external parameters such as temperature and hydrostatic pressure as well as electric and magnetic fields and the incorporation of free charge carriers. The excellent quantitative agreement between theoretical calculations using the envelope function approximation and numerous experimental results depends on the quantitative determination of the corresponding band structure parameters in the $\mathbf{k} \cdot \mathbf{p}$ perturbation theory required to correctly describe the electronic properties of the bulk semiconductors in the heterostructure in question.

In order to understand numerous experiments on bulk semiconductors it is not necessary to know the band structure in the entire Brillouin zone. Knowledge is merely required near the corresponding band structure extrema. In the experiments considered here on the II-VI materials of HgTe and CdTe, which crystallize in the zinc blende structure, as well as III-V materials such as GaAs and GaAlAs, the Γ- point in the center of the Brillouin zone is of primary importance, where the Γ_6 conduction band has a minimum and the Γ_8 valence band a maxima.

Since 1988 Molecular beam epitaxy (MBE) has been employed at the physics department (Physikalisches Institut) of the University of Würzburg to produce semiconducting heterostructures based on $Hg_{1-x}Cd_xTe$. With this method it is possible to produce materials with a particular band structure and specific properties (band structure engineering). Among these new heterostructures, type III superlattices represent an unique class. In these structures, thin layers (30 - 100) Å of only a few atomic layers of the semimetallic HgTe are alternated with layers of the $Hg_{1-x}Cd_xTe$ alloy to form a superlattice. The resulting growth by the MBE method permits superlattices with the desired band structure to be produced and the corresponding optical absorption in the infrared spectral range.

From a comparison of the band structure of these type III superlattices by means of the envelope function approximation and the resulting absorption spectrum with the experimental results from infrared spectroscopy it was possible for the first time to determine a precise value for the valence band offset, Λ, a characteristic heterostructure parameter, as well as its temperature dependence, i.e., $\Lambda(T) = (570 - 0.40\,T/\mathrm{K})\,\mathrm{meV}$. Hereby HgTe thicknesses were determined by high resolution x-ray diffraction.

Structure in the absorption spectra could be quantitatively assigned to dipole transitions between the involved subbands of the type III superlattice.

The quantitative description of the optical properties of semiconducting heterostructures from the Ansatz that known bulk properties result in new and tailor made properties can also be stated conversely; from known heterostructure properties unknown properties of bulk materials can be determined. Using this corollary, first direct experimental determination of the difference of the hydrostatic deformation potentials, $C - a$, of HgTe with high precision, $(-3.69 \pm 0.10)\,\mathrm{eV}$, by means of hydrostatic pressure experiments on type III superlattices were carried out.

Calculations of the electron states in heterostructures were carried out in this dissertation.

Hereby the envelope function approximation was employed whereby the numerical eigenvalue problem was formulated in terms of the matrix method in which the individual components of the envelope functions were expanded from a complete set of functions.

Because of the poor convergence in the calculations of interface states in type III quantum well structures, a new set of functions was constructed, which results in the required convergence for all heterostructures: from a p-type inversion channel in Ge bi-crystals, including GaAs-GaAlAs quantum well structures, to type III superlattices. The individual components of the envelope functions were very precisely approximated by only a very few, 10 - 20, basis functions. This allowed Pfeuffer-Jeschke [1] to self-consistently calculate the electron states in a magnetic field, Landau levels, for type III heterostructures.

[1] A. Pfeuffer-Jeschke, Ph.D. thesis, Physikalisches Institut der Univerität Würzburg, (2000)

Danksagung

Bei Herrn Prof. Dr. Gottfried Landwehr bedanke ich mich für die erlebnisreichen und schönen Jahre an seinem Lehrstuhl für Experimentelle Physik III am Physikalischen Institut der Universität Würzburg. In dieser Zeit habe ich viele Mitarbeiter an der Fakultät für Physik und Astronomie kennen gelernt und durfte in vielen Projekten mit ihnen wissenschaftlich arbeiten: unvergessen die Arbeiten mit Herrn Dr. Eike Bangert, der leider viel zu früh verstorben ist.

Einem Mitarbeiter gilt mein besonderer Dank: Herr Dr. Charles Becker hat die erforderlichen Experimente organisiert und durchgeführt und meine Arbeiten in seiner herzlichen Art unterstützt und in Geduld begleitet.

Anhang A

Legendre-Approximation

Die grundlegende Idee der Matrixmethode zur Berechnung der Envelopefunktion elektronischer Zustände in Halbleiterheterostukturen zeigt sich im Konstruktionsprinzip der Basisfunktionen: Die Envelopefunktion wird nach einem vollständigen Satz lokal orthogonaler Funktionen entwickelt [2]. Als Bausteine dieser Entwicklungsfunktionen haben sich die Legendrepolynome [12] bestens bewährt. In diesem Anhang sind daher einige nützliche Beziehungen der Legendrepolynome aufgelistet, soweit sie für die numerische Umsetzung der Matrixmethode benötigt werden. Darüber hinaus werden wesentliche Eigenschaften der Legendrepolynome im Zusammenhang mit der Approximation von Funktionen diskutiert.

Wir beginnen mit der Formel von Rodriguez [12], die als Definitionsgleichung der Legendrepolynome angesehen werden kann

$$ p_i(x) := \frac{1}{2^i i!} \frac{\mathrm{d}^i}{\mathrm{d}x^i} \left[(x^2 - 1)^i \right] \qquad \text{für} \quad i = 0, 1, \ldots $$

Damit lauten die ersten Legendrepolynome explizit:
$p_0(x) = 1$, $p_1(x) = x$, $p_2(x) = \frac{1}{2}(3x^2 - 1)$, $p_3(x) = \frac{1}{2}(5x^3 - 3x)$, $p_4(x) = \frac{1}{8}(35x^4 - 30x^2 + 3), \ldots$.
Die Legendrepolynome bilden ein vollständiges orthogonales Funktionensystem im Intervall $I = [-1, 1]$[1]. Aus der Formel von Rodriguez lassen sich die beiden grundlegenden Rekursionsbeziehungen der Legendrepolynome herleiten. Wir geben sie an dieser Stelle an:

$$
\begin{aligned}
p_{-1}(x) &\equiv 0 \\
p_0(x) &\equiv 1 \\
p_{i+1}(x) &= \frac{2i+1}{i+1} x p_i(x) - \frac{i}{i+1} p_{i-1}(x) \\
& \qquad\qquad\qquad\qquad \text{für} \quad i \geq 0 \\
\frac{\mathrm{d}}{\mathrm{d}x} p_{i+1}(x) &= \frac{\mathrm{d}}{\mathrm{d}x} p_{i-1}(x) + (2i+1) p_i(x)
\end{aligned}
$$

(A.1)

(A.2)

---

[1]Die Legendrepolynome bilden eine Hilbertbasis [13]. Sie spannen den Hilbertraum $\mathbf{L}^2[-1, 1]$ der quadratintegrablen Funktionen im Intervall $I = [-1, 1]$ auf. Das Skalarprodukt ist definiert als $< n'|n > := \int_{-1}^{1} f_{n'}(x) f_n(x)\, \mathrm{d}x$.

In Kenntnis dieser Rekursionsbeziehungen wird die Berechnung der Integrale, die wir im Rahmen der Matrixmethode benötigen, sehr vereinfacht. Die rekursive Berechnung kann häufig analytisch oder numerisch exakt durchgeführt werden. Weiterhin kann die Anwendung von Rekursionen in der folgenden Darstellung auf andere Funktionensysteme abgebildet werden. Am Ende des letzten Abschnitts wird dies für das Orthogonalsystem der Laguerrepolynome gezeigt.

A.1 Matrixelemente

Wir benötigen für die numerische Umsetzung der Matrixmethode die Berechnung der folgenden Integraltypen:

$$I_{i',i}^{(0)}(f) \quad := \quad \int_{-1}^{1} f(x) p_{i'}(x) p_i(x) \, \mathrm{d}x \tag{A.3}$$

$$I_{i',i}^{(1)}(f) \quad := \quad \frac{1}{2} \int_{-1}^{1} f(x) \left[p_{i'}(x) \frac{\mathrm{d}}{\mathrm{d}x} p_i(x) - p_i(x) \frac{\mathrm{d}}{\mathrm{d}x} p_{i'}(x) \right] \mathrm{d}x \tag{A.4}$$

$$I_{i',i}^{(2)}(f) \quad := \quad \int_{-1}^{1} f(x) \frac{\mathrm{d}}{\mathrm{d}x} p_{i'}(x) \frac{\mathrm{d}}{\mathrm{d}x} p_i(x) \, \mathrm{d}x \tag{A.5}$$

Die Integrale $I_{i',i}^{(j)}(f)$ erfüllen unter Indexvertauschung die Symmetrierelationen

$$I_{i,i'}^{(j)}(f) = (-1)^j I_{i',i}^{(j)}(f) \qquad \text{für} \quad j = 0, 1, 2 \quad . \tag{A.6}$$

Im weiteren können wir uns daher bei der Anwendung der Rekursionsbeziehungen Gl.(A.1) und Gl.(A.2) auf den Fall $i' \geq i$ beschränken. Aus der Symmetrierelation Gl.(A.6) folgt für $j = 1$ sofort:

$$I_{i,i}^{(1)}(f) = 0$$

Die Gleichung (A.1) führt auf eine Rekursionsbeziehung der Integrale $I_{i',i}^{(0)}(f)$:

$$\frac{i+1}{2i+1} I_{i',i+1}^{(0)}(f) + \frac{i}{2i+1} I_{i',i-1}^{(0)}(f) - \left[\frac{i'+1}{2i'+1} I_{i'+1,i}^{(0)}(f) + \frac{i'}{2i'+1} I_{i'-1,i}^{(0)}(f) \right] = 0 \tag{A.7}$$

Eine genaue Inspektion von Gl.(A.7) zeigt, daß eine Auswertung der Rekursion nur durch Vorgabe einiger Integrale möglich ist. Beschränken wir uns auf $i', i = 0, 1, \ldots, N-1$, so sind $N \times N$ Integrale zu berechnen, die wir in einem entsprechenden Matrixschema anordnen. Die Vorgabe der $I_{i,0}^{(0)}(f)$ für $i = 0, 1, \ldots, N-1$ reicht dabei nicht aus, wir müssen zusätzlich die $I_{i,i}^{(0)}(f)$ für $i = 1, 2, \ldots, N-1$ angeben, d. h. es müssen $2N - 1$ Matrixelemente vorgegeben werden. Die Matrixelemente $I_{i,0}^{(0)}(f)$ entsprechen bis auf einen konstanten Faktor den Legendrekoeffizienten der Funktion $f(x)$, die in Abschnitt A.2 im Zusammenhang mit der Approximation von Funktionen durch Legendrepolynome diskutiert werden. Die Matrixelemente $I_{i,i}^{(0)}(f)$ sind dagegen nicht direkt zugänglich. Es ist daher viel geschickter die Rekursionsbeziehung Gl.(A.7) für das $N \times N$ Matrixschema mit der Angabe der Integrale $I_{i,0}^{(0)}(f)$ für $i = 0, 1, \ldots, 2N - 2$ zu starten. Dies erfordert lediglich die Kenntnis der ersten $2N - 1$ Legendrekoeffizienten von $f(x)$, wir werden später noch einmal auf diesen wichtigen Sachverhalt zurückkommen.

Die beiden Integraltypen $I_{i',i}^{(1)}(f)$ und $I_{i',i}^{(2)}(f)$ aus Gln.(A.4) und (A.5) enthalten jeweils die erste Ableitung der Legendrepolynome, so daß die Rekursionsbeziehungen der Matrixelemente im $N \times N$ Matrixschema aus Gl.(A.2) gewonnen werden. Wir fassen die Ergebnisse für $j = 1, 2$ zusammen:

$$I_{i'+1,i+1}^{(j)}(f) - I_{i'-1,i+1}^{(j)}(f) - \left[I_{i'+1,i-1}^{(j)}(f) - I_{i'-1,i-1}^{(j)}(f) \right] = c_{i'+1,i+1}^{(j)}(f) \quad \text{für} \quad j = 1, 2 \quad \text{(A.8)}$$

$$
\begin{aligned}
c_{i'+1,i+1}^{(1)}(f) &:= \frac{2i+1}{2} \left[I_{i'+1,i}^{(0)}(f) - I_{i'-1,i}^{(0)}(f) \right] - \frac{2i'+1}{2} \left[I_{i',i+1}^{(0)}(f) - I_{i',i-1}^{(0)}(f) \right] \\
c_{i'+1,i+1}^{(2)}(f) &:= (2i'+1)(2i+1) I_{i',i}^{(0)}(f)
\end{aligned}
\quad \text{(A.9)}
$$

Das Symmetrieverhalten der $c_{i',i}^{(j)}(f)$ unter Indexvertauschung lautet: $c_{i,i'}^{(1)}(f) = -c_{i',i}^{(1)}(f)$ und $c_{i,i'}^{(2)}(f) = c_{i',i}^{(2)}(f)$. Mit Gleichung (A.8) ist die Berechnung der benötigten Integraltypen über die Definition der $c_{i',i}^{(j)}(f)$ aus Gl.(A.9) insgesamt auf die Bestimmung der Legendrekoeffizienten von $f(x)$ reduziert. Die Rekursion der Matrixelemente $I_{i',i}^{(j)}(f)$ mit $j = 1, 2$ wird gestartet durch den folgenden einfachen Zusammenhang:

$$I_{i'+1,0}^{(j)}(f) - I_{i'-1,0}^{(j)}(f) = c_{i'+1,0}^{(j)}(f) \qquad \text{für} \quad j = 1, 2$$

Geben wir noch an, daß für $i', i < 0$ gilt: $I_{i',i}^{(j)}(f) \equiv 0$, so wird die Berechnung der gerade diskutierten Integrale innerhalb des $N \times N$ Matrixschemas durchgeführt.

Wir halten fest: Die Matrixelemente $I_{i',i}^{(j)}(f)$ für $j = 0, 1, 2$ im $N \times N$ Matrixschema sind über die entspechenden Rekursionsformeln Gln.(A.7) und (A.8) verknüpft und durch Vorgabe der ersten $2N - 1$ Legendrekoeffizienten $(\propto I_{i,0}^{(0)}(f))$ exakt bestimmt. Das aber heißt, daß in dem $N \times N$ Matrixschema der Funktion $f(x)$ ausschließlich die Information der ersten $2N - 1$ Legendrekoeffizienten enthalten ist, zusätzliche Koeffizienten müssen nicht berechnet werden.

Ein wichtiges Beispiel für die Anwendung der Rekursionsrelationen Gln.(A.7),(A.8) ist die Berechnung der Integrale für die Funktion $f(x) \equiv 1$, die wir unter Einbeziehung der Orthogonalitätsrelation der Legendrepolynome analytisch angeben können. Die Orthogonalitätsrelation lautet [12]:

$$\int_{-1}^{1} p_{i'}(x) p_i(x) \, \mathrm{d}x = \frac{2}{2i+1} \delta_{i',i} \qquad \text{für} \quad i', i = 0, 1, \ldots \quad \text{(A.10)}$$

Die linke Seite von Gl.(A.10) entspicht der Definition der $I_{i,0}^{(0)}(f)$ aus Gl.(A.3) mit $f(x) \equiv 1$.

Damit sind die benötigten Matrixelemente bestimmt [2]:

$$I_{i',i}^{(0)}(1) = \frac{2}{2i+1}\delta_{i',i}$$

$$I_{i',i}^{(1)}(1) = -1\delta_{2[\frac{i'+i}{2}],i'+i-1} \quad \text{für} \quad i' \geq i \quad \text{mit} \quad I_{i,i'}^{(1)}(1) = -I_{i',i}^{(1)}(1)$$

$$I_{i',i}^{(2)}(1) = i(i+1)\delta_{2[\frac{i'+i}{2}],i'+i} \quad \text{für} \quad i' \geq i \quad \text{mit} \quad I_{i,i'}^{(2)}(1) = I_{i',i}^{(2)}(1) \quad.$$

Wenden wir uns nun der Diskussion über die Approximation von Funktionen durch Legendrepolynome zu, die eine elegante Bestimmung der Legendrekoeffizienten einer beliebigen Funktion $f(x)$ aufzeigt und die Berechnung der Matrixelemente $I_{i',i}^{(j)}(f)$ abschließt.

A.2 Approximation von Funktionen

Eine Anwendung der Vollständigkeit der Legendrepolynome $p_i(x)$ auf dem Intervall $[-1,1]$ ist die eindeutige Darstellung der Funktion $f(x)$ durch ihre Legendrekoeffizienten f_i:

$$f(x) = \sum_{i=0}^{\infty} f_i p_i(x)$$

$$f_i := \int_{-1}^{1} f(x)p_i(x)\,\mathrm{d}x \tag{A.11}$$

Die im Allgemeinen rasche Konvergenz der Folge $\{f_i\}$ legt die Approximation der Funktion $f(x)$ durch eine endliche Anzahl von Legendrekoeffizienten nahe:

$$f(x) \approx \sum_{i=0}^{N-1} f_i p_i(x) \tag{A.12}$$

In Gleichung (A.12) wird N so gewählt, daß der Defekt $D_N(f)$ kleiner als eine vorgegebene reelle Zahl $\epsilon > 0$ ist.

$$D_N(f) := \int_{-1}^{1} (f(x))^2\,\mathrm{d}x - \sum_{i=0}^{N-1} \frac{2}{2i+1} f_i^2 < \epsilon$$

Die Legendrekoeffizienten f_i Gl.(A.11) werden über die Gaußsche Integrationsmethode [7] berechnet:

$$\int_{-1}^{1} f(x)\,\mathrm{d}x \approx \sum_{j=1}^{N} \omega_j f(x_j) \quad \text{mit} \quad p_N(x_j) = 0, \quad j = 1, 2, \ldots, N \tag{A.13}$$

---

[2]Die symbolische Schreibweise $\left[\frac{n}{2}\right]$ ist für n ganz wie folgt definiert:

$$\left[\frac{n}{2}\right] := \begin{cases} \dfrac{n}{2} & \text{für } n \text{ gerade} \\[2mm] \dfrac{n-1}{2} & \text{für } n \text{ ungerade} \end{cases}$$

$$\text{und} \quad \omega_j = 2\frac{1 - x_j^2}{[Np_{N-1}(x_j)]^2}$$

$$f_i \quad \approx \quad \frac{2i+1}{2} \sum_{j=1}^{N} \omega_j f(x_j) p_i(x_j) \tag{A.14}$$

In dieser Formulierung ist die Integrationsmethode exakt für Polynome $f(x)$ vom Grad $\leq 2N-1$. Nehmen wir nun an die Approximation der Legendrekoeffizienten Gl.(A.14) sei exakt, dann ist die Approximation der Funktion $f(x)$ Gl.(A.12) an den N Nullstellen x_j von $p_N(x)$ gleichfalls exakt[3]:

$$f(x_j) \quad = \quad \sum_{i=0}^{N-1} f_i p_i(x_j) \quad \text{mit} \quad p_N(x_j) = 0, \quad j = 1, 2, \ldots, N \tag{A.15}$$

$$f_i \quad := \quad \frac{2i+1}{2} \sum_{j=1}^{N} \omega_j f(x_j) p_i(x_j) \tag{A.16}$$

Wir greifen die Orthogonalitätsrelation der Legendrepolynome Gl.(A.10) auf und beweisen die Behauptung Gl.(A.15) mit Hilfe der Gaußschen Integrationsmethode Gl.(A.13):

$$\frac{2}{2i+1}\delta_{i',i} = \int_{-1}^{1} p_{i'}(x)p_i(x)\,\mathrm{d}x = \sum_{j=1}^{N} \omega_j p_{i'}(x_j)p_i(x_j) \quad \text{für} \quad i' + i \leq 2N - 1 \tag{A.17}$$

Aus der Definition der Legendrekoeffizienten Gl.(A.16) folgt:

$$\frac{2}{2i'+1}f_{i'} = \sum_{i=0}^{N-1} \frac{2}{2i+1}f_i \delta_{i',i} = \sum_{j=1}^{N} \omega_j f(x_j) p_{i'}(x_j) \tag{A.18}$$

Wir ersetzen $\delta_{i',i}$ aus Gl.(A.18) durch den entsprechenden Term in Gl.(A.17):

$$\sum_{i=0}^{N-1} f_i \sum_{j=1}^{N} \omega_j p_{i'}(x_j)p_i(x_j) \quad = \quad \sum_{j=1}^{N} \omega_j f(x_j) p_{i'}(x_j)$$

$$\sum_{j=1}^{N} \omega_j \left[f(x_j) - \sum_{i=0}^{N-1} f_i p_i(x_j) \right] p_{i'}(x_j) \quad = \quad 0 \quad \text{für} \quad i' = 0, 1, \ldots, N - 1$$

Ein Vergleich mit Gl.(A.17) schließt den Beweis ab:

$$f(x_j) - \sum_{i=0}^{N-1} f_i p_i(x_j) = p_N(x_j) = 0$$

Wir halten fest: Sind die Funktionswerte $f(x_j)$, $j = 1, 2, \ldots, N$ einer beliebigen Funktion an den Stellen x_j, den Nullstellen des Legendrepolynoms $p_N(x)$, vorgegeben, so ist die Legendre

---

[3]Die Nullstellen $x_j, j = 1, 2, \ldots, N$ von $p_N(x)$ sind reell und einfach; sie liegen alle im offenen Intervall (-1,1): $-1 < x_1 < x_2 < \ldots < x_N < 1$.

Approximation dieser Funktion an eben diesen Stellen exakt. Die zugehörigen Legendrekoeffizienten f_i, $i = 0, 1, \ldots, N - 1$ werden über ihre Definition Gl.(A.16) berechnet. Sämtliche in Abschnitt A.1 diskutierten Integraltypen werden durch folgenden Zusammenhang ausgewertet:

$$I_{i,0}^{(0)}(f) = \frac{2}{2i + 1} f_i \qquad \text{für} \quad i = 0, 1, \ldots$$

Im weiteren listen wir einige Anwendungen der Legendre Approximation auf: Berechnung von Funktionswerten, Ableitung, Stammfunktion bzw. Nullstellen. Die beiden Rekursionsbeziehungen Gl.(A.1) und Gl.(A.2) spielen hierbei eine zentrale Rolle.

Der Funktionswert $f(x)$ an einer beliebigen Stelle x im Intervall $[-1, 1]$ wird auf sehr elegante Weise aus der Clenshaw Rekursion [14] gewonnen:

$$
\begin{aligned}
a_{N+1} = a_N &= 0 \\
a_i &= \frac{2i + 1}{i + 1} x a_{i+1} - \frac{i + 1}{i + 2} a_{i+2} + f_i \qquad \text{für} \quad i = N - 1, N - 2, \ldots, 0 \\
f(x) &= a_0
\end{aligned}
$$

Die Ableitung einer beliebigen Funktion $f(x)$ wird durch die Legendrekoeffizienten f_i' der Legendre Approximation eindeutig dargestellt:

$$\frac{\mathrm{d}}{\mathrm{d}x} f(x) = \sum_{i=0}^{N-1} \frac{\mathrm{d}}{\mathrm{d}x} p_i(x) = \sum_{i=0}^{N-1} f_i' p_i(x)$$

Einsetzen der Rekursionsbeziehung Gl.(A.2) und sortieren nach Legendrepolynomen ergibt folgendes Berechnungsschema:

$$
\begin{aligned}
f_N' = f_{N-1}' &= 0 \\
f_{i-1}' &= \frac{2i - 1}{2i + 3} f_{i+1}' + (2i - 1) f_i \qquad \text{für} \quad i = N - 1, N - 2, \ldots, 1
\end{aligned}
$$

Die Anwendung der Legendre Approximation auf die Integration der Funktion $f(x)$ beruht auf den Stammfunktionen der Legendrepolynome. Die Integration der Rekursionsbeziehung Gl.(A.2) liefert

$$\int_{-1}^{x} p_i(x') \, \mathrm{d}x' = \frac{p_{i+1}(x) - p_{i-1}(x)}{2i + 1} \quad .$$

Die Legendrekoeffizienten F_i des unbestimmten Integrals von $f(x)$ ergeben sich zu

$$F_i = \frac{1}{2i - 1} f_{i-1} - \frac{1}{2i + 3} f_{i+1} \qquad \text{für} \quad i > 0$$

mit einer frei wählbaren Integrationskonstanten F_0. Die Berechnung der Ableitung oder des Integrals von $f(x)$ geschieht wieder über die Clenshaw Rekursion mit den entsprechend transformierten Legendrekoeffizienten; diese sind identisch mit den Koeffizienten der jeweiligen Legendre Approximation *ab initio*. Der Wert des bestimmten Integrals wird bereits über die Orthogonalitätsrelation der Legendrepolynome festgelegt:

$$\int_{-1}^{1} f(x) \, \mathrm{d}x = 2f_0$$

Bis hierher sind wir dem Leser die Berechnung der Nullstellen von $p_N(x)$ schuldig geblieben, das wird nun nachgeholt. Im *Handbook of Mathematical Functions* [12] sind die Nullstellen x_j mit ihren Gewichten ω_j aus Gl.(A.13) für unterschiedliches N tabelliert. Die im folgenden skizzierte Herleitung [7],[14] erlaubt eine Verallgemeinerung auf die Bestimmung der Nullstellen in der Legendre Approximation einer beliebigen Funktion $f(x)$ und wird daher kurz diskutiert. Der Übersichtlichkeit wegen führen wir die Orthonormalpolynome $P_i(x)$ ein

$$P_i(x) := \sqrt{\frac{2i+1}{2}} p_i(x) \qquad \text{mit} \quad \int_{-1}^{1} P_{i'}(x) P_i(x)\, \mathrm{d}x = \delta_{i',i}$$

und greifen die Rekursionsbeziehung der Legendrepolynome Gl.(A.1) auf:

$$
\begin{aligned}
P_{-1}(x) &\equiv 0 \\
xP_i(x) &= b_i P_{i-1}(x) + b_{i+1} P_{i+1}(x) \qquad \text{für} \quad i \geq 0
\end{aligned}
\tag{A.19}
$$

Die Rekursionskoeffizienten b_i sind wie folgt definiert:

$$
\begin{aligned}
b_0 &\equiv 0 \\
b_i &:= \frac{i}{\sqrt{4i^2 - 1}} \qquad \text{für} \quad i \geq 1
\end{aligned}
$$

Wir schreiben die Rekursionsbeziehung Gl.(A.19) für $i = 0, 1, \ldots, N-1$ auf und erhalten folgendes Matrixschema

$$
x \begin{bmatrix} P_0 \\ P_1 \\ \vdots \\ P_{N-2} \\ P_{N-1} \end{bmatrix} = \begin{bmatrix} 0 & b_1 & & & \\ b_1 & 0 & b_2 & & \\ & \vdots & \vdots & & \\ & & b_{N-2} & 0 & b_{N-1} \\ & & & b_{N-1} & 0 \end{bmatrix} \cdot \begin{bmatrix} P_0 \\ P_1 \\ \vdots \\ P_{N-2} \\ P_{N-1} \end{bmatrix} + \begin{bmatrix} 0 \\ 0 \\ \vdots \\ 0 \\ b_N P_N(x) \end{bmatrix}
$$

oder

$$x\mathbf{P} = [\mathbf{J}] \cdot \mathbf{P} + b_N P_N(x)\mathbf{e}_N \tag{A.20}$$

Hier ist $[\mathbf{J}]$ eine symmetrische Tridiagonalmatrix, $\mathbf{P}$ der Spaltenvektor $(P_0, P_1, \ldots, P_{N-1})^T$ und $\mathbf{e}_N$ der Einheitsvektor $(0, 0, \ldots, 1)^T$. Eine genaue Inspektion von Gleichung (A.20) zeigt den wichtigen Sachverhalt: Die Berechnung der Nullstellen x_j von $P_N(x)$, also $P_N(x_j) = 0$ ist äquivalent mit der Bestimmung der Eigenwerte von $[\mathbf{J}]$. Darüberhinaus sind die Gewichte ω_j über die erste Komponente des jeweiligen Eigenvektors $\mathbf{v}_j$ bestimmt [14]:

$$\omega_j = 2\left(v_j^{(1)}\right)^2 \qquad \text{mit} \quad \mathbf{v}_j^T \cdot \mathbf{v}_j \qquad j = 1, 2, \ldots, N$$

Die Eigenwerte und Eigenvektoren einer symmetrischen Tridiagonalmatrix oder Jacobimatrix werden mit Hilfe von numerischen Diagonalisierungsverfahren [9] gewonnen.

Die Bestimmung der Nullstellen $f(x) = 0$ in der Legendre Approximation wird ebenfalls auf die Diagonalisierung der entsprechenden Matrix $[\mathbf{H}]$ abgebildet:

$$f(x) = \sum_{i=0}^{N} f_i p_i(x) = \sum_{i=0}^{N} c_i P_i(x)$$

$$c_i := \sqrt{\frac{2}{2i+1}} f_i \qquad \text{mit} \quad c_N \neq 0$$

Wir ersetzen $P_N(x)$ durch die Rekursionsbeziehung Gl.(A.19) für $i = N - 1$ und erhalten

$$f(x) = \sum_{i=0}^{N-1} c_i P_i(x) + \frac{c_N}{b_N} \left[x P_{N-1}(x) - b_{N-1} P_{N-2}(x) \right]$$

und damit

$$x P_{N-1}(x) = \frac{b_N}{c_N} f(x) + \sum_{i=0}^{N-1} a_i P_i(x) + b_{N-1} P_{N-2}(x) \qquad \text{mit} \quad a_i := -\frac{b_N}{c_N} c_i / \qquad \text{(A.21)}$$

Gleichung (A.21) wird zusammen mit der Rekursionsbeziehung Gl.(A.19) für $i = 0, 1, \ldots, N - 2$ in das folgende Matrixschema eingetragen

$$x\mathbf{P} = [\mathbf{H}] \cdot \mathbf{P} + \frac{b_N}{c_N} f(x) \mathbf{e}_N$$

mit

$$[\mathbf{H}] = \begin{bmatrix} 0 & b_1 & & & & \\ b_1 & 0 & b_2 & & & \\ & \vdots & \vdots & & & \\ & & & b_{N-2} & 0 & b_{N-1} \\ a_0 & a_1 & a_2 & \cdots & a_{N-3} & a_{N-2}+b_{N-1} & a_{N-1} \end{bmatrix}$$

Der Vergleich mit Gleichung (A.20) weist die Nullstellen von $f(x)$ als die Eigenwerte der Matrix $[\mathbf{H}]$ aus. In dem speziellen Fall $f(x) = c_N P_N(x)$ gilt: $[\mathbf{H}] = [\mathbf{J}]$. Die Matrix $[\mathbf{H}]$ entspricht in ihrer Gestalt einer unteren Hessenbergmatrix und wird numerisch diagonalisiert [9].

Das folgende Anwendungsbeispiel schließt die Diskussion der Legendre Approximation ab. Ausgangspunkt ist die Summendarstellung des Produkts zweier Legendrepolynome

$$p_{i'}(x) p_i(x) = \sum_{j=0}^{i'+i} c_{i',i}^{(j)} p_j(x) \qquad \text{(A.22)}$$

Die Legendrekoeffizienten $c_{i',i}^{(j)}$ werden über die Rekursionsbeziehung der Legendrepolynome Gl.(A.1) rekursiv bestimmt:

$$\begin{aligned} c_{i',-1}^{(j)} &= 0 \\ c_{i',0}^{(j)} &= \delta_{i',j} \\ c_{i',i+1}^{(j)} &= \frac{2i+1}{i+1} \left[\frac{i'+1}{2i'+1} c_{i'+1,i}^{(j)} + \frac{i'}{2i'+1} c_{i'-1,i}^{(j)} \right] - \frac{i}{i+1} c_{i',i-1}^{(j)} \end{aligned}$$

Das Quadrat der Legendre Approximation der Funktion $f(x)$ ergibt sich zu

$$r(x) = (f(x))^2 = \sum_{j=0}^{2(N-1)} r_j p_j(x)$$

Der Vergleich mit Gleichung (A.22) legt die Legendrekoeffizienten r_j der Funktion $r(x)$ eindeutig fest:

$$r_j = \sum_{i',i=0}^{N-1} f_{i'} f_i c_{i',i}^{(j)}$$

Alternativ wird $r(x)$ mit Hilfe der Clenshaw Rekursion an den Nullstellen $p_{2N-1}(x_k) = 0$ mit $k = 1, 2, \ldots, 2N - 1$ ausgewertet

$$r(x_k) = \left(\sum_{i=0}^{N-1} f_i p_i(x_k) \right)^2 \quad .$$

Aus der Definitionsgleichung der Legendrekoeffizienten Gl.(A.16) lesen wir ab:

$$r_j = \frac{2j+1}{2} \sum_{k=1}^{2N-1} \omega_k r(x_k) p_j(x_k) \qquad \text{mit} \quad p_{2N-1}(x_k) = 0$$

Die Approximation ist an den N Nullstellen x_j von $p_N(x)$ exakt, Gl.(A.15).

Die Legendre Approximation ist eine sehr leistungsfähige Methode in der numerischen Behandlung von Funktionen im Intervall $[-1, 1]$. Eine Erweiterung auf Funktionen in einem beliebigen Intervall wird über ein, dem Intervall zugrundeliegendes, orthogonales Funktionensystem erreicht. Die Ausführungen zur Legendre Approximation können in Kenntnis der entsprechenden Rekursionsbeziehungen übertragen werden.

Im Intervall $[0, \infty]$ bilden die mit $e^{-\frac{1}{2}x}$ gewichteten Laguerrepolynome [12] ein vollständiges orthonormiertes Funktionensystem $L_i(x)$:

$$\int_0^\infty L_{i'}(x) L_i(x) \, dx = \delta_{i',i}$$

Aus der Formel von Rodriguez

$$L_i(x) := \frac{e^{\frac{1}{2}x}}{i!} \frac{d^i}{dx^i} \left[x^i e^{-x} \right]$$

leiten sich die beiden wichtigen Rekursionsbeziehungen der Basisfunktionen ab. Wir geben sie an dieser Stelle an:

$$
\begin{aligned}
L_{-1}(x) &\equiv 0 \\
L_0(x) &= e^{-\frac{1}{2}x} \\
(i+1) L_{i+1}(x) &= (2i + 1 - x) L_i(x) - i L_{i-1}(x) \\
\frac{d}{dx} L_{i+1}(x) &= \frac{d}{dx} L_i(x) - \frac{1}{2} L_{i+1}(x) - \frac{1}{2} L_i(x) \qquad \text{für} \quad i \geq 0 \; .
\end{aligned}
$$

Anhang B

Elektronische Zustände in Germanium-Bikristallen

Self-Consistent Calculations of Landau Levels
for Symmetric p-Type Inversion Layers

By V. Latussek, E. Bangert, G. Landwehr

Physikalisches Institut der Universität Würzburg, Würzburg, Germany

Dedicated to the "Annalen der Physik" on the occasion of their two-hundredth birthday.

Abstract. A method for calculating the Landau levels of symmetric p-type inversion layers is presented. Using the envelope function approach in the Hartree approximation the magnetic field is incorporated into the Hamiltonian. In order to characterize the energy levels and to obtain a detailed understanding of the unusual Landau scheme, an analysis of the wave functions is made. Special effects are discussed for the inversion layers adjacent to the grain boundary of a Ge-bicrystal, with two occupied subbands. The simulation of Shubnikov-de Haas data by a density of states analysis shows that the different oscillatory periods are not directly related to the subband occupations.

Selbstkonsistente Berechnungen von Landau-Niveaus
in symmetrischen p-Typ-Inversionsrandschichten

Inhaltsübersicht. Es wird eine Methode zur Berechnung des Landau-Schemas in symmetrischen p-Typ-Inversionsrandschichten vorgestellt. Im Formalismus der Envelopefunktionen kann das Magnetfeld vollständig in die Hartree-Näherung eingearbeitet werden. Ein vertieftes Verständnis des ungewöhnlichen Landau-Schemas wird durch die Analyse der Wellenfunktionen zur Charakterisierung der Energieniveaus erreicht. Am Beispiel eines Ge-Bikristalls werden die Besonderheiten des Landau-Schemas erläutert, wobei im Inversionskanal entlang der Korngrenze zwei elektrische Subbänder besetzt sind. Die Simulation von Shubnikov-de Haas-Meßkurven durch die Zustandsdichte zeigt, daß die einzelnen Perioden der Oszillationen nicht unmittelbar den Subbandbesetzungen zugeordnet werden dürfen.

1. Introduction

During the last two decades two-dimensional electronic systems at semiconductor interfaces have been intensively studied. Due to the confinement of charge-carriers by an electric field perpendicular to the interface bound states are generated, which result in electrical subbands. In silicon MOSFETs and in modulation doped GaAs-(GaAl)As heterostructures the interface potential can be roughly characterized by an asymmetric triangular potential with a steep rise at the interface. Symmetric triangular potential

wells have been realised in δ-doped semiconductor structures. There is another system in which potential wells of the latter kind have shown up: grain boundaries in germanium bicrystals. In crystals of this kind p-type accumulation or inversion layers have been observed [1, 2]. The hole concentration is usually of the order 10^{12} cm^{-2} which results in quasi metallic conduction. The p-type nature of the space charge layer causes complications in the interpretation of the experimental data due to the complex structure of the valence band. This problem was for the first time addressed in p-type silicon inversion layers at the Si—SiO$_2$ interface of MOSFETs [3, 4]. Self-consistent solutions of Schrödinger's and Poisson's equations taking into account the actual valence band structure making use of Luttinger's $\mathbf{k} \cdot \mathbf{p}$ matrix formulation [5] clearly indicated that the subband structure was significantly influenced by the strong electric field at the interface. After modulation-doped p-type GaAs-(GaAl)As heterostructures showed an unusually high hole mobility at low temperatures various groups calculated the structure of the electronic subbands in detail. The results by Sham et al. [6—9], Ando [10, 11], Ekenberg and Altarelli [12—16] and Bangert et al. [17—19] agreed essentially, although minor differences due to the parameters used in the calculations showed up. The coupling between the light and heavy hole bands is strongly modified by the surface potential.

Usually it is anticipated that a strong magnetic field does not essentially modify the band structure of a semiconductor. It is frequently assumed that Landau quantisation by application of a strong magnetic field splits the electronic bands into magnetic subbands. Analysis of the magneto optical and transport data for p-type GaAs-(GaAl)As heterostructures showed however, that this assumption is not justified. Actually the structure of the hole subbands is influenced by magnetic fields.

After magneto-transport experiments on high quality germanium bicrystals revealed Shubnikov-de Haas oscillations, self-consistent calculations of electric subbands were performed [20]. The calculations for asymmetric triangular potentials cannot directly be applied to inversion layers adjacent to the grain boundary of germanium bicrystals because in this case the potential is symmetric. This has the consequence that the bulk inversion symmetry is not destroyed as in GaAs-(GaAl)As heterostructures and in MOSFETs and that the spin degeneracy is not lifted. Only an external magnetic field can produce spin splitting of the subbands as in n-type heterostructures. A further complication arises due to the occupation of two electric subbands the population of which depend on the strength of the applied magnetic field. Additional Shubnikov-de Haas experiments [21, 22], in which the magnetic field was tilted from a direction perpendicular to the grain boundary to the parallel orientation required improved subband calculations, in which the magnetic field was taken into account ab initio. These calculations have allowed a detailed interpretation of the experimental data.

In the subsequent sections the procedure of the calculations will be outlined. In order to make the calculations managable, it was assumed that the grain boundary plane is uniformly charged by electrons and that the electronic structure of the subbands is entirely determined by free holes and the background impurity charge. Also the tilt angle of the bicrystal was not taken into account for simplicity, which should not be a serious drawback.

We present our calculations here in some detail because we believe that they can be generalized and applied to other symmetric p-type 2D-systems like δ-doped heterostructures. Especially in narrow gap materials the occupation of more than one subband can occur. There is also a relation to models which have been developed in order to interpret electric subbands in n-type structures realized in HgCdTe- and InSb bicrystals [23—25].

2. Procedure of Calculation

The structure of the electrical subbands can be described by the following effective mass equation

$$\begin{bmatrix} A_+ + V(z) - E & C & B & 0 \\ C^\dagger & A_- + V(z) - E & 0 & B \\ B^\dagger & 0 & A_- + V(z) - E & -C \\ 0 & B^\dagger & -C^\dagger & A_+ + V(z) - E \end{bmatrix}$$

$$\times \begin{bmatrix} F_{\frac{3}{2}}(r) \\ F_{\frac{1}{2}}(r) \\ F_{-\frac{1}{2}}(r) \\ F_{-\frac{3}{2}}(r) \end{bmatrix} = 0. \tag{1}$$

The Luttinger matrix [5] in Eq. (1) represents the degenerate Γ_8-bands at the top of the valence band for the diamond structure. According to the envelope function method the potential energy connected with the band bending at the grain boundary is added to the diagonal elements. The z-axis is chosen to be normal to the grain boundary, which is positioned at $z = 0$. The abbreviations inside the Luttinger matrix are

$$A_\pm = -\frac{\hbar^2}{2m}[(\gamma_1 \mp 2\gamma_2)k_z^2 + (\gamma_1 \pm \gamma_2)k_\parallel^2],$$

$$B = -\frac{\hbar^2}{2m}\frac{\sqrt{3}}{2}[(\gamma_3 + \gamma_2)k_-^2 - (\gamma_3 - \gamma_2)k_+^2], \tag{2}$$

$$C = \frac{\hbar^2}{2m}2\sqrt{3}\,\gamma_3 k_- ik_z,$$

where

$$k_\parallel^2 = k_x^2 + k_y^2,$$

$$k_\pm = k_x \pm ik_y.$$

The Luttinger parameters $\gamma_1, \gamma_2, \gamma_3$ for Ge used in our calculations are listed in [26]. It should be noted that we did not only solve Eq. (1) with the 4×4 Luttinger matrix, but also included the Γ_7-spin-orbit split off band using the 6×6 Luttinger matrix. It was found, however that the effect of the Γ_7-band is negligibly small due to the large spin-orbit energy of 0.29 eV, which is larger by one order of magnitude than the subband energies. Equation (1) is applied to both sides of the grain boundary, which means that we neglect the tilting of the bicrystal in the Luttinger matrix. It would be very difficult to formulate the correct boundary conditions in the envelope function framework [27, 28].

The potential energy $V(z)$ is obtained from Poisson's equation and is decomposed into three contributions

$$V(z) = V_d(z) + V_g(z) + V_H(z). \tag{3}$$

The first term $V_d(z)$ is the electrostatic potential of the fixed space charges namely the positive depletion charge of the empty donors above the Fermi energy. The second term $V_g(z)$ is the potential energy due to the density of the negative grain boundary charges

$$n_g(z) = N_g\delta(z).$$

$$V_d(z) + V_g(z) = \begin{cases} \dfrac{e^2}{\varepsilon\varepsilon_0} N_d \dfrac{z_d}{4}\left(\left|\dfrac{z}{z_d}\right| - 1\right)^2 & |z| \le z_d, \\ 0 & |z| > z_d, \end{cases}$$

with $N_d = 2N_D z_d$ where N_D is the concentration of the empty donors states. ε is the static dielectric constant of Ge [26]. The third term is the Hartree potential $V_H(z)$ given by the density of holes $n(z)$ in the p-channel

$$V_H(z) = \frac{e^2}{\varepsilon\varepsilon_0} \int_\infty^z (z - z')\, n(z')\, dz'. \tag{4}$$

The neutrality condition connects the three terms

$$N_d - N_g + \int n(z)\, dz = 0.$$

The main difficulty concerning the p-channel is to calculate $V_H(z)$ arising from the complicated structure of wave functions, which are solutions of Eq. (1).

Regarding the homogeniety parallel to the grain boundary we make the following ansatz for the envelope functions

$$F_m(\boldsymbol{r}) = e^{i(k_x x + k_y y)} g_{m,k_x,k_y}(z), \tag{5}$$

which transforms (1) into a set of four coupled differential equations for the $g_{m,k_x,k_y}(z)$, where in (2) k_z stands for $-i\dfrac{\partial}{\partial z}$. For each pair k_x, k_y we must solve this set of four coupled differential equations. The corresponding eigenvalues $E(k_x, k_y)$ are the electric subbands. The boundary conditions for the $g_{m,k_x,k_y}(z)$ are

$$g_{m,k_x,k_y}(-\infty) = g_{m,k_x,k_y}(+\infty) = 0, \quad m = \frac{3}{2}, \frac{1}{2}, -\frac{1}{2}, -\frac{3}{2}. \tag{6}$$

The fundamental idea of our self-consistent calculation is to choose one complete set of functions $f_i(z)$, $i = 0, 1, 2, \ldots$ in which each $g_{m,k_x,k_y}(z)$ is expanded. The $f_i(z)$ satisfy the boundary conditions $f_i(\pm\infty) = 0$ like (6) with $\langle i' \mid i \rangle = \delta_{i',i}$. Eq. (1) becomes

$$\begin{bmatrix} A_+ + V(z) - E & C & B & 0 \\ C^\dagger & A_- + V(z) - E & 0 & B \\ B^\dagger & 0 & A_- + V(z) - E & -C \\ 0 & B^\dagger & -C^\dagger & A_+ + V(z) - E \end{bmatrix}$$

$$\times \begin{bmatrix} \sum_i c_{\frac{3}{2},i}(k_x, k_y) f_i(z) \\ \sum_i c_{\frac{1}{2},i}(k_x, k_y) f_i(z) \\ \sum_i c_{-\frac{1}{2},i}(k_x, k_y) f_i(z) \\ \sum_i c_{-\frac{3}{2},i}(k_x, k_y) f_i(z) \end{bmatrix} = 0. \tag{7}$$

The formulation in Eq. (7) leads effectively to a matrix representation of the eigenvalue problem, where the eigenvectors with components $c_{m,i}(k_x, k_y)$ and the corresponding eigenvalues are obtained by matrix diagonalisation. If a proper set of functions $f_i(z)$ is explicitly given, then matrix elements like $\left\langle i' \left| \dfrac{\partial}{\partial z} \right| i \right\rangle$, $\left\langle i' \left| \dfrac{\partial^2}{\partial z^2} \right| i \right\rangle$, and $\langle i' \mid V_d + V_g \mid i \rangle$ can be found easily.

The matrix elements $\langle i' | V_H | i \rangle$ are calculated in the following way. The density of holes $n(z)$ in the p-channel is given by

$$n(z) = \sum_{(l, k_x, k_y)} | \psi_{l, k_x, k_y}(z) |^2, \tag{8}$$

where $\sum_{(l, k_x, k_y)}$ means the sum over all occupied hole states and $\psi_{l, k_x, k_y}(z)$ is an eigenfunction to the corresponding eigenvalue $E_l(k_x, k_y)$ of (7). Inserting $\psi_{l, k_x, k_y}(z)$ given by (7) leads to

$$
\begin{aligned}
n(z) &= \sum_{(l, k_x, k_y)} \sum_{m=-\frac{3}{2}}^{\frac{3}{2}} \sum_{j', j} c_{m,j'}^{l*}(k_x, k_y) \, c_{m,j}^{l}(k_x, k_y) f_{j'}^*(z) f_j(z) \\
&= \sum_{j', j} Q_{j', j} f_{j'}^*(z) f_j(z),
\end{aligned}
\tag{9}
$$

where

$$
\begin{aligned}
Q_{j', j} &= \sum_{(l, k_x, k_y)} \sum_{m=-\frac{3}{2}}^{\frac{3}{2}} c_{m,j'}^{l*}(k_x, k_y) \, c_{m,j}^{l}(k_x, k_y) \\
&= \sum_l \frac{2}{(2\pi)^2} \int_{F_l} \left[\sum_m c_{m,j'}^{l*} c_{m,j}^{l}(k_x, k_y) \right] dk_x \, dk_y.
\end{aligned}
\tag{10}
$$

In (10) the sum over k_x, k_y is transformed to an integral over the occupied area F_l of the 2D-k-space of subband l. The factor 2 shows the twofold degeneracy of the subband states of the symmetric potential. The constants $Q_{j', j}$ are related to the total hole concentration N,

$$N = \int_{-\infty}^{\infty} n(z) \, dz = \sum_{j', j} Q_{j', j} \int_{-\infty}^{\infty} f_{j'}^*, f_j(z) \, dz = \sum_j Q_{j, j}. \tag{11}$$

For a given hole concentration N, Eqs. (10, 11) determine the occupied k-space areas F_l, which are bordered by the Fermi contours $E(k_x, k_y) = E_F$. Thus (10, 11) define the Fermi energy E_F with respect to the subband structure. On the other hand E_F is fixed at the donor level of the bulk material. The equivalence of both E_F-definitions is achieved by a proper depletion length z_d.

We continue our calculation of the Hartree potential $V_H(z)$ by inserting $n(z)$ of (9) into the Poisson equation (4)

$$V_H(z) = \frac{e^2}{\varepsilon \varepsilon_0} \sum_{j', j} Q_{j', j} \int_{\infty}^{z} (z - z') f_{j'}^* f_j(z') \, dz' \tag{12}$$

and obtain the matrix elements of V_H

$$\langle i' | V_H | i \rangle = \frac{e^2}{\varepsilon \varepsilon_0} \sum_{j', j} Q_{j', j} R_{i', i, j' j}, \tag{13}$$

with

$$R_{i', i, j', j} = \int_{-\infty}^{\infty} dz f_{i'}^* f_i(z) \int_{\infty}^{z} (z - z') f_{j'}^* f_j(z') \, dz'. \tag{14}$$

The $R_{i', i, j', j}$ are constants which depend only on the set of functions $f_i(z)$ and not on the Hartree potential $V_H(z)$. They must be calculated only once — usually numerically — for a given set f_j. Therefore the $Q_{j', j}$ contain all information about the Hartree potential.

The self-consistent calculation starts with a set $Q_{j',j}$ which satisfy the condition $\Sigma_j Q_{j,j} = N$. The calculation is terminated, when

$$Q_{j',j}^{out} = Q_{j',j}^{in}.$$

The main advantage of our self-consistent calculation is that despite of the complicated degenerate valence band structure the Hartree approximation can be completely realized. The essential basis for a successful application of our method is to choose an adequate set of functions $f_i(z)$. A proper set $f_i(z)$ is found, if the exact envelope functions $g_{m,k_x,k_y}(z)$ can be composed from only a few $f_i(z)$. In other words the expansion $g_{m,k_x,k_y}(z) = \Sigma_i c_{m,i}(k_x, k_y) f_i(z)$ has to converge rapidly. It is clear that this criterium must hold especially for the occupied subbands.

For the description of the symmetric band bending near the grain boundary we used the system

$$f_i(z) = \sqrt{\frac{2i+1}{2}} \, x \, \frac{1}{\cosh(xz)} \, P_i(\tanh(xz)), \quad i = 0, 1, 2, \ldots,$$

where P_i are the Legendre polynomials [29]. These functions fulfill all requirements mentioned above. Additionally the parameter x defines the spread of the $f_i(z)$ and is utilized to optimize the set of functions, e.g. $x = 2\times 10^6$ cm^{-1} for $N = 1.8\times 10^{12}$ cm^{-2}. Then it is found that the first 10 functions form a system which is complete enough for a quantitative calculation. Thus diagonalisation of 40×40 matrices achieves excellent convergence of the Hartree approximation. The matrix dimension is reduced by a factor of two for the case of grain boundaries due to the inversion symmetry of the potential. Since the numerical results of our calculation have already be publisfed [17, 30] we will summarize the important findings only. For carrier concentrations of about 1.5×10^{12} cm two occupied electric subbands are found, one heavy hole and one light hole band. The band dispersions $E(k_x, k_y)$ are both strongly nonparabolic and the heavy hole band is highly anisotropic, whereas the light hole band is almost isotropic. The symmetric band bendings have also be shown in [17] and [30].

3. External Magnetic Field

It is well known from p-channel GaAs-(GaAl)As heterostructures that a high magnetic field strongly modifies the Luttinger matrix in such a way that the Landau levels cannot directly be derived from the subband structure. Because nearly all the relevant experimental information about 2D-systems has been obtained from magneto-transport and magneto optical measurements, it is necessary to include the magnetic field from the beginning in the Landau level calculations.

We introduce the magnetic field $\boldsymbol{B} = (0, 0, B)$ oriented perpendicular to the grain boundary into Eq. (1) by the substitution

$$\boldsymbol{k} \to \boldsymbol{k} + \frac{e}{\hbar} \boldsymbol{A}, \quad \nabla \times \boldsymbol{A} = \boldsymbol{B},$$

where the new wave vector $\boldsymbol{k}$ satisfies the commutation rule

$$\boldsymbol{k} \times \boldsymbol{k} = -i\frac{e}{\hbar} \boldsymbol{B}.$$

We will use the operators a and a^+ defined by

$$a = \frac{l}{\sqrt{2}} (k_x - ik_y),$$

$$a^+ = \frac{l}{\sqrt{2}} (k_x + ik_y),$$

(15)

with the magnetic length $l = \sqrt{\dfrac{eB}{\hbar}}$. These operators have the following properties

$$
\begin{aligned}
&[a, a^{\dagger}] = 1, \\
&a^{\dagger}a|n\rangle = n|n\rangle, \\
&a|n\rangle = \sqrt{n}|n-1\rangle, \qquad n = 0, 1, 2, \ldots, \\
&a^{\dagger}|n\rangle = \sqrt{n+1}|n+1\rangle.
\end{aligned}
\tag{16}
$$

Choosing the Landau gauge $A = (0, Bx, 0)$ the states $|n\rangle$ correspond to the wave functions

$$
\langle r \mid n \rangle = e^{-i\frac{X}{l^2}y}\varphi_n(x - X),
\tag{17}
$$

where $\varphi_n(x)$ are the oscillator functions and X is the center of motion coordinate. The number of possible X-coordinates determines the degeneracy p of each Landau level

$$
p = \frac{1}{2\pi l^2} = \frac{eB}{2\pi\hbar}.
$$

Inserting a and $a^{\dagger}$ to Eq. (2) we get for the operators $A_{\pm}$, B and C inside the Luttinger matrix

$$
A_{\pm} = -\frac{\hbar^2}{2m}\left[(\gamma_1 \mp 2\gamma_2)\,k_z^2 + (\gamma_1 \pm \gamma_2)\frac{1}{l^2}(2a^{\dagger}a + 1)\right],
$$

$$
B = -\frac{\hbar^2}{2m}\frac{\sqrt{3}}{l^2}[(\gamma_3 + \gamma_2)\,a^2 - (\gamma_3 - \gamma_2)\,a^{\dagger 2}],
\tag{18}
$$

$$
C = \frac{\hbar^2}{2m}2i\frac{\sqrt{6}}{l}\gamma_3 a k_z.
$$

Furthermore we have to add the Zeeman term due to the Bloch functions u_m to the Hamiltonian of (1)

$$
-2\varkappa\mu_B JB = -2\varkappa\mu_B J_z B = -2\varkappa\mu_B B
\begin{bmatrix}
\frac{3}{2} & & & \\
& \frac{1}{2} & & \\
& & -\frac{1}{2} & \\
& & & -\frac{3}{2}
\end{bmatrix}.
\tag{19}
$$

The parameter $\varkappa$ has been listed in [26].

The construction of a suitable ansatz is performed by two steps. We observe that the plane wave in (5) must be replaced by the wave functions of (17) with different oscillator functions for the spinor components F_m.

First we neglect the term $(\gamma_3 - \gamma_2)\,a^{\dagger 2}$ in B of (18) which describes the in plane anisotropy. Inspection of the Hamiltonian shows that the arrangment of a and $a^{\dagger}$ require

the following structure for the solution

$$\Phi_n = e^{-i\frac{X}{l^2}y}\begin{bmatrix}\varphi_n g_{\frac{3}{2}}(z)\\[4pt] \varphi_{n+1}g_{\frac{1}{2}}(z)\\[4pt] \varphi_{n+2}g_{-\frac{1}{2}}(z)\\[4pt] \varphi_{n+3}g_{-\frac{3}{2}}(z)\end{bmatrix}. \tag{20}$$

Luttinger already pointed out [5] that for negative n $\varphi_n = 0$ holds. Therefore in Eq. (20) the spinors $\Phi_{-3}, \Phi_{-2}, \Phi_{-1}$ only have one, two, or three nonzero components, respectively. We insert the ansatz (20) into the Hamiltonian (1) with the elements (18) and make use of the properties of a and $a^\dagger$ given in Eq. (16). Including also the Zeeman term of Eq. (19) we get the following set of four coupled differential equations for the z-dependence $g_{\frac{3}{2}}(z)$ to $g_{-\frac{3}{2}}(z)$ of the envelope functions

$$\frac{\hbar^2}{2m}\begin{bmatrix}
\begin{array}{c}-(\gamma_1+\gamma_2)\dfrac{1}{l^2}(2n+1)-3\varkappa\dfrac{1}{l^2}+\\[4pt] (\gamma_1-2\gamma_2)\dfrac{\partial^2}{\partial z^2}+\dfrac{2m}{\hbar^2}(V(z)-E)\end{array} & 2\sqrt{6}\,\gamma_3\dfrac{1}{l}\sqrt{n+1}\,\dfrac{\partial}{\partial z} \\[16pt]
-2\sqrt{6}\,\gamma_3\dfrac{1}{l}\sqrt{n+1}\,\dfrac{\partial}{\partial z} & \begin{array}{c}-(\gamma_1-\gamma_2)\dfrac{1}{l^2}(2n+3)-1\varkappa\dfrac{1}{l^2}+\\[4pt] (\gamma_1+2\gamma_2)\dfrac{\partial^2}{\partial z^2}+\dfrac{2m}{\hbar^2}(V(z)-E)\end{array} \\[16pt]
-\dfrac{\sqrt{3}}{l^2}(\gamma_3+\gamma_2)\sqrt{n+2}\sqrt{n+1} & 0 \\[12pt]
0 & -\dfrac{\sqrt{3}}{l^2}(\gamma_3+\gamma_2)\sqrt{n+2}\sqrt{n+3}
\end{bmatrix}$$

$$\begin{bmatrix}
-\dfrac{\sqrt{3}}{l^2}(\gamma_3+\gamma_2)\sqrt{n+2}\sqrt{n+1} & 0 \\[12pt]
0 & -\dfrac{\sqrt{3}}{l^2}(\gamma_3+\gamma_2)\sqrt{n+2}\sqrt{n+3} \\[12pt]
\begin{array}{c}-(\gamma_1-\gamma_2)\dfrac{1}{l^2}(2n+5)+1\varkappa\dfrac{1}{l^2}+\\[4pt] (\gamma_1+2\gamma_2)\dfrac{\partial^2}{\partial z^2}+\dfrac{2m}{\hbar^2}(V(z)-E)\end{array} & -2\sqrt{6}\,\gamma_3\dfrac{1}{l}\sqrt{n+3}\,\dfrac{\partial}{\partial z} \\[16pt]
\sqrt{6}\,\gamma_3\dfrac{1}{l}\sqrt{n+3}\,\dfrac{\partial}{\partial z} & \begin{array}{c}-(\gamma_1+\gamma_2)\dfrac{1}{l^2}(2n+7)+3\varkappa\dfrac{1}{l^2}+\\[4pt] (\gamma_1-2\gamma_2)\dfrac{\partial^2}{\partial z^2}+\dfrac{2m}{\hbar^2}(V(z)-E)\end{array}
\end{bmatrix}\begin{bmatrix}g_{\frac{3}{2}}(z)\\[8pt] g_{\frac{1}{2}}(z)\\[8pt] g_{-\frac{1}{2}}(z)\\[8pt] g_{-\frac{3}{2}}(z)\end{bmatrix}=0. \tag{21}$$

This set must be solved for each n seperately. The eigenvalues $E_n^j(B)$ are the Landau levels of the 2D-hole system for the axial symmetrical approximation. The corresponding

eigenfunctions are the Φ_n^l of ansatz (20) containing different oscillator functions. Since for each n several eigenvalues are obtained we have added the index l, which accounts for heavy hole and light hole states, for both 'spin-components' of each heavy and light hole state and also for the ground and excited subbands. In principle the explicit solution of Eq. (21) together with the Hartree approximation can be calculated in the same way as for the case for $B = 0$. At present only the structure of the axial symmetric solution Φ_n^l is important, therefore the details of our calculation will be described later on.

We perform now the second step announced before, which allows for the anisotropy term $(\gamma_3 - \gamma_2)\, a^{\dagger 2}$ neglected so far. The matrix of this anisotropy contribution $H_\square$ is given by

$$H_\square = -\frac{\hbar^2}{2m}\,(\gamma_3 - \gamma_2)\begin{bmatrix} & & a^{\dagger 2} & \\ & & & a^{\dagger 2} \\ a^2 & & & \\ & a^2 & & \end{bmatrix}.$$ (22)

The structure of the Φ_n in Eq. (20) leads to the following matrix elements

$$\langle \Phi_{n'} | H_\square | \Phi_n \rangle \propto \delta_{n',n\pm 4}.$$ (23)

The selection rule $\Delta n = \pm 4$ reflects the fourfold symmetry axis perpendicular to the grain boundary. The selection rule implies that the wave functions of the total Hamiltonian including the anisotropy $H_\square$ are linear combinations of the Φ_n with $\Delta n = 4$. Four different types of wave functions Ψ_k are possible

$$\Psi_1 = \sum_{n=-3,1,\ldots} c_n \Phi_n, \qquad \Psi_2 = \sum_{n=-2,2,\ldots} c_n \Phi_n,$$
$$\Psi_3 = \sum_{n=-1,3,\ldots} c_n \Phi_n, \qquad \Psi_4 = \sum_{n=0,4,\ldots} c_n \Phi_n.$$ (24)

Thus each Landau level corresponds to a rather complicated wave function. The quantum number k is related to the fourfold symmetry axis. The transformation properties of the Ψ_k according to $\frac{\pi}{2}$-rotations will be analysed in the following subsection.

Now we demonstrate that the Hartree approximation can be worked out completely. To this end we have to analyse the z-dependence of the wavefunctions Ψ_k

$$\Psi_k = \sum_{\substack{n=k-4, \\ k,k+4,\ldots}} c_n \Phi_n = e^{-i\frac{X}{l^2}y}\begin{bmatrix} \sum_{n=k-4,\ldots} c_n \varphi_n \; g_{\frac{3}{2},n}(z) \\ \sum_{n=k-4,\ldots} c_n \varphi_{n+1} g_{\frac{1}{2},n}(z) \\ \sum_{n=k-4,\ldots} c_n \varphi_{n+2} g_{-\frac{1}{2},n}(z) \\ \sum_{n=k-4,\ldots} c_n \varphi_{n+3} g_{-\frac{3}{2},n}(z) \end{bmatrix}.$$ (25)

All the $g_{m,n}(z)$ in Eq. (25) are expanded into the same set of functions $f_i(z)$ which were already applied in the case for $B = 0$

$$\Psi_k = e^{-i\frac{X}{l^2}y}\begin{bmatrix} \sum_{n,i} c_{\frac{3}{2},i}(n)\; \varphi_n f_i(z) \\ \sum_{n,i} c_{\frac{1}{2},i}(n+1)\; \varphi_{n+1} f_i(z) \\ \sum_{n,i} c_{-\frac{1}{2},i}(n+2)\; \varphi_{n+2} f_i(z) \\ \sum_{n,i} c_{-\frac{3}{2},i}(n+3)\; \varphi_{n+3} f_i(z) \end{bmatrix}.$$ (26)

54

The eigenvector components $c_{m,i}\left(n + \dfrac{3}{2} - m\right)$ of one Landau state are explicitly obtained by numerical diagonalisation of the matrix for the total Hamiltonian H of Eqs. (21, 22)

$$\langle n'i'|H| ni\rangle \qquad n', n = k - 4, k, k + 4, \ldots \tag{27}$$

Then one state contributes to the charge density $n(z)$

$$|\Psi_k|^2 = \sum_{m=-\frac{3}{2}}^{\frac{3}{2}} \sum_{n',n} \sum_{i',i} c_{m,i'}^*(n') \, c_{m,i}(n) \, \varphi_{n'}^* \varphi_n(x - X) f_{i'}^* f_i(z) . \tag{28}$$

Summing over all coordinates X of Eq. (17) we get the contribution of one Landau level of the degeneracy $p = \dfrac{eB}{2\pi\hbar}$

$$\sum_X |\Psi_k|^2 = \frac{eB}{2\pi\hbar} \sum_m \sum_{\substack{n=k-4, \\ k,k+4\ldots}} \sum_{i',i} c_{m,i'}^*(n) \, c_{m,i}(n) f_{i'}^* f_i(z) , \tag{29}$$

where use was made of the relation

$$\sum_X \varphi_{n'}^*(x - X) \, \varphi_n(x - X) = \frac{eB}{2\pi\hbar} \, \delta_{n',n} .$$

Our consideration from (20) to (29) shows that the expansion of the wave function Ψ into oscillator functions with symmetry induced arrangement combined with the f_i expansion of the z-dependence leads to the matrix representation in Eq. (27). The eigenvalues of this matrix are the Landau levels, the eigenvectors determine the z-dependence of the charge density, which is the basis of the Hartree approximation. Since we have four types of wave functions Ψ_k we have to work out the procedure mentioned above four times seperately to calculate all Landau levels.

The hole concentration N in the p-channel defines the filling factor η, which is the number of occupied Landau levels

$$\eta = \frac{N}{p} = \frac{2\pi\hbar}{e} N \frac{1}{B} . \tag{30}$$

Therefore the charge density $n(z)$ is derived by summing the expression of Eq. (29) over the η highest Landau levels

$$n(z) = \sum_{l=1}^{\eta} \left(\sum_X |\Psi_k^l|^2 \right) = \frac{eB}{2\pi\hbar} \sum_{l=1}^{\eta} \sum_m \sum_{\substack{n=k-4, \\ k,k+4\ldots}} \sum_{i',i} c_{m,i'}^{l*}(n) \, c_{m,i}^l(n) f_{i'}^* f_i(z)$$

$$= \sum_{i',i} Q_{i',i} f_{i'}^*(z) f_i(z) , \tag{31}$$

where

$$Q_{i',i} = Q_{i',i}(B) = \frac{eB}{2\pi\hbar} \sum_{l=1}^{\eta} \sum_{\substack{n=k-4, \\ k,k+4\ldots}} \sum_m c_{m,i'}^{l*}(n) \, c_{m,i}^l(n) . \tag{32}$$

Since (31) is quite similar to (10) of the calculation for $B = 0$ the Hartree potential $V_H(z)$ and the matrix elements $\langle i'|V| i\rangle$ inside the matrix of Eq. (27) are computed in the same way as described before.

The Landau scheme must be calculated self-consistently for each magnetic field B seperately, consequently the Hartree potential depends on the magnetic field, which enters from the field dependent $Q_{i',i}(B)$.

We like to notice that 10 functions $f_i(z)$ suffice similar to the case for $B = 0$. We checked by numerical tests that for a calculation of η occupied Landau levels the anisotropy is adequately treated, if the sum over n in Eq. (24) runs up to $\eta + 10$, e.g. for $\eta = 10$ the dimension of the matrix in Eq. (27) is $4 \times 10 \times 6 = 240$.

4. Quantum Numbers

We will characterize each Landau level by a set of four quantum numbers two of them are strict quantum numbers which are symmetry induced, the other two characterize the levels only approximately. The symmetry group of our system is C_{4h}, where the fourfold axis is perpendicular to the grain boundary and parallel to the magnetic field. First we demonstrate that the function Ψ_k defined in Eq. (25) belong to different representations of C_{4h} [31]. To this end we apply the rotation C_4 on Ψ_k and verify the relation

$$R(C_4)\, \Psi_k = -e^{-i\frac{\pi}{4}}\, i^k \Psi_k. \tag{33}$$

In detail we perform the C_4-rotation by the following substitutions

$$x \to -y,$$

$$y \to x,$$

$$A = (0, Bx, 0) \to (-By, 0, 0) = A + \nabla(-Bxy). \tag{34}$$

The rotated oscillator functions in the Landau gauge $A = (0, Bx, 0)$ are found by the gauge transformation with respect to Eq. (34)

$$e^{-i\frac{1}{l^2}Xy}\, \varphi_n(x - X) \to e^{-i\frac{e}{\hbar}Bxy}\left(e^{i\frac{1}{l^2}Yx}\, \varphi_n(-y + Y)\right).$$

Now we make use of the degeneracy of the levels with respect to the center coordinate Y by forming a superposition of all Y-centered functions with an appropriate weight factor $\dfrac{1}{\sqrt{2\pi l^2}} \exp\left(-i\dfrac{1}{l^2} X Y\right)$

$$\frac{1}{\sqrt{2\pi l^2}} \int e^{-i\frac{1}{l^2}XY}\, e^{-i\frac{1}{l^2}xy}\, e^{i\frac{1}{l^2}Yx}\, \varphi_n(-y + Y)\, dY$$

$$= \frac{1}{\sqrt{2\pi l^2}}\, e^{-i\frac{1}{l^2}Xy} \int e^{i\frac{1}{l^2}(x-X)(-y+Y)}\, \varphi_n(-y + Y)\, dY$$

$$= e^{-i\frac{Xy}{l^2}}\, i^n \varphi_n(x - X), \tag{35}$$

where we applied the fact the the Fourier transform like Eq. (35) transforms the oscillator function φ_n again into the oscillator function φ_n with a phase factor i^n, We summerize our considerations by

$$R(C_4)\left[e^{-i\frac{Xy}{l^2}}\, \varphi_n(x - X)\right] = i^n\left[e^{-i\frac{Xy}{l^2}}\, \varphi_n(x - X)\right]. \tag{36}$$

The transformation properties of the Bloch functions u_m are

$$R(C_4)\, u_m = e^{im\frac{\pi}{2}}\, u_m, \qquad m = \frac{3}{2}, \frac{1}{2}, -\frac{1}{2}, -\frac{3}{2}. \tag{37}$$

Inserting Ψ_k according to Eq. (25) into the left hand side of Eq. (33) using the relations (36) and (37) one verifies immediately Eq. (33).

Since the group C_{4h} contains the inversion I we have states of even $(+)$ and odd $(-)$ parity. We observe that for the special arrangement of the oscillator functions in Eq. (25) the following relation holds

$$R(I) \left[e^{-i\frac{X}{l^2}y} \sum_{\substack{n=k-4,k,\\k+4,\dots}} \varphi_n(x - X) \right] = (-1)^k \left[e^{-i\frac{X}{l^2}y} \sum_{\substack{n=k-4,k,\\k+4,\dots}} \varphi_n(x - X) \right].$$

Therefore we get

$$R(I)\,\Psi_k = (-1)^k\, e^{-i\frac{X}{l^2}y} \begin{bmatrix} \sum\limits_{n=k-4,\dots} c_n\varphi_n g_{\frac{3}{2},n}(-z) \\ \sum\limits_{n=k-4,\dots} c_n\varphi_{n+1}\left(-g_{\frac{1}{2},n}(-z)\right) \\ \sum\limits_{n=k-4,\dots} c_n\varphi_{n+2} g_{-\frac{1}{2},n}(-z) \\ \sum\limits_{n=k-4,\dots} c_n\varphi_{n+3}\left(-g_{-\frac{3}{2},n}(-z)\right) \end{bmatrix}$$

$$= \begin{cases} (-1)^k\,\Psi_k; & g_{\frac{3}{2},-\frac{1}{2}}(z) \text{ even and } g_{\frac{1}{2},-\frac{3}{2}}(z) \text{ odd,} \\ -(-1)^k\,\Psi_k; & g_{\frac{3}{2},-\frac{1}{2}}(z) \text{ odd and } g_{\frac{1}{2},-\frac{3}{2}}(z) \text{ even.} \end{cases}$$

Thus for each k we have $(+)$ and $(-)$ parity. Therefore we will label the Landau levels by the symmetry quantum numbers $k_{\pm}$. A further qualitative but physically more reasonable characterization of the Landau levels can be found by analysing the eigenvectors. Because the wave function is a superposition of many oscillator functions and contains heavy and light hole contributions we will extract the respective dominant contributions. We begin with the normalisation condition of the wave function defined in Eq. (26)

$$1 = \langle \Psi_k \mid \Psi_k \rangle = \sum_{m=-\frac{3}{2}}^{\frac{3}{2}} \left[\sum_{n=k-4,\dots} \sum_i \left| c_{m,i}\left(n + \frac{3}{2} - m\right) \right|^2 \right], \tag{38}$$

$$= \sum_{\substack{n=k-4,k,\\k+4,\dots}} \sum_m \left[\sum_i \left| c_{m,i}\left(n + \frac{3}{2} - m\right) \right|^2 \right], \tag{39}$$

$$= \sum_i \left[\sum_{n=k=4,\dots} \sum_m \left| c_{m,i}\left(n + \frac{3}{2} - m\right) \right|^2 \right]. \tag{40}$$

The bracket in Eq. (38) represents the contribution corresponding to the Bloch function u_m. The largest of the four contributions determines the main character of Ψ_k, where we choose the notation: ha, la, lb, hb for $m = \frac{3}{2}, \frac{1}{2}, -\frac{1}{2}, -\frac{3}{2}$.

The bracket in Eq. (39) represents the contribution corresponding to the oscillator function $\varphi_{n+\frac{3}{2}-m}$. The largest one determines the main character of Ψ_k noted by the corresponding integer.

The bracket in Eq. (40) represents the contribution corresponding to the basis function f_i. The largest one again determines the main character of Ψ_k, where the $f_0, f_1, \dots$ correspond to the ground and excited subbands.

In summary we have shown that besides the symmetry induced quantum numbers we can characterize the states by additional labels, which give insight into the structure of the wave functions.

5. The Landau Level Scheme

Different from the usual magnetic quantisation, which is impressed on a field free self-consistent calculation, we included the magnetic field in the self-consistent computations. As already pointed out by Trott et al. [32, 33] this treatment reveals effects, which have not been considered before: at magnetic fields, where the Fermi energy jumps from one Landau level to the next one the distribution of the free carriers changes, because the two Landau levels have different z-dependent envelope functions. Hence the self-consistent Hartree potential changes. This leads to magnetic field dependent oscillations of the Landau levels. This effect is particular to p-channels, because of the coupling between the carrier motions parallel and perpendicular to the interface. In n-channels such effects occur only, if more than one subband is occupied and the Fermi energy jumps between Landau levels of different subbands.

In our case, where both occupied subbands have ground state like envelope functions, the fluctuation of the Landau levels is not very pronounced, as can be seen from the dashed lines in Fig. 1. Therefore the Landau scheme presented in Fig. 1 has been calculated for all magnetic field values with a fixed self-consistent potential, which was obtained for $B = 3$ T. This simplification is well justified, because for our system the level separations, which are the physically important energies, are equal for both self-consistent methods.
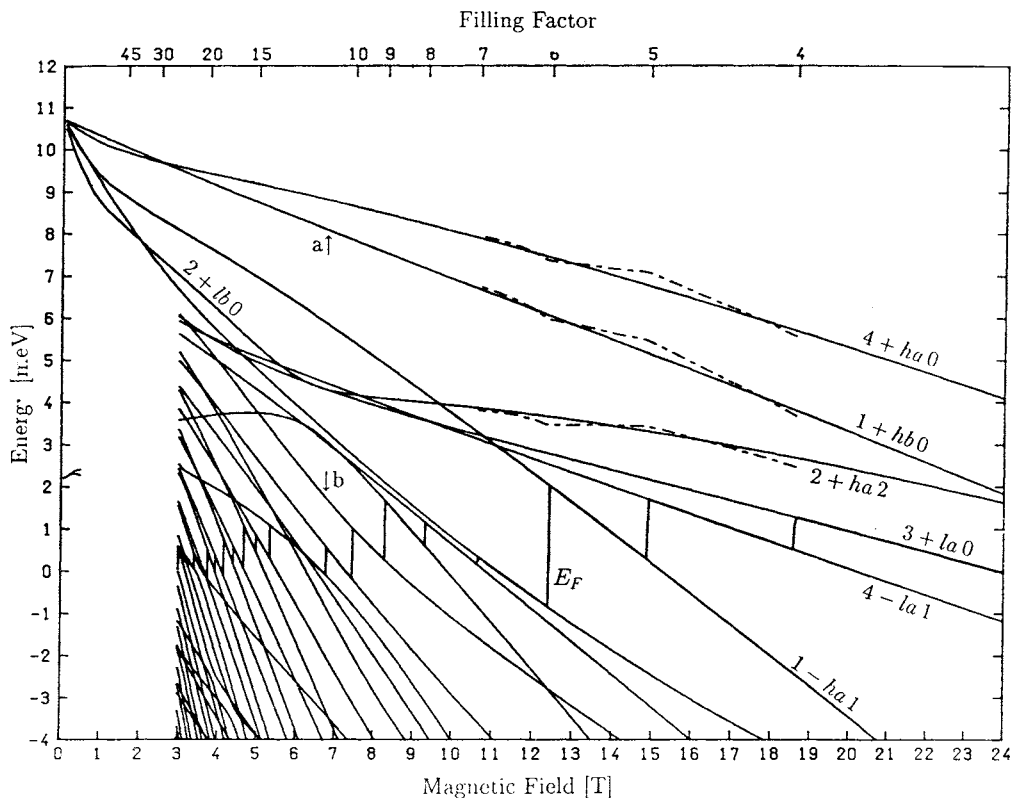
Fig. 1. Landau scheme for the p-channel of a n-type Ge-bicrystal with $N = 1.8 \times 10^{12}$ cm^{-2}. Dashed lines: Self-consistent results from the magnetic field dependent Hartree potential. Bold line: Fermi energy E_F. Entier filling factors are marked at the top.

The Landau level scheme of Fig. 1 shows a nonlinear B-dependence of nearly all levels, furthermore one observes level crossings and repulsions. Several levels are labelled with quantum numbers according to our notation. Only levels with different symmetry quantum numbers $k\pm$ are allowed to cross. For magnetic fields lower than 3 T only a few Landau levels are drawn to indicate the light hole and the heavy hole band edge at $B = 0$.

Fig. 2 is a plot of bulk germanium Landau levels $E(B, k_z)$, where $k_z = 1.15 \times 10^6$ cm^{-1} is chosen, such that the $B = 0$ heavy and light hole separation is equal to the subband splitting for the case of the p-channel. Since Fig. 1 and Fig. 2 are based both on the same bulk band structure, their comparison clearly demonstrates the fundamental influence of the confining potential on the energy spectrum.
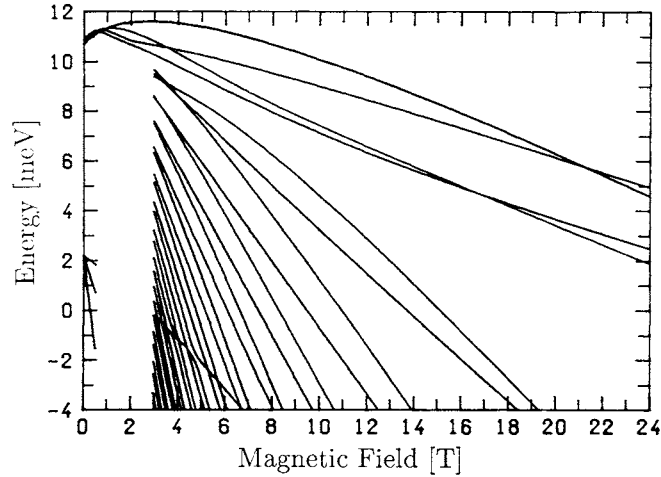
Fig. 2. Landau scheme of bulk Ge for $k_z = 1.15 \times 10^6$ cm^{-1}.

Let us demonstrate the origin and character of the quantum numbers by two examples. The decomposition of the eigenvectors according to Eqs. (38)—(40) is performed in Tab. 1 for the states, which are marked by the arrows (a) and (b) in Fig. 1. From (a) in Tab. 1 we conclude: The Bloch function $u_{\frac{3}{2}}$ gives the dominant contribution (96%, column 1), therefore we denoted the level by hb. The oscillator function φ_0 dominates (96%, column 2), therefore the level is characterized by hb 0. The basis function $f_0(z)$ dominates (94%, column 3), therefore, including the symmetry quantum number $1+$, the complete level description is $1 + hb$ 0 *ground state*. The *ground state* notation is omitted in Fig. 1, because all states are of this type. Such dominant characters are not present in the second example. Part (b) in Tab. 1 shows that this state is strongly mixed due to both Bloch functions (column 1) and oscillator functions (column 2). Therefore the quantum numbers 3-lb 3 for this state are rather insufficient.

A description of our Landau levels in terms of effective masses, g-values and Landau fans due to separate electric subbands, which are well defined quantities in n-channels is not possible or at least very doubtful. It is quite obvious that an effective mass cannot be attached to the curved Landau levels.

Due to the symmetric confinement the subband states for $B = 0$ with a finite k_z-value are twofold degenerate. This degeneracy is lifted by the magnetic field, therefore an introduction of g-values seems reasonable. In n-channels the g-values are defined by the energy seperation of two levels, which both have a common envelope function,

but have time reversed spin dependent Bloch functions. Inspection of the Landau states in Eq. (25) shows that such pairs of states do not exist in p-channels as a consequence of the bulk valence band structure. Thus a definition of g-values like in n-channels is not possible for our system.

Table 1. Decomposition (Eqs. (38—40)) of two eigenvectors corresponding to the energies marked in Fig. 1 by arrows: (a) $1 + hb\ 0$ and (b) $3 - lb\ 3$. The following abbreviation is used:

$$c_{m,i,n} = c_{m,i}\left(n + \frac{3}{2} - m\right).$$

a)						b)					
$\sum_n \sum_i |c_{m,i,n}|^2$		$\sum_i |c_{m,i,n}|^2$		$\sum_n \sum_m |c_{m,i,n}|^2$		$\sum_n \sum_i |c_{m,i,n}|^2$		$\sum_i |c_{m,i,n}|^2$		$\sum_n \sum_m |c_{m,i,n}|^2$	
m		n		i		m		n		i	
$\frac{3}{2}$	0.0058	0	0.9560	0	0.9446	$\frac{3}{2}$	0.3435	0	0.0044	0	0.7805
$\frac{1}{2}$	0.0293	1	0.0057	1	0.0064	$\frac{1}{2}$	0.0538	1	0.2512	1	0.1332
$-\frac{1}{2}$	0.0006	2	0.0288	2	0.0482	$-\frac{1}{2}$	0.5200	2	0.0618	2	0.0812
$-\frac{3}{2}$	0.9643	3	0.0007	3	0.0002	$-\frac{3}{2}$	0.0827	3	0.3298	3	0.0027
		4	0.0081	4	0.0003			4	0.0481	4	0.0015
		5	0.0001	5	0.0000			5	0.2570	5	0.0005
		6	0.0005	6	0.0003			6	0.0201	6	0.0003
		7	0.0001	7	0.0000			7	0.0133	7	0.0001
		:	0.0000	8	0.0000			8	0.0012	8	0.0000
				9	0.0000			9	0.0115	9	0.0000
								10	0.0008		
								11	0.0004		
								12	0.0000		
								13	0.0004		
								:	0.0000		

Generally the Landau levels cannot be attached to a single electric subband, which will be shown by the following example: at 4 T the third Landau level is characterized by $2 + lb\ 0$. The characterisation of the same level at 15 T is $2 + ha\ 2$. Therefore the same Landau level has changed from a light hole to a heavy hole state. At the end of this section we would like to emphasize that the Landau levels are not degenerate due to 'spin'-components, but a description by g-values is not possible however as demonstrated above.

6. Density of States

Up to now most of the experimentally obtained information about the electronic structure of p-channels have been drawn from Shubnikov-de Haas oscillations (SdH). On the one hand it seems rather difficult to decide, whether SdH oscillations are compatible or not with a complicated Landau scheme like that of Fig. 1. Therefore in order

to compare experimental and theoretical results it is desirable to calculate the conductivity $\sigma(B)$ based on the theoretical Landau levels. On the other hand such a calculation is not feasible, because a transport problem involving scattering between initial and final states as given in Eq. (25) cannot be solved with sufficient accuracy. To overcome this difficulty we calculate the density of states $D(E_F, B)$ at the Fermi energy as a function of the magnetic field instead of $\sigma(B)$. This is reasonable, because the oscillatory character given by the positions of maxima and minima is similar for both $\sigma(B)$ and $D(E_F, B)$, only the shapes of the individual extrema are different. Such a simulation of $\sigma(B)$ by $D(E_F, B)$ is useful, if one takes appropriately level broadening into account. This holds not only for p-channels, but also for those complicated n-channel systems, where more than one electric subband is occupied, so that intersecting Landau fans have to be considered. For Landau levels $E_\nu(B)$ of Gaussian shape the density of states reads

$$D(E, B) = \frac{eB}{2\pi\hbar} \sum_\nu \frac{1}{\sqrt{\pi}\,\Gamma} \exp\left[-\left(\frac{(E - E_\nu(B))}{\Gamma}\right)^2\right],\tag{41}$$

where Γ is a phenomenological broadening parameter, which is chosen as $\Gamma = \Gamma_0\sqrt{B}$ according to Ando [34].

$$N = \int\limits_{E_F(B)}^{\infty} D(E, B)\, dE \tag{42}$$

relates the Fermi energy $E_F(B)$ to a given concentration N ($T = 0$). Inserting $E_F(B)$ from Eq. (42) into Eq. (41) defines $D_F(B) = D(E_F(B), B)$, which simulates the conductivity $\sigma(B)$.

Before applying the simulation to the p-channel Landau level scheme of Fig. 1, we will treat the simpler n-channel case with two occupied subbands for convenience. In Eq. (41) all Landau levels contribute to $D_F(B)$ independently, whether they belong to the same or to different subbands, whether they have the same or different 'spin'-alignments, or have simple (n-channel) or complicated (p-channel) wave functions. Therefore the period $\Delta\left(\frac{1}{B}\right)$ of the oscillations of $D_F(B)$ is related to the total carrier concentration N by

$$\Delta\left(\frac{1}{B}\right) = \frac{e}{2\pi\hbar}\,\frac{1}{N},\tag{43}$$

which holds even in those cases, where the carrier concentration N is distributed over several subbands. This is so, because Eq. (43) essentially reflects the degeneracy $\frac{eB}{2\pi\hbar}$, which is identical for all Landau levels [35]. In the past SdH oscillations of 2D-systems involving the occupation of several subbands have been frequently analysed in such a way, that the lowest oscillatory period $\Delta\left(\frac{1}{B}\right)$ was attributed to the occupation of the lowest subband [36, 37]. For instance, previous SdH data [22] for a germanium bicrystal have been analysed in this fashion. It has been pointed out by Vinter and Overhauser [38] in conjunction with the degeneracy factor in n-type silicon inversion layers, that the lowest SdH period is entirely determined by the total carrier concentration. This is also borne out by our calculations. In Fig. 3 the results for two model calculations are shown, in order to demonstrate the point. The density of states $D_F(B)$ as a function of the magnetic field has been plotted for a model semiconductor, where the total concentration $N = 1.8 \times 10^{12}$ cm^{-2} is chosen for both cases. In the upper part curve (a) corresponds to a single occupied subband with an effective mass of $0.03\,m_0$, a g-factor of 8,
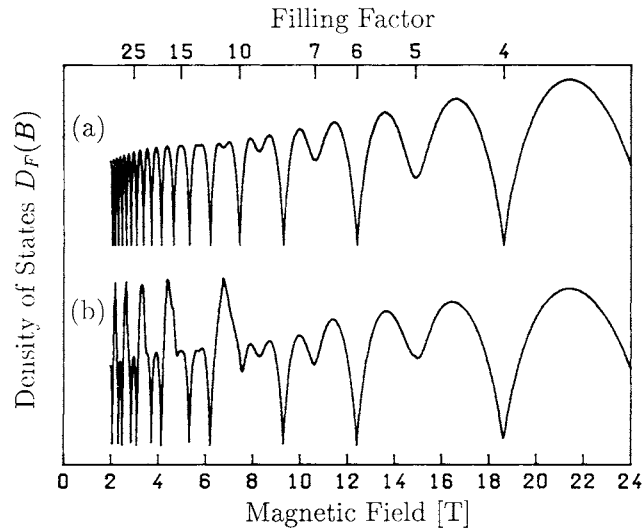
Filling Factor

Fig. 3. Density of states $D_F(B)$ versus magnetic field for n-channels with $N = 1.8 \times 10^{12}$ cm^{-2} (a) one occupied subband, (b) two occupied subbands

and a level broadening parameter $\Gamma_0 = 0.8$ meV, and Landau levels: $E_\nu(B) = \hbar \dfrac{eB}{m^*}$ $\left(\nu + \dfrac{1}{2}\right) \pm \dfrac{1}{2} g\mu_B B$. Regular oscillations are obtained, the spin-splitting is well resolved and the period $\Delta\left(\dfrac{1}{B}\right)$ deduced from neighbouring minima complies exactly with Eq. (43). For curve (b) two occupied subbands are considered with the same parameters (m^*, g, Γ_0) like (a) for each subband. We used an energy difference $\Delta E = 50$ meV for the subband edges, which implies that 68% of the carriers are located within the first and 32% within the second subband. Two different periods can be deduced. The minima for magnetic fields larger than 8 T define a period $\Delta\left(\dfrac{1}{B}\right) = 0.013$ T^{-1}, which yields with Eq. (43) the total carrier concentration $N = 1.8 \times 10^{12}$ cm^{-2}. An analysis of the neighbouring maxima in the field region below 5 T yields a period of $\Delta\left(\dfrac{1}{B}\right) = 0.04$ T^{-1}, which corresponds to $N_2 = 0.6 \times 10^{12}$ cm^{-2} of the second subband. A period, which corresponds to $N_1 = 1.2 \times 10^{12}$ cm^{-2} of the first subband does not exist in (b). From this consideration we conclude, that the smallest period deduced from SdH measurements must be attributed to the total carrier concentration. Further larger periods belong to different subbands.

Now going back to the p-channel Landau scheme of Fig. 1 we calculate the density of states $D_F(B)$ for this case, using a level broadening $\Gamma_0 = 0.1$ meV. The result is shown in Fig. 4 together with a magneto-resistance measurement of a Ge-bicrystal at 2.2 K. From the experimental curve a total carrier concentration of 1.8×10^{12} cm^{-2} is inserted into Eq. (42) of our simulation procedure to define the Fermi energy $E_F(B)$, which is already drawn in Fig. 1. Apart from the special structures of $D_F(B)$ near 6 T and 11 T the minima correspond to the jumps of $E_F(B)$ at magnetic fields of integer filling factors η. It was already pointed out that the Landau levels cannot be attributed to one subband, therefore the minima and consequently the periods cannot be attri-

Filling Factor
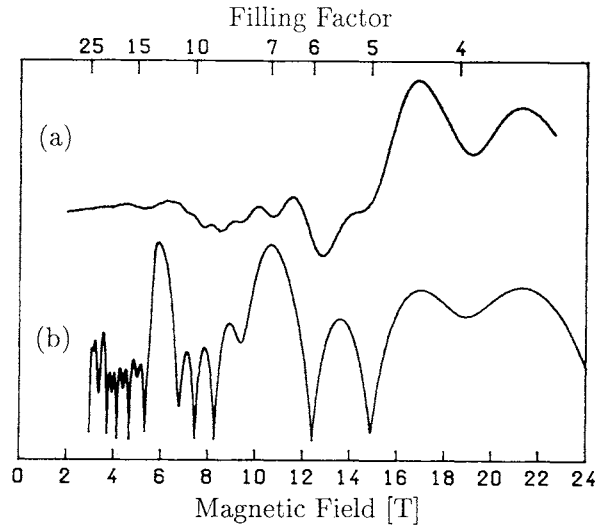
Fig. 4. (a) Magneto-resistance measurement of Ge-bicrystal [19]. (b) Density of states $D_F(B)$ versus magnetic field based on the Landau scheme of Fig. (1).

buted to a particular subband, too. We believe that this special Landau scheme with its complicated mix of wave functions demonstrates this effect very well.

If the Fermi energy meets two degenerate Landau levels for integer filling factor then there is no minimum of $D_F(B)$, because both levels are half filled, such that we have no energy gap between occupied and empty states. Due to level broadening the same holds already for nearly degenerate Landau levels. In Fig. 1 these effects occur near 6 T and 11 T leading to the pronounced maxima of $D_F(B)$ in Fig. 4. Comparing the SdH measurements and the calculated density of states $D_F(B)$ one can see that the general structure is well reproduced by our theory. But it is quite obvious that the details of our Landau scheme cannot be deduced in a unique fashion from the experimental data.

In the last section we extend our previous calculations to an additional magnetic field component $B_{\parallel}$ parallel to the grain boundary, because a more detailed verification of our model is expected. In n-channel systems the effects of $B_{\parallel}$ are dominated by the ratio of the spin-splitting, which depends on the total magnetic field, and the Landau splitting, which depends on the perpendicular component $B_{\perp}$ only. It is evident that such intuitive considerations are not possible for p-channel systems, therefore a $B_{\parallel}$ component must be inserted into the calculations from the very beginning. We do not describe the extensive details of the calculation, but mention the following essential features. The fourfold symmetry of our system is destroyed leading to a coupling of Landau levels with $\Delta n = \pm 1$, thus the matrix dimension is enlarged by a factor of four compared to our previous calculations. The Hartree approximation must be performed for each tilt angle separately. The resulting Landau scheme has a similar structure as that of Fig. 1, but several level crossings are lifted due to the elimination of k as a good quantum number. Only the parity serves as a good quantum number. A much more direct insight into the influence of $B_{\parallel}$ is obtained from the density of states than from the Landau scheme. Therefore in Fig. 5 we have plotted the functions $D_F(B_{\perp})$ for five different angles ϑ: $\boldsymbol{B} = (B \sin \vartheta, 0, B \cos \vartheta) = (B_{\parallel}, 0, B_{\perp})$. Following the ϑ-dependence of the extrema from $0°$ to $60°$ we distinguish four fundamental features.
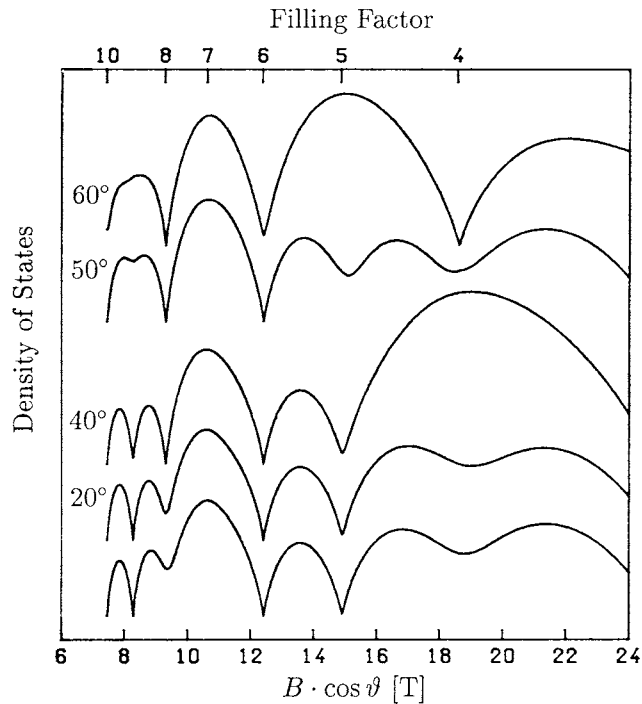
Fig. 5. Density of states $D_F(B_\perp)$ versus perpendicular magnetic field component $B \cdot \cos \vartheta$ for different angles ϑ.

(i) the minimum near $B_\perp = 19$ T for $\vartheta = 0°$ is converted into a well pronounced maximum for $\vartheta = 40°$, which for $\vartheta = 60°$ is changed back into a minimum. (ii) the minimum at about 15 T gets weaker and changes for $\vartheta = 60°$ into a strong maximum. The same behaviour is found for the minimum near 8.3 T. (iii) the maximum close to 11 T stays constant for all angles. (iv) the weak minimum at about 9.5 T shows a fixed position, but gets stronger with increasing ϑ-values.

Since the level broadening Γ is equal for all curves, the metamorphosis of these structures indicates that a considerable change of the level seperations results from $B_\parallel$. But these changings do not appear systematically, because e.g. the seperation of those levels do not change, which contribute to the constant maximum close to 11 T. In conclusion, an in plane field component $B_\parallel$ produces remarkable but not systematic changes of the density of states $D_F(B_\perp)$, which are expected to be reflected in SdH experiments under inclined field orientation conditions. Indeed tilted field magneto-resistance measurements show all the effects [22], which have been described in (i) to (iv).

7. Summary

We have developed a method to calculate electric subbands for symmetric p-channels of Ge-bicrystals in the Hartree approximation including an external magnetic field directed perpendicular as well as inclined to the grain boundary. For a special hole concentration $N = 1.8 \times 10^{12}$ cm^{-2} a numerical procedure is performed and a complicated and unusual Landau scheme is obtained. By a detailed analysis of the wave functions

it is shown that a description of the Landau levels in terms of conventional ideas like effective masses and g-values is not possible. In addition from a study of the magnetic field dependent density of states it was demonstrated that an assignment of Shubnikov-de Haas periods to separate subbands fails for the p-channel system. Even for the simpler n-channel system with multi subband occupation it was demonstrated that the determination of the subband occupations from magneto-resistance measurements has to be done carefully. Especially it was shown that the smallest SdH period corresponds to the total carrier concentration. The method presented here can also be applied to other symmetric 2D-hole systems.

References

[1] Bangert, E.; Klitzing, K. v.; Landwehr, G.: Proc. 12th Int. Conf. Physics of Semiconductors, Stuttgart. (M. H. Pilkuhn, Ed.) Teubner Verlag, 1974.

[2] Bangert, E.; Landwehr, G.: Surf. Sci. 58 (1976) 138.

[3] Landwehr, G.; Handler, P.: J. Phys. Chem. Solids 23 (1962) 891.

[4] Ohkawa, F. J.; Uemura, Y.: Prog. Theor. Phys. 57 (1975) 164.

[5] Luttinger, J. M.: Phys. Rev. 102 (1956) 1030.

[6] Broido, D. A.; Sham, L. J.: Phys. Rev. B 31 (1985) 888.

[7] Eric Yang, S.-R.; Broido, D. A.; Sham, L. J.: Phys. Rev. B 32 (1985) 6630.

[8] Sham, L. J.: Surf. Sci. 174 (1986) 105.

[9] Broido, D. A.; Sham, L. J.: Phys. Rev. B 34 (1986) 3917.

[10] Ando, T.: J. Phys. Soc. Jpn. 54 (1985) 1528.

[11] Iwasa, Y.; Miura, N.; Tarucha, S.; Okamoto, H.; Ando, T.: Surf. Sci. 170 (1986) 587.

[12] Ekenberg, U.: Surf. Sci. 170 (1986) 601.

[13] Ekenberg, U.: Phys. Rev. B 38 (1988) 12664.

[14] Altarelli, M., Festkörperprobleme XXV, Pergamon 381 (1985).

[15] Ekenberg, U.; Altarelli, M.: Phys. Rev. B 32 (1985) 3712.

[16] Altarelli, M.; Ekenberg, U.; Fasolino, A.: Phys. Rev. B 32 (1985) 5138.

[17] Landwehr, G.; Bangert, E.: Springer Series Solid State Sci. 53 (1987) 40.

[18] Bangert, E.; Landwehr, G.: Superlattices and Microstructures 1 (1985) 363.

[19] Bangert, E.; Landwehr, G.: Surf. Sci. 170 (1986) 593.

[20] Uchida, S.; Landwehr, G.; Bangert, E.: Solid State Commun. 45 (1983) 869.

[21] Uchida, S.; Remenyi, G.; Landwehr, G.: Springer Series Solid State Sci. 71 (1987) 353.

[22] Kraus, M.; Mrotzek, H.; Steinmetz, N.; Bangert, E.; Landwehr, G.; Remenyi, G.: Springer Series Solid State Sci. 87 (1989) 194.

[23] Grabecki, G.; Suski, T.; Dietl, T.; Shoskiewicz, T.; Glinski, M.: Springer Series Solid State Sci. 71 (1987) 127.

[24] Nachtwei, G.; Bassom, N. J.; Nicholas, R. J.; Preppernau, U.; Herrmann, R.: Semicond Sci. Technol. 4 (1989) 747.

[25] Gobsch, G.; Paasch, G.; Übensee, H.: Phys. Status Solidi B 135 (1986) 283.

[26] $\gamma_1 = 13.35$, $\gamma_2 = 4.24$, $\gamma_3 = 5.69$, $\varkappa = 3.41$, and $\varepsilon = 15.36$

[27] Altarelli, M.: In: Lecture Notes in Phys. 177 (1983) 174.

[28] Altarelli, M.: Phys. Rev. B 28 (1983) 842.

[29] Abramowitz, M.; Stegun, I. A.: Handbook of Mathematical Functions, Dover Publications 1970.

[30] Landwehr, G.; Uchida, S.: Surf. Sci. 170 (1986) 719.

[31] Koster, G. F.: Properties of the 32 Point Groups, M. I. T. Press, 1963.

[32] Trott, S.; Paasch, G.; Gobsch, G.; Trott, M.: Phys. Rev. B 39 (1989) 10232.

[33] Paasch, G.; Trott, S.; Gobsch, G.: to be published.

[34] Ando, T.; Fowler, A. B.; Stern, F.: Rev. Mod. Phys. 54 (1982) 437.

[35] RAZEGHI, M.; DUCHEMIN, J. P.; PORTAL, J. C.; DMOWSKI, L.; REMENYI, G.; NICHOLAS, R. J.; BRIGGS, A.: App. Phys. Lett. **38** (1986) 712.

[36] SINGLETON, J.; NICHOLAS, R. J.; NASIR, F.; SARKAR, C. K.: J. Phys. **C 19** (1986) 35.

[37] GULDNER, Y.; VIEREN, J.P.; VOOS, M.; DELAHAYE, F.; DOMINGUEZ, D.; HIRTZ, J. P.; RAZEGHI, M.: Phys. Rev. **B 33** (1986) 3990.

[38] VINTER, B.; OVERHAUSER, A. W.: Phys. Rev. Lett. **44** (1980) 47.

Anschr.d. Verf.: V. LATUSSEK,
Dr. E. BANGERT,
Prof. G. LANDWEHR
Physikalisches Institut der Universität Würzburg,
Am Hubland
W-8700 Würzburg, Germany

Anhang C

Optische Eigenschaften von Typ-III-Halbleiterheterostrukturen

Deformation potentials of the semimetal HgTe

V. Latussek, C. R. Becker,* and G. Landwehr

Physikalisches Institut der Universität Würzburg, Am Hubland, 97074 Würzburg, Germany

R. Bini and L. Ulivi[†]

European Laboratory for Non-Linear Spectroscopy, University of Florence, Polo Scientifico, Via Carrara 1, 50019 Sesto Fiorentino, Florence, Italy

(Received 13 October 2004; revised manuscript received 11 November 2004; published 10 March 2005)

It has been demonstrated that the hydrostatic deformation potential $C-a$ of a semimetal can be determined from the pressure dependence of intersubband transitions in superlattices containing the semimetal. By means of an investigation of optical absorption in HgTe/Hg$_{0.3}$Cd$_{0.7}$Te superlattices at hydrostatic pressures up to 3 GPa at room temperature the following values have been determined: $C-a=-3.69\pm0.10$ eV and $a^{HgTe}-a^{CdTe}=1.31\pm0.10$ eV, where C and a are the deformation potentials of the conduction and valence bands, respectively. Bulk HgTe normally undergoes a phase transition to the cinnabar structure at ≈1.3 GPa. However, this phase transition is frustrated in HgTe/Hg$_{0.3}$Cd$_{0.7}$Te superlattices and the HgTe layers are super-pressed above 1.3 GPa.

I. INTRODUCTION

The hydrostatic deformation potentials for the conduction and valence bands in a semiconductor, C and a, respectively, are important parameters; however, they cannot be directly determined experimentally. Their difference, $C-a$, can be determined from the hydrostatic pressure dependence of the band gap by means of excitonic absorption or photoluminescence.[1] Obviously this is not possible with a semimetal or many narrow-gap semiconductors. Nevertheless, in this article we shall demonstrate a direct method to determine the deformation potentials of either a semimetal or a narrow-gap semiconductor. In this method the hydrostatic pressure dependence of intersubband transitions in a superlattice or a multiple quantum well will be exploited.

As an example, type-III superlattices consisting of semimetallic HgTe and semiconducting Hg$_{1-x}$Cd$_x$Te layers will be considered in this article. The band structure and optical properties of these superlattices have been the subject of numerous investigations.[2] For moderately wide Hg$_{1-x}$Cd$_x$Te layers, it has been demonstrated that the band structure and the optical properties are primarily determined by the HgTe layer.[3] Consequently, this system offers a unique opportunity to investigate the band structure of semimetallic HgTe in a more direct manner. The nearly perfect match of the lattice constants makes this system ideal for such studies. Intersubband transitions in these superlattices have been investigated by means of optical absorption[2–4] and magnetoabsorption[5] experiments in conjunction with theoretical calculations. These intersubband transitions, and in particular the lowest energy gap, have also been linked to photoluminescence (PL) peaks in a number of investigations.[6]

Cheong *et al.*[7] have concluded that the hydrostatic pressure dependence of the observed PL peaks for a HgTe/Hg$_{1-x}$Cd$_x$Te superlattice is much less than that predicted by $\boldsymbol{k} \cdot \boldsymbol{p}$ band calculations based on the envelope function approximation (EFA). Their most prominent peak, which has been assigned to recombination across the SL

band gap, has a pressure coefficient of ≤ 10 meV/GPa. However, their calculations employing the EFA with a range of reasonable SL parameters predict a pressure coefficient of at least ~ 65 meV/GPa for the band gap.

In contrast, the pressure dependence of the band gap of a number of semiconductors is in reasonable agreement with theoretical calculations.[8] More recent work has corroborated these results for II-VI semiconductors. In particular, this is true for CdTe whose experimental pressure dependence at pressures below 2 GPa lies between 79 and 83 meV/GPa at room temperature, independent of experimental method— i.e., a shift of either the absorption edge,[9] the corresponding PL peak,[10] or the reflectivity.[11] Values as low as 65 meV/GPa have been determined at 2–5 K for PL peaks involving excitons.[12,13] Furthermore, the pressure dependences of the PL peak energies in CdTe/ZnTe-stained layer superlattices[14] and GaAs/Al$_{0.32}$Ga$_{0.68}$As quantum wells[15] are comparable in magnitude to that of their constituents and are in good agreement with theoretical expectations.

In this investigation we have shown that the observed structure in transmission spectra of HgTe/Hg$_{0.3}$Cd$_{0.7}$Te superlattices which correspond to intersubband transitions does depend on pressure as is expected. More importantly, information concerning the hydrostatic deformation potentials of HgTe has been extracted from the pressure dependence of the intersubband transitions.

II. EXPERIMENTAL DETAILS

The two superlattices employed in this investigation were grown on Cd$_{0.96}$Zn$_{0.04}$Te(001) substrates in a Riber 2300 molecular beam epitaxial system at the University of Würzburg as has been described in detail elsewhere.[3] The thicknesses of the HgTe and Hg$_{0.3}$Cd$_{0.7}$Te layers were chosen such that the corresponding intersubband transitions were >280 meV in order to allow high-pressure transmission measurements in a diamond anvil cell. These measurements were carried

out at the European laboratory for nonlinear spectroscopy (LENS) in Florence.

The samples were carefully polished, mechanically, and then chemomechanically, to a thickness of $\sim 25-35$ μm. No change in the transmission spectra was observed after polishing. They were then cleaved such that a nearly square sample with dimensions of $\sim 120 \times 120$ μm^2 resulted. A sample together with a small ruby crystal, which was used to calibrate the pressure, was then loaded into a membrane diamond anvil cell from the Betsa company. Ar gas was employed as the pressure medium in the cell and hydrostatic pressure on the sample was generated by means of a membrane containing He gas. Type-IIa diamonds were employed which allowed transmission measurements to be carried out above an energy of 280 meV. The measurements were carried out using a Fourier transform spectrometer, Bruker HR-120, and additional components which have been described elsewhere.[16] The infrared radiation was focused onto the sample such that all light would have to pass through the sample.

III. THEORETICAL DETAILS

The absorption coefficient α and the transmission have been calculated using the envelope function method, as has been described in detail elsewhere.[3] The full 8×8 Kane Hamiltonian including all second-order terms representing the far-band contributions has been employed. A revised set of values for the band parameters deduced from measurements on bulk HgTe and Hg$_{1-x}$Cd$_x$Te by Weiler[17] was employed which nevertheless reproduces the same bulk band structure at room temperature.

The Hamiltonian was modified according to Bir and Pikus[18] in order the include the influence of pressure in the model:

$$\Delta E_c(P) = C(x)3\epsilon(P), \tag{1}$$

$$\Delta E_v(P) = a(x)3\epsilon(P), \tag{2}$$

where $\Delta E_c(P)$ and $\Delta E_v(P)$ are the changes in the conduction and valence bands due to the hydrostatic pressure P, $C(x)$ and $a(x)$ are the deformation potentials of the conduction and valence bands,[19] and x is the Cd concentration of the layer in question. This was accomplished by using Murnaghan's equation of state[20]

$$\epsilon(P) = \frac{1}{3}\left[-1 + \left(1 + \frac{B_1}{B_0}P\right)^{-1/B_1}\right], \tag{3}$$

where B_0 is the bulk modulus and $B_1 = dB_0/dP$. The values of B_0 and B_1 for HgTe and CdTe employed in the model are listed in Table I. Both B_0 and B_1 are assumed to vary linearly with the composition x of the material in question. Consequently $\epsilon(P)$ is also a function of material composition.

IV. RESULTS AND DISCUSSION

In this investigation, the shift of intersubband transitions with hydrostatic pressure is of primary importance. This can be shown to be systematically correlated to the correspond-

TABLE I. Summary of band gap pressure dependence, $C-a$, and strain parameters at room temperature. α calculated using Eq. (7) or (A3), β present investigation, and δ calculated using Eq. (A4).

Parameter	HgTe	Ref.	CdTe	Ref.
γ_0 (meV/GPa)	70–138[a]	23	79–83	9–11
B_0 (GPa)	42.3	24	42.50	25
B_1	3.78	26	4.20	25
$(C-a)$ (eV)	-4.4 ± 1.5	α	-3.42 ± 0.10	α
$(C-a)$ (eV)	-3.69 ± 0.10	β		
γ_0 (meV/GPa)	87.2 ± 2.5	α,β		
γ_1 (meV/GPa^2)	-4.61 ± 0.16	δ,β		

[a]At 4 and 77 K.

ing absorption edges in the smoothed transmission spectra shown in Fig. 1. The two steps correspond to the $H1$-$E1$ and $L1$-$E1$ intersubband transitions, where H, L, and E refer to heavy hole, light hole, and electron subbands, respectively. The band structure of this superlattice as well as these two intersubband transitions are shown in Fig. 2.

The presence of interference fringes shown in Fig. 1 due to the sample as well as to cavities between the sample and the diamond windows makes a determination of the absorption edge less precise. Therefore we have attempted to eliminate these interference fringes by taking the ratio of two transmission spectra at nearly the same pressure; see Fig. 3. The resulting extrema correspond to the transmission edges at the mean pressure if the pressure dependence is linear as is the case for small pressure differences. It can be easily shown that for a small shift in the transmission spectrum T,
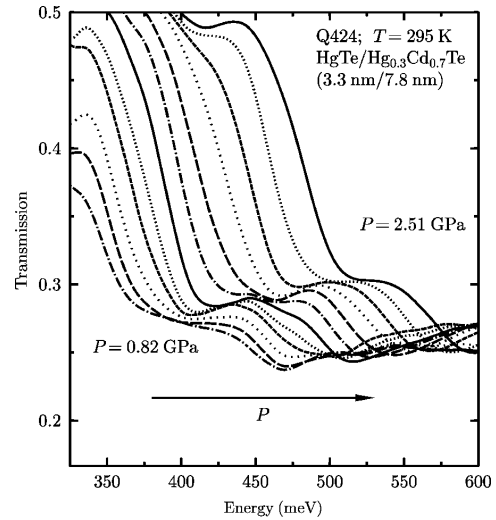

FIG. 1. Transmission spectra of Q424 at 295 K for pressures between 0.82 and 2.51 GPa. The two steps at lower and higher energies correspond to the $H1$-$E1$ and $L1$-$E1$ intersubband transitions, respectively.
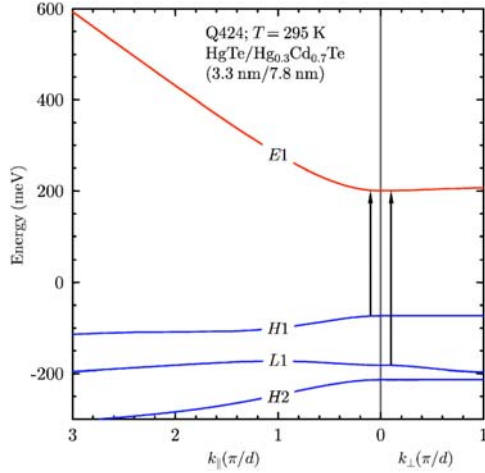
FIG. 2. The band structure of Q424 at 295 K and ambient pressure. The in-plane and perpendicular components of the wave vector, $k_\parallel$ and $k_\perp$, are in units of π/d where d is the superlattice period.

$$\frac{\Delta T}{T} \approx d\Delta\alpha, \qquad (4)$$

where d and α are the thickness and absorption coefficient, respectively.

Obviously the resulting transmission ratio and $d\alpha/dE$ shown in Fig. 3 are in good agreement with experiment. In addition, the ratio of the amplitudes of the two maxima is in good agreement with the theoretically calculated ratio of the corresponding intersubband transitions—i.e., $H1$-$E1$ and
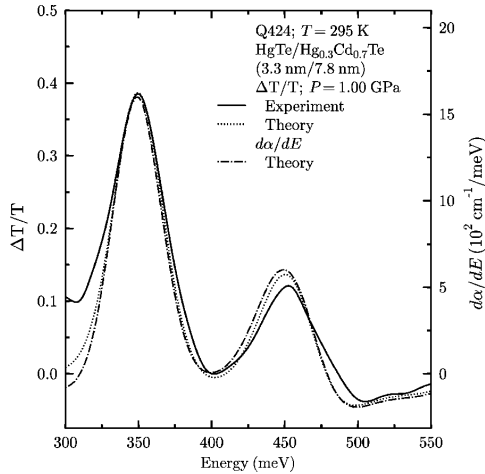
FIG. 3. Experimental and theoretical transmission spectra ratios ($T_{1.18\ \text{GPa}}/T_{0.82\ \text{GPa}}-1$), as well as $d\alpha/dE$ for Q424 at 295 K and a pressure of 1.00 GPa. The minima at lower and higher energies correspond to the $H1$-$E1$ and $L1$-$E1$ intersubband transitions, respectively.
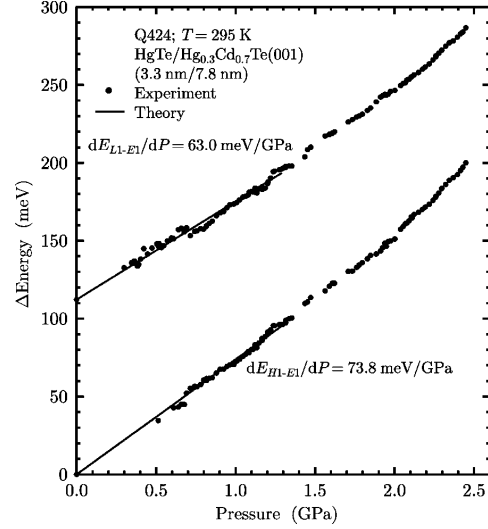
FIG. 4. Pressure dependences of the $H1$-$E1$ and $L1$-$E1$ intersubband transitions for Q424 at 295 K. The theoretical dependences according to the EFA calculations described in the text are indicated by solid lines up to the expected phase transition in HgTe at $\sim$1.3 GPa.

$L1$-$E1$—see Fig. 3. Agreement for the amplitude ratio is good for all pressures with experimentally accessible transition energies—i.e., above 280 meV.

Since dE_{i-f}/dP and not the absolute values of E_{i-f} are of interest, the theoretical and experimental intersubband transition energies as a function of pressure for Q424 have been normalized to the values at atmospheric pressure as is shown in Fig. 4. At pressures below 1.0 GPa, the slopes for $H1$-$E1$ and $L1$-$E1$ are 73.8±1.0 and 63.0±1.0 meV/GPa, respectively.

From the pressure dependence, knowledge of the conduction and valence band deformation potentials of HgTe and CdTe can be gained. $C(x)$ and $a(x)$ are assumed to vary linearly with the composition x of the Hg$_{1-x}$Cd$_x$Te layer. These parameters are related to the pressure dependence of the respective band gaps, dE_0/dP, according to

$$\frac{dE_0}{dP} = -(C-a)\frac{1}{B_0}. \qquad (5)$$

Normally the pressure dependence of the band gap, E_0, of bulk materials is analyzed by means of a quadratic equation:

$$E_0(P) = E_0(0) + \gamma_0 P + \gamma_1 P^2. \qquad (6)$$

Most authors either cite values of dE_0/dP assuming a linear dependence or determine γ_0 and γ_1 independently. However, it should be pointed out that γ_0 and γ_1 are not independent and γ_1 is not negligible. Frogley et al.[21] have advocated that the linear pressure coefficient should be defined and reported as dE_0/dP at zero pressure. However, in order to compare results from different materials it is necessary to use the ap-

TABLE II. Experimental and theoretical values of the pressure dependence of intersubband transition energies, dE_{i-f}/dP at 295 K.

| | d_{HgTe} | d_{HgCdTe} | dE_{i-f}/dP (meV/GPa) | | | |
| | ± 0.2 | ∓ 0.2 | Experiment | | Theory | |
	(nm)	(nm)	$H1$-$E1$	$L1$-$E1$	$H1$-$E1$	$L1$-$E1$
Q230	3.1	7.5	71.5 ± 3.0	62.0 ± 3.0	74.3	63.8
Q424	3.3	7.8	73.8 ± 1.0	63.0 ± 1.0	73.8	63.0

propriate quadratic analysis since γ_0 and γ_1 are material dependent.

If higher terms of a Taylor expansion of Eq. (3) are neglected, then γ_0 and γ_1 are equal to

$$\gamma_0 = -(C-a)\frac{1}{B_0}, \tag{7}$$

$$\gamma_1 = -\frac{1+B_1}{2B_0}\gamma_0. \tag{8}$$

This normally leads to a very good approximation of the results of an analysis by means of Murnaghan's equation of state. Moreover, the values of γ_0 and γ_1 can be corrected, depending on the range of pressures over which the analysis is conducted. This is demonstrated in detail in the Appendix.

According to

$$\frac{\gamma_1}{\gamma_0} = -\frac{1+B_1}{2B_0}, \tag{9}$$

$E(P)$ is always sublinear; however, in the present investigation $E(P)$ is hyperlinear above approximately 1.3 GPa. This coincides with the phase transition of HgTe from zinc blende to cinnabar.[22] Obviously this phase transition is suppressed by the superlattice, since no evidence for a phase transition is observed; $dE/dP(P)$ is a smooth function and no abrupt change in the experimental frequencies or relative amplitudes of the $H1$-$E1$ and $L1$-$E1$ intersubband transitions is observed.

Published values of dE_0/dP, or in most cases γ_0, for CdTe (Refs. 9–11) are reasonably consistent between 79 and 83 meV/GPa, whereas those for HgTe (Ref. 23) are not— i.e., 70–138 meV/GPa. The uncertainty in the HgTe values is compounded by the fact that they result from investigations of $Hg_{1-x}Cd_xTe$, not HgTe, and do not result from a direct measurement of a shift of the band gap. Moreover, even more uncertainty exists in individual deformation potentials C and a. Values for $C-a$ are summarized in Table I. To our knowledge, nothing has been published concerning $C-a$ for the $Hg_{0.3}Cd_{0.3}Te$ alloy. Therefore we have assumed that $C-a$ varies linearly with Cd concentration. $C-a$ for HgTe and $a^{\text{HgTe}}-a^{\text{CdTe}}$ have been used as the only adjustable parameters in the following calculations.

By fitting the experimental data, it has been shown that the pressure dependence of the $H1$-$E1$ and $H2$-$E2$ intersubband transitions depend on $(C-a)^{\text{HgTe}}$ but are nearly independent of $(C-a)^{\text{CdTe}}$:

$$\frac{dE_{H1-E1}}{dP} = f((C-a)^{\text{HgTe}}) \tag{10}$$

or

$$\frac{dE_{H2-E2}}{dP} = f((C-a)^{\text{HgTe}}). \tag{11}$$

The uncertainty in $C-a$ for CdTe given by 3.42 ± 0.10 eV results in a much smaller uncertainty in $C-a$ for HgTe expressed by 3.69 ± 0.02 eV. Furthermore, the difference in the pressure dependence between the $H1$-$E1$ and $L1$-$E1$ transitions depends directly on the difference in a between HgTe and CdTe,

$$\frac{dE_{H1-E1}}{dP} - \frac{dE_{L1-E1}}{dP} = f(a^{\text{HgTe}} - a^{\text{CdTe}}), \tag{12}$$

and consequently on the pressure dependence of the valence band offset between HgTe and CdTe.

It should be mentioned here that other parameters including the $\mathbf{k} \cdot \mathbf{p}$ parameters do not significantly influence the calculated pressure dependence. The calculated values of dE_{i-f}/dP up to 1.0 GPa, which are listed in Table II and also plotted in Fig. 4, are in excellent agreement with the experimental values. This results directly in $C-a = -3.69 \pm 0.10$ eV for HgTe and $a^{\text{HgTe}} - a^{\text{CdTe}} = 1.31 \pm 0.10$ eV. These uncertainties are due to a combination of uncertainties in parameters taken from the literature and the experimental data.

Agreement between the calculated results and the experimental data for Q230 at 295 K is also good, even though the statistical significance of the data is less than that of Q424. Substitution of $C-a = -3.69 \pm 0.10$ eV into Eq. (7) results in $\gamma_0 = 87.2 \pm 2.5$ meV/GPa for HgTe.

The energy difference between the first heavy hole and the first light hole subbands is determined primarily by the valence band offset Λ between HgTe and CdTe.[3] Consequently, a difference in the pressure dependence of the $H1$-$E1$ and $L1$-$E1$ intersubband transitions is due to the pressure dependence of Λ. Because B_0 and B_1 are nearly equal for HgTe and CdTe—i.e., $\epsilon^{\text{HgTe}}(P) \approx \epsilon^{\text{CdTe}}(P)$—using Eqs. (2) and (3) its follows that

$$\Delta E_v^{\text{HgTe}} - \Delta E_v^{\text{CdTe}} = (a^{\text{HgTe}} - a^{\text{CdTe}})3\epsilon^{\text{CdTe}}(P), \tag{13}$$
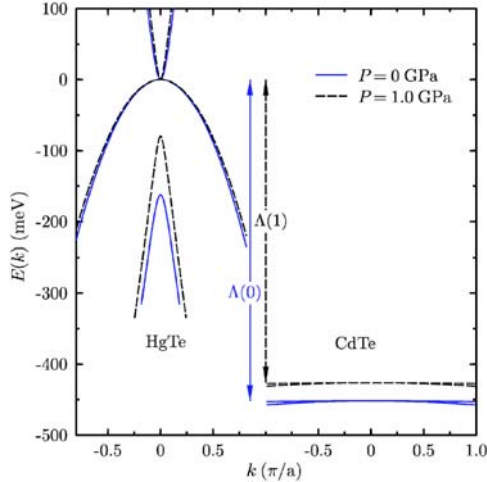
FIG. 5. The energy dispersion $E(\mathbf{k})$ of the light and heavy hole valence bands for HgTe and CdTe as well as the first conduction band for HgTe for two different pressures at 295 K. The dispersion of the CdTe valence bands is much flatter due to its larger hole effective masses. The valence band offset $\Lambda(P)$ at 0 and 1.0 GPa is indicated.

$$a^{\mathrm{HgTe}} - a^{\mathrm{CdTe}} \approx -B_0^{\mathrm{CdTe}} \frac{d\Lambda}{dP}. \tag{14}$$

It is note worthy that $d\Lambda/dP$, which is a heterostructure parameter, results from knowledge of the bulk parameters.

The calculated energy dispersion $E(\mathbf{k})$ of the light and heavy hole valence bands for HgTe and CdTe as well as the first conduction band for HgTe is shown in Fig. 5 for 0.0 and 1.0 GPa at room temperature. Due to the large heavy and light hole effective masses for CdTe, its valence band dispersion is very flat. In contrast the electron and light hole dispersion for HgTe, and even that of its heavy hole, is much more pronounced. The pressure dependence of Λ for $P \leq 1.0$ GPa at 300 K is indicated in Fig. 5 and is also given by

$$\Lambda(P) = \Lambda(0) + \frac{d\Lambda}{dP}P, \tag{15}$$

where $\Lambda(0) = 450$ meV according to Ref. 3 and $d\Lambda/dP = -25$ meV/GPa.

It should be pointed out that the intersubband transition pressure dependence, which is a salient feature of this investigation, is nearly independent of the values of the superlattice parameters over a wide range of values. For example, as shown in Fig. 6, an uncertainty in the HgTe width of ± 0.5 nm leads to an error of merely ± 0.10 eV in $C-a$ for HgTe as well as ± 0.10 eV in $a^{\mathrm{HgTe}} - a^{\mathrm{CdTe}}$.

In addition, if the $H1$-$E1$ intersubband transition is below 280 meV and therefore not observable, then the pressure dependence of $H2$-$E2$ can be employed to determine $C-a$ according to Eq. (11).
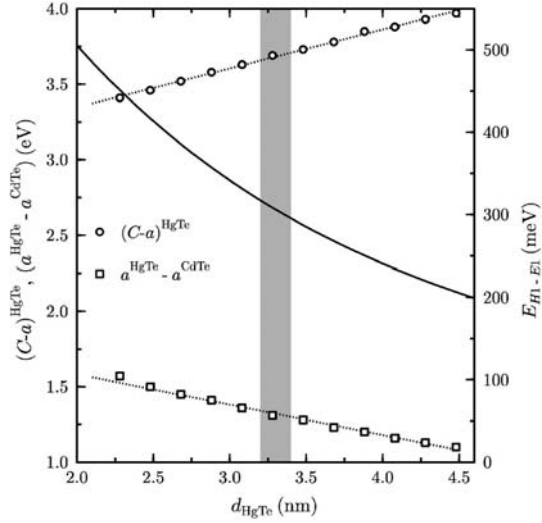
FIG. 6. Values of $(C-a)^{\mathrm{HgTe}}$ and $a^{\mathrm{HgTe}} - a^{\mathrm{CdTe}}$ versus the HgTe thickness, d_{HgTe}, necessary to reproduce the experimentally determined values of γ_0 for the $H1$-$E1$ and $L1$-$E1$ intersubband transitions for Q424 at 295 K. The dotted lines are merely guides to the eye. Values of $E_{H1\text{-}E1}$ versus d_{HgTe} are also plotted as a solid line. The long vertical gray area corresponds to the uncertainty in d_{HgTe}.

Only theoretical values or indirectly determined experimental values for either a^{HgTe} or a^{CdTe} have been published—for example, according to the tight-binding calculations of Merad *et al.*,[27] $a^{\mathrm{CdTe}} = 0.76$ eV. In addition, according to Takita and Landwehr,[28] $a^{\mathrm{HgTe}} = 3.8$ eV. This would require that $C \approx 0$. In other words, almost the entire pressure dependence would be due to a shift of the valence band and none to that of the conduction band. This is not the case for any other material to our knowledge. In all fairness, it should be mentioned that the results of Takita and Landwehr were obtained by means of a less direct method involving multiple phonons. Regardless of the individual values, the present method allows $a^{\mathrm{HgTe}} - a^{\mathrm{CdTe}}$ to be experimentally determined with excellent precision.

At pressures below 1.0 GPa, dE_{i-f}/dP for $H1$-$E1$ and $L1$-$E1$ with values of 73.8 ± 1.0 and 63.0 ± 1.0 meV/GPa, respectively, are in good agreement with theory as can be seen in Fig. 4. Above 1.3 GPa the experimental results can not be explained by our model. Bulk HgTe undergoes a phase transition from zinc blende to cinnabar at ~ 1.3 GPa.[22] However, there is no sharp change in the intersubband energies and no destructive change in the sample at pressures near 1.3 GPa. Moreover, the experimental results are reversible up to at least 2.5 GPa. Therefore it seems reasonable to suggest that the observed increase in dE_{i-f}/dP is due to a frustration of this phase transition. In other words, these thin HgTe layers are stabilized by the neighboring $Hg_{0.3}Cd_{0.7}Te$ layers; i.e., they are superpressed.

V. CONCLUSION

We conclude that the hydrostatic deformation potential, $C-a$, for a semimetal can be determined by means of the

pressure dependence of intersubband transitions of a super-lattice containing the semimetal. In addition a precise value of $a^{HgTe} - a^{CdTe}$ results from $dE_{H1-E1}/dP - dE_{L1-E1}/dP$. In this investigation $C - a = -3.69 \pm 0.10$ eV for HgTe and $a^{HgTe} - a^{CdTe} = 1.31 \pm 0.10$ eV.

In contrast to the photoluminescence results of Cheong *et al.*,[7] we have shown that the observed structure in transmission spectra of HgTe/Hg$_{0.3}$Cd$_{0.7}$Te superlattices which correspond to intersubband transitions does depend on pressure as is expected. Furthermore, employment of this model results in the correct electronic band structure of HgTe/Hg$_{1-x}$Cd$_x$Te superlattices and the correct dependence on hydostatic pressure. Bulk HgTe normally undergoes a phase transition to the cinnabar structure at ≈ 1.3 GPa. However, this phase transition is frustrated in HgTe/Hg$_{0.3}$Cd$_{0.7}$Te superlattices and the HgTe layers are superpressed above 1.3 GPa.

ACKNOWLEDGMENTS

APPENDIX

If the equation

$$E_0(P) = E_0(0) + \gamma_0 P + \gamma_1 P^2 \qquad (A1)$$

is considered to be the result of a least-squares fit of an equation involving Murnaghan's equation of state,[20] where higher terms are neglected, then the values of the coefficients γ_0 and γ_1 depend on the range of pressure involved in the analysis of the data. Assuming that range is given by

$$\frac{P}{P_m} \in [0,1], \quad \frac{B_1}{B_0} P_m \lesssim 1, \qquad (A2)$$

then

$$\gamma_0 = -(C - a)\frac{1}{B_0}(1 - S_0), \qquad (A3)$$

$$\gamma_1 = -\left[\frac{1 + B_1}{2B_0}(1 - S_1)\right]\gamma_0, \qquad (A4)$$

where

$$S_i = \frac{P_m}{B_0}\left[Z_{i1} + Z_{i2}B_1 + (Z_{i3} + Z_{i4}B_1)\frac{P_m}{B_0}\right]. \qquad (A5)$$

A least-squares analysis results in the values

$$Z_{01} = 0.1182, \quad Z_{11} = 0.9338,$$

$$Z_{02} = -0.0207, \quad Z_{12} = 0.4850,$$

$$Z_{03} = -1.2677, \quad Z_{13} = 0.1069,$$

$$Z_{04} = 0.6235, \quad Z_{14} = -0.9101.$$

If P_m is sufficiently small, then $S_0 \ll 1$ and $S_1 \ll 1$, and Eqs. (A3) and (A4) reduce to the first two coefficients of a Taylor's expansion of Murnaghan's equation of state:

$$\gamma_0 = -(C - a)\frac{1}{B_0}, \qquad (A6)$$

$$\gamma_1 = -\frac{1 + B_1}{2B_0}\gamma_0. \qquad (A7)$$

In this investigation P_m has been taken to be 1.0 GPa, and consequently $S_0 \approx 0.0016$ and $S_1 \approx 0.064$. Therefore only one of the two conditions—i.e., $S_0 \ll 1$—is fulfilled. The value of ≈ 0.064 for S_1 results in an approximately 6.4% smaller value of $|\gamma_1|$.

*Electronic address: becker@physik.uni-wuerzburg.de

†Present affiliation: Istituto dei Sistemi Complessi-CNR, Via della Madonna del Piano, 50019 Sesto Fiorentino, Italy.

[1] K. H. Yoo, R. L. Aggarwal, L. R. Ram-Mohan, and O. K. Wu, J. Vac. Sci. Technol. A **8**, 1194 (1990).

[2] J. R. Meyer, C. A. Hoffman, T. H. Myers, and N. C. Giles, in *Handbook on Semiconductors*, edited by T. S. Moss (Vol. 3 edited by S. Mahajan (North-Holland, Amsterdam, 1994), p. 535.

[3] C. R. Becker, V. Latussek, A. Pfeuffer-Jeschke, G. Landwehr, and L. W. Molenkamp, Phys. Rev. B **62**, 10 353 (2000).

[4] N. F. Johnson, H. Ehrenreich, P. M. Hui, and P. M. Young, Phys. Rev. B **41**, 3655 (1990).

[5] M. von Truchsess, V. Latussek, F. Goschenhofer, C. R. Becker, G. Landwehr, E. Batke, R. Sizmann, and P. Helgesen, Phys. Rev. B **51**, 17 618 (1995).

[6] J. P. Baukus, A. T. Hunter, J. N. Schulman, and J. P. Faurie, J. Appl. Phys. **64**, 283 (1988).

[7] H. M. Cheong, J. H. Burnett, W. Paul, P. M. Young, Y. Lansari, and J. F. Schetzina, Phys. Rev. B **48**, 4460 (1993).

[8] D. L. Camphausen, G. A. N. Connell, and W. Paul, Phys. Rev. Lett. **26**, 184 (1971).

[9] W. Shan, S. C. Shen, and H. R. Zhu, Solid State Commun. **55**, 475 (1985).

[10] J. R. Mei and V. Lemos, Solid State Commun. **52**, 785 (1984).

[11] G. A. Babonas, R. A. Bendoryus, and A. Y. Shileika, Sov. Phys. Semicond. **5**, 392 (1971).

[12] D. J. Dunstan, B. Gil, C. Preister, and K. P. Homewood, Semicond. Sci. Technol. **4**, 241 (1989).

[13] M. Prakash, M. Chandrasekhar, H. R. Chandrasekhar, I. Miotkowski, and A. K. Ramdas, Phys. Rev. B **42**, 3586 (1990).

[14] B. Gil, D. J. Dunstan, J. Calatayud, H. Mathieu, and J. P. Faurie, Phys. Rev. B **40**, 5522 (1989).

[15] U. Venkateswaran, M. Chandrasekhar, H. R. Chandrasekhar, B. A. Vojak, F. A. Chambers, and J. M. Meese, Phys. Rev. B **33**,

74

8416 (1986).

[16] R. Bini, L. Ulivi, H. J. Jodl, and P. R. Salvi, J. Chem. Phys. **103**, 1353 (1995).

[17] M. H. Weiler, in *Semiconductors and Semimetals*, edited by R. Willardson and A. C. Beer (Academic Press, New York, 1981), Vol. 16, p. 119.

[18] G. L. Bir and G. E. Pikus, *Symmetry and Strain-induced Effects in Semiconductors* (Wiley, Chichester, 1974).

[19] E. G. Novik, A. Pfeuffer-Jeschke, T. Jungwirth, V. Latussek, C. R. Becker, G. Landwehr, H. Buhmann, and L. W. Molenkamp, cond-mat/0409392 (unpublished).

[20] F. D. Murnaghan, Proc. Natl. Acad. Sci. U.S.A. **30**, 244 (1944).

[21] M. D. Frogley, J. L. Sly, and D. J. Dunstan, Phys. Rev. B **58**, 12 579 (1998).

[22] J. Blair and A. C. Smith, Phys. Rev. Lett. **7**, 124 (1961).

[23] *Numerical Data and Functional Relationships in Science and Technology*, Landolt-Börnstein, New Series, Vol. 17b (Springer, Berlin, Heidelberg, 1982), pp. 239, and references cited therein.

[24] R. I. Cottam and G. A. Saunders, J. Phys. Chem. Solids **36**, 187 (1975).

[25] P. Maheswaranathan, R. J. Sladek, and U. Debska, Phys. Rev. B **31**, 5212 (1985).

[26] J. A. Tuchman and I. P. Herman, Phys. Rev. B **45**, 11 929 (1992).

[27] A. E. Merad, M. B. Kanoun, J. Cibert, H. Aourag, and G. Merad, Phys. Lett. A **315**, 143 (2003).

[28] K. Takita and G. Landwehr, Phys. Status Solidi B **106**, 259 (1981).

Band structure and its temperature dependence for type-III HgTe/Hg$_{1-x}$Cd$_x$Te superlattices and their semimetal constituent

C. R. Becker,* V. Latussek, A. Pfeuffer-Jeschke, G. Landwehr, and L. W. Molenkamp
Physikalisches Institut der Universität Würzburg, Am Hubland, 97074 Würzburg, Germany
(Received 15 March 2000)

Intersubband transitions in HgTe/Hg$_{1-x}$Cd$_x$Te superlattices and their dependence on temperature have been investigated for a large number of superlattices with widely different parameters. It has been shown by means of the envelope function approximation using the full 8×8 Kane Hamiltonian, that the valence band offset is primarily responsible for the separation between the $H1$-$E1$ and $L1$-$E1$ intersubband transition energies of semiconducting HgTe/Hg$_{1-x}$Cd$_x$Te superlattices with a normal band structure. To a good approximation, all other relevant superlattice parameters have little or no effect on this energy difference. This leads to an unequivocal determination of the valence band offset between HgTe and CdTe Λ which is 570 ± 60 meV at 5 K for both the (001) and the (112)B orientations. The temperature dependence of both intersubband transition energies can only be explained by the following conditions: Λ is also temperature dependent as expressed by $d\Lambda/dT=-0.40\pm0.04$ meV/K; the anisotropic heavy hole effective mass has a significant temperature dependence; and E_g(HgTe,300 K)$=-160\pm5$ meV which is appreciably lower than the extrapolated values found in the literature.

I. INTRODUCTION

The band structure of type-III superlattices (SL's) and their related properties are largely determined by that of the quantum well. Conversely, an investigation of the optical and electrical properties of type-III superlattices can lead to information about the zero gap or semimetallic material used in the quantum well. Hence one has the unique opportunity to investigate properties of the semimetal which cannot easily be investigated by other methods.

For example, the band gap of HgTe and its temperature dependence directly influences the temperature dependence of the superlattice subbands and thus the temperature dependence of the intersubband transition energies. The magnitude of the negative band gap of HgTe at room temperature is subject to large experimental uncertainties due to difficulties in the conventional magneto-optical method at temperatures above 100 K.[1] Another such property is the deformation potential of HgTe relative to that of CdTe, which has only recently been experimentally determined by means of an optical absorption investigation of HgTe/Hg$_{0.32}$Cd$_{0.68}$Te superlattices under hydrostatic pressure.[2] Furthermore, it will be shown that the valence-band offset is to a good approximation primarily responsible for the energy difference between the first heavy-hole $H1$ and the first light-hole $L1$ subband of a HgTe/Hg$_{1-x}$Cd$_x$Te superlattice with normal band structure. This energy difference is nearly independent of other superlattice parameters, and consequently leads to a precise determination of the valence-band offset between HgTe and CdTe Λ.

The band structure and consequently the optical properties depend on the band structure of the quantum wells and barriers, i.e., HgTe and Hg$_{1-x}$Cd$_x$Te, their widths, and the potential energy differences between these two components. The latter depends in turn on their composition, the valence-band offset as well as the shape and width of the Cd concen-

tration profile across the interfaces. A profile described by an error function similar to an experimental profile according to Kim *et al.*[3] is assumed and leads to a consistent description of the experimental results. Finally, the width of this interface, d_t, has been shown to be a convenient variable for the study of interdiffusion in these superlattices.[4]

In order to accomplish the above, one has to determine the relevant experimental intersubband transition energies. However, this is not a trivial undertaking due, to a large extent, to a lack of knowledge about the position of a particular band gap relative to the frequency of photoluminescence peaks,[5–7] or that of the absorption edges.[8] The method we propose and demonstrate here, is to determine the position of the absorption edge and then its position relative to the intersubband transition energy itself. This can be accomplished by calculating the transition energies as well as the corresponding absorption coefficient. Finally, by fitting the theoretical and experimental absorption coefficients, one can determine the experimental intersubband transition energies relative to their absorption edges.

II. EXPERIMENTAL DETAILS

Epitaxial growth was carried out in a Riber 2300, molecular beam epitaxial system that has been modified to permit the growth of Hg-based materials as has been described elsewhere.[4] After the growth of a thin CdTe buffer layer, the HgTe/Hg$_{1-x}$Cd$_x$Te superlattices were grown on (001) and (112)B oriented Cd$_{0.96}$Zn$_{0.04}$Te and CdTe substrates at 180 °C with the exception of three (112)B SL's at 188 °C. The substrate temperature was determined with an accuracy of $\pm$ 2 °C by means of a thermocouple which was in physical contact with a molybdenum substrate holder. The thermocouple was carefully calibrated at the melting points of indium and tin.

The composition of the barrier material has been determined by means of transmission measurements[9] on thick test

layers of $Hg_{1-x}Cd_xTe$ grown under identical conditions with the exception of the absence of the HgTe layers. At a growth temperature of 180 °C, $x = 0.68 \pm 0.02$ and $x = 0.95 \pm 0.02$ for the (001) and (112)B orientations, respectively. This value has been corroborated by a determination of the barrier TO phonon frequency for several (001) SL's.[10] Cd has been found in some thin layers of HgTe grown under similar conditions by means of *in situ* x-ray photoelectron spectroscopy. If the Cd is evenly distributed throughout the layer then an average concentration in the well x_w can be calculated. Usually this value was below the sensitivity of the spectrometer, i.e., much less than 0.5%, however, 3.0% was determined on one occasion. The latter value was shown to be due to sublimation from the hot CdTe shutter, which depends on what was grown previously. Nonlinear diffusion[11] may also account for the presence of small amounts of Cd in the HgTe wells.

The superlattice period is readily accessible by x-ray diffraction experiments; however well and barrier thicknesses are not so easily determined. Historically well and barrier thicknesses have been inferred from the growth parameters, measured by transmission electron microscopy[12] or determined by means of a simulation of high resolution x-ray diffraction results.[13,14] In this investigation we have determined the well thickness and hence that of the barrier of (001) superlattices via a dynamic simulation of the (002) and (004) Bragg reflections measured in a five crystal x-ray diffractometer. The rather strong (002) Bragg reflection in these superlattices is caused primarily by the HgTe layer: The structure factor for the (002) Bragg reflection is much larger for HgTe than for CdTe.[13] This is due to the larger Hg atom with its greater number of electrons. In fact the structure factor goes to zero for $Hg_{1-x}Cd_xTe$ with an x value of about 0.88. A simulation of (001) oriented superlattices results in an accuracy as low as $\pm$ 1 Å but which is usually ± 2 Å, depending on the number of satellites and the position of the first order zero points relative to the satellites.

X-ray diffraction in (112)B oriented heterostructures is more complicated and the results less accurate. First of all, there is only one useful reflection (224) which is not stronger for either HgTe or CdTe. Second, shear strain results in a monoclinic distortion which must be taken into account before the data can be correctly simulated.[15,16]

Optical transmission and reflection measurements were carried out in the middle and near infrared with a Fourier transform spectrometer, Bruker IFS88. A $LiTaO_3$ detector was usually employed rather than a liquid nitrogen cooled detector, e.g., $Hg_{1-x}Cd_xTe$, because of its better linearity. The aperature was kept as small as possible for the same reason, i.e., a diameter of 2–3 mm. The absorption coefficient was determined by fitting the experimental transmission spectra to a theoretical description of the multilayer system using standard matrix procedures.[17]

It can be easily shown that a transmission spectrum divided by a slightly different spectrum, e.g., measured at a different temperature, is proportional to the corresponding change in the absorption coefficient

$$\frac{\Delta T}{T} = \frac{T_2}{T_1} - 1 \approx d\Delta\alpha, \qquad (1)$$

where T and d are the transmission and sample thickness, respectively. Hence a good approximation of $\Delta\alpha$, see Fig. 4, can be obtained merely from a ratio of the transmission spectra without the complications and uncertainties in calculating the absorption spectrum of the SL in a multilayer structure.[17] If the temperature difference is kept small, $\Delta T = 20-40$ K, residual interference effects can be effectively reduced near the transition itself and nearly elliminated at other frequencies. The index of refraction n undergoes a change of up to about 5%–10% near an intersubband transition, however, this has been shown to result in a negligible shift of the experimental absorption edge of $\leqslant 1$ meV.

The transmission spectra of most of the SL's were measured at various temperatures. In most cases this was done from 5 to 300 K with a temperature interval of 10 K, in order to improve the statistical significance of the data.

III. THEORETICAL DETAILS

A large number of $\mathbf{k} \cdot \mathbf{p}$ band structure calculations using the envelope function approximation for the $HgTe/Hg_{1-x}Cd_xTe$ superlattice have been published during the last decade.[18–21] Wood and Zunger[22] have compared the predictions of a pseudopotential approach, which includes all bands and their dispersion throughout the Brillouin zone and produces wave functions with full Bloch symmetry, with predictions of an 8×8 multiband $\mathbf{k} \cdot \mathbf{p}$ approach in the envelope function approximation. The authors conclude that the latter model works well for heterostructures when their states are derived from bulk states which are *well* described by $\mathbf{k} \cdot \mathbf{p}$, i.e., from states near the Γ point. Ram-Mohan, Yoo, and Aggarwal[18] employed the envelope function method and developed a transfer matrix procedure to calculate the superlattice states. They accounted for the full 8×8 Kane Hamiltonian including all second order terms representing the farband contributions, but did not apply their results to a calculation of the optical constants. On the other hand Johnson *et al.*[19] applied a slightly different version of the envelope function method, and deduced optical constants from their superlattice energies and eigenfunctions. But in their approach they used a simplified band model, which omits all the second order far-band contributions, with the exception of a finite heavy hole mass. In order to overcome these shortcomings, we have combined the essential aspects of both approaches.[23] This enables us to calculate the optical constants based on a realistic band structure model, which includes all second order higher band contributions.

The bands of both bulk HgTe and CdTe are described by Kane's four-band model ($8 \times 8 \mathbf{k} \cdot \mathbf{p}$) including second order remote band contributions. The envelope function method in the axial approximation is widely used to calculate the band structure of the HgTe/CdTe SL.[18,19] The axial approximation gives exact results for the band gaps of (001) oriented systems, because nonaxial terms in the Hamiltonian vanish for $\mathbf{k}_\parallel = 0$. It is well known that the axial approximation is not exact for growth directions other than [001] and [111] even for $\mathbf{k}_\parallel = 0$.[24] Therefore we have taken the approach of Los, Fasolino, and Catellani[25] and transformed the Hamiltonian into symmetry adapted basis functions for the [112] growth direction. We then compared the band structure using this adapted Hamiltonian with an axial approximation for the

[112] direction. The results of the axial approximation are not exact, however, they give a good approximation, within 1 or 2 meV, for the subband energies at $\mathbf{k}_{\parallel}=0$ as well as for an average of the subband dispersion over all $\mathbf{k}_{\parallel}$ directions. Consequently all absorption coefficient calculations and most intersubband transition energy calculations were carried out using this adapted Hamiltonian in the axial approximation, in order to reduce the calculation time. Moreover our band structure model is equivalent to that used by Schultz et al.[26] to calculate Landau levels in (112)B HgTe quantum wells.

The effects of strain due to lattice mismatch were also taken into consideration. The lattice mismatch between HgTe and its environment is less than 0.1% which results in a shift in intersubband transition energies of less than 3 meV and can therefore be neglected. In contrast to the [001] direction,[20] the strain tensor for the [112] direction has a shear strain component. This results in a piezoelectric field in the growth direction.[27] We have calculated the strain for a free standing, strained (112)B SL and a fully strained (112)B SL on a $Cd_{0.96}Zn_{0.04}Te$ substrate. From these results the piezoelectric field has been calculated to be less than 5 mV/100 Å whose influence on intersubband transition energies is less than 1 meV and can therefore be neglected in the calculations.

A revised set of values for the band parameters deduced from measurements on bulk HgTe and $Hg_{1-x}Cd_xTe$ by Weiler[28] were employed which nevertheless reproduce the same bulk band structure ($\Delta = 1.0$ eV, $\gamma_1 = 4.1$, $\gamma_2 = 0.5$, $\gamma_3 = 1.3$, $F = 0$, and $E_p = 18.8$ eV):

$$m_{\text{hh}}^*(112) = \left[\gamma_1 - 2\gamma_2 - \frac{3}{2}(\gamma_3 - \gamma_2) \right]^{-1} m_0 = 0.53 m_0, \tag{2}$$

$$m_{\text{hh}}^*(001) = (\gamma_1 - 2\gamma_2)^{-1} m_0 = 0.32 m_0 \quad \text{at} \quad 5 \quad \text{K.} \tag{3}$$

The SL band structure is primarily determined by that of the quantum well and is influenced to a much lesser degree by the band structure of the barrier. Therefore the above values were employed for both the HgTe quantum wells and the $Hg_{1-x}Cd_xTe$ barriers. According to Weiler[28] the only parameter that changes significantly with alloy composition and temperature is the energy gap. The energy gaps of HgTe and $Hg_{1-x}Cd_xTe$ were taken from the empirical $E_g(x,T)$ relationship according to Laurenti et al.[9] with the exception of HgTe at temperatures greater than 5 K as discussed in the following sections. The valence band offset between HgTe and $Hg_{1-x}Cd_xTe$ is employed as an adjustable variable and is assumed to vary linearly with x for $Hg_{1-x}Cd_xTe$, i.e., $x\Lambda$.[29] An interface width d_t which results during growth or from interdiffusion of the two types of layers was integrated into the theory. The concentration profile across the interface is described by an error function similar to an experimental profile according to Kim et al.[3]

The complex dielectric constant can be written as

$$\varepsilon(\omega) = \varepsilon_R(\omega) + i\frac{\sigma(\omega)}{\omega \epsilon_0}, \tag{4}$$

where $\varepsilon_R(\omega)$ is the residual contribution of the lattice and higher subbands which is assumed to be constant over the
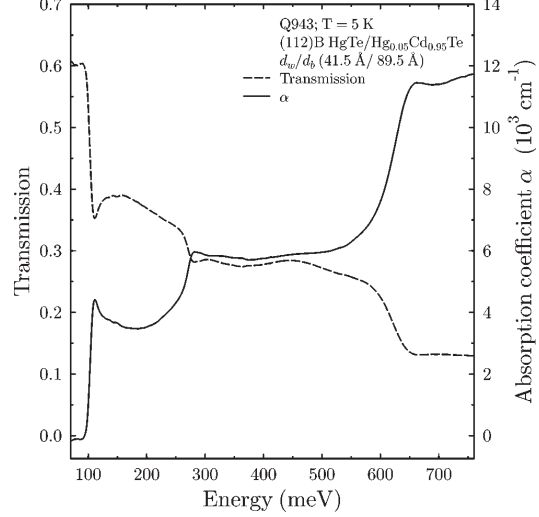

FIG. 1. Transmission and absorption spectra of the (112)B HgTe/$Hg_{0.05}Cd_{0.95}$Te superlattice Q943 at 5 K.

frequencies of interest in this investigation, $\varepsilon_R(\omega) \approx 10$. The complex dynamic conductivity, $\sigma(\omega)$, is determined by making use of Kubo's formula[23] and finally the absorption coefficient is given by

$$\alpha(\omega) = \frac{\omega}{c} \frac{\sqrt{2}\varepsilon_2(\omega)}{\sqrt{\varepsilon_1(\omega) + |\varepsilon(\omega)|}}, \tag{5}$$

where $\varepsilon_1(\omega)$ and $\varepsilon_2(\omega)$ are the real and imaginary components of $\varepsilon(\omega)$, respectively.

IV. RESULTS AND DISCUSSION

A. (112)B orientation

The transmission and absorption spectra for a (112)B HgTe/$Hg_{0.05}Cd_{0.95}$Te SL at 5 K are shown in Fig. 1. Three distinctive steps are observed which we have assigned to the $H1$-$E1$, $L1$-$E1$, and $H2$-$E2$ intersubband transitions. H, L, and E are the heavy hole, light hole, and electron subbands, respectively. In contrast, Yang et al.[6] attributed the first two steps at lower energies in a similar SL to the $H1$-$E1$ and $H2$-$E2$ transitions, and the weak shoulder near 240 meV to $L1$-$E1$. In order to insure a correct assignment, there must be agreement between the calculated transition probabilities and the observed absorption coefficient spectrum as well as between the calculated and experimental frequencies. That this is the case here, is demonstrated in Fig. 2 where the experimental and theoretical absorption as well as the calculated absorption for the three individual transitions are plotted versus energy. The relative heights of the three steps are in good agreement with experiment, even though their absolute magnitudes are underestimated due to the neglect of Coulomb interaction between electron and hole.[30] The energies of the $H1$-$E1$ and $L1$-$E1$ transitions are in good agreement whereas agreement is only fair at higher energies, e.g., for $H2$-$E2$, as expected for a perturbation theory. The weak
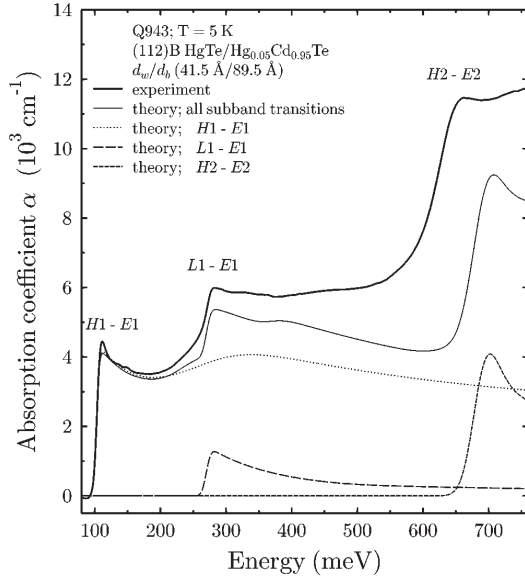
FIG. 2. Experimental and theoretical absorption coefficients of the (112)B HgTe/Hg$_{0.05}$Cd$_{0.95}$Te superlattice Q943 at 5 K. Also shown are the individual contributions of the $H1$-$E1$, $L1$-$E1$, and $H2$-$E2$ intersubband transitions.

shoulder near 240 meV is due to the $H2$-$E1$ transition which is allowed only for $\mathbf{k} > 0$. For these reasons and others which will become apparent below, we shall concentrate on the $H1$-$E1$ and $L1$-$E1$ transitions.

1. Intersubband transition energies

The absorption edges have been determined by two different methods. In the first method, the absorption edge is defined as the energy at the maximum value of the first derivative of the absorption coefficient. This is schematically demonstrated in Fig. 3 for $Q943$ at 5 K. The full widths at half maximum FWHM of the derivative for the $H1$-$E1$ and $L1$-$E1$ transitions are 8.5 and 13 meV, respectively. Also shown is a theoretically calculated α and its derivative, together with the calculated intersubband transition energies. The dispersion for these transitions is indicated by the width of the two vertical lines, i.e., ≈ 0.5 and ≈ 1.8 meV for these two transitions. A small energy dispersion and hence a wide barrier is desired in order to minimize uncertainties in the transition energies. The barrier widths of most of the SL's in this investigation are $\geqslant 80$ Å, which result in a dispersion of $\leqslant 1.0$ and $\leqslant 3.5$ meV, respectively. The shape and width of the experimental α and $d\alpha/dE$ of $Q943$ were simulated by assuming a Gaussian distribution of quantum well widths with $\Gamma = 1.5$ Å.[31] As can be seen, the absorption edges coincide with the intersubband transition energies to within ± 1 meV. In this investigation an uncertainty of $\leqslant \pm 2$ meV holds for all samples, with one exception in which a systematic discrepancy of 4 meV for $L1$-$E1$ is observed. This is due to interference effects which have not been completely removed but being known can be taken into account.
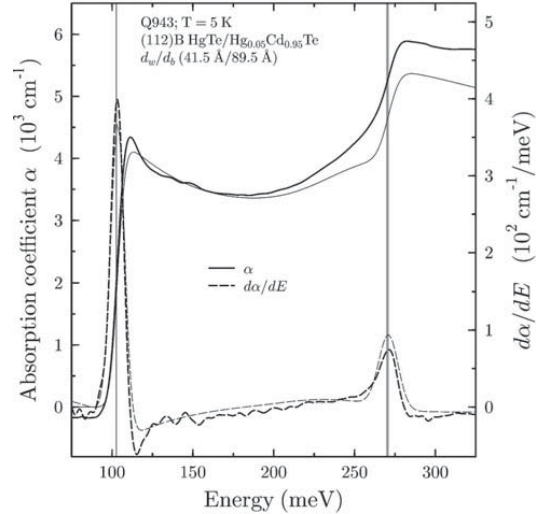
FIG. 3. Experimental (thick line) and theoretical (thin line) absorption coefficients, and their first derivatives (thick and thin dashed lines, respectively) for the (112)B HgTe/Hg$_{0.05}$Cd$_{0.95}$Te SL $Q943$ at 5 K. The intersubband transition energies are indicated by vertical lines and their dispersion for $\mathbf{q} \| \mathbf{z}$, the miniband width, by the width of these vertical lines.

In the second method the absorption edge is determined from the change in the absorption coefficient according to Eq. (1). The near equivalence of these two methods of determining the band edges and consequently the intersubband transition energies are demonstrated in Fig. 4. In this figure the dashed line represents $d\alpha/dE$ at 40 K and the solid line represents $T_{60 K}/T_{20 K} - 1$ whose effective temperature is 40
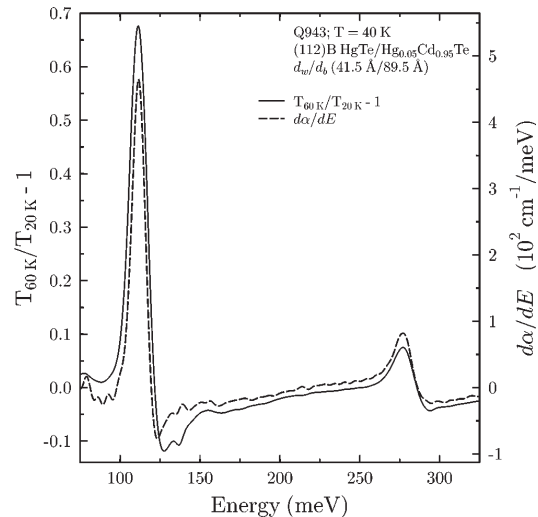
FIG. 4. Ratio of transmission T spectra at $T = 60$, and $T = 20$ K (solid line) is compared with the first derivative of α (dashed line) for Q943 at 40 K.
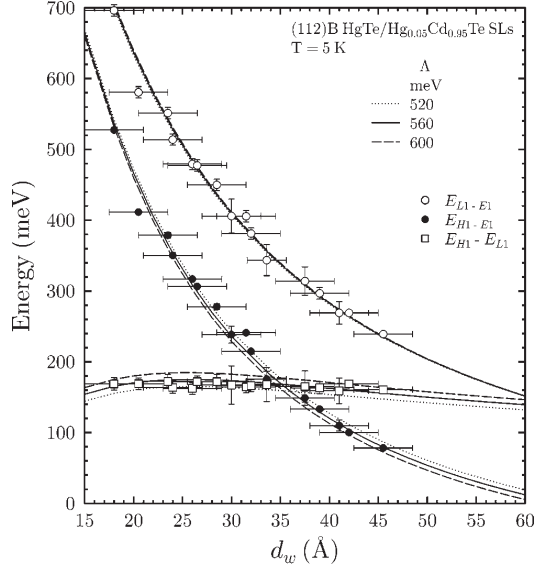
FIG. 5. Experimental values for $E_{H1\text{-}E1}$ (filled circles), $E_{L1\text{-}E1}$ (empty circles), and the energy difference $E_{H1} - E_{L1}$ (empty squares) for all (112)B SL's together with theoretical results at 5 K (lines) are plotted vs d_w. Calculated results using $d_t = 24$ Å and $x_w = 0.00$ for possible values of Λ are shown. d_t is the interface width.
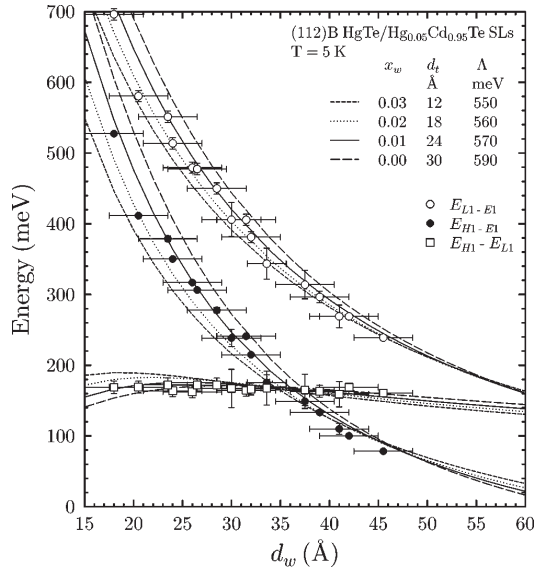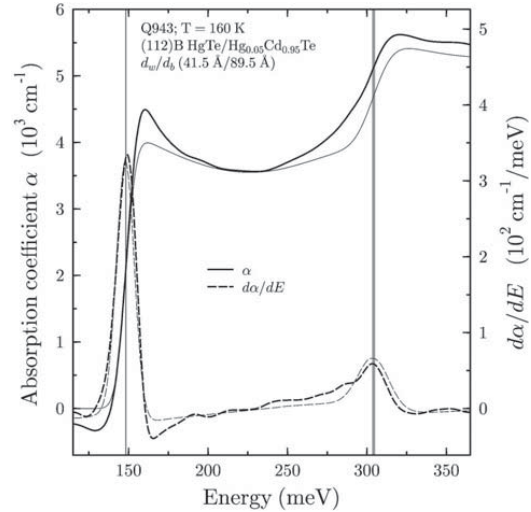
TABLE I. Average value of the valence-band offset between HgTe and CdTe, $\bar{\Lambda}$, necessary to predict the experimental value of $E_{H1} - E_{L1}$ and its standard error for a range of all feasible superlattice parameters for the (112)B and (001) orientations at 5 K.

	d_t (Å)	x_w	$\bar{\Lambda}$ (meV)
(112)B	18	0.02	556 ± 12
	24	0.00	561 ± 7
	24	0.01	573 ± 8
	30	0.00	590 ± 7
(001)	18	0.03	546 ± 9
	24	0.02	552 ± 7
	30	0.00	552 ± 7
	30	0.01	565 ± 7
	36	0.00	583 ± 8

K. The experimental transition energy defined as the energy at the maximum value of $T_{60\,K}/T_{20\,K} - 1$ is in good agreement with the corresponding energy for $d\alpha/dE$, in this case the energy difference is ≤ 1 meV for both transitions.

The energies of the $H1$-$E1$ and $L1$-$E1$ transitions at 5 K for all of the investigated (112)B SL's are plotted versus quantum well width, d_w, in Fig. 5. Also shown is the energy difference between these two intersubband transitions, i.e., E_{H1}-$E_{L1} = E_{L1\text{-}E1} - E_{H1\text{-}E1}$. Obviously both transitions have a strong inverse dependence on d_w, whereas E_{H1}-E_{L1} is nearly independent of d_w. On the other hand, E_{H1}-E_{L1} depends nearly linearly on the valence band offset Λ. Hence a determination of Λ is possible which is not influenced by uncertainties in d_w. The three sets of lines in Fig. 5 are the

FIG. 6. Experimental values for $E_{H1\text{-}E1}$ (filled circles), $E_{L1\text{-}E1}$ (empty circles), and $E_{H1} - E_{L1}$ (empty squares) for all (112)B SL's together with theoretical results at 5 K (lines) are plotted vs d_w. Calculated results for possible values of Λ and superlattice parameters are shown.

FIG. 7. Experimental (thick line) and theoretical (thin line) absorption coefficients, and their first derivatives (thick and thin dashed lines, respectively) for the (112)B HgTe/Hg$_{0.05}$Cd$_{0.95}$Te SL $Q943$ at 160 K. The intersubband transition energies are indicated by vertical lines and their dispersion for $\mathbf{q}\|\mathbf{z}$, the miniband width, by the width of these vertical lines.
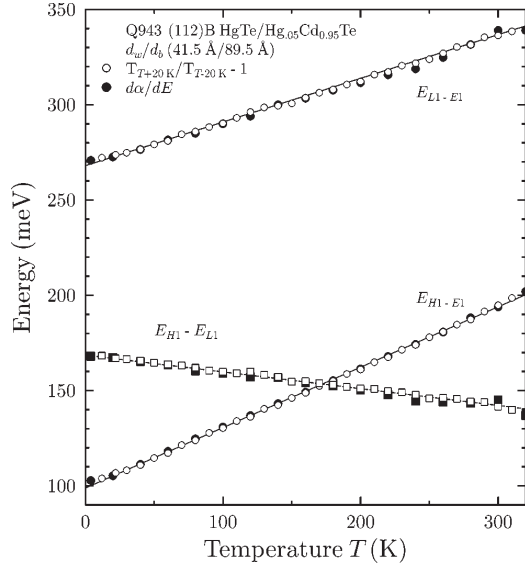
FIG. 8. Experimental $H1$-$E1$ and $L1$-$E1$ intersubband transition energies as well as $E_{H1} - E_{L1}$ are plotted as a function of temperature. Values determined from $d\alpha/dE$ are represented by filled symbols and those from the transmission ratio by empty symbols. The lines are the results of theoretical calculations using the SL parameters indicated in the figure and discussed in the text.

results of the theory for these intersubband energies for a series of values for Λ assuming $d_t = 24$ Å and $x_w = 0.0$.

Even though the growth conditions for these SL's were as similar as possible, with the exception of the growth temperature for three SL's, a variation in SL parameters such as x_w and d_t is possible. A number of superlattice parameter sets give good to acceptable agreement with the experimental values, however, Λ is nearly independent of the set chosen. This is schematically illustrated in Fig. 6. As can be seen the experimental and calculated energies for the $H1$-$E1$ and $L1$-$E1$ intersubband transitions agree within the experimental uncertainties in these energies and in d_w. In addition the experimental values for E_{H1}-E_{L1} agree with the calculations employing the values of Λ shown in Fig. 6. The above is true for this range of superlattice parameters. SL parameters which do not fulfill this criterion have been excluded from the following statistical analysis.

Because the values of x_w and d_t and their variations are uncertain, an analysis for each feasible set of parameters has been carried out. The calculated value of Λ necessary to reproduce the experimental value of E_{H1}-E_{L1} for each of the 16 SL's has been averaged. This average value of Λ and its standard error are tabulated for each set of parameters in Table I. The Λ values for each SL have been weighted in inverse proportion to the experimental uncertainties in E_{H1}-E_{L1} shown in Figs. 5 and 6. The results may be summarized as a range of possible values at 5 K expressed as $\Lambda = 570 \pm 26$ meV.

2. Temperature dependence

Spectra of the absorption coefficient and its derivative for $Q943$ at 160 K are reproduced in Fig. 7. The absorption
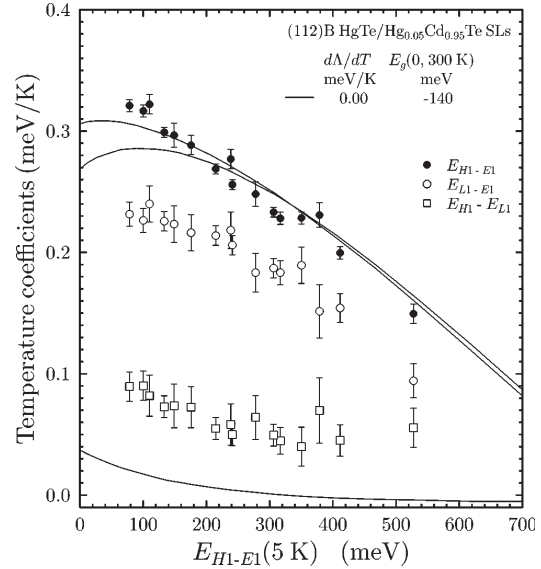
FIG. 9. Linear temperature coefficients for $E_{H1\text{-}E1}$ (filled circles), $E_{L1\text{-}E1}$ (empty circles), as well as $E_{H1} - E_{L1}$ (empty squares) are plotted vs $E_{H1\text{-}E1}$ at 5 K for all (112)B SL's. Calculated results for $d_t = 24$ Å, $x_w = 0.00$, $\Lambda_0 = 560$ meV and taking Λ to be independent of temperature, $d\Lambda/dT = 0.0$ meV/K, are reproduced as solid lines.

edges as defined by $d\alpha/dE$ are shifted to higher energies and are slightly broader with a FWHM of 15 and 22 meV for the $H1$-$E1$ and $L1$-$E1$ intersubband transitions, respectively. However their shapes are similar to those at 5 K and the intersubband transition energies coincide with the peaks of $d\alpha/dE$ within ± 2 meV. This is true up to room temperature, therefore, an accurate temperature coefficient for these transitions can be determined. The $H1$-$E1$ and $L1$-$E1$ intersubband transition energies for $Q943$ are shown as a function of temperature in Fig. 8. Values determined from the transmission ratio by empty circles and those from $d\alpha/dE$ by filled circles. The energies from these two methods are nearly equal: Most of the latter symbols are obscured by the former. As can be seen there is less scatter in the data from the transmission ratio method. A small Burstein-Moss[32] shift of about 2 meV can be seen at temperatures below 50 K.

Experimental values of E_{H1}-E_{L1}, which are plotted versus temperature as empty and filled squares, display a significant temperature dependence. Therefore according to the conclusions presented above, Λ is also temperature dependent. Linear temperature coefficients have been calculated for these three energies using the SL parameters determined below, and are displayed in Fig. 8 as three lines. Obviously, the calculated results are in excellent agreement with the experimental values. Because the temperature dependence of E_{H1}-E_{L1} is linear within experimental uncertainties, we propose that this is also the case for Λ:

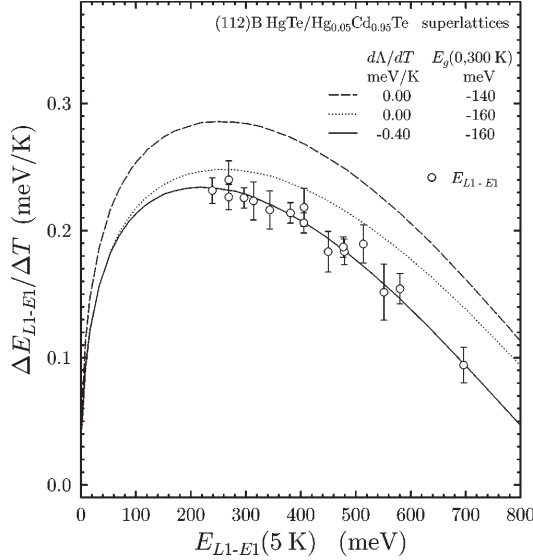$$\Lambda(T) = \Lambda_0 + \frac{d\Lambda}{dT} T. \qquad (6)$$

82

FIG. 10. Linear temperature coefficient for $E_{L1\text{-}E1}$ (empty circles) is plotted vs $E_{L1\text{-}E1}$ at 5 K for all (112)B SL's. Calculated results are shown for the following values of $E_g(0,300\,\text{K})$ and $d\Lambda/dT$: -140 meV and 0.0 meV/K (dashed line), respectively; -160 meV and 0.0 meV/K (dotted line); -160 meV and -0.40 meV/K (solid line).

In order to determine the magnitude of this temperature dependence, we have employed a procedure which relies only on experimentally determined energies and not on d_w or other SL parameters. This is illustrated in Fig. 9 where the temperature coefficients for $E_{H1\text{-}E1}$, $E_{L1\text{-}E1}$, and $E_{H1}\text{-}E_{L1}$ are plotted versus $E_{H1\text{-}E1}$ (5 K) for the (112)B SL's. The curves are results of the theory when Λ is assumed to be temperature independent and the energy gap of HgTe at room temperature, $E_g(0,300\,\text{K})$, is taken to be -140 meV.[33] Even though the temperature dependence of the $H1$-$E1$ transition can be reproduced, this is clearly not the case for either $L1$-$E1$ or the energy separation between these two transitions, $E_{H1}\text{-}E_{L1}$. Consequently the results of previous investigations, which are based merely on the $H1$-$E1$ transition can be misleading. For example the conclusion of von Truchsess *et al.*[34] that Λ is temperature independent, is obviously incorrect.

It will be demonstrated below that the temperature dependence of the $L1$-$E1$ intersubband transition is determined by

the temperature dependence of both the HgTe band gap and Λ:

$$\frac{dE_{L1\text{-}E1}}{dT} = f\left(\frac{dE_g(0,T)}{dT}, \frac{d\Lambda}{dT}\right). \tag{7}$$

The calculated temperature dependence of $E_{L1\text{-}E1}$ is compared with experiment in Fig. 10. Calculated values for $E_{L1\text{-}E1}$ approach zero for very wide quantum well widths, i.e., pure HgTe, and consequently this is also true for $\Delta E_{L1\text{-}E1}/\Delta T$. Shown in Fig. 10 are calculations assuming Λ to be independent of temperature together with both $E_g(0,300\,\text{K}) = -140$ and -160 meV, dashed and dotted line, respectively. Decreasing this energy from -140 to -160 meV improves the fit at low energies whereas the shape at higher energies is increasingly determined by the value of $d\Lambda/dT$. A least square fit of Eq. (7) to the experimental values, shown as a solid line in Fig. 10, results in $E_g(0,300\,\text{K}) = -160 \pm 2$ meV and $d\Lambda/dT = -0.40 \pm 0.04$ meV/K, which are listed in Table II. This value for $E_g(0,300\,\text{K})$ differs appreciably from literature values of -140 and -120 meV,[33,9] which clearly lie outside of the experimental uncertainties in this investigation. However, these two values are not experimental values: They have been determined by extrapolating experimental results for $T < 100$ K up to room temperature. The empirical relationship for the band gap of $Hg_{1-x}Cd_x$Te according to Laurenti *et al.*[9] has been modified as follows in order to incorporate our value for HgTe:

$$E_g(x,T) = -303(1-x) + 1606x - 132x(1-x)$$
$$+ [4.95(1-x) + 3.25x - 3.93x(1-x)]$$
$$\times 10^{-1}T^2/[11(1-x) + 78.7x + T] \tag{8}$$

in units of meV. This empirical equation reproduces the $E_g(x,T)$ values of Laurenti *et al.*[9] to within 2 meV for all x values and low temperatures as well as for $x > 0.6$ and temperatures up to 300 K. In particular, $E_g(1,T)$ is unchanged for CdTe.

On the basis of x-ray photoemission spectroscopy (XPS) and ultraviolet spectroscopy (UPS) Sporken *et al.*[35] concluded that the valence-band offset between CdTe and HgTe was independent of temperature between 50 K and room temperature with an uncertainty of ± 0.25 meV/K. However the valence-band offset was not determined at $\mathbf{k} = 0$: Their UPS samples were sputtered and they employed the He I and He II emission lines whose energies correspond to a position in the Brillouin zone far removed from $\mathbf{k} = \mathbf{0}$.[36]

TABLE II. Experimentally determined values together with their uncertainties for E_g (0,300 K), Λ_0, Λ (300K), $d\Lambda/dT$, and m_{hh}^* (300 K) for the (112)B and (001) orientations.

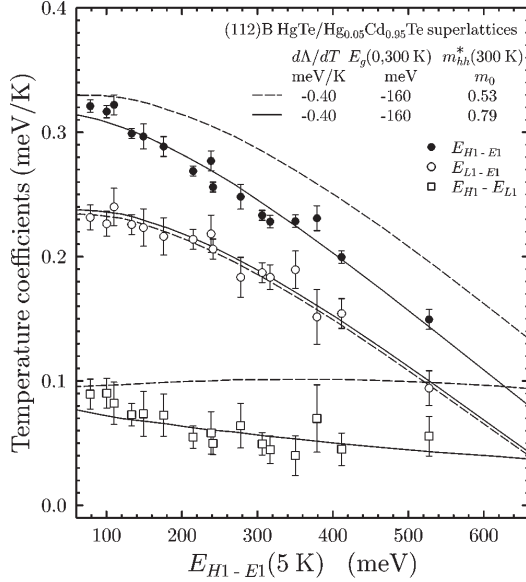|	$E_g(0,300\,\text{K})$ (meV)	Λ_0 (meV)	Λ (300 K) (meV)	$\dfrac{d\Lambda}{dT}$ (meV/K)	m_{hh}^* (5 K)[a] m_0	m_{hh}^* (300 K) m_0
(112)B	-160 ± 2	572 ± 26	452 ± 32	-0.40 ± 0.04	0.53	0.79 ± 0.04
(001)	-157 ± 4	566 ± 27	458 ± 34	-0.41 ± 0.10	0.32	0.40 ± 0.11

[a]After Ref. 28.

FIG. 11. Linear temperature coefficients for $E_{H1\text{-}E1}$ (filled circles), $E_{L1\text{-}E1}$ (empty circles), as well as $E_{H1}-E_{L1}$ (empty squares) are plotted vs $E_{H1\text{-}E1}$ at 5 K for all (112)B SL's. Calculated results for $d_t = 24$ Å, $x_w = 0.00$, $\Lambda_0 = 560$ meV, and $d\Lambda/dT = -0.40$ meV/K are reproduced as dashed lines, and the results when in addition m_{hh}^* is temperature dependent as solid lines.

FIG. 12. Experimental values for $E_{H1\text{-}E1}$ (filled circles), $E_{L1\text{-}E1}$ (empty circles), and $E_{H1}-E_{L1}$ (empty squares) for all (001) SL's together with theoretical results at 5 K (lines) are plotted vs d_w. Calculated results using $d_t = 30$ Å and $x_w = 0.00$ for possible values of Λ are shown. d_t is the interface width.

The experimental temperature dependence of $E_{L1\text{-}E1}$, and that of $E_{H1\text{-}E1}$, as will be demonstrated below, cannot be explained unless Λ is temperature dependent. Since the energy gaps of HgTe and CdTe as well as either their conduction bands, valence bands, or a combination of both, depend on temperature, it would be a remarkable coincidence if the valence-band offset between the two were independent of temperature. Particularly since the band gap of HgTe increases with temperature and that of CdTe decreases.

The results for $E_{H1\text{-}E1}$, $E_{L1\text{-}E1}$, and $E_{H1}-E_{L1}$ using a linear temperature coefficient for Λ of -0.40 meV/K are displayed in Fig. 11 by the dashed lines. Agreement with experiment at lower values of $E_{H1\text{-}E1}$ (5 K) is good as previously reported,[37] however, at higher energies this is not the case. Better agreement with experiment over the entire energy range can only be achieved by assuming that the heavy hole effective mass is also temperature dependent: One or more of the band structure parameters γ_1, γ_2, and γ_3 are temperature dependent. Analogous to the above treatment, the temperature dependence of the $H1\text{-}E1$ intersubband transition can be expressed as

$$\frac{dE_{H1\text{-}E1}}{dT} = f\left(\frac{dE_g(0,T)}{dT}, \frac{d\Lambda}{dT}, \frac{dm_{hh}^*}{dT}\right). \quad (9)$$

The first two temperature coefficients have been determined above and will be held constant. A least square fit of Eq. (9) to the experimental values of $E_{H1\text{-}E1}$, which is shown as a solid line in Fig. 11 results in $m_{hh}^*(112) = 0.79 \pm 0.04 \, m_0$ at 300 K, see Table II.

B. (001) orientation

This more symmetric surface has a number of advantages but also distinct disadvantages. For example, the more symmetric Hamiltonian does not lead to a monoclinic distortion or a piezoelectric effect as is the case for (112).[15,16] As mentioned above, values for the well and barrier widths via x-ray diffraction are more accurate, however, the Cd concentration in the barriers is appreciably lower, 0.68 instead of 0.95. This has two important consequences. First, due to the lower energy barrier the useful experimental data are limited to a smaller energy range. Second, the absorption edges are at least a factor of 2.5 broader, apparently due to greater alloy fluctuations in the barriers.[31]

The experimental energies for the $H1\text{-}E1$ and $L1\text{-}E1$ transitions at 5 K for all of the investigated (001) SL's are plotted versus quantum well width in Fig. 12. The energy difference between these two intersubband transitions is also shown. Both transitions display a strong inverse dependence on d_w, whereas $E_{H1}\text{-}E_{L1}$ is nearly independent of d_w. As is the case for the (112)B SL's, $E_{H1}\text{-}E_{L1}$ is, within experimental error, linearly dependent on the valence-band offset Λ which permits a determination of Λ independent of uncertainties in d_w. The three sets of lines in Fig. 12 are the results of the theory for these intersubband energies for a series of values for Λ assuming $d_t = 30$ Å and $x_w = 0.0$.

As demonstrated above for (112)B SL's, good to acceptable agreement with the experimental values of $E_{H1}\text{-}E_{L1}$ can also be achieved for (001) SL's with a number of SL parameters, however, Λ is nearly independent of the set chosen. This is schematically illustrated in Fig. 13. The calculated value of Λ for each set of SL parameters necessary to repro-
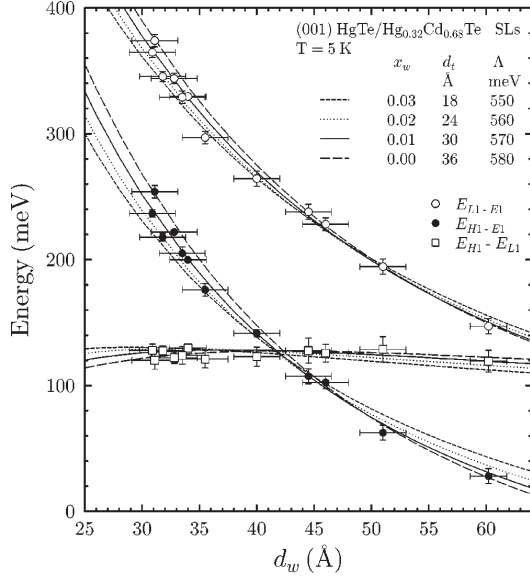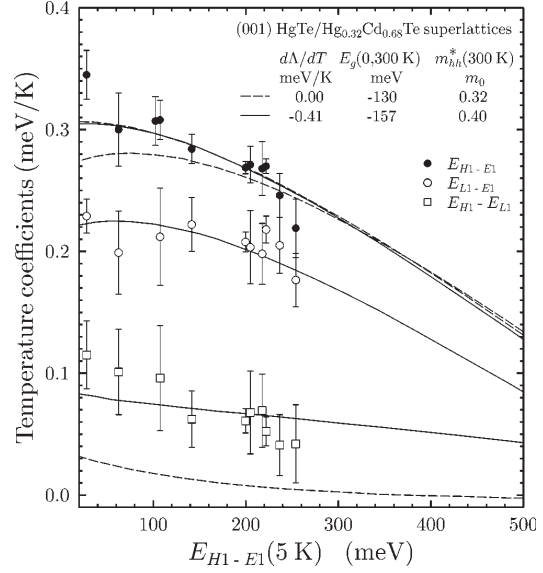
FIG. 13. Experimental values for $E_{H1\text{-}E1}$ (filled circles), $E_{L1\text{-}E1}$ (empty circles), and $E_{H1}-E_{L1}$ (empty squares) for all (001) SL's together with theoretical results at 5 K (lines) are plotted vs d_w. Calculated results for possible values of Λ and superlattice parameters are shown.

FIG. 14. Linear temperature coefficients for $E_{H1\text{-}E1}$ (filled circles), $E_{L1\text{-}E1}$ (empty circles), as well as $E_{H1}-E_{L1}$ (empty squares) are plotted vs $E_{H1\text{-}E1}$ at 5 K for all (001) SL's. Calculated results for $d_t = 30$ Å, $x_w = 0.00$ and $\Lambda_0 = 560$ meV together with the presumption that Λ and m_{hh}^* are independent of temperature are reproduced as dashed lines and results of a least square fit in which Λ and m_{hh}^* are temperature dependent as solid lines.

duce the experimental value of $E_{H1}\text{-}E_{L1}$ for the 12 SL's has been averaged. These average values of Λ and their standard errors are tabulated for each set of parameters in Table I. The Λ values for each SL have been weighted in inverse proportion to the experimental uncertainties in $E_{H1}\text{-}E_{L1}$ shown in Figs. 12 and 13. A range of possible values which can generate the experimental results at 5 K is given by $\Lambda = 564 \pm 27$ meV.

The experimental linear temperature coefficients for $E_{H1\text{-}E1}$, $E_{L1\text{-}E1}$, and $E_{H1}\text{-}E_{L1}$ together with calculations assuming a temperature-independent Λ and $E_g(0, 300 \text{ K}) = -130$ meV are displayed in Fig. 14 by the dashed lines. Agreement with experiment for the temperature dependence of $E_{H1\text{-}E1}$ is reasonable, however, that is obviously not the case for either $E_{L1\text{-}E1}$ or $E_{H1}-E_{L1}$. A least square fit of $E_{L1\text{-}E1}$ to the calculated relationship of Eq. (7) and that of $E_{H1\text{-}E1}$ to Eq. (9), which is shown in Fig. 14 as solid lines, results in $d\Lambda/dT = -0.41 \pm 0.10$ meV/K, $E_g(0, 300 \text{ K}) = -157 \pm 4$ meV, and $m_{hh}^*(001) = 0.40 \pm 0.11 \, m_0$ at 300 K, as listed in Table II.

C. $E_g(0, 300 \text{ K})$, $\Lambda(T)$, and $m_{hh}^*(T)$

The valence-band offset between HgTe and CdTe, Λ, has been the subject of a long standing controversy, which has been reviewed by, for example, Meyer et al.[38] In early magneto-optical experiments on semiconducting superlattices, both a small offset of 40 meV and a larger value of approximately 350 meV were deduced.[39,12] In contrast, x-ray and ultraviolet photoelectron spectroscopy have provided a consistent value of approximately 350 meV.[40,35,29] Johnson, Hui, and Ehrenreich[41] resolved the apparent controversy in

favor of the larger Λ, demonstrating that with increasing Λ, HgTe/CdTe superlattices would change from semiconducting behavior to semimetallic and back to semiconducting behavior due to crossing and uncrossing of the $H1$ and $E1$ subbands. The authors showed that the electron cyclotron mass observed in previous magneto-optical experiments[39] could be explained better with 350 meV as opposed to 40 meV. The most widely accepted value has been 350 meV from XPS and UPS measurements, however, values for Λ up to 800 meV have been subsequently reported for magneto-optical experiments.[42] An offset of 550 meV at liquid helium temperatures have been deduced from photoluminescence and magneto-optical spectra, however, this value is the offset between HgTe and $Hg_{0.15}Cd_{0.85}Te$ which scales linearly to about 650 meV between HgTe and CdTe.[6] A magneto-optical investigation of the electron effective mass at the conduction band edge together with the energy of all four observed intersubband transitions for a (001) SL by von Truchsess et al.[10] resulted in a value of 550 ± 50 meV at 4.2 K. From the crossing of a Landau level from the conduction subband with one from the valence subband in an (112)B HgTe/CdTe quantum well with inverted band structure, Schultz et al.[26] obtained a value of 610 meV for Λ.

In the present investigation we have demonstrated that $\Lambda = 570 \pm 30$ meV at 5 K for both the (001) and the (112)B orientation, by taking advantage of the fact that the valence band offset between HgTe and CdTe is primarily responsible for the separation between the $H1$-$E1$ and $L1$-$E1$ transition energies of $HgTe/Hg_{1-x}Cd_x$Te superlattices with a normal band structure. Values for either $E_{H1\text{-}E1}$ or $E_{L1\text{-}E1}$ can be

C. R. BECKER *et al.*

simulated by varying one or more of the many superlattice parameters, however, to a good approximation, all relevant superlattice parameters have little or no effect on this energy difference, with the exception of Λ. This leads to an unambiguous value or range of values for Λ. This range of possible values, ± 30 meV, is due to a weak dependence on other superlattice parameters x_w and d_t and uncertainties in their values. According to Wood and Zunger[22] the accuracy of subband energies near the Γ point for the $\mathbf{k} \cdot \mathbf{p}$ method in the envelope function approximation primarily reflects the accuracy of the $\mathbf{k} \cdot \mathbf{p}$ band parameters for the bulk constituents, weighted by the magnitude of their presence in the superlattice. Consideration of the experimental uncertainties in the parameters for the bulk constituents[28] as well as the uncertainties in the superlattice parameters discussed above, result in $\Lambda = 570 \pm 60$ meV for (001) and (112)B at 5 K.

In most UPS investigations[35] Λ was not determined at $\mathbf{k} = \mathbf{0}$ and XPS experiments average over all $\mathbf{k}$ values. Dispersion in $\mathbf{k}$ space is quite different in HgTe and CdTe, and the extrapolation method of determining the valence band maximum can be less accurate for $\mathbf{k} \neq \mathbf{0}$.[36] In spite of the possibility of large systematic errors due to these facts, a value of ≈ 350 meV at 300 K has been consistently obtained. The study of Eich *et al.*[36] at $\mathbf{k} \approx 0$ is a notable exception which reports a value of 530 ± 30 meV at 300 K. The room temperature value determined here, 450 ± 60 meV, lies between these two values.

The temperature dependence of both $H1$-$E1$ and $L1$-$E1$ intersubband transitions can only be explained, if $E_g(0,300\,\mathrm{K}) = -160 \pm 5$ meV and if both Λ and m_{hh}^* have a significant temperature dependence. This requisite dependence in both cases can be expressed as a linear dependence. In the former case, $d\Lambda/dT = -0.40 \pm 0.04$ meV/K for (112)B and, even though there is no *a priori* reason that Λ and its temperature coefficient must be equivalent for these two orientations, within experimental error, this is the case, i.e., $d\Lambda/dT = -0.41 \pm 0.10$ meV/K for (001). Sporken *et al.*[35] concluded from an XPS and UPS study that the valence-band offset between HgTe and CdTe was independent of temperature between 50 K and room temperature with an uncertainty of ± 0.25 meV/K. However, the authors did not determine the valence-band offset at $\mathbf{k} = \mathbf{0}$, which can lead to large systematic errors according to the arguments given above. In the latter case, $m_{hh}^*(112) = 0.79 \pm 0.04 \, m_0$ at 300 K when the literature value[28] of $m_{hh}^*(112) = 0.53 \, m_0$ at 5 K is employed, and $m_{hh}^*(001) = 0.40 \pm 0.11 \, m_0$ at 300 K compared to the value employed at 5 K, $m_{hh}^*(001) = 0.32 \, m_0$,[28] see Table II. If these values for $m_{hh}^*(001)$ according to Eq. (3) are inserted into Eq. (2) then the resulting anisotropic component of $m_{hh}^*(112)$, i.e., $(\gamma_3 - \gamma_2)$, is temperature independent, within experimental uncertainty.

The resulting temperature coefficients for $H1$-$E1$ and $L1$-$E1$ are in good agreement with experiment as can be seen in Figs. 11 and 14. Meyer *et al.*[7] have determined the temperature coefficient of the photoluminescence peak for several (112)B HgTe/Hg$_{0.10}$Cd$_{0.90}$Te SL's. These values are also in reasonably good agreement with our model within the uncertainty in the position of the peak relative to the $H1$-$E1$ intersubband transition energy.[43]

The band gap of HgTe has been determined by conventional magneto-optical methods only for temperatures up to approximately 100 K.[1] These values have been combined with Hg$_{1-x}$Cd$_x$Te band gap energies for $x \geq 0.23$ and temperatures up to room temperature in empirical relationships,[33,9] which extrapolate to values for $E_g(0,300\,\mathrm{K})$ of -140 and -120 meV, respectively. These values are significantly larger than the experimentally determined value in this investigation, i.e., $E_g(0,300\,\mathrm{K}) = -160 \pm 5$ meV.

V. CONCLUSIONS

Intersubband transitions and their dependence on temperature in semiconducting HgTe/Hg$_{1-x}$Cd$_x$Te superlattices with normal band structure have been investigated for a large number of superlattices. It has been demonstrated that Λ is primarily responsible for the separation between the $H1$-$E1$ and $L1$-$E1$ transition energies of HgTe/Hg$_{1-x}$Cd$_x$Te superlattices with normal band structure. To a good approximation, all other relevant superlattice parameters have little or no effect on this energy difference. This leads to a value for the valence band offset between HgTe and CdTe given by $\Lambda = 570 \pm 60$ meV at 5 K for both the (001) and the (112)B orientations. This uncertainty in Λ is due to uncertainties in the $\mathbf{k} \cdot \mathbf{p}$ band parameters of the bulk constituents as well as due to a weak dependence on x_w and d_t and uncertainties in their values.

An explanation of the temperature dependence for both of these intersubband transition energies leads to the following unambiguous conclusions. Λ is temperature dependent as described by the linear temperature coefficient of -0.40 ± 0.04 and -0.41 ± 0.10 meV/K for (112)B and (001), respectively. Within experimental error, these values are equivalent. Thus $\Lambda = 450 \pm 60$ meV at 300 K for both orientations. Second, the energy gap of HgTe at 300 K is given by $E_g(0,300\,\mathrm{K}) = -160 \pm 5$ meV. This value is appreciably lower than the extrapolated values found in the literature. Finally the anisotropic heavy hole effective mass for HgTe was shown to have a significant temperature dependence, however, the anisotropic component of $m_{hh}^*(112)$ is, within experimental uncertainty, independent of temperature.

---

*Email: becker@physik.uni-wuerzburg.de

[1] M. Dobrowolska, A. Mycielski, and W. Dobrowolski, Solid State Commun. **27**, 1233 (1978).

[2] V. Latussek, C. R. Becker, G. Landwehr, R. Bini, and L. Ulivi (unpublished).

[3] Y. Kim, A. Ourmazd, M. Bode, and R. D. Feldman, Phys. Rev. Lett. **63**, 636 (1989).

[4] C. R. Becker, V. Latussek, W. Spahn, F. Goschenhofer, S. Oehling, and G. Landwehr, Proc. SPIE **2554**, 6 (1995).

[5] K. A. Harris, R. W. Yanka, L. M. Mohnkern, A. R. Riesinger, T.

H. Myers, Z. Yang, Z. Yu, S. Hwang, and J. F. Schetzina, J. Vac. Sci. Technol. B **10**, 1574 (1992).

[6] Z. Yang, Z. Yu, Y. Lansari, S. Hwang, J. W. Cook, Jr., and J. F. Schetzina, Phys. Rev. B **49**, 8096 (1994).

[7] J. R. Meyer, A. R. Reisinger, K. A. Harris, R. W. Yanka, L. M. Mohnkern, and L. R. Ram-Mohan, J. Cryst. Growth **138**, 981 (1994).

[8] C. L. Cesar, M. N. Islam, R. D. Feldman, R. F. Austin, D. S. Chemla, L. C. West, and A. E. DeGiovanni, Appl. Phys. Lett. **56**, 283 (1990).

[9] J. P. Laurenti, J. Camassel, A. Bouhemadou, B. Toulouse, R. Legros, and A. Lusson, J. Appl. Phys. **67**, 6454 (1990).

[10] M. von Truchsess, V. Latussek, F. Goschenhofer, C. R. Becker, G. Landwehr, E. Batke, R. Sizmann, and P. Helgesen, Phys. Rev. B **51**, 17 618 (1995).

[11] A. Tardot, A. Hamoudi, N. Magnea, P. Gentile, and J. L. Pautrat, Appl. Phys. Lett. **62**, 2548 (1993).

[12] J. N. Schulman, O. K. Wu, E. A. Patten, Jeong W. Han, Y. Lansari, L. S. Kim, J. W. Cook, Jr., and J. F. Schetzina, Appl. Phys. Lett. **53**, 2420 (1988).

[13] M. Möller, R. N. Bicknell-Tassius, and G. Landwehr, J. Appl. Phys. **72**, 5108 (1992).

[14] C. R. Becker, L. He, M. M. Regnet, M. M. Kraus, Y. S. Wu, G. Landwehr, X. F. Zhang, and H. Zhang, J. Appl. Phys. **74**, 2486 (1993).

[15] M. Li, C. R. Becker, R. Gall, W. Faschinger, and G. Landwehr, Appl. Phys. Lett. **71**, 1822 (1997).

[16] M. Li, R. Gall, C. R. Becker, T. Gerhard, W. Faschinger, and G. Landwehr, J. Appl. Phys. **82**, 4860 (1997).

[17] D. Fasold, K. Heil, and S. Jetschke, Phys. Status Solidi A **86**, 125 (1984).

[18] L. R. Ram-Mohan, K. H. Yoo, and R. L. Aggarwal, Phys. Rev. B **38**, 6151 (1988).

[19] N. F. Johnson, H. Ehrenreich, P. M. Hui, and P. M. Young, Phys. Rev. B **41**, 3655 (1990).

[20] A. Simon, D. Bertho, D. Boiron, and C. Jouanin, Phys. Rev. B **42**, 5221 (1990).

[21] J. R. Meyer, C. A. Hoffman, and F. J. Bartoli, Semicond. Sci. Technol. **5**, S90 (1990).

[22] D. M. Wood and Alex Zunger, Phys. Rev. B **53**, 7949 (1996).

[23] E. Bangert, P. Boege, V. Latussek, and G. Landwehr, Semicond. Sci. Technol. **8**, S99 (1993).

[24] R. Winkler and A. I. Nesvizhskii, Phys. Rev. B **53**, 9984 (1996).

[25] J. Los, A. Fasolino, and A. Catellani, Phys. Rev. B **53**, 4630 (1996).

[26] M. Schultz, U. Merkt, A. Sonntag, U. Rössler, R. Winkler, T. Colin, P. Helgesen, T. Skauli, and S. Løvold, Phys. Rev. B **57**, 14 772 (1998).

[27] Liberato De Caro and Leander Tapfer, Phys. Rev. B **51**, 4374 (1995).

[28] M. H. Weiler, in *Semiconductors and Semimetals*, edited by R. Willardson and A. C. Beer (Academic, New York, 1981), Vol. 16, p. 119.

[29] C. K. Shih and W. E. Spicer, Phys. Rev. Lett. **58**, 2594 (1987).

[30] Christian Tanguy, Phys. Rev. Lett. **75**, 4090 (1995), and references therein.

[31] C. R. Becker, A. Pfeuffer-Jeschke, V. Latussek, M. Li, K. Ortner, V. Daumer, S. Oehling, W. Tang, and G. Landwehr, J. Cryst. Growth **184/185**, 1185 (1998).

[32] E. Burstein, Phys. Rev. **93**, 632 (1954); T. S. Moss, Proc. Phys. Soc. London, Sect. B **76**, 775 (1954).

[33] G. L. Hansen, J. L. Schmit, and T. N. Casselman, J. Appl. Phys. **53**, 7099 (1982).

[34] M. von Truchsess, V. Latussek, C. R. Becker, and E. Batke, J. Cryst. Growth **159**, 1128 (1996).

[35] R. Sporken, S. Sivananthan, J. P. Faurie, D. H. Ehlers, J. Fraxedas, L. Ley, J. J. Pireaux, and R. Caudano, J. Vac. Sci. Technol. A **7**, 427 (1989).

[36] D. Eich, K. Ortner, U. Groh, Z. N. Chen, C. R. Becker, G. Landwehr, R. Fink, and E. Umbach, Phys. Status Solidi A **173**, 261 (1999).

[37] C. R. Becker, V. Latussek, M. Li, A. Pfeuffer-Jeschke, and G. Landwehr, J. Electron. Mater. **28**, 826 (1999).

[38] J. R. Meyer, C. A. Hoffman, T. H. Myers, and N. C. Giles, in *Handbook on Semiconductors*, edited by S. Mahajan (North-Holland, Amsterdam, 1994), Vol. 3, p. 535.

[39] Y. Guldner, G. Bastard, J. P. Vieren, M. Voos, J. P. Faurie, and A. Million, Phys. Rev. Lett. **51**, 907 (1983); J. M. Berroir, Y. Guldner, J. P. Vieren, M. Voos, and J. P. Faurie, Phys. Rev. B **34**, 891 (1986).

[40] Steven P. Kowalczyk, J. T. Cheung, E. A. Kraut, and R. W. Grant, Phys. Rev. Lett. **56**, 1605 (1986).

[41] N. F. Johnson, P. M. Hui, and H. Ehrenreich, Phys. Rev. Lett. **61**, 1993 (1988).

[42] K. H. Yoo, R. L. Aggarwal, L. R. Ram-Mohan, and O. K. Wu, J. Vac. Sci. Technol. A **8**, 1194 (1990).

[43] Agreement is good if the photoluminescence peak E_p is shifted according to Eq. (1) in Ref. 7: $E_p = E_{H1\text{-}E1} + v k_B T$ with $v \approx 0.5$.

Inverted band structure of type-III HgTe/Hg$_{1-x}$Cd$_x$Te superlattices and its temperature dependence

C. R. Becker,* V. Latussek, G. Landwehr, and L. W. Molenkamp
Physikalisches Institut der Universität Würzburg, Am Hubland, 97074 Würzburg, Germany
(Received 22 January 2003; published 2 July 2003)

Intersubband transitions in (001)- and (112)B-orientated HgTe/Hg$_{1-x}$Cd$_x$Te superlattices with an inverted band structure have been investigated in order to determine their band structure. The results are compared with $\boldsymbol{k \cdot p}$ calculations in the envelope function approximation using the full 8×8 Kane Hamiltonian. Up to six intersubband transitions and their temperature dependences have been observed. Three transitions display a positive dependence on temperature and the remaining three a negative dependence. Agreement with theory for all observed transitions and both orientations is good. Due to the close proximity of the first conduction subband and the Fermi energy, the influence of the charge carriers must be taken into account.

I. INTRODUCTION

As is well known the optical and magnetotransport properties of HgTe/Hg$_{1-x}$Cd$_x$Te quantum wells (QW's) and superlattices (SL's) are determined by their band structure, which particularly in type-III superlattices is largely determined by that of the quantum well. This has been demonstrated for the optical properties of semiconducting superlattices with a normal band structure, i.e., with a quantum well width of $d_w \lesssim 6$ nm.[1,2] Recently large Rashba[3] spin-orbit (SO) splitting has been observed in n-type modulation-doped HgTe/Hg$_{1-x}$Cd$_x$Te quantum wells with an inverted band structure, i.e., $d_w \gtrsim 6$ nm, by means of Shubnikov–de Haas (SdH) oscillations.[4,5] Rashba SO splitting magnitudes of up to 17 meV in these QW's were shown by Zhang *et al.*[5] to be due to the heavy-hole nature of the conduction subband. The authors were able to quantatively describe the observed Rashba SO splitting by means of self-consistent Hartree calculations of the band structure based on an 8×8 $\boldsymbol{k \cdot p}$ model. The valence-band structure has been the subject of investigations of mixed conductivity in HgTe/Hg$_{1-x}$Cd$_x$Te multiple quantum wells and superlattices.[6,7] Ortner *et al.*[8] have recently investigated the valence-band structure via magnetotransport experiments on p-type modulation-doped HgTe/Hg$_{0.3}$Cd$_{0.7}$Te(001) quantum wells and have demonstrated that QW's with an inverted band structure are indirect semiconductors; i.e., their valence band has a maximum at finite $\boldsymbol{k}_\parallel$.

However, a systematic study of the optical properties of HgTe/Hg$_{1-x}$Cd$_x$Te quantum wells or superlattices with an inverted band structure has yet to be published. An investigation of the optical properties of HgTe/Hg$_{1-x}$Cd$_x$Te SL's with normal band structure has led to information about the quantum-well material and valence-band discontinuity between barrier and well.[2] The temperature dependence of the intersubband transition energies is directly influenced by that of the band gap of HgTe, which has led to a determination of the negative band gap of HgTe at room temperature as well as the temperature dependence of the heavy-hole effective mass. Furthermore, it was demonstrated that the valence-band offset is to a good approximation primarily responsible for the energy difference between the first heavy-hole, $H1$, and the first light hole, $L1$, subband of a HgTe/Hg$_{1-x}$Cd$_x$Te superlattice with normal band structure. This energy difference was shown to be nearly independent of other superlattice parameters and, consequently, has led to a precise determination of the valence-band offset between HgTe and CdTe, Λ.

In this article it will be shown that the optical properties and the corresponding inverted band structure of SL's can be equally well described by means of the parameters used in calculations for SL's with normal band structure. In the latter case the band structure and consequently the optical properties strongly depend on the quantum well width, whereas this dependence is less pronounced for the former case.

II. EXPERIMENTAL DETAILS

Epitaxial growth was carried out in a Riber 2300, molecular beam epitaxial (MBE) system which has been modified to permit the growth of Hg-based materials as has been described elsewhere.[9] After the growth of a thin CdTe buffer layer, the HgTe/Hg$_{1-x}$Cd$_x$Te superlattices were grown on (001)- and (112)B-oriented Cd$_{0.96}$Zn$_{0.04}$Te substrates at 180 °C. The substrate temperature was determined with an accuracy of ± 2 °C by means of a thermocouple which was in physical contact with a molybdenum substrate holder and was carefully calibrated at the melting points of indium and tin.

The composition of the barrier material has been determined by means of transmission measurements[10] on thick test layers of Hg$_{1-x}$Cd$_x$Te grown under identical conditions with the exception of the absence of the HgTe layers. At a growth temperature of 180 °C, $x = 0.70 \pm 0.02$ and $x = 0.95 \pm 0.02$ for the (001) and (112)B orientations, respectively. The first value has been corroborated by a determination of the barrier TO phonon frequency for several (001) SL's.[11]

In this investigation the well thickness d_w and hence that of the barrier, d_b, of (001) superlattices have been deter-

mined by means of a dynamic simulation of the (002) and (004) Bragg reflections measured in a six-crystal x-ray diffractometer.[12,13] The intensity of the normally weak (002) Bragg reflection is about 15% of that of the (004) Bragg reflection in these superlattices. This is caused primarily by the HgTe layer: the structure factor for the (002) Bragg reflection is much larger for HgTe than for CdTe.[12] This is due to the larger Hg atom with its greater number of electrons.

X-ray diffraction in (112)B-oriented heterostructures is more complicated and the results are less accurate. First of all, there is only one useful reflection, (224), which is essentially equally strong for HgTe and CdTe. Second, shear strain results in a monoclinic distortion which must be taken into account before the data can be correctly simulated.[14,15]

Optical transmission measurements were carried out in the middle infrared regime with a Fourier transform spectrometer, Bruker IFS88. The lowest experimental frequency was limited by absorption due to multiple-phonon processes in the substrate and SL as well as the transmission of the optical windows in the cryostat. A LiTaO$_3$ detector was usually employed rather than a liquid-nitrogen-cooled detector—e.g., Hg$_{1-x}$Cd$_x$Te—because of its better linearity. The absorption coefficient was determined by fitting the experimental transmission spectra to a theoretical description of the multilayer system using standard matrix procedures.[16]

The position of the absorption edge was determined relative to that of the corresponding intersubband transition energy; the transition energies were calculated and the shape of the theoretical absorption coefficient was adapted to that of the experimental coefficient. Employment of a Gaussian distribution of either the quantum well and barrier widths or the composition of the wells results in good agreement with experiment. In general, absorption edges, defined by the corresponding maxima in the first derivative of the absorption coefficient, agree well with the intersubband transition energies with the exception of transitions which are not completely resolved. Hence we can confidently assign intersubband transition energies to the corresponding maxima in the first derivative.

It has been demonstrated that the absorption edges can also be determined from the transmission spectra directly.[2] If a transmission spectrum at one temperature is divided by a spectrum at a slightly different temperature, the result is proportional to the corresponding change in the absorption coefficient:

$$\frac{\Delta T}{T} \approx d\Delta\alpha, \tag{1}$$

where T and d are the transmission and sample thickness, respectively. Hence a good approximation of $\Delta\alpha$ can be obtained merely from a ratio of the transmission spectra[2] without the complications and uncertainties in calculating the absorption spectrum of the SL in a multilayer structure.[16] By keeping the temperature difference small, $\Delta T = 10$–40 K, residual interference effects are effectively reduced near the transition itself and nearly eliminated at other frequencies. The index of refraction undergoes a change of up to about 5%–10% near an intersubband transition; however, this has
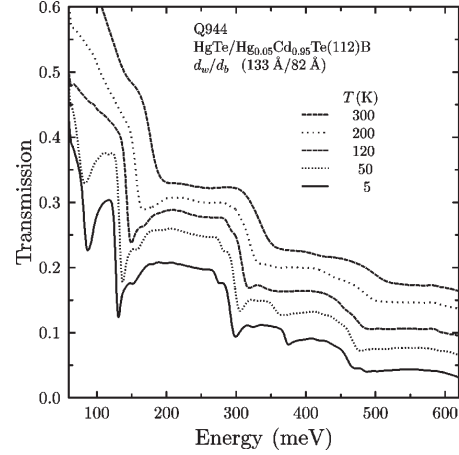

FIG. 1. The transmission spectra of a HgTe/Hg$_{0.05}$Cd$_{0.95}$Te(112)B superlattice, Q944, at several temperatures. The spectra are shifted along the vertical axis for clarity.

been shown to result in a negligible shift of the experimental absorption edge of ≤ 1 meV.[2]

The transmission spectra of the SL's were measured at various temperatures; see, for example, Fig. 1. This was done for temperatures of 5–320 K with a temperature interval of 5 K at low temperatures and 10 K at higher temperatures, in order to improve the statistical significance of the data.

III. THEORETICAL DETAILS

Numerous $\boldsymbol{k} \cdot \boldsymbol{p}$ band structure calculations using the envelope function approximation for the HgTe/Hg$_{1-x}$Cd$_x$Te superlattice have been published.[17–20] A brief review of the these calculations can be found in Ref. 2

In this investigation the bands of both bulk HgTe and CdTe are described by Kane's four-band model (8×8 $\boldsymbol{k} \cdot \boldsymbol{p}$) including all second-order remote band contributions. The envelope function method in the axial approximation has been employed to calculate the band structure of the HgTe/CdTe SL.[17,18] The axial approximation gives exact results for the band gaps of (001)-oriented systems, because nonaxial terms in the Hamiltonian vanish for $\boldsymbol{k}_\parallel = 0$; however, it is well known that the axial approximation is not exact for growth directions other than [001] and [111] even for $\boldsymbol{k}_\parallel = 0$.[21] Therefore we have taken the approach of Los et al.[22] and transformed the Hamiltonian into symmetry-adapted basis functions for the [112] growth direction. The band structure using this adapted Hamiltonian has been compared with an axial approximation for the [112] direction. The results of the axial approximation are not exact; however, they give a good approximation, within 1 or 2 meV, for the subband energies at $\boldsymbol{k}_\parallel = 0$ as well as for an average of the subband dispersion over all $\boldsymbol{k}_\parallel$ directions. Consequently, in order to reduce the calculation time, all absorption coefficient calculations and most intersubband transition energy

calculations were carried out using this adapted Hamiltonian in the axial approximation.

The effects of strain due to lattice mismatch were also taken into consideration, even though the lattice mismatch between HgTe and the $Hg_{1-x}Cd_xTe$ barriers is less than 0.1%. This results in a shift in intersubband transition energies of less then 3 meV and can therefore be neglected. In contrast to the [001] direction,[19] the strain tensor for the [112] direction has a shear strain component. This results in a piezoelectric field in the growth direction.[23] The strains for a free-standing, strained (112)B SL and a fully strained (112)B SL on a $Cd_{0.96}Zn_{0.04}Te$ substrate have been calculated. Due to the lack of a substrate in the former case, the shear strain component between the SL and its environment is zero. From these results the piezoelectric field has been calculated to be less than 5 mV/100 Å whose influence on intersubband transition energies is less than 1 meV and can therefore be neglected in the calculations.

A revised set of values for the band parameters deduced from measurements on bulk HgTe and $Hg_{1-x}Cd_xTe$ by Weiler[24] was employed which nevertheless reproduces the same bulk band structure ($\Delta = 1.0$ eV, $\gamma_1 = 4.1$, $\gamma_2 = 0.5$, $\gamma_3 = 1.3$, $F = 0$, and $E_p = 18.8$ eV). Since the SL band structure is primarily determined by that of the quantum well and is influenced to a much lesser degree by the band structure of the barrier, the above values were employed for both the HgTe quantum wells and the $Hg_{1-x}Cd_xTe$ barriers. This results in no significant changes in the calculated band structure. According to Weiler[24] the only parameter that changes significantly with alloy composition and temperature is the energy gap. The energy gaps of HgTe and $Hg_{1-x}Cd_xTe$ were taken from a slight alteration of the empirical $E_g(x,T)$ relationship according to Laurenti *et al.,*[10] which takes a recently determined value for HgTe at room temperature into account.[2] The valence-band offset between HgTe and CdTe was taken to be

$$\Lambda(T) = \Lambda_0 + \frac{d\Lambda}{dT}T \qquad (2)$$

where $\Lambda_0 = 570$ meV and $d\Lambda/dT = -0.40$ meV/K according to Becker *et al.*[2] and $\Lambda(T)$ is assumed to vary linearly with x for $Hg_{1-x}Cd_xTe$, i.e., $x\Lambda(T)$.[25] An interface width which results during growth or from interdiffusion of the two types of layers was integrated into the theory. The concentration profile across the interface is described by an error function similar to an experimental profile according to Kim *et al.*[26]

The complex dielectric constant can be written as

$$\varepsilon(\omega) = \varepsilon_R(\omega) + i\frac{\sigma(\omega)}{\omega\epsilon_0}, \qquad (3)$$

where $\varepsilon_R(\omega)$ is the residual contribution of the lattice and higher subbands which is assumed to be constant over the frequencies of interest in this investigation, $\varepsilon_R(\omega) \approx 10$. The complex dynamic conductivity $\sigma(\omega)$ is determined by making use of Kubo's formula,[27] and finally the absorption coefficient is given by
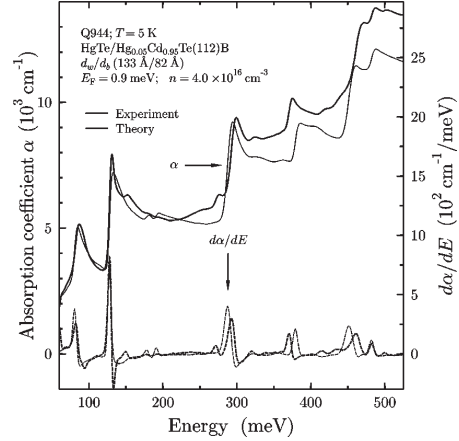

FIG. 2. The experimental (thick line) and theoretical (thin line) absorption coefficients and their first derivatives (thick and thin dashed lines, respectively) for a $HgTe/Hg_{0.05}Cd_{0.95}Te(112)B$ SL, Q944, at 5 K.

$$\alpha(\omega) = \frac{\omega}{c}\frac{\sqrt{2}\varepsilon_2(\omega)}{\sqrt{\varepsilon_1(\omega) + |\varepsilon(\omega)|}}, \qquad (4)$$

where $\varepsilon_1(\omega)$ and $\varepsilon_2(\omega)$ are the real and imaginary components of $\varepsilon(\omega)$, respectively.

IV. RESULTS AND DISCUSSION

A. (112)B orientation

Transmission spectra of an (112)B-oriented SL are shown in Fig. 1 at several temperatures. Numerous distinctive steps are visible, which with decreasing temperature become more pronounced. The three broad steps at 300 K have been assigned to the $H2$-$E2$, $H3$-$E3$, and $H4$-$E4$ intersubband transitions. H, L, and E are the heavy-hole, light-hole, and electron subbands, respectively. In the inverted band regime the valence subbands and the conduction subbands at low energies are mixed to varying degrees at finite k; however, for the sake of brevity we shall continue to use these designations. With decreasing temperature fine structure becomes readily discernable: at lower temperatures numerous minima are visible and noteworthy are the pronounced minima at the band edges near 128 and 288 meV, a feature which is normally associated with an exciton. The absorption spectrum together with the first derivative of the absorption coefficient for this SL at 5 K is shown in Fig. 2. At least three additional peaks at approximately 80, 368, and 482 meV are now visible which are assigned to the $E1$-$H1$, $L2$-$H1$, and $L2$-$E2$ intersubband transitions.

The calculated absorption coefficient spectrum, which is also shown in Fig. 2, is in good agreement with experiment. This agreement between the calculated transition probabilities and the observed absorption coefficient spectrum, as well as between the calculated and experimental frequencies, cor-
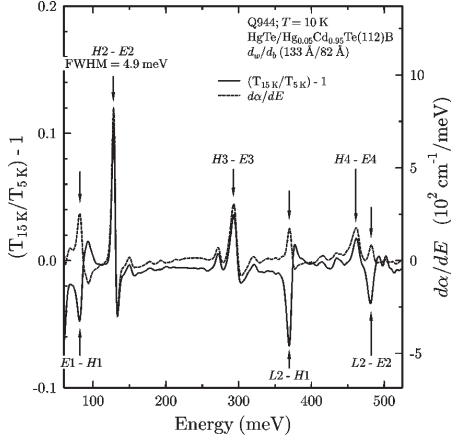
FIG. 3. The ratio of the transmission T at $T = 15$ and $T = 5$ K (solid line) is compared with the first derivative of α (dashed line) for Q944 at 10 K. The intersubband transitions are indicated by arrows. Minima are observed in the transmission ratio for those with a negative temperature dependence.
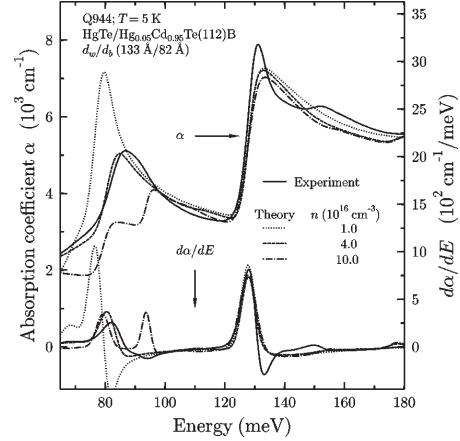

FIG. 4. The experimental (solid line) and theoretical (dotted, dashed, and dash-dotted lines) absorption coefficients and their first derivatives for a HgTe/Hg$_{0.05}$Cd$_{0.95}$Te(112)B SL, Q944, for three different electron concentrations at 5 K.

raborates the above-mentioned assignments. The relative heights of the corresponding steps are in good agreement with experiment, even though the absolute magnitude of the absorption coefficient α is underestimated due to the neglect of Coulomb interaction between electron and hole.[28]

1. Intersubband transition energies

The absorption edges have been determined from both the transmission and absorption spectra. In the latter case, the absorption edge is defined as the energy at the maximum value of the first derivative of the absorption coefficient. This is schematically demonstrated in Fig. 2 for Q944 at 5 K. The full widths at half maximum (FWHM) of the derivative for the $E1$-$H1$ and $H2$-$E2$ transitions are 7.2 and 4.9 meV, respectively. Also shown are a theoretically calculated α and its derivative. The shape and width of the experimental α and $d\alpha/dE$ for Q944 in Fig. 2 were simulated by assuming a Gaussian distribution of quantum well widths with $\sigma = 4.0$ Å.[29] The absorption edges coincide with the intersubband transition energies of $H2$-$E2$ to within ± 2 meV for all samples. The agreement for most of the other transitions is not as good due to their close proximity, e.g., $H4$-$E4$ and $L2$-$E2$, as well as due to the influence of the Fermi energy on some intersubband transitions as discussed below.

With the other method the absorption edge is determined from the change in the absorption coefficient according to Eq. (1). The near equivalence of these two methods of determining the band edges and consequently the intersubband transition energies is demonstrated in Fig. 3. In this figure the dashed line represents $d\alpha/dE$ at 10 K and the solid line represents $T_{15 K}/T_{5 K} - 1$ whose effective temperature is also 10 K. The experimental transition energies defined as the energies at the maximum or minimum values of $T_{15 K}/T_{5 K}$

-1 are in good agreement with the corresponding energies for $d\alpha/dE$; i.e., the energy difference is ≤ 1 meV for all six transitions. Because the $E1$-$H1$, $L2$-$H1$, and $L2$-$E2$ intersubband transitions are negatively dependent on temperature, minima in $T_{15 K}/T_{5 K} - 1$ are observed instead of the maxima for the other three intersubband transitions.

Because the Fermi energy is close to the $H1$ subband and strongly depends on the charge carrier concentration due to the small effective electron mass, the $E1$-$H1$ and $L2$-$H1$ intersubband transitions are influenced by the electron density n. This is illustrated for $E1$-$H1$ in Fig. 4 in which the theoretical α for three values of n is plotted together with the experimental absorption coefficient. At low carrier densities one sharp peak in $d\alpha/dE$ is visible, which with increasing densities shifts to higher energies and becomes broader. Finally, at higher carrier concentrations, two broad steps are expected. The higher-energy feature is due to the Burstein-Moss[30] shifted $E1$-$H1$ intersubband transition, whereas the expected lower-energy feature is a result of the $H4$-$H1$ transition. These two intersubband transitions at different carrier densities are schmatically shown as arrows in a diagram of the band structure dispersion shown in Fig. 5. The transition probability of the $H4$-$H1$ transition at low densities, i.e., at $k \approx 0$, is negligible but is finite for $k > 0$, according to the calculated dipole matrix elements shown in Fig. 6.

In addition the $L2$-$H1$ intersubband transition also shifts to higher energies with increasing n. Therefore these results indicate that a rough estimate of n can be obtained from transmission measurements.

2. Temperature dependence

The intersubband transition energies for Q944 are shown as a function of temperature in Fig. 7. Values determined from the transmission ratio are indicated by solid circles and
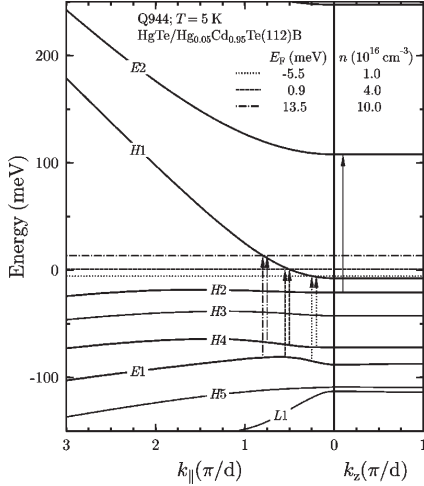
FIG. 5. The band structure dispersion for a HgTe/Hg$_{0.05}$Cd$_{0.95}$Te(112)B SL, Q944, at 5 K. The intersubband transitions; $E1$-$H1$, $H4$-$H1$, and $H2$-$E2$; are indicated by arrows for three different Fermi energies, i.e., electron concentrations, at 5 K.
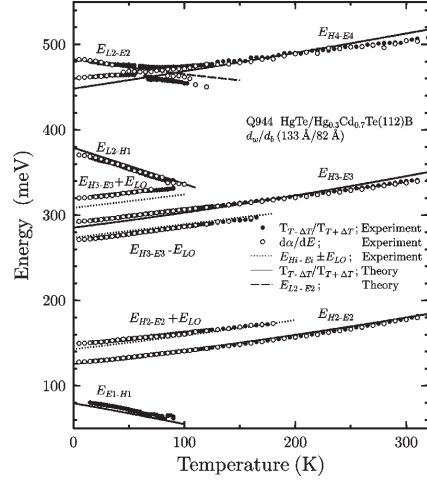

FIG. 7. Experimental values of the observed intersubband transitions from $d\alpha/dE$ (open circles) and $T_{T+\Delta T}/T_{T-\Delta T}$ (solid circles) together with theoretical results (lines) for a HgTe/Hg$_{0.05}$Cd$_{0.95}$Te(112)B SL, Q944, as a function of temperature.

those from $d\alpha/dE$ by open circles. The energies from these two methods are nearly equal: most of the former symbols are obscured by the latter. As can be seen there is less scatter in the data from the transmission ratio method. The experimental values of the $H2$-$E2$, $H3$-$E3$, and $H4$-$E4$ intersubband transition energies display a significant positive temperature dependence. In contrast, the temperature dependence of the $E1$-$H1$, $L2$-$H1$, and $L2$-$E2$ transition energies is negative. The temperature dependence of the initial subband is less than that of the final subband for $H2$-$E2$, $H3$-$E3$, and $H4$-$E4$ and vice versa for the other three inter-

subband transitions. Noteworthy are the weaker features in Fig. 7, whose temperature dependence is similar to that of the neighboring $H2$-$E2$ and $H3$-$E3$ intersubband transitions. In addition their energies are approximately equal to that of the respective transitions plus or minus the LO phonon energy, $E_{LO} \approx 17$ meV, of HgTe.[31] The agreement for $E_{H3-E3} + E_{LO}$ is not as good, due to the resonance induced minimum on the high-frequency side of $H3$-$E3$.

Using the temperature dependence of the valence-band offset, the HgTe band gap, and the heavy-hole effective mass according to Becker *et al.*,[2] the temperature dependence of the six primary transitions from the initial subband i to the final subband j have been calculated:

$$\frac{dE_{i-j}}{dT} = f\left(\frac{dE_g(\text{HgTe},T)}{dT}, \quad \frac{d\Lambda}{dT}, \quad \frac{m_{hh}^*}{dT} \right). \quad (5)$$

The theoretical intersubband transition energies have been determined from the ratio of the calculated transmission via Eq. (1), with the exception of energies of an unresolved transition, i.e., $L2$-$E2$, which have been determined from the band structure. All values are plotted together with the experimental results in Fig. 7 and are obviously in good agreement with the experimental values. The agreement is excellent for $H2$-$E2$, but is not as good for transitions at progressively higher energies as expected for a perturbation theory or for unresolved transitions.

B. (001) orientation

This more symmetric surface has a number of advantages but also distinct disadvantages. For example, the more symmetric Hamiltonian does not lead to a monoclinic distortion or a piezoelectric effect as is the case for (112).[14,15] As mentioned above, values for the well and barrier widths via x-ray

FIG. 6. The dipole matrix elements for a HgTe/Hg$_{0.05}$Cd$_{0.95}$Te(112)B SL, Q944, at 5 K.
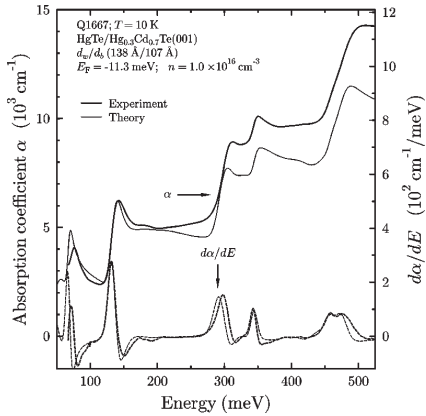
FIG. 8. The experimental (thick line) and theoretical (thin line) absorption coefficients and their first derivatives (thick and thin dashed lines, respectively) for a HgTe/Hg$_{0.3}$Cd$_{0.7}$Te(001) SL, Q1667, at 10 K.

diffraction are more accurate; however, the Cd concentration in the barriers is appreciably lower, 0.70 instead of 0.95. This has an important consequence. The absorption edges are up to a factor of 2.5 broader, apparently due to greater alloy fluctuations in the barriers.[29]

The experimental and theoretical absorption coefficients and their derivatives for a (001) SL, Q1667, at 10 K are plotted in Fig. 8. Agreement between experiment and theory is good, as is the case for the (112)B-oriented SL, Q944, and for two additional (001)-oriented SL's not shown here. Because the band structure for these two orientations is similar, the $E1$-$H1$ and $L2$-$H1$ intersubband transitions are also strongly influenced by the electron density for the (001) orientation. This is illustrated for $E1$-$H1$ in Fig. 9 in which the
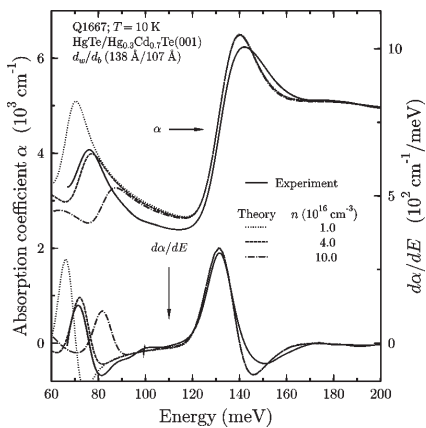
FIG. 9. The experimental (solid line) and theoretical (dotted, dashed, and dash-dotted lines) absorption coefficients and their first derivatives for a HgTe/Hg$_{0.3}$Cd$_{0.7}$Te(001) SL, Q1667, for three different electron concentrations at 10 K.
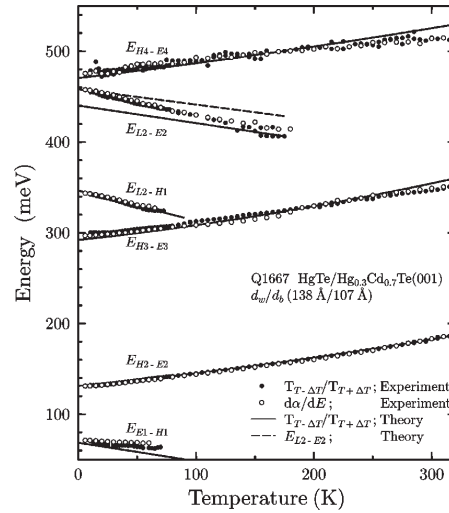
FIG. 10. Experimental values of the intersubband transition energies from the maximum value of $d\alpha/dE$ (open circles) and the ratio of the transmission spectra (T$_{T+\Delta T}$/T$_{T-\Delta T}$, solid circles), together with theoretical results (lines) for a HgTe/Hg$_{0.3}$Cd$_{0.7}$Te(001) SL, Q1667, vs temperature.

theoretical α for three values of n are plotted together with the experimental absorption coefficient. The sharp peak in $d\alpha/dE$ at low carrier densities shifts to higher energies and becomes broader with increasing densities. And as is the case for Q944, two broad steps are expected at higher carrier concentrations, which are due to the Burstein-Moss[30] shifted $E1$-$H1$ intersubband transition and the $H4$-$H1$ transition for $\mathbf{k}>0$. Again demonstrating that a rough estimate of n can be obtained from transmission measurements.

The intersubband transition energies for Q1667 are plotted as a function of temperature in Fig. 10. Results from the transmission ratio method are represented by solid circles and those from $d\alpha/dE$ by open circles. Here these two methods are also nearly equivalent and there is less scatter in the data from the transmission ratio method. Since features in α are much less pronounced in the (001)-oriented SL's, the transitions involving the LO phonon were not observed. The calculated temperature dependence of the observed intersubband transitions, which are displayed as lines in Fig. 10, is obviously in good agreement with the experimental values. As can be seen, agreement is better for transitions at lower energies, especially for $H2$-$E2$, as is expected for a perturbation theory.

V. CONCLUSIONS

Intersubband transitions and their dependence on temperature in semiconducting HgTe/Hg$_{1-x}$Cd$_x$Te superlattices with an inverted band structure have been investigated for the (001) and (112)B orientations. $\mathbf{k}\cdot\mathbf{p}$ calculations in the envelope function approximation using the full 8×8 Kane Hamiltonian are in good agreement with experiment. Re-

cently published values for $\Lambda(T)$, $E_g(HgTe,T)$, and m_{hh}^* from an investigation of HgTe/Hg$_{1-x}$Cd$_x$Te superlattices with a normal band structure have been employed. Of the six observed intersubband transitions, the temperature dependences of three are positive and those of the other three are negative. Transitions have been observed in a (112)B-oriented SL, which involve the $H2$-$E2$ and $H3$-$E3$ intersubband transitions, and the LO phonon. Furthermore, the charge carrier density strongly influences the $E1$-$H1$ and $L2$-$H1$ intersubband transitions. Hence a rough estimate of n can be determined from the optical absorption.

*Electronic address: becker@physik.uni-wuerzburg.de

[1] J. R. Meyer, C. A. Hoffman, T. H. Myers, and N. C. Giles, in *Handbook on Semiconductors*, edited by T. S. Moss, Vol. 3 edited by S. Mahajan (North-Holland, Amsterdam, 1994), p. 535.

[2] C. R. Becker, V. Latussek, A. Pfeuffer-Jeschke, G. Landwehr, and L. W. Molenkamp, Phys. Rev. B **62**, 10 353 (2000).

[3] E. I. Rashba, Fiz. Tverd. Tela **2**, 1224 (1960) [Sov. Phys. Solid State **2**, 1109 (1960)]; Yu. A. Bychkov and E. I. Rashba, Pis'ma Zh. Éksp. Teor. Fiz. **39**, 66 (1984) [JETP Lett. **39**, 78 (1984)].

[4] M. Schultz, F. Heinrichs, U. Merkt, T. Colin, T. Skauli, and S. Løvold, Semicond. Sci. Technol. **11**, 1168 (1996).

[5] X. C. Zhang, A. Pfeuffer-Jeschke, K. Ortner, V. Hock, H. Buhmann, C. R. Becker, and G. Landwehr, Phys. Rev. B **63**, 245305 (2001).

[6] C. A. Hoffman, J. R. Meyer, F. J. Bartoli, J. W. Han, J. W. Cook, J. F. Schetzina, and J. N. Schulman, Phys. Rev. B **39**, 5208 (1989).

[7] J. R. Meyer, C. A. Hoffman, and F. J. Bartoli, Physica B **191**, 171 (1993), and references therein.

[8] K. Ortner, X. C. Zhang, A. Pfeuffer-Jeschke, C. R. Becker, G. Landwehr, and L. W. Molenkamp, Phys. Rev. B **66**, 075322 (2002).

[9] C. R. Becker, V. Latussek, W. Spahn, F. Goschenhofer, S. Oehling and G. Landwehr, in *Growth and Characterization of Materials for Infrared Detectors*, edited by R. E. Longshore and J. W. Baars [Proc. SPIE **2554**, 6 (1995)].

[10] J. P. Laurenti, J. Camassel, A. Bouhemadou, B. Toulouse, R. Legros, and A. Lusson, J. Appl. Phys. **67**, 6454 (1990).

[11] M. von Truchsess, V. Latussek, F. Goschenhofer, C. R. Becker, G. Landwehr, E. Batke, R. Sizmann, and P. Helgesen, Phys. Rev. B **51**, 17 618 (1995).

[12] M. Möller, R. N. Bicknell-Tassius, and G. Landwehr, J. Appl. Phys. **72**, 5108 (1992).

[13] C. R. Becker, L. He, M. M. Regnet, M. M. Kraus, Y. S. Wu, G. Landwehr, X. F. Zhang, and H. Zhang, J. Appl. Phys. **74**, 2486 (1993).

[14] M. Li, C. R. Becker, R. Gall, W. Faschinger, and G. Landwehr, Appl. Phys. Lett. **71**, 1822 (1997).

[15] M. Li, R. Gall, C. R. Becker, T. Gerhard, W. Faschinger, and G. Landwehr, J. Appl. Phys. **82**, 4860 (1997).

[16] D. Fasold, K. Heil, and S. Jetschke, Phys. Status Solidi A **86**, 125 (1984).

[17] L. R. Ram-Mohan, K. H. Yoo, and R. L. Aggarwal, Phys. Rev. B **38**, 6151 (1988).

[18] N. F. Johnson, H. Ehrenreich, P. M. Hui, and P. M. Young, Phys. Rev. B **41**, 3655 (1990).

[19] A. Simon, D. Bertho, D. Boiron, and C. Jouanin, Phys. Rev. B **42**, 5221 (1990).

[20] J. R. Meyer, C. A. Hoffman, and F. J. Bartoli, Semicond. Sci. Technol. **5**, S90 (1990).

[21] R. Winkler and A. I. Nesvizhskii, Phys. Rev. B **53**, 9984 (1996).

[22] J. Los, A. Fasolino, and A. Catellani, Phys. Rev. B **53**, 4630 (1996).

[23] Liberato De Caro and Leander Tapfer, Phys. Rev. B **51**, 4374 (1995).

[24] M. H. Weiler, in *Semiconductors and Semimetals*, edited by R. Willardson and A. C. Beer (Academic Press, New York, 1981), Vol. 16, p. 119.

[25] C. K. Shih and W. E. Spicer, Phys. Rev. Lett. **58**, 2594 (1987).

[26] Y. Kim, A. Ourmazd, M. Bode, and R. D. Feldman, Phys. Rev. Lett. **63**, 636 (1989).

[27] E. Bangert, P. Boege, V. Latussek, and G. Landwehr, Semicond. Sci. Technol. **8**, S99 (1993).

[28] Christian Tanguy, Phys. Rev. Lett. **75**, 4090 (1995), and references therein.

[29] C. R. Becker, A. Pfeuffer-Jeschke, V. Latussek, M. Li, K. Ortner, V. Daumer, S. Oehling, W. Tang, and G. Landwehr, J. Cryst. Growth **184/185**, 1185 (1998).

[30] E. Burstein, Phys. Rev. **93**, 632 (1954); T. S. Moss, Proc. Phys. Soc. London, Sect. B **76**, 775 (1954).

[31] R. Dornhaus and G. Nimtz, in *Narrow-Gap Semiconductors*, edited by G. Höhler and E. A. Niekisch (Springer-Verlag, Berlin, 1983), Vol. 98, p. 119.

94

Valence Band Offset in HgTe/Hg$_{1-x}$Cd$_x$Te Superlattices

C.R. BECKER,[1,2] V. LATUSSEK,[1] M. LI,[1] A. PFEUFFER-JESCHKE,[1] and G. LANDWEHR[1]

1.—Physikalisches Institut der Universität Würzburg, 97074 Würzburg, Germany. 2.—email: becker@physik.uni-wuerzburg.de

The valence band offset (Λ) between HgTe and CdTe has been determined by means of an optical investigation of (112)B oriented HgTe/Hg$_{1-x}$Cd$_x$Te superlattices. Based on the fact that the difference in energy between the first heavy hole and the first light hole subband is to a good approximation due primarily to Λ, it has been shown that $\Lambda = 580 \pm 40$ meV at 5K. In addition Λ has a significant temperature dependence with a linear coefficient of -0.34 ± 0.02 meV/K, i.e., Λ is 480 ± 40 meV at room temperature.

Key words: HgTe/Hg$_{1-x}$Cd$_x$Te, molecular beam epitaxy (MBE), optical properties, superlattice, valence band offset

INTRODUCTION

The valence band offset (Λ) between HgTe and CdTe has been the subject of a number of investigations.[1,2] Here we have determined Λ by means of an optical investigation of (112)B oriented HgTe/Hg$_{1-x}$Cd$_x$Te superlattices (SLs). Theoretical calculations of the band structure and consequently the absorption coefficient by means of the envelope function approximation using the complete 8×8 k·p Hamiltonian, have been compared to experiment. The energy separation between the transition from the first heavy hole subband to the first conduction subband, H1 – E1, and the transition from the first light hole subband to the first conduction subband, L1 – E1, is to a good approximation due primarily to Λ. Consequently, an accurate value for Λ can be determined in spite of uncertainties in SL parameters.

EXPERIMENTAL DETAILS

The (112)B HgTe/Hg$_{1-x}$Cd$_x$Te SLs were grown on Cd$_{0.96}$Zn$_{0.04}$Te substrates by molecular beam epitaxy (MBE) in a Riber 2300 system, as have been described elsewhere in more detail.[3] The quantum well widths of these SLs fall between 30 and 45Å, corresponding to the semiconducting regime. The growth temperature was 180°C as measured with a thermocouple which was in contact with the molybdenum sample holder. An approximately 600Å thick CdTe buffer was grown at 315°C. The composition of the barriers, x, was

826

found to be 0.95 ± 0.02 rather than 0.68 ± 0.02 for a (001) sample which was grown simultaneously. This provides a stronger confinement in the (112)B HgTe layers. The period as well as the quantum well and barrier thicknesses, d, d$_w$, and d$_b$, respectively, were determined by means of x-ray diffraction. These values are not as accurate as the corresponding values for (001) SLs due to the presence of shear strain as well as tensile strain in the monoclinically distorted (112)B SL, which must be taken into account.[4]

The optical absorption coefficient, α, was determined from experimental transmission spectra using a matrix method for a multi-layer system. A Fourier transform spectrometer, Bruker IFS 88, was employed for transmission measurements.

Theoretical calculations of the band structure and consequently the absorption coefficient by means of the envelope function approximation using a Kane four band (8×8 k·p) Hamiltonian are compared with experiment.[5] An interface between the wells and barriers with a width of d$_t$ has been incorporated into the theory in order to determine its influence and that of its homogeneity on the absorption coefficient. Initially an error function has been employed which corresponds to an experimentally determined interface for a similar SL according to Kim et al.[6] Their results corresponds to an error function with a d$_t$ of 18Å.

RESULTS AND DISCUSSION

The experimental and theoretical absorption coefficients for a (112)B HgTe/Hg$_{1-x}$Cd$_x$Te SL at 5K together with their first derivatives are shown in Fig.

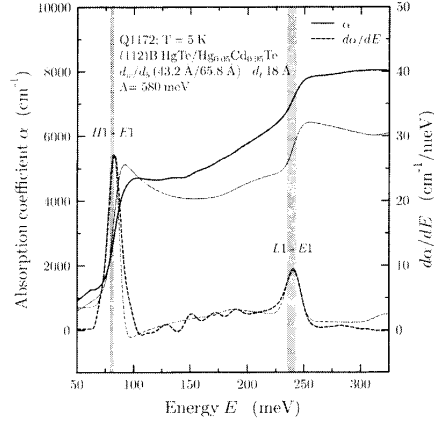Valence Band Offset in HgTe/Hg$_{1-x}$Cd$_x$Te Superlattices

Fig. 1. The experimental (thick line) and theoretical (thin line) absorption coefficients, and their derivative (thick and thin dashed lines, respectively) for the (112)B oriented Q1172 at 5K.
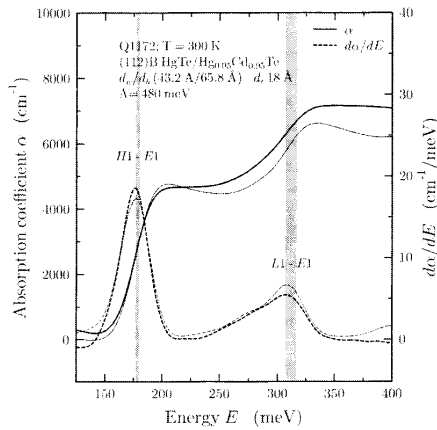

Fig. 2. The experimental (thick line) and theoretical (thin line) absorption coefficients, and their derivative (thick and thin dashed lines, respectively) for the (112)B oriented Q1172 at 300K.

Fig. 3. Temperature dependence of the H1 – E1 and L1 – E1 subband transition energies as well as that of the separation between these two transitions in Q1172. The filled and empty circles represent the experimental maxima in dα/dE and in the ratio of optical transmissions. The lines are the results of the theory described in the text.

1. The energy dispersion in q ‖ z, the miniband width, is indicated by the gray strips for the transition from the first heavy hole subband to the first conduction subband, H1 – E1, and the transition from the first light hole subband to the first conduction subband, L1 – E1. These are the miniband widths at k = 0, i.e., for unoccupied subbands. In this investigation, the absorption edge is defined as the energy at the maximum value of dα/dE. These absorption edges are appreciably sharper than those in (001) oriented SLs.[3] In this case, the full width at half maximum of

dα/dE for H1 – E1 and L1 – E1 are only 9 and 12 meV, respectively. This allows an accurate determination of the absorption edges which are nearly equivalent to the subband transition energies. From a comparison of the theoretically determined dα/de and subband transition energies as shown by the gray strips in Fig. 1, good agreement between these two values is demonstrated and hence their equivalence within ±1 to 2 meV. In order to simulate the absorption coefficient and, in particular, the full width at half maximum of dα/dE to a good approximation, a Gaussian distribution of the quantum well width and barrier concentration has been assumed with a full width at half maximum of 1.4Å and 0.12, respectively.

In Fig. 2, the experimental and theoretical absorption coefficients for the same (112)B HgTe/Hg$_{1-x}$Cd$_x$Te SL together with their first derivatives for 300K are shown. Even though the absorption edges are broader and the experimental uncertainities are approximately 50% larger, the above statements are still valid. The temperature dependence of the H1 – E1 and L1 – E1 subband transitions from 5 to 300K is shown in Fig. 3. Also shown is the difference between these two transitions, $E_{L1} - E_{H1}$, as a function of temperature. At temperatures below 50K, a small but reproducible Burstein-Moss shift of the H1 – E1 subband transition is visible. A similar shift is expected in the L1 – E1 subband transition which is apparently masked by the larger experimental uncertainty.

The subband transition energies depend on a number of parameters such as quantum well and

96

Table I. The Influence of the Interface Transition width and the Cd Concentration in
the Well, x_w on the Value Λ between HgTe and CdTe at 5K

	d	d_t	x_w %	d_w	Λ (5K) meV
Q1172	109.0	12 ± 6	0.5 ± 0.5	44.5 ± 2.8	580 ± 30
	109.0	12 ± 6	1.0 ± 1.0	44.5 ± 2.8	590 ± 42
	109.0	18 ± 9	1.0 ± 1.0	44.5 ± 3.8	600 ± 52
Q943	131.0	12 ± 6	0.5 ± 0.5	40.0 ± 2.7	572 ± 30
	131.0	12 ± 6	1.0 ± 1.0	40.0 ± 2.7	583 ± 42
range		12 ± 6	0.5 ± 0.5		580 ± 40

Note: The range of values for d_t and x_w given in this table result in a corresponding range of values for Λ. The H1 – E1 and L1 – E1 transition energies were held constant by varying the quantum well width, d_w, over the values given in this table while maintaining a constant period thickness, d.

barrier widths, quantum well and barrier compositions, the interface width and the valence band offset between HgTe and CdTe. However, to a good approximation, $E_{L1} - E_{H1}$ depends only on Λ. This is demonstrated in Table I for two (112)B oriented SLs and is discussed below.

Results from interdiffusion experiments on (001) oriented SLs suggest that the interface transition width is at least 6Å and could be up to about 30Å,[7,8] which is in reasonable agreement with the value according to Kim et al.[6] By means of x-ray photoemission spectroscopy (XPS), we have detected Cd in some HgTe epitaxial layers. Assuming a uniform distribution throughout the HgTe quantum well, this concentration, x_w, would be less than 1.0%. Apparently Cd can be emitted from the closed CdTe shutter when the CdTe cell is hot. Uncertainties in the values of these parameters result in a relatively small uncertainty in Λ. Making the reasonable assumptions that d_t =12 ± 6Å and x_w = 0.5 ± 0.5% results in a range of values given by Λ = 580 ± 40 meV at 5K. The H1 – E1 and L1 – E1 transition energies were held constant by varying the quantum well width within the range given in Table I. This range of values for Λ is in good agreement with the value of 550 ± 50 meV according to von Truchsess et al.[5] The lowest possible value for Λ at 5K is 520 meV which would occur if the interface were absolutely sharp, d_t = 0, and there were no Cd in the HgTe layer, x_w = 0.

The temperature dependence of $E_{L1} - E_{H1}$, as shown in Fig. 3 clearly demonstrates that Λ is temperature dependent, which was found to have a linear coefficient of –0.34 ± 0.02 meV/K. At room temperature Λ = 480 ± 40 meV. In contrast, Sporken et al.[9] found no temperature dependence within their estimated uncertainity of ±60 meV in an investigation employing XPS and angle integrated ultra violet photoemission spectroscopy (UPS).

As is well known, a number of XPS and UPS investigations have resulted in a value near 350 ± 60 meV with no appreciable temperature dependence. However, this value would result in values for $E_{L1} - E_{H1}$ which are too low by approximately 50 and 32 meV at 5 and 300K, respectively. This is clearly outside of the experimental uncertainity of ≤ 5 meV.

Furthermore, recent k resolved UPS experiments employing the Ar I emission line, hv = 11.70 eV, and a monochromator with a resolution of approximately 100 meV results in a value given by Λ = 530 ± 30 meV at room temperature.[10] This value is in good agreement with our result, i.e., Λ = 480 ± 40 meV at 300K. Under the experimental conditions used by Eich et al.,[10] the Ar I emission line corresponds to k ≈ 0, whereas previous ultra violet and x-ray photoemission spectroscopic experiments have averaged over all k values,[1,2,9] which can lead to systematic errors because dispersion in HgTe is not the same as that in CdTe.

CONCLUSIONS

The energy separation between the H1 – E1 and L1 – E1 subband transitions is to a good approximation due primarily to the valence band offset. Consequently, an accurate value for Λ can be determined in spite of uncertainities in SL parameters. A Λ value has been determined to be 580 ± 40 meV at 5K for a number of (112)B oriented SLs whose quantum well widths fall between 30 and 45Å, corresponding to the semiconducting regime. In addition, a significant linear temperature dependence of –0.34 ± 0.02 meV/K has been found, i.e., Λ = 480 ± 40 meV at 300K. Taking experimental error and the uncertainity in SL parameters into consideration, Λ for (001) HgTe/Hg$_{1-x}$Cd$_x$Te SLs has been found to have the same value.[5,11]

REFERENCES

1. P.M. Amirtharaj and J.H. Burnett, Narrow-gap II-VI Compounds for Optoelectronic and Electromagnetic Applications, ed. P. Capper, (New York: Chapman & Hall, London, Weinheim, 1997), p. 133.
2. J.R. Meyer, C.A. Hoffman, T.H. Myers and N.C. Giles, Handbook on Semiconductors, T.S. Moss, Vol. 3, ed. S. Mahajan (Amsterdam: North-Holland, 1994). p. 535.
3. C.R. Becker, A. Pfeuffer-Jeschke, V. Latussek, M. Li, K. Ortner, V. Daumer, S. Oehling, W. Tang and G. Landwehr, J. Cryst. Growth 184/185, 1185 (1998).
4. M. Li, R. Gall, C.R. Becker, T. Gerhard, W. Faschinger and G. Landwehr, J. Appl. Phys. 82, 4860 (1997).
5. M. von Truchsess, V. Latussek, F. Goschenhofer, C.R. Becker,

G. Landwehr, E. Batke, R. Sizmann and P. Helgesen, *Phys. Rev.* **51**, 17618 (1995).

6. Y. Kim, A. Ourmazd, M. Bode and R.D. Feldman, *Phys. Rev. Lett.* **63**, 636 (1989).

7. F. Goschenhofer, V. Latussek, S. Einfeldt, M.O. Möller, C.R. Becker and G. Landwehr, *Narrow Gap Semiconductors 1995*, ed. J.L. Reno, *Proc. 7th Intl. Conf. on Narrow Gap Semiconductors Santa* (Bristol, U.K.: Institute of Physics Publishing, 1995), p. 55.

8. C.R. Becker, V. Latussek, W. Span, F. Goschenhofer, S. Oehling and G. Landwehr, *Growth and Characterization of Materials for Infrared Dee* ed. R.E. Longshore and J.W. Baars, 2554, (SPIE, 1995), p. 6.

9. R. Sporken, S. Sivananthan, J.P. Faurie, D.H. Ehlers, J. Fraxedas, L. Ley, J.J. Pireaux and R. Caudano, *J. Vac. Sci. Technol.* **7** 427 (1989).

10. D. Eich, K. Ortner, U. Groh, Z.H. Chen, C.R. Becker, G. Landwehr, R. Fink and E. Umbach, to be published.

11. C.R. Becker, unpublished.

98

Growth and optical properties of (1 1 2)B HgTe/Hg$_{1-x}$Cd$_x$Te superlattices

C.R. Becker[a], A. Pfeuffer-Jeschke[a], V. Latussek[a], M. Li[a], K. Ortner[a], V. Daumer[a], S. Oehling[a], W. Tang[b], G. Landwehr[a]

[a] *Physikalisches Institut der Universität Würzburg, Am Hubland, 97074 Würzburg, Germany*
[b] *Institute of Technical Physics, Chinese Academy of Sciences, Shanghai 200033, People's Republic of China*

Abstract

The molecular beam epitaxial growth and the optical properties of (1 1 2)B oriented HgTe/Hg$_{1-x}$Cd$_x$Te superlattices (SLs) are compared with those of (0 0 1) orientated SLs. First of all, the Hg$_{1-x}$Cd$_x$Te barriers have a much higher Cd concentration than those in (0 0 1) grown under similar conditions, i.e. $x = 0.95 \pm 0.02$ as opposed to $x = 0.68 \pm 0.02$ at a growth temperature of 180°C. In addition the optical absorption edges are appreciably sharper than those in (0 0 1) oriented SLs grown under similar conditions, by a factor of at least two. Analogously, the full-width at half-maximum of the photoluminescence (PL) peak, e.g. 8 meV for a band gap of 100 meV at 4 K, is at least a factor of two narrower than that in our best (0 0 1) oriented SLs. This can be explained by a more homogeneous growth laterally, i.e. in the plane perpendicular to the growth direction: either more homogeneous quantum well and barrier thicknesses or a more homogeneous interface width. © 1998 Elsevier Science B.V. All rights reserved.

1. Introduction

The optical properties of HgTe/Hg$_{1-x}$Cd$_x$Te SLs have been the subject of numerous experimental and theoretical investigations [1–7]. The sharpness of the step-like features in the absorption coefficient depends on the energy dispersion in $q \| z$ (miniband width). This in turn depends on SL parameters such as the widths and compositions of the quantum well and barrier. In addition, the quality of the sample, in other words the homogeneity of

these parameters, should have a large influence on the sharpness of the absorption edges. One finds a large variation in the literature but with an apparent improvement with time.

We have investigated about 50 (0 0 1) HgTe/ Hg$_{1-x}$Cd$_x$Te SLs which also display a large variation in the quality of their optical properties from those with smeared-out features comparable to those with well resolved sharp features [6]. However all six (1 1 2)B oriented HgTe/Hg$_{1-x}$Cd$_x$Te SLs, which have been grown to date, have

absorption edges which are at least a factor of two steeper than those of our best (0 0 1) oriented SLs.

2. Experimental details

The (1 1 2)B HgTe/Hg$_{1-x}$Cd$_x$Te SLs were grown on Cd$_{0.96}$Zn$_{0.04}$Te substrates by molecular beam epitaxy in a Riber 2300 system under as close to the same conditions as possible as for the (0 0 1) orientation, which have been described elsewhere in more detail [3,6]. The growth temperature was 180°C as measured with a thermocouple which was in contact with the molybdenum sample holder. An approximately 600 Å thick CdTe buffer was grown at 315°C using both Cd and CdTe sources. The quantum wells were grown using the Hg and Te sources and the barriers using the Hg and CdTe sources. The fluxes as measured with an ionization gauge were 2, 5 and 10 × 10^{-7} Torr for Cd, CdTe and Te, respectively, and 2.6 × 10^{-4} Torr for Hg.

The composition of the (1 1 2)B orientated Hg$_{1-x}$Cd$_x$Te barriers was determined from the optical absorption edge of a thick epitaxial layer which was grown under the same conditions as the barriers. x was found to be 0.95 ± 0.02 rather than 0.68 ± 0.02 for a (0 0 1) sample which was grown simultaneously. This should provide a stronger confinement in the quantum well.

The period as well as the quantum well and barrier thicknesses were determined by means of X-ray diffraction [8,3]. An analysis of X-ray diffraction data for a (1 1 2)B oriented SL is more complicated than that for a (0 0 1) SL due to the presence of shear strain [9]. Nevertheless, the quantum well and barrier widths have been determined, albeit with less accuracy than for (0 0 1). These values are listed in Table 1. The diffraction profiles for the (2 2 4) Bragg reflection have values for the full-width at half-maximum (FWHM) which are far from exceptional, i.e. between 90 and 300 arcsec. In contrast, the diffraction profiles for the (0 0 4) Bragg reflection for the (0 0 1) oriented SLs have lower values even though there is a large amount of variation from 22 up to 300 arcsec.

The optical absorption coefficient was determined from experimental transmission spectra using the standard matrix method for a multi-layer

system. A Fourier spectrometer, Bruker IFS 88, was used for both transmission and PL measurements. A double-modulation technique using a Si diode laser with a maximum output intensity of 100 mW was employed for the latter.

Theoretical calculations of the band structure and, consequently, the absorption coefficient by means of the envelope function approximation using a Kane four band (8 × 8 $k \cdot p$) Hamiltonian are compared with experiment. An interface between the wells and barriers with a finite width has been incorporated into the theory in order to determine its influence as well as the influence of its homogeneity on the absorption coefficient. Initially, an error function has been employed which corresponds to an experimentally determined interface for a similar SL [10]. A valence band offset of 570 ± 40 meV at 5 K between HgTe and CdTe has been employed. This value is necessary in order to correctly predict the difference in energies between the $H1$–$E1$ and $L1$–$E1$ interband transitions and to explain magneto-absorption results [7].

3. Results and discussion

The experimental and theoretical absorption coefficients for a (1 1 2)B HgTe/Hg$_{1-x}$Cd$_x$Te SL, Q943, together with their first derivatives are shown in Fig. 1. For comparison the results for one of our best (0 0 1) oriented SL, Q424, are shown in Fig. 2. For both of these SLs, the energy dispersion in $q \| z$, the miniband width, of the $H1$–$E1$ interband transition is small, i.e. 0.4 and 6.6 meV for Q943 and Q424, respectively, compared to the width of the absorption edge. As can be seen in Table 1, the absorption edge, dα/dE, for Q943 is about 3.0 times steeper than that of Q424, and the full-width at half-maximum (FWHM) of dα/dE for Q943 is 9 meV which is a factor of 3.5 narrower than that of Q424. The expected dispersion in $H1$–$E1$ for Q1104, Q1105 and Q1103 is ≈ 20 meV which is very similar to that for the (0 0 1) SL Q204. Even though these theoretically calculated miniband widths are comparable to the experimental values of the absorption edge widths and should be taken into account in order to determine the influence of inhomogeneity, a direct comparison shows that the
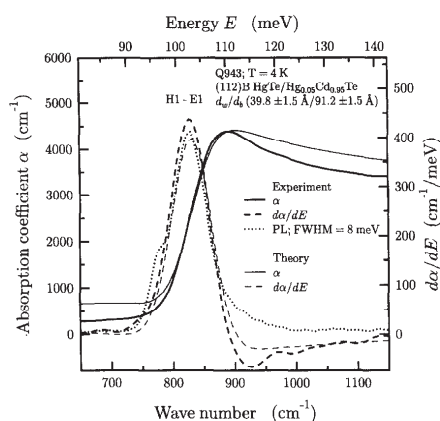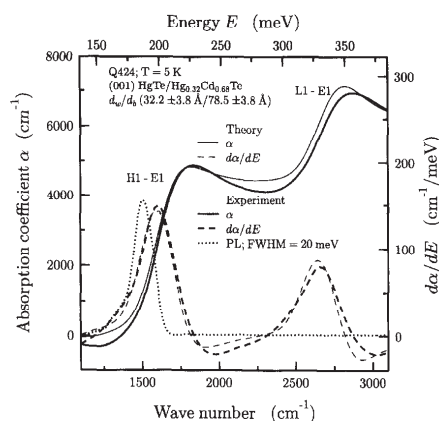
Fig. 1. The experimental (thick line) and theoretical (thin line) absorption coefficients, their derivative (thick and thin dashed lines, respectively) for the (1 1 2)B oriented Q943 and PL at 4 K (dotted line).

Fig. 2. The experimental (thick line) and theoretical (thin line) absorption coefficients, their derivative (thick and thin dashed lines, respectively) for the (0 0 1) oriented Q424 and PL at 5 K (dotted line).

absorption edges of these (1 1 2)B SLs are at least a factor of two steeper. Finally, two SLs with an inverted band structure were investigated. As can be seen in Table 1, the maximum value of $d\alpha/dE$ of the $H2$–$E2$ interband transition for the (1 1 2)B oriented SL is about a factor of 5.5 larger than that for the (0 0 1) sample. Analogously, the FWHM is about a factor of 3.5 narrower.

As can be seen in Figs. 1 and 2, the PL peak at 4 K for the (1 1 2)B SL is more than a factor of two narrower than that of the (0 0 1) SL. In addition this peak lies at nearly the same energy and has almost the same width as the first derivative of the absorption coefficient. As can be seen this is not the case for the peak for the (0 0 1) sample which falls on the low energy flank of $d\alpha/dE$. However, this statement is valid for all three (1 1 2)B samples for which PL experiments were conducted.

The experimental absorption edge widths can be simulated by assuming a Gaussian distribution of either the quantum well and barrier widths, quantum well and barrier compositions or transition widths of the interface. No significant differences are expected in the growth direction because the same growth conditions were chosen for both orientations. The homogeneity in the growth direction

should depend primarily on the stability of the fluxes and the growth temperature. The simulations shown in Figs. 1 and 2 have been accomplished by assuming a Gaussian distribution of the quantum well and barrier widths. In the case of SLs with a normal band structure, ± 0.5 monolayers (ML) is required for all (1 1 2)B oriented SLs compared to the ± 1.2 to 2 ML or more which is necessary for the (0 0 1) orientated SLs. The interface of a (0 0 1) SL grown under similar conditions according to Kim et al. [10] has a width of about 18 Å ($\sim$6 ML). A distribution corresponding to $\geqslant \pm 4$ ML is required for a simulation of the (0 0 1) results whereas this is merely $\leqslant \pm 2$ ML for the (1 1 2)B orientation. These results are summarized in Table 1.

In the case of SLs with an inverted band structure, the inhomogeneities that are required in order to simulate the absorption edge of the $H2$–$E2$ interband transition are larger. As listed in Table 1, a Gaussian distribution of ± 3 ML is required for the (0 0 1) orientation whereas the corresponding value is only ± 1 ML for (1 1 2)B. Even though these absolute values are larger than those for the SLs with a normal band structure, relative to the quantum-well widths they are not. This would indicate that inhomogeneities in the growth increase

Table 1
Included in this table are: the average period width $(\bar{d})$, the average quantum-well width $(\bar{d}_w)$, the H_j–E_j ($H2$–$E2$ for Q846 and Q944, and $H1$–$E1$ for all other SLs) interband transition energy at 5 K, the energy dispersion $\Delta E = E_{q=\pi/d} - E_{q=0}$, the maximum value and the full-width at half-maximum (FWHM) of $d\alpha/dE$, as well as the Gaussian distribution of the quantum-well width (Δd_w), transition width of the interface (Δd_t) and the quantum well (Δx_w) and barrier (Δx_b) concentrations which are necessary in order to simulate the absorption coefficient to a good approximation

(hkl)	$\bar{d}$ ±2 Å	$\bar{d}_w$ ±4 Å	Hj–Ej 5 K meV	ΔE meV	$d\alpha/dE$ maximum cm⁻¹/meV	FWHM meV	Δd_w ±Å	Δd_t ±Å	Δx_w ±	Δx_b ±
(0 0 1)										
Q424	110.7	32.2	200	6.6	145	32	3.8	13	0.03	0.14
Q204	95.8	40.2	138	24	124	37	6.0			
Q846	209.8	137.6	127	1.3	210	16	10.0	>18		
(1 1 2)B										
Q943	131.0	39.8	99	0.4	440	9	1.5	4	0.01	>0.05
Q1104	84.0	41.2	108	20	280	19	1.6			
Q1105	78.0	36.0	140	23	320	24	1.5			
Q1103	77.0	35.0	176	22	370	22	1.6	6	0.02	>0.05
Q944	215.0	133.0	126	0.4	1150	4.5	3.0	8		

with increasing thickness. This very preliminary result suggests that this dependence is less than linear with thickness.

An inhomogeneity in the composition of the wells is also capable of reproducing the absorption edge widths, however, it is hard to imagine a process which could cause such a distribution. Alloy fluctuations in the barriers of the (0 0 1) SLs due to the statistics of incorporation could possibly be of the required magnitude, however, should occur over very short distances and it is unknown if they could be responsible for the observed differences in the absorption edges.

In an attempt to test the hypothesis that alloy fluctuations in the barriers are responsible for the difference, two (0 0 1) SLs were grown under the same conditions mentioned above, except that during the barrier growth an excess of Cd flux was employed resulting in nearly pure CdTe barriers. The absorption edges were, however, even less pronounced than the previously grown (0 0 1) samples as described above. This is not a conclusive negative result because the growth temperature of 180°C is lower than that required for good epitaxial growth of CdTe.

From an investigation using a scanning tunnel microscopy (STM), (0 0 1) HgTe is known to grow by the step-flow mechanism at 180°C, forming structures with monolayer steps which are about 500 Å wide [11]. These terraced structures are up to 10 nm high. Even though a very thorough in situ STM investigation of these SLs at various growth stages is necessary, an initial attempt has been made to investigate the lateral homogeneity of the as grown SLs by atomic force microscopy (AFM). The preliminary results for the (0 0 1) samples show the presence of a large number of structures similar to those found on (0 0 1) HgTe epitaxial layers but whose heights range between 30 and 100 nm. These structures are not present on the (1 1 2)B SLs or are much smaller than those on the (0 0 1) samples.

4. Conclusions

Several (1 1 2)B SLs have been investigated whose quantum-well widths fall between approximately 30 and 140 Å, corresponding to a band structure which ranges from the normal to the inverted regime. In conclusion, their absorption

102

edges are appreciably sharper by a factor of two or more than those in (0 0 1) oriented SLs grown under similar conditions and which therefore have comparable parameters such as quantum-well widths and energy dispersion in $q\|z$. Analogously, the full-width at half maximum of the PL peak, e.g. 8 meV for a band gap of 100 meV at 4 K, is at least a factor of two narrower than that in (0 0 1) oriented SLs.

These experimental results can be explained by one of the following: a more homogeneous growth laterally or a reduction in alloy fluctuations in the barrier. A consequence of the former phenomenological explanation would require a nonuniformity in the lateral distribution of the quantum-well widths of ± 0.5 ML or less for (1 1 2)B SLs, and the much larger value of ± 1.2 or more monolayers for (0 0 1) SLs. Alternatively, the results can be explained by more homogeneous interfaces between the wells and barriers. On the other hand, composition fluctuations in the barrier should be less in (1 1 2)B oriented samples due to its higher Cd concentration, i.e. $x = 0.95$ for (1 1 2)B instead of 0.68 for (0 0 1) at a growth temperature of 180°C. These fluctuations would occur over very short distances and are outside of the scope of this investigation. Which of these explanations or combinations thereof is correct or possibily another, is unknown at the present, however, the preliminary AFM results seem to point to differences in the homogeneity in the lateral growth.

Acknowledgements

References

[1] N.F. Johnson, H. Ehrenreich, P.M. Hui, P.M. Young, Phys. Rev. B 41 (1990) 3655.

[2] A. Simon, D. Bertho, D. Boiron, C. Jonanin, Phys. Rev. B 42 (1990) 5221.

[3] C.R. Becker, L. He, M.M. Regnet, M.M. Kraus, Y.S. Wu, G. Landwehr, X.F. Zhang, H. Zhang, J. Appl. Phys. 74 (1993) 2486.

[4] J.R. Meyer, C.A. Hoffman, T.H. Myers, N.C. Giles, in: T.S. Moss (Ed.), Handbook on Semiconductors, vol. 3, S. Mahajan (Ed.), North-Holland, Amsterdam, 1994, p. 535.

[5] Z. Yang, Z. Yu, Y. Lansari, S. Hwang, J.W. Cook Jr., J.F. Schetzina, Phys. Rev. B 49 (1994) 8096.

[6] C.R. Becker, V. Latussek, W. Spahn, F. Goschenhofer, S. Oehling, G. Landwehr, in: R.E. Longshore, J.W. Baars (Eds.), Growth and Characterization of Materials for Infrared Detectors, SPIE Proc. Vol. 2554, 1995, p. 6.

[7] M. von Truchsess, V. Latussek, F. Goschenhofer, C.R. Becker, G. Landwehr, E. Batke, R. Sizmann, P. Helgesen, Phys. Rev. B 51 (1995) 17618.

[8] M. Möller, R.N. Bicknell-Tassius, G. Landwehr, J. Appl. Phys. 72 (1992) 5108.

[9] M. Li, R. Gall, C.R. Becker, T. Gerhard, W. Faschinger, G. Landwehr, J. Appl. Phys., accepted.

[10] Y. Kim, A. Ourmazd, M. Bode, R.D. Feldman, Phys. Rev. Lett. 63 (1989) 636.

[11] S. Oehling, M. Ehinger, W. Spahn, A. Waag, C.R. Becker, G. Landwehr, J. Appl. Phys. 79 (1996) 748.

Temperature dependent investigation of the HgTe/CdTe valence band offset

M. von Truchsess *, V. Latussek, C.R. Becker, E. Batke

Physikalisches Institut der Universität Würzburg, Am Hubland, D-97074 Würzburg, Germany

Abstract

We report here on a temperature dependent magneto-optical investigation of the valence band offset between HgTe and CdTe. The H1–E1 gap and the conduction band edge mass of various HgTe–(HgCd)Te superlattices were studied in a wide regime from liquid helium to nearly room temperature. With an offset of 550 meV which was determined previously at liquid helium temperatures and the temperature dependence of the Γ_6–Γ_8 gap of bulk $Hg_{1-x}Cd_xTe$, a nearly perfect description of the experimental data was obtained. Our experiment provides strong evidence that a temperature dependence of the band offset can essentially be neglected.

1. Introduction

A reliable prediction of the band structure of heterostructures based on $Hg_{1-x}Cd_xTe$ has not been possible until recently. Due to the uncertainty in the size of the valence band offset between the semimetal HgTe and the wide gap semiconductor CdTe, a quantitative comparison with experimental data was limited. The offsets determined at liquid helium temperatures from magneto-optical experiments scatter considerably between about 40 and 800 meV, and do not agree with the offset of 350 meV determined from X-ray (XPS) and ultraviolet photoelectron spectroscopy (UPS), as reviewed in Ref. [1]. The discrepancy between magneto-optical investigations and XPS and UPS experiments has not yet been resolved

satisfactorily. However, a reliable value of 550 ± 50 meV was recently determined from magneto-optical studies at liquid helium temperatures [1]. With this value the band structures of various heterostructures at liquid helium temperatures are in good agreement with experiment [1,2].

Previously, a possible temperature dependence of the offset was studied by magneto-optical investigations only on inverted semiconducting superlattices [3]. Here we present a summary of our magneto-optical experiments performed on different superlattices in magnetic fields up to 14 T and a temperature regime from 5 to 250 K. The experimental H1–E1 band gap and the electron effective mass at the conduction band edge are compared to the predictions of a 8×8 $\mathbf{k \cdot p}$ band structure calculation including the influence of strain and graded interfaces. A satisfactory description of the experiment is obtained if one considers a temperature dependence for only the gap between the bands of Γ_6 and Γ_8 symmetry in bulk $Hg_{1-x}Cd_xTe$. This provides strong

---

* Corresponding author. Fax: +49 931 888 5143; E-mail: truchs@wpfx33.physik.uni-wuerzburg.de.

Table 1
Sample parameters for HgTe–Hg$_{1-x}$Cd$_x$Te superlattices with period $d = d_W + d_B$, where d_W and d_B represent, respectively, the well and barrier widths; the alloy composition in the barriers is $x = 0.68$ equal for all samples; the fifth column indicates the type of the superlattice at liquid helium temperatures

Sample	d_W (nm)	d_B (nm)	Periods	Type at 5 K
A	6.09	6.52	110	Semiconducting
B	8.60	4.85	100	Inverted
C	6.30	4.30	100	Semimetallic
D	6.77	4.48	100	Semimetallic
E	6.20	4.61	100	Semiconducting

evidence that a temperature dependence of the offset, if present, is small.

2. Sample growth and experimental details

All superlattices investigated in the present experiment are listed in Table 1. All samples were grown at a temperature of 180°C on (100) Cd$_{0.96}$Zn$_{0.04}$Te substrates by molecular beam epitaxy (MBE) [4]. The frequency dependent transmission experiments in Faraday geometry were performed with a rapid-scan Fourier transform spectrometer with unpolarized radiation covering a spectral range between 20 and 1200 cm^{-1}. To correct for the spectral characteristic of the measurement system, we normalized all magnetic field dependent transmission spectra $T(B)$ to the transmission spectrum at zero magnetic field strength, $T(0)$.

3. Results and discussions

In Fig. 1 we show the temperature dependences of the transmission spectra for two superlattices A and B. Sample A is of the semiconducting type over the whole temperature regime. This can be judged from the temperature induced shifts of both interband and intraband transitions. The broad minimum in $T(B)/T(0)$ at the higher frequencies is due to an interband transition between the Landau-levels of the H1 and E1 bands, whereas the weaker minima, which increase in strength with increasing temperature, reflect cyclotron resonances of electrons in the E1 conduction band. Two cyclotron transitions are

clearly resolved at higher temperatures. The intensities of higher cyclotron transitions are enhanced at higher temperatures due to a larger thermal population of higher Landau-levels. Please note that the interband transition energy increases with temperature, whereas the cyclotron transition frequency decrease slightly. This can be expected in the semiconducting regime, since band coupling phenomena across the temperature dependent gap dominates the nonparabolicity of the conduction band as well as the mass at the band edge. An increase in the gap results in a reduced nonparabolicity and an enhanced band edge mass, which essentially determines the cyclotron resonance positions.

Sample B is of inverted type at liquid helium temperatures as we shall demonstrate below. It clearly shows semiconducting behaviour, i.e. increasing interband transition energies and decreasing cyclotron transition frequencies, only at temperatures higher than 150 K. A separation of intraband and interband transitions below 150 K cannot be performed in a simple manner and requires an appropriate theory from first principles, which includes a magnetic field. This is beyond the scope of this article in which we shall concentrate on the normal semiconducting regimes of the superlattices. We analyze the temperature dependence of the H1–E1 gap and mass at the conduction band edge E1 by extrapolating to zero magnetic field, the hole to electron Landau-level transition energies and cyclotron masses as deter-
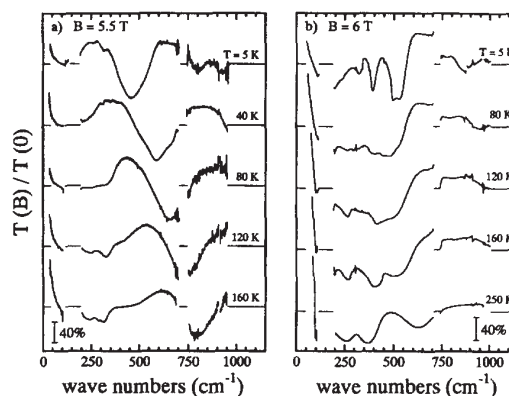

Fig. 1. Normalized transmission $T(B)/T(0)$ versus energy for (a) sample A and (b) sample B at magnetic fields of 5.5 and 6 T, respectively, for various temperatures. The horizontal lines mark $T(B)/T(0) = 1$ lines.
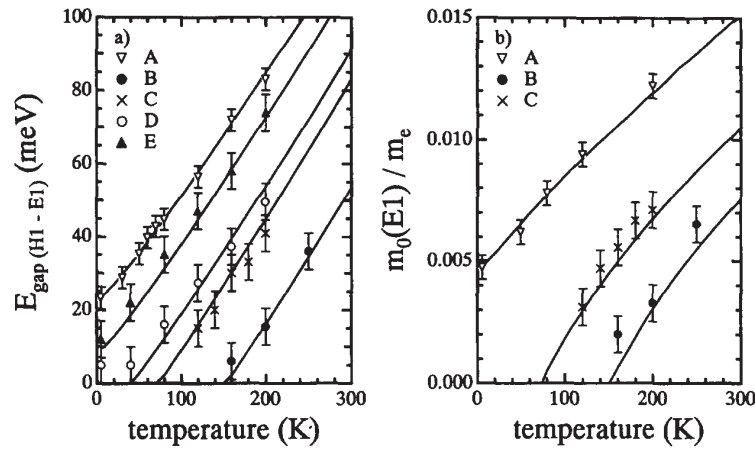
Fig. 2. Temperature dependence of (a) the H1–E1 gap and (b) the effective mass at the conduction band edge E1 for the samples of Table 1 obtained in the normal semiconducting regimes. Lines represent results from band structure calculations as described in the text.

mined from $m_c = eB/\omega_c$ for different Landau-level transitions $N \rightarrow N + 1$.

Fig. 2 summarizes the values of the temperature dependent gap and the band edge mass obtained in this manner for the superlattices listed in Table 1. The solid lines are predicted temperature dependences. Our numerical calculation takes into account the full 8×8 Kane Hamiltonian including all second-order terms representing the far-band contributions [5] including the strain which originates from the lattice mismatch between $Hg_{1-x}Cd_xTe$ and HgTe as well as a finite interface width [6,7]. Since a depth dependence of the interface widths could not be deduced in recent infrared absorption experiments on a similar superlattice [8], we consider this an indication that in addition to interdiffusion a mechanism inherent to the MBE growth process has to be included. From X-ray photoelectron spectroscopy performed on epitaxial HgTe layers grown on top of a superlattice structure we conclude that the superlattice wells contain about 3% Cd. Whether this is true only for our MBE system or is a general feature of the MBE growth process of such superlattice structures, has to be clarified. Since the presence of Cd in the wells was not confirmed until very recently we previously simulated its effect by assuming the presence of nonlinear diffusion according Tardot et al. [9]. We note that the value of the valence band offset is not affected by this treatment. Concentration pro-

files calculated assuming nonlinear interdiffusion with an appropriate diffusion constant are essentially the same as those with a certain Cd content in the wells and an assumed grading of the interfaces. Our calculation is based on an improved set of bulk band parameters [1,2] which deviate slightly from the ones given by Weiler [10]. In our calculation the only temperature dependent parameter is the gap:

$$\Delta E_{\Gamma_6 - \Gamma_8}(x,T)$$
$$= -0.303(1 - x) + 1.606x - 0.132x(1 - x)$$
$$+ \{[6.3(1 - x) - 3.25x$$
$$- 5.92x(1 - x)]10^{-4}T^2\}$$
$$\times [11(1 - x) + 78.7x + T]^{-1}, \qquad (1)$$

between the bands of Γ_6 and Γ_8 symmetry in the bulk which was taken from Ref. [11]. In addition, the valence band offset between HgTe and $Hg_{1-x}Cd_xTe$ was assumed to depend linearly on the composition. Taking the valence band offset between HgTe and CdTe of 550 meV which we determined recently at liquid helium temperatures and the bulk gap Eq. (1) we obtained a satisfactory agreement with the experimental data as is shown in Fig. 2. Thus, we conclude that a possible temperature dependence of the offset, if present at all, is small and can be neglected to a very good approximation.

In Fig. 3 the temperature dependence of the band structure for superlattices A and B is shown. Sample
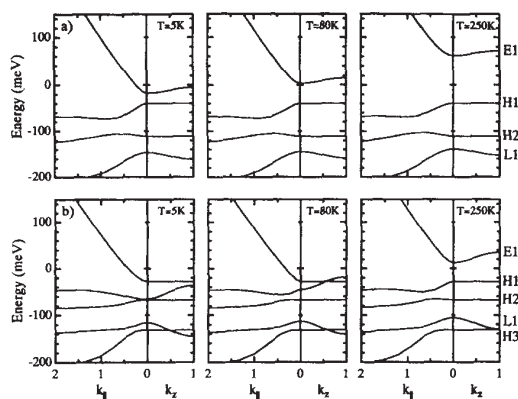
Fig. 3. Calculated temperature dependence of the band structures for (a) sample A and (b) sample B at zero magnetic field strength. $k_\parallel$ and k_z are wave vectors in the layer plane and in growth direction, respectively, given in units of π / d, where $d = d_W + d_B$ is the superlattice period.

A is as observed of the normal semiconducting type at all temperatures. For sample B the theory predicts that a temperature induced shift from inverted to semimetallic and finally to semiconducting behaviour should occur. The theoretical prediction is in agreement with the experimental observation. Experimentally we observe a qualitative change of the spectra at temperatures of 60 and 150 K. This is in agreement with the prediction that superlattice B is of inverted type below 60 K, changes to the semimetallic type at temperatures between 60 and 150 K and becomes a normal semiconductor at higher temperatures.

4. Conclusion

In summary, we investigated the temperature dependence of the H1–E1 gap and the conduction band edge mass in order to derive information on a possible temperature dependence of the valence band offset between HgTe and CdTe. A very satisfactory agreement between experiment and theory is obtained if the offset is independent of temperature.

Using an offset of 550 meV at liquid helium temperatures and the composition and temperature dependence of the Γ_6–Γ_8 gap of bulk $Hg_{1-x}Cd_xTe$ all experimental temperature dependences can be described. Our observation is in agreement with previous XPS and UPS experiments where also no significant temperature dependence was deduced [12].

Acknowledgements

References

[1] M. von Truchsess, V. Latussek, R. Sizmann, P. Helgesen, F. Goschenhofer, C.R. Becker, G. Landwehr and E. Batke, Phys. Rev. B 51 (1995) 17618.

[2] M. von Truchsess, V. Latussek, C.R. Becker and E. Batke, in: Proc. Int. Workshop on Semimagnetic Semiconductors, Linz, Austria, 1994.

[3] Z. Yang, Z. Hu, Y. Lansari, S. Hwang, J.W. Cook, Jr. and J.F. Schetzina, Phys. Rev. B 49 (1994) 8096.

[4] C.R. Becker, L. He, M.M. Regnet, M.M. Kraus, Y.S. Wu, G. Landwehr, X.F. Zhang and H. Zhang, J. Appl. Phys. 74 (1993) 2486.

[5] E. Bangert, P. Boege, V. Latussek and G. Landwehr, Semicond. Sci. Technol. 8 (1993) S99.

[6] Y. Kim, A. Ourmazd, M. Bode and R.D. Feldman, Phys. Rev. Lett. 63 (1989) 636.

[7] A. Simon, D. Bertho, D. Boiron and C. Jouanin, Phys. Rev. B 42 (1990) 5221.

[8] F. Goschenhofer, V. Latussek, S. Einfeldt, M.O. Möller, C.R. Becker and G. Landwehr, in: Proc. Int. Conf. on Narrow Gap Semiconductors, Santa Fe, USA, 1994, in press.

[9] A. Tardot, A. Hamoudi, N. Magnea, P. Gentile and J.L. Pautrat, Semicond. Sci. Technol. 8 (1993) S277.

[10] M.H. Weiler, in: Semiconductors and Semimetals, Vol. 16, Defects, (HgCd)Se, (HgCd)Te, Eds. R.K. Willardson and A.C. Beer (Academic Press, New York, 1981) p. 119.

[11] J.P. Laurenti, J. Camassel, A. Bouhemadou, B. Toulouse, R. Legros and A. Lussau, J. Appl. Phys. 67 (1990) 6454.

[12] R.S. Sporken, S. Sivananthan, J.P. Faurie, D.H. Ehlers, J. Fraxedos, L. Ley, J.J. Pireaux and R. Caudano, J. Vac. Sci. Technol. A 7 (1989) 427.

Magneto-optics and valence-band discontinuity in a HgTe-Hg$_{1-x}$Cd$_x$Te superlattice

M. von Truchseß, V. Latussek, F. Goschenhofer, C. R. Becker, G. Landwehr, and E. Batke

Physikalisches Institut der Universität Würzburg, Am Hubland, D-97074 Würzburg, Federal Republic of Germany

R. Sizmann and P. Helgesen

Norwegian Defence Research Establishment, Division Electronics, P.O. Box 25, N-2007 Kjeller, Norway

(Received 27 December 1994)

We report here on infrared magneto-optical studies of band gaps and electron cyclotron resonances of a narrow-gap HgTe-Hg$_{1-x}$Cd$_x$Te superlattice. The experimental electron effective mass at the conduction-band edge and four different interband transition energies are compared to the prediction of a 8×8 k·p band-structure calculation in order to determine the valence-band discontinuity between HgTe and CdTe. At liquid-helium temperatures an excellent description of the experiment is obtained with a band offset of 550 meV. Agreement between experiment and theory is not satisfactory with the valence-band offset of 350 meV as deduced from x-ray and ultraviolet photoelectron spectroscopy.

Type-III superlattices composed of the semimetal HgTe and the wide-gap semiconductor CdTe have the unique feature that their band gap can be continuously changed from the semimetallic to the semiconducting regime by varying the thicknesses of the wells and the barriers.[1] Another important quantity governing the transition from semimetallic to semiconducting behavior is the valence-band discontinuity Λ. There is still a continuing controversy regarding the size of Λ. In early magneto-optical experiments on semiconducting samples, both a small offset of 40 meV and a roughly 10 times larger value were deduced.[2,3] In contrast, techniques such as x-ray and ultraviolet photoelectron spectroscopy provide consistent valence-band offsets somewhere around 350 meV.[4-6] Johnson, Hui, and Ehrenreich[7] solved the apparent conflict in favor of the larger offset, demonstrating that with increasing offset, HgTe-CdTe superlattices would undergo a transition from a semiconducting to a semimetallic and then again to a semiconducting regime. However, values for the valence-band discontinuity up to 800 meV have been recently reported for magneto-optical experiments.[8]

In this article, it is our intention to accurately determine the size of the valence-band offset from magneto-optical spectra and to estimate the results of uncertainties in the sample parameters. The advantage of the present investigation compared to previous work is that we have simultaneously investigated interband as well as intraband transitions in a narrow-gap HgTe-Hg$_{1-x}$Cd$_x$Te superlattice and compared all of the results to the predictions of a 8×8 k·p calculation taking into account an improved set of bulk band parameters, influences of strain, and a finite interface width. The experiments have been performed on a specially designed superlattice such that electron cyclotron resonance and up to four different hole-band-to-electron-band transitions can be resolved. We shall demonstrate that the best agreement between experiment and theory is obtained with a valence-band offset of 550 meV between HgTe and CdTe. This value is significantly larger than that reported from x-ray and ultraviolet-photoelectron-spectroscopy experiments.

Our HgTe/Hg$_{0.32}$Cd$_{0.68}$Te superlattice was grown at a temperature of 180 °C on a (100) Cd$_{0.96}$Zn$_{0.04}$Te substrate by molecular-beam epitaxy as described elsewhere.[9] It consists of 110 periods with well and barrier widths of 6.1 and 6.6 nm, respectively. The period and well widths of the superlattice were determined from x-ray diffraction.[10] Uncertainties in well and barrier thicknesses are approximately 0.1 nm. The cadmium content of the barriers was determined from the band gap of an epitaxial layer grown under the same conditions. This value was corroborated by annealing experiments on superlattices as well as from spectroscopic data of transverse-optical-phonon absorption as discussed below. The sample was not intentionally doped but showed n-type behavior.

Frequency-dependent transmission experiments were performed with a rapid-scan Fourier transform spectrometer in the far and mid infrared. A wide spectral range between 20 and 5000 cm^{-1} was covered. The unpolarized radiation was directed by means of waveguide optics to the sample, which was mounted in a helium cryostat with a superconducting solenoid, and cooled by helium exchange gas to a temperature of 5 K. All magnetic-field-dependent investigations were performed in the Faraday geometry. Signal detection was performed at lower frequencies, 20–2000 cm^{-1}, with a Si bolometer, and at higher frequencies, 500–5000 cm^{-1}, with a photoconductive Hg$_{1-x}$Cd$_x$Te detector. The magnetic-field-dependent transmission spectra $T(B)$ were normalized to the transmission spectrum of the spectrometer with or without a substrate at the same magnetic-field strength, or to the transmission spectrum of a sample at zero magnetic-field strength, $T(0)$.

In Fig. 1 is shown the normalized transmission for low frequencies. Please note the logarithmic energy scale that has been chosen to emphasize lower frequency characteristics. In traces 1(a)–1(c), the sample spectra were normalized to the spectrum of a Cd$_{0.96}$Zn$_{0.04}$Te substrate. The two sharp spectral lines at 14.4 and 15.7 meV are due to transverse-optical phonons in the wells and barriers, respectively.[11,12] From the measured phonon frequencies, we were able to confirm that the alloy composition in the barriers is $x \approx 0.68$. The two broad spectral structures in Fig. 1(a), whose lower energy flanks occur at
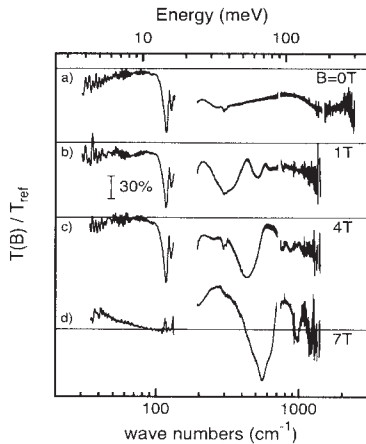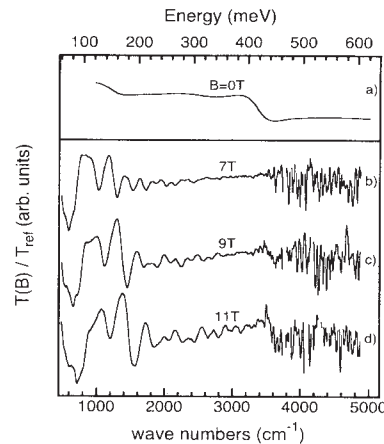
FIG. 1. Normalized transmission of a HgTe (6.1 nm/$Hg_{0.32}Cd_{0.68}Te$ (6.6 nm) superlattice with 110 periods at various magnetic-field strengths B. In traces (a)–(c), the sample spectra $T(B)$ are normalized to the transmission of a $Cd_{0.96}Zn_{0.04}Te$ substrate and in (d) to the $T(0)$ spectrum. Horizontal lines represent the $T(B)/T_{ref}=1$ baselines.

FIG. 2. Normalized transmission of a HgTe (6.1 nm)/$Hg_{0.32}Cd_{0.68}Te$ (6.6 nm) superlattice with 110 periods at various magnetic-field strengths B. In trace (a) the sample spectrum at $B=0$ is normalized to the spectrum obtained without sample, and in (b)–(d) the $T(B)/T(0)$ ratios are shown.

approximately 25 and 130 meV, are due to interband transitions between hole and electron bands in the superlattice. It will be established later that these are transitions from heavy-hole- ($H1$) and light-hole- ($L1$) like ground states to the lowest conduction band ($E1$).

At the finite magnetic-field strengths shown in Figs. 1(b) and 1(c), transitions between the Landau ladders of electronlike and holelike bands are observed. The strong absorption lines above the reststrahlen region (18–23 meV) of the substrate in 1(b) and 1(c) reflect transitions between Landau levels belonging to the lowest hole band ($H1$) and the first conduction band ($E1$). The strongest electric dipole transitions between hole and electron Landau levels for radiation with wave vector parallel to the growth direction, are expected to occur for $\Delta i =0$ and $\Delta N = \pm 1$, where i and N indicate subband and Landau-level quantum numbers, respectively. This can be ascertained from the selection rules, which require Δi to be an even integer and $\Delta N = \pm 1$ for hole to electron subband transitions in a single quantum well. As is apparent from Figs. 1(b) and 1(c), the oscillator strength decreases with increasing N. The transmission ratio $T(7 \text{ T})/T(0)$ in Fig. 1(d) provides a better signal-to-noise ratio than the $T(B)/T_{subs}(B)$ ratios shown in Figs. 1(b) and 1(c). In addition, phonon contributions are largely suppressed. However the line shapes are influenced by the magnetic field and one has to be careful in analyzing resonance half-widths and excitation strengths. Hence, $T(B)/T_{subs}(B)$ ratios provide easier access to phonon absorption and their half-widths, and excitation strengths of interband Landau-level transitions, whereas $T(B)/T(0)$ ratios are very useful for the determination of resonance positions.

In the upper trace of Fig. 2, which is for higher frequencies, the sample transmission $T(0)$ has been normal-

ized to the transmission without a sample. Note that a third interband transition near 420 meV is clearly resolved, which could be identified as a transition between the first excited hole and electron levels, $H2$ and $E2$, respectively. Traces 2(b)–2(d) are $T(B)/T(0)$ ratios at different magnetic-field strengths. The pronounced minima at energies below 400 meV are due to Landau-level transitions from the $H1$ and $L1$ subbands to the $E1$ subband. The weaker minima at higher energies are caused by $H2$-$E2$ Landau-level transitions.

In the process of determining the intrinsic band gaps from spectra at zero magnetic-field strength, one has to be careful. In special cases the onset of the absorption could occur at energies below the experimentally accessible region or could even be hidden by phonon-absorption bands of the superlattice substrate material. In the case of n-type doping, the small electron effective mass could lead to relatively large Fermi energies and shift the absorption edge to higher energies due to the Burstein-Moss shift.[13,14] Contrarily, band-tail states[15] and impurity-band formation[16] can shift the onset to lower energies compared to the intrinsic gap. A further complication can arise from optical interference effects in thick superlattices that can impose Fabry-Pérot–type resonances on the normalized spectra. Many of the above-mentioned problems can be avoided or minimized by comparing magnetic-field-dependent spectra $T(B)$ to $T(0)$. Applying this technique, the absorption edges can be determined by extrapolating hole to electron Landau-level transition energies to the $B=0$ limit. Unlike the case in the bulk, where all interband transition energies merge at the bulk band-gap energy for zero magnetic field, in superlattices they merge at different energy gaps, which correspond to the hole to electron subband separations.

The positions of the transmission minima in $T(B)/T(0)$ are plotted versus the magnetic-field strength
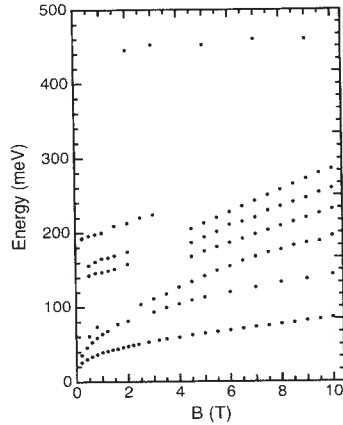
FIG. 3. Hole to electron Landau-level interband transition energies vs magnetic-field strength. For clarity not all measured values are shown.
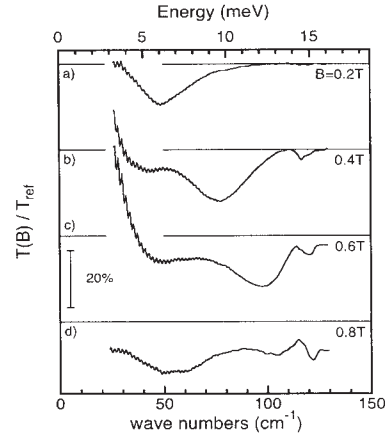

FIG. 4. Experimental electron cyclotron resonances at different magnetic-field strengths. Traces (a)–(c) are normalized to $T(0)$, and trace (d) to $T(8\ \mathrm{T})$. Horizontal lines indicate the $T(B)/T_{\mathrm{ref}} = 1$ base lines.

in Fig. 3. Only the positions of the most prominent Landau-level interband transition have been plotted, and line-shape fine structures were not considered. For example, in Fig. 1 the half-width of the lowest $H1$-$E1$ Landau-level transition is significantly larger than the half-width of the higher ones. This line splits with increasing magnetic-field strength, exhibiting weak shoulders on both sides of a dominating resonance. Here we are probably confronted with overlapping hole to electron transitions with nearly the same energy or with the influence of inhomogeneity. An assignment of individual Landau-level interband transitions is beyond the scope of this article, which is restricted to the discussion of properties at zero magnetic-field strength. The curvature of the interband-transition energies with magnetic-field strength is believed to result largely from the dependence of the electron Landau levels on magnetic-field strength, since hole bands generally exhibit a weaker dispersion in a magnetic field due to their heavier masses.[17] Extrapolating the resonance positions to the limit of zero magnetic-field strength, we have obtained band gaps of 22 ± 3, 138 ± 5, and 440 ± 10 meV. At small magnetic-field strengths, some data points extrapolate to an energy of 192 ± 5 meV. The associated spectral structures in $T(B)/T(0)$ are, however, very weak.

In Fig. 4 experimental electron cyclotron resonances at small magnetic-field strengths are shown. The spectra in Figs. 4(a)–4(c) were normalized to the corresponding spectra at zero magnetic field, and the 4(d) spectrum was normalized to $T(8\ \mathrm{T})$. A resonance at approximately 6 meV for $B = 0.2$ T is shifted gradually to higher energies with increasing magnetic-field strength. In the frequency region of the optical phonons in the wells, the line shape is influenced, which could either be of optical origin or due to polaron coupling. We attribute this resonance to a transition from the ground level to the first excited Landau level in the $E1$ conduction band. The increase in the normalized transmission with decreasing energy, ap-

parent in Figs. 4(b) and 4(c), is due to the Drude absorption of free electrons at $B = 0$. The integrated absorption strength of the cyclotron resonance corresponds to an electron concentration of about 10^{11} cm^{-2}. The electron density is sufficiently low that one is in the magnetic quantum limit even if we assume that the electrons are distributed only in a small part of the superlattice. The origin of a second resonance appearing at $B = 0.8$ T with an energy of about 6 meV is not yet clear. It could possibly be the result of a higher electron Landau-level transition or a hole cyclotron resonance.

The cyclotron mass, $m_c = eB/\omega_c$, has a pronounced magnetic-field dependence as a result of strong band-coupling phenomena in the superlattice. To obtain the band-edge mass, one can extrapolate the experimental values to the $B = 0$ limit. In systems with weak nonparabolicity a linear extrapolation is possible,[18] however, here the cyclotron mass shows a significant nonlinear dependence on B. In this case, it is tempting to fit the data to a quadratic polynomial equation. From the fit we have obtained an effective mass at the conduction subband edge of $0.0048\pm0.0008m_e$. We expect that a mass enhancement due to the nonresonant polaron effect is possible but that it would be smaller than our mass uncertainty.

In Fig. 5, the electron and hole band dispersion for the in-plane wave vector $\mathbf{k}_{\parallel}$ and the wave vector $\mathbf{k}_z$, which is perpendicular to the layers, are illustrated for our superlattice structure. The numerical calculation takes into account the full 8×8 Kane Hamiltonian including all second-order terms representing the far-band contributions.[19] In addition, strain is included, which originates from the lattice mismatch between $\mathrm{Hg}_{0.32}\mathrm{Cd}_{0.68}\mathrm{Te}$ and HgTe (Ref. 8) as well as a finite interface width with a graded gap. Interdiffusion during growth is a mechanism that can cause an interface grading in layered structures composed of HgTe and $\mathrm{Hg}_{1-x}\mathrm{Cd}_x\mathrm{Te}$, and one can expect
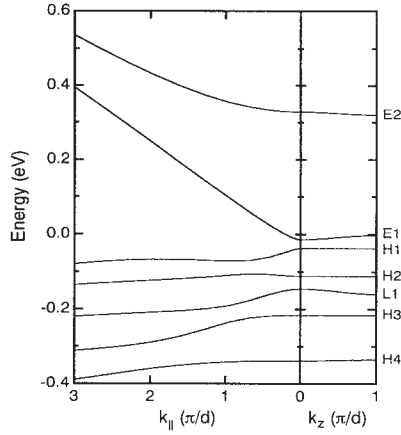
FIG. 5. Calculated superlattice band structure for the $k_\parallel$ and k_z, wave vectors parallel and perpendicular to the growth direction, respectively. En, Hn, and Ln indicate the nth conduction, heavy-hole, and light-hole bands, respectively.

TABLE I. List of sample parameters used in the calculation. ε_∞ is the background dielectric constant of the superlattice. The bulk band parameters of the alloy are assumed to be independent of composition.

$d_{well} = 6.1 \pm 0.1$ nm	$E_p = 18.8$ eV
$d_{barrier} = 6.6 \pm 0.1$ nm	$F = 0$
$x_{barrier} = 0.68 \pm 0.02$	$\gamma_1 = 4.1$, $\gamma_2 = 0.5$, $\gamma_3 = 1.3$
$\varepsilon_\infty = 10.4$	$\Delta_0 = 1.0$ eV

a depth dependence of the gap profile. However, no evidence for a depth dependence could be deduced in recent absorption experiments on a similar superlattice.[20] We consider this as an indication that in addition to interdiffusion also a mechanism inherent to the molecular-beam-epitaxy growth process might have to be considered. In view of this uncertainty we have compared results when linear and nonlinear diffusion profiles are included in our calculations. Best agreement with the experiment is obtained if we assume nonlinear diffusion[21] and an average concentration profile for the superlattice period. The concentration profile is described by a diffusion length of 1.4 ± 0.1 nm.[22] Please note that linear diffusion does not provide a satisfactory description. We like to view the calculated concentration profile as a mod-

TABLE II. Comparison of experimental and calculated subband separations and the masses at $E1$ and $H1$ band edges. $m_{E1,\parallel}$ and $m_{H1,\parallel}$ are the electron and hole masses for motion parallel to the layers, respectively. As usual, positive and negative mass values indicate positive and negative curvatures of the bands. $|m_{E1,\perp}/m_{E1,\parallel}|$ is the electron mass ratio at the $E1$ band edge for parallel and perpendicular motion. Due to the very weak hole dispersion in superlattice direction, the equivalent ratio for holes is nearly infinite. In the first row, experimental values are given. Best agreement with experiment is obtained with a valence-band offset of 550 meV between HgTe and CdTe if strain and graded interfaces by nonlinear interdiffusion are included. In rows 3-5, we show results if strain and/or interdiffusion are neglected. In rows 6-11, we demonstrate the sensitivity to changes in the valence-band discontinuity between HgTe and CdTe. Negative $H1$-$E1$ energies indicate a semimetallic or in the case of $\Lambda = 850$ meV an inverted semiconducting superlattice.

	$H1$-$E1$ (meV)	$L1$-$E1$ (meV)	$H3$-$E1$ (meV)	$H2$-$E2$ (meV)	$\dfrac{m_{E1,\parallel}}{m_e}$	$\dfrac{m_{H1,\parallel}}{m_e}$	$\left\|\dfrac{m_{E1,\perp}}{m_{E1,\parallel}}\right\|$
Experiment	22±3	138±5	192±5	440±10	0.004 80		
$\Lambda = 550$ meV	23.6	131.5	201.5	432.6	0.004 83	−0.005 87	16.2
$\Lambda = 550$ meV[a]	22.8	133.1	201.2	430.9	0.004 70	−0.005 67	16.2
$\Lambda = 550$ meV[b]	−8.1	106.2	164.4	390.7	−0.002 38	0.002 16	29.3
$\Lambda = 550$ meV[c]	−9.2	108.0	163.8	388.6	−0.002 66	0.002 40	25.6
$\Lambda = 250$ meV	69.1	120.0	196.0	445.3	0.012 40	−0.020 7	4.2
$\Lambda = 350$ meV	53.9	125.5	205.6	443.4	0.009 96	−0.015 1	6.2
$\Lambda = 450$ meV	38.7	129.2	205.5	438.9	0.007 47	−0.010 2	9.4
$\Lambda = 650$ meV	8.5	132.9	195.4	424.9	0.001 98	−0.002 14	42.4
$\Lambda = 750$ meV	−6.6	133.5	187.9	415.6	−0.001 75	0.001 64	50.2
$\Lambda = 850$ meV	−21.8	133.4	179.4	404.3	−0.006 00	0.004 83	14.9
$\Lambda = 350$ meV[c]	25.1	101.5	174	401.6	0.005 75	−0.007 41	9.1

[a]Without strain.
[b]Without interdiffusion.
[c]Without strain and interdiffusion.

el profile in order to describe the experiment, whether its origin is due to the diffusion mechanism is not clear. The boundary conditions including interface grading are handled as described in Ref. 22. Our calculation is based on an improved set of bulk band parameters, which are listed in Table I. A further parameter is the composition and temperature-dependent Γ_6-Γ_8 energy gap in the bulk, which was taken from Ref. 23. Even though our bulk band parameters deviate from the ones given by Weiler,[24] they reproduce essentially the same bulk band structure. The valence-band offset between HgTe and $Hg_{1-x}Cd_xTe$ was assumed to depend linearly on the composition and is treated as a fit parameter. Best agreement with the experiment was obtained with a valence-band offset between HgTe and CdTe of 550 meV as shown in Table II. According to our calculation, the experimentally determined gap at 22 meV corresponds to the $H1$-$E1$ transition. The gap at 138 meV is related to the $L1$-$E1$ transition, the gap at 192 meV to the $H3$-$E1$ transition and the gap at 440 meV to the $H2$-$E2$ transition. Our calculation is also in good agreement with the electron band-edge mass for motion parallel to the layers as determined from cyclotron resonance. If we assume that the electron concentration is evenly distributed in the superlattice, we calculate a Fermi energy of roughly 2 meV. This establishes the fact that the Burstein-Moss[13,14] shift of the hole to $E1$ transitions is small, on the order of the experimental gap uncertainty.

We have also evaluated the optical dipole matrix elements as a function of $k_\parallel$ and k_z for all interband transitions in order to calculate the transmission of our sample. In Figs. 6 and 7, we show the matrix elements and the normalized transmission, $T(0)/T_{subs}$. The calculated transmission curve takes full account of the layer sequence in our superlattice. The calculation predicts relative strengths of $H1$-$E1$:$L1$-$E1$:$H3$-$E1$:$H2$-$E2 = 10:7:2:7$ for $k_\parallel = k_z = 0$. The calculated transmission is in excellent agreement with the experimentally derived curve and
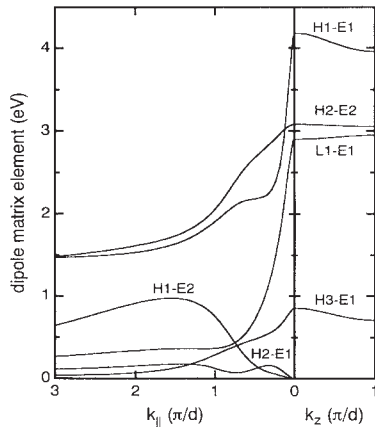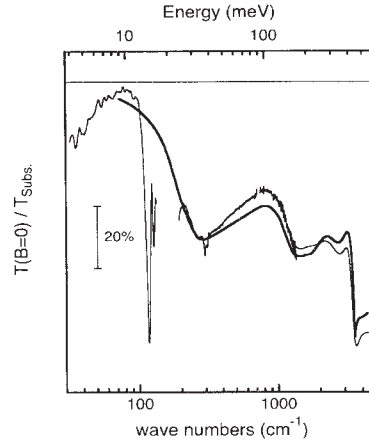
FIG. 7. Experimental and calculated (bold line) normalized transmission $T(0)/T_{subs}$ for a HgTe (6.1 nm)/$Hg_{0.32}Cd_{0.68}Te$ (6.6 nm) superlattice vs energy.

supports our interpretation.

Our valence-band offset is significantly larger than the ones determined from x-ray and ultraviolet photoelectron spectroscopy. An offset of 550 meV at liquid-helium temperatures was recently deduced from magneto-optical spectra.[25] However, this value applies to the valence-band discontinuity between HgTe and $Hg_{0.15}Cd_{0.85}Te$. A linear scaling with composition gives an offset of about 650 meV between HgTe and CdTe. An illustration of the sensitivity to variations in the superlattice parameters is summarized in Table II, which lists subband separations and band-edge masses for parallel and perpendicular motion in the electron $(E1)$ and hole $(H1)$ subbands. Strain has a minor influence on the calculation, band separations are shifted on the order of a few meV, whereas interdiffusion has a strong influence. If one neglects interdiffusion and $\Lambda = 550$ meV, then the investigated superlattice is predicted to be semimetallic. Calculated band separations and band-edge masses for a band offset of 350 meV including strain and interdiffusion, do not agree with experiment. In contrast, a valence-band offset of 850 meV seems to explain the experiment well, i.e., the band-edge masses and the absolute values of the band separations are in reasonable agreement. For this offset an inverted semiconducting superlattice is predicted. However, we can exclude the possibility that our sample is of the inverted type from temperature-dependent measurements of the $H1$-$E1$ band separation, which show that this separation increases almost linearly with temperature. Our superlattice is of the normal semiconducting type at all temperatures. The best alternative description of the experimental data is obtained with $\Lambda = 350$ meV if interdiffusion is neglected. However, the agreement with experiment is far from satisfactory.

We have studied four hole to electron interband optical transitions and electron cyclotron resonance in a $HgTe/Hg_{0.32}Cd_{0.68}Te$ superlattice in order to determine

FIG. 6. Various interband dipole matrix elements for light polarized perpendicular to the superlattice growth direction vs $k_\parallel$ and k_z wave vectors. d is the superlattice period.

112

the size of the valence-band discontinuity between HgTe and CdTe at liquid-helium temperatures. Best agreement between theory and experiment is obtained with a surprisingly large offset of 550 meV. The uncertainty is of the order of 50 meV due to uncertainties in the sample parameters. Taking into account all uncertainties in the sample parameters, the experiment cannot be explained satisfactorily with an offset of 350 meV as measured by

x-ray and ultraviolet photoelectron spectroscopy. Further work is needed to clarify the discrepancy between magneto-optical and photoelectron experiments.

[1]J. N. Schulman and T. C. McGill, Appl. Phys. Lett. **34**, 663 (1979).

[2]Y. Guldner, G. Bastard, J. P. Vieren, M. Voos, J. P. Faurie, and A. Million, Phys. Rev. Lett. **51**, 907 (1983).

[3]J. N. Schulman, O. K. Wu, E. A. Patten, J. W. Han, Y. Lansari, L. S. Kim, J. W. Cook, and J. F. Schetzina, Appl. Phys. Lett. **53**, 2420 (1988).

[4]S. P. Kowalczyk, J. T. Cheung, E. A. Kraut, and R. W. Grant, Phys. Rev. Lett. **56**, 1605 (1986).

[5]R. S. Sporken, S. Sivananthan, J. P. Faurie, D. H. Ehlers, J. Fraxedos, L. Ley, J. J. Pireaux, and R. Caudano, J. Vac. Sci. Technol. A **7**, 427 (1989).

[6]C. K. Shih and W. E. Spicer, Phys. Rev. Lett. **58**, 2594 (1987).

[7]N. F. Johnson, D. M. Hui, and H. Ehrenreich, Phys. Rev. Lett. **61**, 1993 (1988).

[8]K. H. Yoo, R. L. Aggarwal, L. R. Ram-Mohan, and O. K. Wu, J. Vac. Sci. Technol. A **8**, 1194 (1990).

[9]C. R. Becker, L. He, M. M. Regnet, M. M. Kraus, Y. S. Wu, G. Landwehr, X. F. Zhang, and H. Zhang, J. Appl. Phys. **74**, 2486 (1993).

[10]M. O. Möller, R. N. Bicknell-Tassius, and G. Landwehr, J. Appl. Phys. **72**, 5109 (1992).

[11]D. Rajavel and S. Perkowitz, J. Electron. Mater. **17**, 25 (1988).

[12]S. P. Kozyrev, L. K. Vodopyanov, and R. Triboulet, Solid State Commun. **45**, 383 (1983).

[13]E. Burstein, Phys. Rev. **93**, 632 (1954).

[14]T. S. Moss, Proc. Phys. Soc. London, Sect. B **76**, 775 (1954).

[15]K. H. Herrmann, M. Happ, H. Kissel, K.-P. Möllmann, J. W. Tomm, C. R. Becker, M. M. Kraus, S. Yuan, and G. Landwehr, J. Appl. Phys. **73**, 3486 (1993).

[16]F. Stern and J. R. Dixon, J. Appl. Phys. **30**, 268 (1959).

[17]J. R. Meyer, R. J. Wagner, F. J. Bartoli, C. A. Hoffman, M. Dobrowolska, T. Wojtowicz, J. K. Furdyna, and L. R. Ram-Mohan, Phys. Rev. B **42**, 9050 (1990).

[18]E. Batke, K. Bollweg, U. Merkt, C. M. Hu, K. Köhler, and P. Ganser, Phys. Rev. B **48**, 8761 (1993).

[19]E. Bangert, P. Boege, V. Latussek, and G. Landwehr, Semicond. Sci. Technol. **8**, S99 (1993).

[20]F. Goschenhofer, V. Latussek, S. Einfeldt, M. O. Möller, C. R. Becker, and G. Landwehr (unpublished).

[21]A. Tardot, A. Hamoudi, N. Magnea, P. Gentile, and J. L. Pautrat, Semicond. Sci. Technol. **8**, S277 (1993).

[22]A. Simon, D. Bertho, D. Boiron, and C. Jouanin, Phys. Rev. B **42**, 5221 (1990).

[23]J. P. Laurenti, J. Camassel, A. Bouhemadou, B. Toulouse, R. Legros, and A. Lussau, J. Appl. Phys. **67**, 6454 (1990).

[24]M. H. Weiler, in *Defects, (HgCd)Se,(HgCd)Te*, edited by R. K. Willardson and A. C. Beer, Semiconductors and Semimetals Vol. 16 (Academic, New York, 1981), p. 119.

[25]Z. Yang, Z. Hu, Y. Lansari, S. Hwang, J. W. Cook, Jr., and J. F. Schetzina, Phys. Rev. B **49**, 8096 (1994).

Landau-split and spin-split cyclotron resonance of two-dimensional electron systems in HgTe quantum wells

M. von Truchsess *, V. Latussek, C.R. Becker, E. Batke

Physikalisches Institut der Universität Würzburg, Am Hubland, D-97074 Würzburg, Germany

Abstract

Cyclotron resonances of high-mobility electrons in inverted semiconducting type HgTe quantum wells were investigated at liquid helium temperatures by far-infrared Fourier transform spectroscopy. Due to the energy dependence of the electron effective mass and the high electron mobilities in excess of $70\,000$ cm^2 V^{-1} s^{-1}, the spin-splitting and the Landau-splitting of the cyclotron resonance could be resolved. At the conduction subband edge an effective mass $m_0^* \approx 0.016$ m_e and a Landé g-factor $|g_0| \approx 20$ was obtained. The experiment is in good agreement with predictions based on the single-particle approximation.

1. Introduction

In semiconductors the electron–phonon interaction and band coupling phenomena result in the energy dependence of the electron effective mass. Since the separations of the Landau-levels are dependent on the Landau index N and the spin quantum number s, the Landau-splitting and the spin-splitting of the cyclotron resonance (CR), where one induces electric dipole transitions $(N, s) \to (N+1, s)$, can be resolved, provided that the electron mobility is sufficiently high. This is well known from experiments on non-degenerate electron systems in bulk semiconductors [1–3]. The expression Landau-splitting addresses the splitting of the CR due to transitions originating from two different Landau-levels, whereas the expression spin-splitting is restricted to the transitions originating from the same Landau level for electrons with different spin orientations.

For non-degenerate bulk electrons, where influences of electron–electron interactions on the CR can be neglected, the experiments are in good agreement with predictions based on the single-particle approximation. However, for degenerate quasi two-dimensional electron inversion layers in semiconductor heterostructures, electron–electron interactions can couple the CR transitions, such that the positions and intensities can no longer be estimated in the single-particle approximation [4–6]. To our knowledge CR of electron inversion layers in quantum wells based on $Hg_{1-x}Cd_xTe$ have not yet been studied. We report here the first observation of the CR Landau- and spin-splitting for a multiple HgTe quantum well sample. At sufficiently high magnetic field strengths, the experiment can be analyzed in the framework of the single-particle approximation and allows one to determine the effective mass and the Landé g-factor at the conduction subband edge.

* Corresponding author. Fax: +49 931 888 5143; E-mail: truchs@wpfx33.physik.uni-wuerzburg.de.

2. Sample growth and experimental details

Our multiple quantum well sample was grown at a temperature of 180°C on a (100) CdTe substrate by molecular beam epitaxy (MBE) [7]. The layer sequence is as follows: 20 nm CdTe buffer and 3 periods of (9.5 ± 0.5 nm HgTe, 25 ± 1 nm $Hg_{0.3}Cd_{0.7}Te$). Although the sample was not intentionally doped it showed n type behaviour with electron mobilities on the order of 70 000 cm^2 V^{-1} s^{-1}.

Frequency dependent transmission experiments in Faraday geometry at 5 K were performed with a rapid-scan Fourier transform spectrometer in the far-infrared covering a spectral range between 20 and 500 cm^{-1}. The unpolarized radiation was directed by means of wave guide optics to the sample which was mounted in a helium cryostat with a superconducting solenoid. The signal was detected with a Si-bolometer. To correct for the spectral characteristic of the measurement system, we normalized all transmission spectra $T(B)$ to the transmission spectrum at zero magnetic field strength, $T(0)$ [8].

3. Results and discussions

In Fig. 1 we show experimental electron cyclotron resonances for various magnetic field strengths. The frequency regime between about 140 and 200 cm^{-1} is not accessible in transmission, since the transmission is blocked due to the strong absorption in the reststrahlen regimes of the substrate and the buffer layer. At $B = 1.3$ T we observe two well resolved resonances with the stronger one at lower frequencies. From the integrated strength of the resonances we obtain electron densities of about 5.2×10^{11} and 2.4×10^{11} cm^{-2}. Since both resonances shift nearly linearly with magnetic field strength with no change in the relative intensities, we conclude that they are due to cyclotron resonances from wells with different charge densities. Presumably due to an electron transfer from localized states in the CdTe buffer layer an electric field is formed across the interface that shifts the subband levels of adjacent wells with respect to one other. Thus, the total electron density which is given by $N_s = N_{s1} + N_{s2} + N_{s3} \approx 7.6 \times 10^{11}$
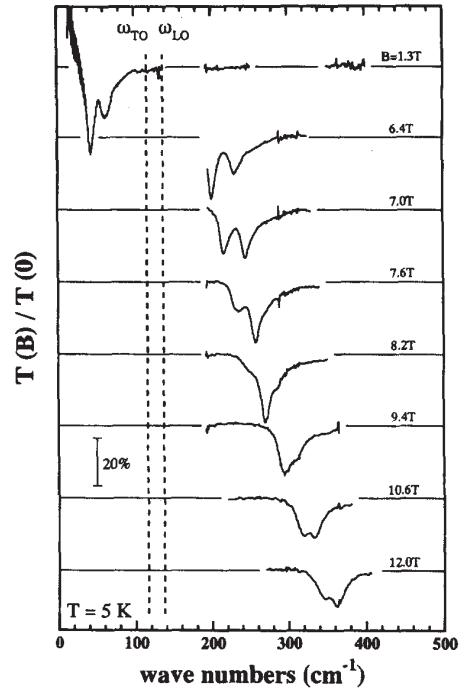
Fig. 1. Normalized transmission $T(B)/T(0)$ versus energy for a multiple quantum well structure with three HgTe wells with a width of 9.5 nm for various magnetic field strengths B. The horizontal lines denote the $T(B)/T(0) = 1$ base lines. The vertical dashed lines indicate the longitudinal (LO) and transverse (TO) phonon frequencies of bulk HgTe.

cm^{-2}, is distributed according to the ratio $N_{s1} : N_{s2} : N_{s3} \approx 4.5 : 1 : 1$. The different resonance positions are a consequence of the energy dependence of the electron effective mass, since CR at small magnetic field strengths is determined by the mass value at the Fermi-energy. By increasing B we shift the resonances through the opaque reststrahlen regime of the substrate. The Landau- and spin-splitting of the CR is clearly resolved at magnetic fields higher than about 6.4 T. In the regime from 6.4 to 8.2 T we observe the Landau-splitting of the $(0, +1) \rightarrow (1, +1)$ and $(1, -1) \rightarrow (2, -1)$ transitions, and at higher fields the spin-splitting of the $(0, \pm 1) \rightarrow (1, \pm 1)$ transitions.

Fig. 2 shows cyclotron resonance positions ω_{exp} interpreted in terms of a cyclotron mass $m_{N,s} = eB/\omega_{exp}$. The full and open circles reflect, respec-
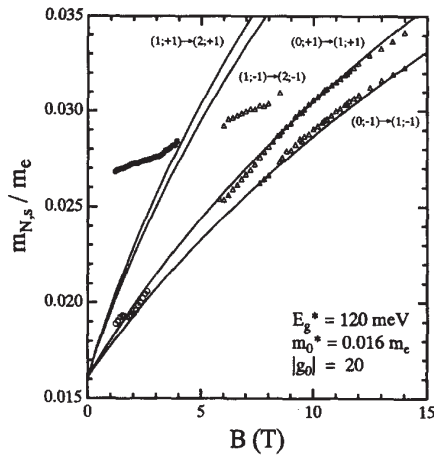
Fig. 2. Cyclotron resonance positions of electrons in a multiple quantum well structure with three HgTe wells with a width of 9.5 nm interpreted in terms of a cyclotron mass versus magnetic field strength. The solid lines show Landau-level separations calculated according to Eq. (1).

calculation of the energy dependence of the cyclotron mass to band coupling phenomena and the non-resonant polaron coupling, since there is no evidence for an influence of the resonant polaron effect. With $E_g^* = 120$ meV, $m_0^* = 0.016$ m_e and $|g_0| = 20$ we obtain an excellent description of the mass values for the $(0, \pm 1) \to (1, \pm 1)$ transitions. Note that at low fields we also reproduce the mass values of the weaker resonance. Above about 2 T the cyclotron mass for this resonance increases nearly linearly with magnetic field strength. This is expected if the magnetic quantum limit $\nu = 2\pi l^2 N_s \leqslant 2$, which is dominated by the magnetic length $l = (\hbar/eB)^{1/2}$, is established at this field. This is a strong indication that the corresponding charge density of about 2.4×10^{11} cm^{-2}, estimated from the integrated strength of the resonance, is distributed equally in two wells. The quantum limes $\nu = 2$ for the higher charge density, resulting in the spin-splitting of the $0 \to 1$ transition, is reached for $B > 10.6$ T, whereas for $B = 7.2$ T we calculate $\nu = 3$. From

tively, positions for the two resonances at magnetic fields $B \leq 4$ T, where a splitting is not observed. Triangles indicate resonance positions for magnetic field strengths $B \geq 6.4$ T. Analyzing the mass values requires, in principle, a multiple band $k \cdot p$ calculation including the magnetic field from first principles. This is not what we attempt here. To keep the calculation simple, we essentially parametrize the resonance positions in the framework of the two-band model with an effective energy gap E_g^*. The cyclotron masses are calculated from $m_{N,s} = \hbar eB/(E_{N+1,s} - E_{N,s})$. The Landau-level energies $E_{N,s}$ are determined from the equation:

$$
E_{N,s} = \left[\left(\tfrac{1}{2} E_g^* \right)^2 + E_g^* \left(\frac{\hbar eB}{m_0} \left(N + \tfrac{1}{2} \right) \right. \right.
$$
$$
\left. \left. + \tfrac{1}{2} s g_0 \mu_B B \right) \right]^{1/2} - \tfrac{1}{2} E_g^* , \tag{1}
$$

where m_0 and g_0 are the mass and Landé g-factor at the subband edge, respectively. Influences of the non-resonant polaron effect and the confinement we include by replacing the mass m_0 in Eq. (1) by an effective mass m_0^*. It is justified to restrict the

Fig. 3. Subband dispersions of a 9.5 nm wide HgTe well sandwiched between barriers of $Hg_{0.3}Cd_{0.7}Te$ versus the in plane wave vector $k_\parallel$ in units of π/d_{well}, where d_{well} is the well width. The dashed line represents the in plane dispersion calculated with the two-band model.

116

this we conclude, that in this magnetic field regime only the $(1, -1) \rightarrow (2, -1)$ and the $(0, +1) \rightarrow (1, +1)$ transitions can be observed.

The experimental mass values for the higher transitions $(1, -1) \rightarrow (2, -1)$ appear smaller than the calculated ones. This is not believed to reflect an inadequacy in our approach for calculating the Landau-level energies in the effective two-band model. The transition frequencies might depend on the broadening of the density of states, influences of disorder and/or the screening behaviour of the electron system or the scattering mechanisms that are involved [9], all of which are not included here. Although our mass values for the higher transitions are not well reproduced, a comparison of the in plane dispersions predicted in the effective two-band model for zero magnetic field strength with the results of a multiple band $k \cdot p$ calculation gives excellent agreement. This we consider to be an indication that our calculation of the Landau-levels in a parametrized two-band model is a good approximation.

Fig. 3 shows the predicted subband dispersions obtained with a 8×8 $k \cdot p$ band structure calculation. Details of the calculation are given in Refs. [10,11]. The quantum well is of the inverted semi-conducting type at 5 K, and the conduction subband is formed by a H1 state. The dotted line shows the predicted H1 in plane dispersion within the framework of the effective two-band model. The in plane dispersion is calculated from Eq. (1) by retaining the effective energy gap as determined at finite B but replacing the expression in brackets by $\hbar^2 k^2 / 2m_0^*$. At the H1 subband edge the eight band model predicts a mass of 0.016 m_e, which is in excellent agreement with the experimental value. At the Fermi-energies, corresponding to densities of 5.2×10^{11} and 1.2×10^{11} cm^{-2} we calculate, respectively, effective masses of 0.024 m_e and 0.019 m_e with the eight band model. Thus, the theoretical masses compare well to the observed cyclotron masses of 0.026 m_e and 0.019 m_e in the limit of low magnetic fields.

4. Conclusion

In summary we studied the influence of band coupling phenomena on the cyclotron resonance of quasi two-dimensional electron systems in HgTe quantum wells. From the spin- and Landau splitting of the CR line shape we determined the mass and the Landé g-factor at the H1 conduction subband edge. The experiment is in satisfactory agreement with predictions based on the single-particle approximation.

Acknowledgements

References

[1] E.S. Koteles and W.R. Datars, Phys. Rev. B 14 (1976) 1571.

[2] G. Lindemann, R. Lassnig, W. Seidenbusch and E. Gornik, Phys. Rev. B 28 (1983) 4693.

[3] E. Batke, K. Bollweg, U. Merkt, C.M. Hu, K. Köhler and P. Ganser, Phys. Rev. B 48 (1993) 8761.

[4] N.R. Cooper and J.T. Chalker, Phys. Rev. Lett. 72 (1994) 2057.

[5] C.M. Hu, E. Batke, K. Köhler and P. Ganser, Phys. Rev. Lett. 75 (1995) 918.

[6] C.M. Hu, E. Batke, K. Köhler and P. Ganser, in: Proc. 11th Int. Conf. on Electronic Properties of Two-Dimensional Systems, Nottingham, 1995.

[7] C.R. Becker, L. He, M.M. Regnet, M.M. Kraus, Y.S. Wu, G. Landwehr, X.F. Zhang and H. Zhang, J. Appl. Phys. 74 (1993) 2486.

[8] E. Batke and D. Heitmann, Infrared Phys. 24 (1984) 189.

[9] T. Ando, A.B. Fowler and F. Stern, Rev. Mod. Phys. 54 (1982) 437.

[10] E. Bangert, P. Boege, V. Latussek and G. Landwehr, Semicond. Sci. Technol. 8 (1993) S99.

[11] M. von Truchsess, V. Latussek, R. Sizmann, P. Helgesen, F. Goschenhofer, C.R. Becker, G. Landwehr and E. Batke, Phys. Rev. B 51 (1995) 17618.

Molecular beam epitaxial growth and optical properties of (001) HgTe/Hg$_{1-x}$Cd$_x$Te superlattices

C. R. Becker, V. Latussek, W. Spahn, F. Goschenhofer, S. Oehling and G. Landwehr

Physikalisches Institut der Universität Würzburg, Am Hubland, 97074 Würzburg, Germany

ABSTRACT

The experimental optical absorption coefficient of HgTe/Hg$_{0.32}$Cd$_{0.68}$Te superlattices with a wide range of well and barrier widths have been compared with theoretical calculations. There is good agreement with experiment if the Cd concentration profile across the as-grown interfaces is assumed to have the shape given by an error function together with an additional Cd concentration of 3 % in the quantum wells. The latter concentration was experimentally confirmed. If diffusion is responsible for this concentration profile then a dependence on depth should be present, however, none was observed. Therefore the Cd concentration profile across the interfaces of an as-grown HgTe/Hg$_{0.32}$Cd$_{0.68}$Te superlattice does not result from interdiffusion of the interfaces during growth. In other words, growth mechanisms do not involve interdiffusion of the interfaces.

Keywords: growth, HgTe/Hg$_{1-x}$Cd$_x$Te, superlattice, optical absorption coefficient, band gap, interband transition, interface, diffusion

I. INTRODUCTION

Schulman and McGill[1] proposed in 1979 that the HgTe/CdTe superlattice would be an useful material for a number of infrared optoelectronic devices. The absorption coefficient α of HgTe/Hg$_{1-x}$Cd$_x$Te superlattices displays step-like features as expected for a two dimensional system.[2] These features correspond to subband transitions which depend on various parameters, among which are the band stucture parameters of the binary constituents of this system (HgTe and CdTe), superlattice period, well and barrier thicknesses, composition of the wells and barriers, valence band offset between HgTe and CdTe (Λ), strain and the concentration profile of the interfaces. If these parameters with the exception of the interface profile are known with sufficient accuracy, then a theoretical determination of the absorption coefficient should result in the concentration profile or at least an approximate width of the interfaces. This could lead to some insight into the growth mechanisms of these interfaces.

As just mentioned, a necessary prerequisite is a knowledge of the above parameters with the required accuracy. In the past some of these parameters have usually been estimated from the growth parameters, e.g well and barrier thicknesses. These parameters have then been adjusted to merely fit the band gap and in some cases to fit the theoretical and experimental absorption coefficient.[2,3] As will be shown below, it is not possible to unambiguously determine the interband transition energies

118

from the absorption coefficient. In this investigation, all of the relevant superlattice parameters have been determined experimentally, with the exception of the concentration profile of the interfaces.

In addition, different values of the valence band offset are found in the literature. In early magneto-optical experiments on semiconducting superlattices, both a small offset of 40 meV and a roughly 10 times larger value were deduced.[4,5] In contrast, x-ray and ultraviolet photoelectron spectroscopy (XPS and UPS) provide a consistent value of approximately 350 meV.[6-8] Johnson, Hui and Ehrenreich[9] solved the apparent controversy between small and large Λ, demonstrating that with increasing Λ, HgTe-CdTe superlattices would change from semiconducting behavior to semimetallic and back to semiconducting behavior due to crossing and uncrossing of the $H1$ and $E1$ subbands. The most widely accepted value has been 350 meV from XPS and UPS measurements, however, values for Λ up to 800 meV have been recently reported for magneto-optical experiments.[10] Moreover, a magneto-optical investigation of the electron effective mass at the conduction band edge together with th energy of all four observed interband transitions by von Truchseß *et al.*[11] resulted in a value of 550 meV. In addition we have conducted a comprehensive investigation of the optical absorption coefficient for a large number of $HgTe/Hg_{1-x}Cd_xTe$ superlattices with a wide range of well and barrier widths.[12] This study, which involved the entire relevant spectral range and thus all observable interband transitions, results in a value of 550 ± 50 meV for Λ.

II. EXPERIMENTAL AND THEORETICAL DETAILS

A. Growth

Epitaxial growth was carried out in a multiple chamber RIBER 2300, molecular beam epitaxial (MBE) system. A surface analysis chamber is connected to the growth chambers via an ultra high vacuum transfer system. One of the growth chambers has been modified to permit the growth of Hg based materials. The vacuum in the growth chamber is better than 6×10^{-10} Torr when no Hg ha recently been admitted. Three MBE cells were employed, two of which were commerical cells and which contained high purity CdTe and Te. The third cell is a self designed stainless steel cell for Hg which can be refilled without breaking the vacuum. The flux of the latter cell is stable to within ± 1.5 and ± 3 % over a period of 2 and 30 hours, respectively.

The $HgTe/Hg_{1-x}Cd_xTe$ superlattices were grown on (001) $Cd_{0.96}Zn_{0.04}Te$ and CdTe substrates as has been described in detail elsewhere.[13,14] The substrates were degreased and some were chemo-mechanically polished for several minutes in a weak solution of bromine in methanol and then rinsed in methanol. Immediately prior to mounting the $5 \times 10 \times 1$ mm^3 substrates on a molybdenum holder, they were rinsed in de-ionized water, briefly dipped in hydrochloric acid and then rinsed in de-ionized water so as to remove all of the original oxide and carbon from the substrate surface.[15,16] The substrates were thermally cleaned at temperatures up to about 320°C while monitoring the substrate surface by reflection high energy electron diffraction (RHEED) as described elsewhere.[17] The substrate temperature was measured with an accuracy of ± 2°C by means of a thermocouple

which was in physical contact with a molybdenum substrate holder. The thermocouple was carefully calibrated at the melting points of indium and tin.

Before the superlattice was grown, a thin CdTe buffer was grown on the (001) $Cd_{0.96}Zn_{0.04}Te$ or CdTe substrate at 270°C until the reflection high electron energy diffraction (RHEED) pattern indicated that the surface was smooth by the presence of short streaks. The thickness of this buffer was between 30 and 1000 Å. This surface was characterized by a (2×1) half order reconstruction in the $[\bar{1}10]$ azimuth. We use the convention of refering to the direction of the incident electrons when refering to reconstruction in a particular azimuth. The superlattice was then grown at 180°C with CdTe, Te and Hg fluxes of 3 to 5×10^{-7}, 6 to 10×10^{-7} and 2.8 to 3.2×10^{-4} Torr, respectively. Here pressure is loosely referred to as flux. This Hg flux is roughly 2.5 times larger than the minimum flux necessary to maintain epitaxial growth of HgTe. Finally, on some of the superlattices a CdTe cap layer with a thickness of about 600 Å was grown at 35°C either directly after growth or in one case after several weeks.

B. X-ray diffraction

The superlattice period as well as the well thickness and hence that of the barrier were determined with the help of a five crystal, high resolution x-ray diffractometer.[13,18] This is done by taking advantage of the large HgTe structure factor compared to that of CdTe for the (002) Bragg reflection. The reasons for a measurable (002) Bragg reflection for the zinc blende structure as opposed to the diamond structure where it is forbidden, were discussed by Möller *et al.*.[18] The rather large (002) Bragg reflection in these superlattices is caused primarily by the HgTe well; the structure factor for the (002) Bragg reflection is much larger for HgTe than for CdTe.[18] This is due to the relatively large size of the Hg atom with its large number of electrons. In fact the structure factor goes to zero for $Hg_{1-x}Cd_xTe$ with an x value of about 0.88. Thus an observable envelope of the superlattice satellites is due to the slit function corresponding to the HgTe layers.

In general, the investigated superlattices are of good quality as indicated by the full width at half maximum of their (004) Bragg reflection, i.e. as low as 22 arcsec, and the large number of satellites.[13,14]

C. Composition of wells and barriers

The composition of the initial barrier material was determined to be 0.68 ± 0.02 by means of transmission and reflection measurements on thick test layers of (001) $Hg_{1-x}Cd_xTe$ grown under identical conditions. Knowing the well and barrier thicknesses we have been able to confirm this value for the composition of the barriers by annealing several superlattices and then measuring the composition of the resulting alloy.[13,14] In addition, this value has been corroborated by a determination of the barrier TO phonon frequency for several superlattices.[11]

In order to determine the composition of the wells, *in situ* XPS measurements were carried out on a superlattice which was terminated with a HgTe layer with a thickness of at least 100 Å. This

thickness was chosen to prevent the escape of photoelectrons from the underlying barrier. A value of 3 % was determined for the quantum well.

D. Optical absorption coefficient

1. Experiment

Optical transmission and reflection measurements were carried out in the middle and near infrared with a Fourier transform spectrometer, IFS88, from Bruker Instruments Inc. A deuterated triglycine sulfate detector was employed rather than a liquid nitrogen cooled detector, e.g. $Hg_{1-x}Cd_xTe$, because of its better linearity. The aperature was kept as small as possible for the same reason, i.e. a diameter of 2 to 3 mm. The absorption coefficient was determined by fitting the experiment. transmission and reflection spectra to a theoretical description of the multi-layer system using a standard matrix procedure.[19] Minimizing the difference between experimental and theoretical values of merely the transmission at a constant index of refraction resulted in the same absorption coefficient with the exception of some residual interference fringes. Therefore, in most cases this procedure was carried out for only the transmission using an appropriate constant refractive index.

Diffusion experiments were carried out on the superlattice structures discussed above in vacuum at the growth temperature, i.e. 180°C. After each diffusion step the absorption coefficient was determined and occasionally x-ray diffraction of the sample was measured.

2. Theory

The electronic band structure was calculated with an envelope function method.[20,21] The bands of both bulk HgTe and CdTe are described by Kane's four-band model (8×8 $\mathbf{k} \cdot \mathbf{p}$) including all second order far-band contributions. The effects of strain due to lattice mismatch were also taken into consideration.[21] The numerical values for the band parameters were deduced from measurements on bulk HgTe and $Hg_{1-x}Cd_xTe$ according to Weiler.[22] The valence band offset between HgTe and CdTe was taken to be 550 meV which we have found to be necessary in order to correctly describe subband transition energies and the absorption coefficient.[11,12] The valence band offset for $Hg_{1-x}Cd_xTe$ was then assumed to vary linearly with x.[8] The initial x value for the barrier and well in conjunction with a concentration profile of the interface was integrated into the theory.[23] The concentration profile, as experimentally determined by means of chemical mapping by Kim *et al.*[24] for a similarly grown superlattice, was employed unless otherwise stated.

III. RESULTS AND DISCUSSION

In order to ascertain the influence of interdiffusion on the concentration profile across the inter-faces both during growth and thereafter, a diffusion experiment was conducted. The experimentally
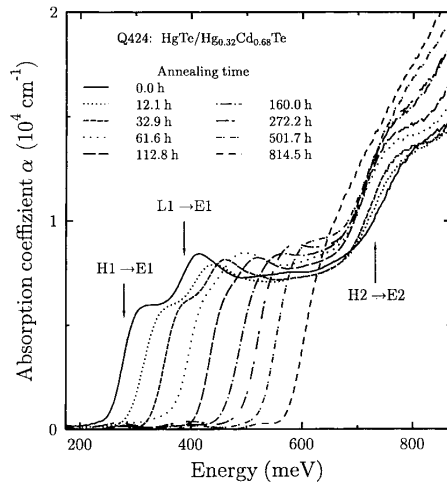
FIG. 1. The experimental optical absorption coefficient at 300 K as a function of energy at various diffusion times for the superlattice Q424. The diffusion temperature was 180°C.
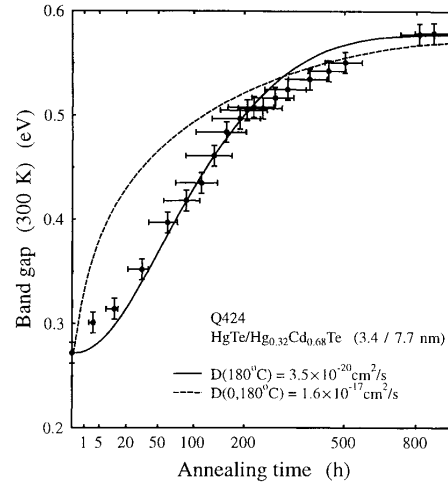
FIG. 2. The shift in the E_o band gap, i.e. $H1 - E1$, of Q424 as a function of the square root of the diffusion time for a diffusion temperature of 180°C. The solid curve corresponds to a linear fit of the data and the dashed curve to a nonlinear fit.

determined optical absorption coefficients before and after some of the annealing steps at 180°C for the superlattice Q424 are shown in Fig.1. Q424 contains 120 periods of quantum wells and barriers which have the widths of 34 and 77 Å, respectively. After the final annealing step, i.e. $\sim$ 800 hours, the superlattice has become an alloy. Theoretically determined energies of various interband transitions before annealing, which are indicated by arrows, correspond to the observed structure in the absorption coefficient. As shown in Fig.2 the observed shift of the band gap can be described either by linear or nonlinear diffusion, however, agreement with experiment is very much better for linear diffusion. A dependence on Cd concentration similar to that of Tardot *et al.*[25] and given by

$$D(x,T) = D(0,T)\exp\left(\frac{-0.50\,x\ \text{eV}}{kT}\right) \quad \text{and} \qquad (1)$$

$$D(0,T) = \exp\left(\frac{-1.51\ \text{eV}}{kT}\right)\ \text{cm}^2/\text{s} \qquad (2)$$

was employed in the nonlinear diffusion calculations. Here x is the Cd concentration of the barrier.

The Cd concentration profile for the as-grown Q424 superlattice for both linear and nonlinear diffusion shown in Fig.3 was used in the theoretical determination of the absorption coefficient. As mentioned above, the former profile is that of Kim *et al.*[24] This profile was sucessfully employed in calculations for a large number of superlattices.[11,12] Both of these profiles yield essentially the same superlattice band structure and consequently the same values for the absorption coefficient. Even
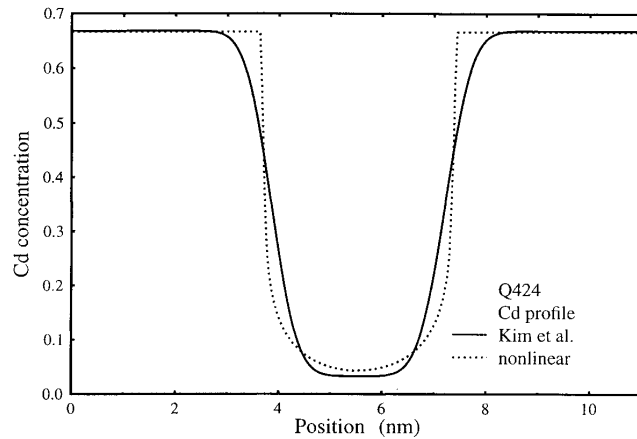
FIG. 3. Two possible Cd concentration profiles for the superlattice Q424 which result in excellent agreement between experimental and theoretical absorption coefficient. The full line is an experimentally determined profile for a similar superlattice according to Ref.24 together with an additional Cd concentration in the quantum well of 3 %. The dotted line is a profile which corresponds to nonlinear diffusion.

though these profiles are quite different, common to both is the $\sim$ 3% Cd in the well. Initially, a nonlinear profile[25] was employed in the theory, because a linear profile with no Cd in the well resulted in much worse agreement with the experimental α. However, the diffusion experiment shown in Fig.2 clearly demonstrated that diffusion in our superlattice with a cap layer is linear. Therefore a profile described by an error function, which is similar to that according to Kim *et al.*,[24] together with 3 % Cd in the well was included in the theory. As mentioned above, this resulted in good agreement for all of the investigated superlattices over a wide range of well and barrier widths.[12]

However, do these superlattices have 3 % in the wells? Surprisingly, according to *in situ* XPS measurements, they do. This was shown to be the case with a series of growth and XPS experiments. ZnTe, HgTe and $HgTe/Hg_{1-x}Cd_xTe$ superlattices were grown on GaAs when the CdTe effusion oven was at the temperature used during growth, $\sim$ 480°C, and when it was at standby temperature. The Cd concentration of the HgTe layers and the HgTe wells is 3 % when the CdTe effusion oven was at $\sim$ 480°C, even though the CdTe shutter was closed. When the oven is at standby temperature the Cd concentration is so small that it is not measurable. Apparently CdTe is evaporated from the CdTe shutter when closed. The necessary CdTe flux requires a shutter temperature of $\sim$ 300°C. This appears to be reasonable but as yet has not been measured.

Another important question is, does the Cd concentration profile across the interface have a depth dependence or, in other words, a dependence on growth time? If growth mechanisms involve interdiffusion of the interfaces then the answer must be yes. According to Feldman *et al.*,[26] the width of the quantum wells in a similar as-grown superlattice is independent of depth. However, the
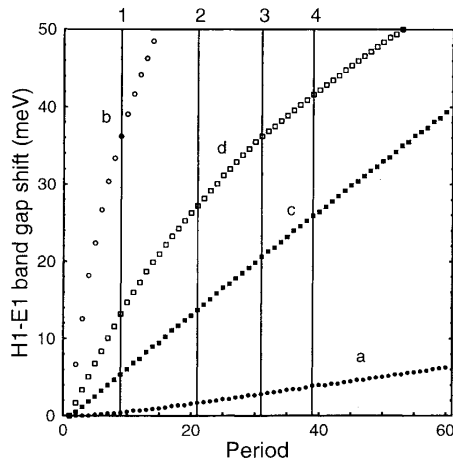
FIG. 4. The shift of the $H1 - E1$ band gap energy at 300 K with distance from the surface of the superlattice Q424 for four different diffusion situations as described in the text, where the symbols denoted by a, b, c and d represent the results for these four cases. The four vertical lines numbered from one to four schematically represent the surface after the corresponding etch.
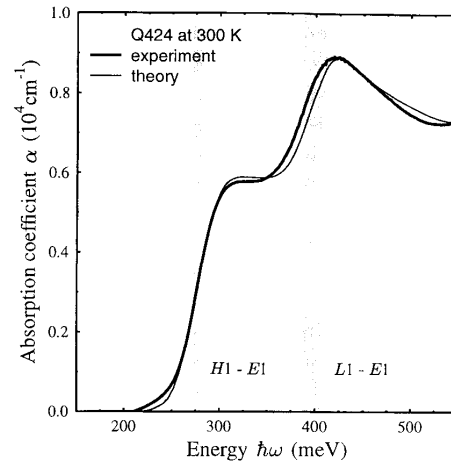
FIG. 5. Comparison of the theoretical and experimental optical absorption coefficient of the superlattice Q424 at 300 K. The shaded vertical bands correspond to the expected widths of the $H1 - E1$ and $L1 - E1$ interband transitions. The left and right sides of the shaded bands correspond to the center and the edge of the superlattice Brillouin zone, respectively.

authors do not mention whether the Cd concentration profile is dependent or independent of depth. Clearly the width of a profile does not depend on its steepness if it has the shape of an error function.

The calculated shift in band gap energy at 300 K corresponding to such a depth dependence for the diffusion of the superlattice Q424 for four different situations is shown in Fig.4. In the first case (a), linear diffusion with $D = 3.5 \times 10^{-20}$ cm^2/s, as determined in the diffusion experiment shown in Figs.1 and 2, was assumed to take place over the 2.5 hour growth time at 180°C. Analogously, for the second case (b), nonlinear diffusion with the resulting $D(0, 180°C) = 1.6 \times 10^{-17}$ cm^2/s was assumed. In the third case (c), linear diffusion with $D = 2 \times 10^{-19}$ cm^2/s was assumed. This value for D results from the assumption that the Cd concentration profile according to Kim *et al.*[24] and shown in Fig.3 is a result of diffusion during superlattice growth according to

$$\bar{d}_t = \frac{2}{3} 2\pi \sqrt{D \cdot t_g} = 18 \text{ Å} \tag{3}$$

where t_g is the growth time of 2.5 hours and the average profile width $\bar{d}_t$ is 18 Å. Analogously, for the fourth case (d), nonlinear diffusion with the resulting $D(0, 180°C) = 3.6 \times 10^{-18}$ cm^2/s was assumed.

Experimentally, the superlattice Q424 was etched in oder to reduce the thickness and then the

124

absorption coefficient of the resulting superlattice was measured. This was repeated four times until only ~ 80 of the original 120 periods were present as is schematically represented by four vertical lines in Fig.4. However within experimental error of about 1 meV, no shift in the band gap energy was observed. For the first case the experimental value is smaller than the prediction and in the other three cases it is negligible. Therefore the experimentally determined Cd concentration profile across the interfaces[24] do not result from interdiffusion of the interfaces during growth.

The experimental and theoretical absorption coefficient for the superlattice Q424 agree very well as is shown in Fig.5. In this calculation is included, the Cd profile according to Kim *et al.*[24] shown in Fig.3 together with a Cd concentration of 3 % in the well and the other parameters discussed above. The slight disagreement in the $L1 - E1$ interband transition energy of ~ 8 meV can be caused by either an incorrect quantum well width, Cd concentration of the well or interface width. The corresponding values are $+0.8$ Å, -1 % or -6 Å, respectively. The shaded vertical bands correspon$^{.}$ to the expected widths of the $H1 - E1$ and $L1 - E1$ interband transitions. The larger experimental band width has been simulated by introducing a Gaussian distribution of the quantum well and barrier widths on the order of $\pm$ one monolayer into the theory.

IV. CONCLUSIONS

The optical absorption coefficient of as-grown $HgTe/Hg_{0.32}Cd_{0.68}Te$ superlattices over a wide range of well and barrier widths is in good agreement with theory if the Cd concentration profile across the interfaces for a similar superlattice[24] is assumed together with an additional Cd concentration of 3 % in the quantum wells. The latter concentration was experimentally confirmed. However no depth dependence for this Cd concentration profile was observed in contrast to predictions based on diffusion constants. Consequently we conclude that the experimentally determined Cd concentration profile across the interfaces of an as-grown $HgTe/Hg_{0.32}Cd_{0.68}Te$ superlattice does not result from interdiffusion of the interfaces during growth. In other words, growth mechanisms do not involv interdiffusion of the interfaces.

V. ACKNOWLEDGEMENTS

[1] J. N. Schulman, and T. C. McGill, *Appl. Phys. Lett.* **34**, 663 (1979).

[2] N. F. Johnson, H. Ehrenreich, P. M. Hui and P. M. Young, *Phys. Rev. B* **41**, 3655 (1990).

[3] Z. Yang, Z. Yu, Y. Lansari, S. Hwang, J. W. Cook, Jr. and J. F. Schetzina, *Phys. Rev. B* **49**, 8096 (1994).

[4] Y. Guldner, G. Bastard, J. P. Vieren, M. Voos, J. P. Faurie and A. Millon, *Phys. Rev. Lett.* **51**, 907 (1983).

[5] J. N. Schulman, O. K. Wu, E. A. Patten, J. W. Han, Y. Lansari, L. S. Kim, J. W. Cook, Jr. and J. F. Schetzina, *Appl. Phys. Lett.* **53**, 2420 (1988).

[6] S. P. Kowalezyk, J. T. Cheung, E. A. Kraut and R. W. Grant, *Phys. Rev. Lett.* **56**, 1605 (1986).

[7] R. S. Sporken, S. Sivananthan, J. P.Faurie, D. H. Ehlers, J. Fraxedos, L. Ley, J. J. Pireaux and R. Caudano, *J. Vac. Sci. Technol. A* **7**, 427 (1989).

[8] C.K. Shih and W.E. Spicer, *Phys. Rev. Lett.* **58**, 2594 (1987).

[9] N. F. Johnson, P. M. Hui and H. Ehrenreich, *Phys. Rev. Lett.* **61**, 1993 (1988).

[10] K. H. Yoo, R. L. Aggarwal, L. R. Ram-Mohan and O. K. Wu, *J. Vac. Sci. Technol. A* **8**, 1194 (1990).

[11] M. von Truchseß, V. Latussek, F. Goschenhofer, C. R. Becker, G. Landwehr, E. Batke, R. Sizmann and P. Helgesen, *Phys. Rev. B* June (1995).

[12] to be published.

[13] C. R. Becker, L. He, M. M. Regnet, M. M. Kraus, Y. S. Wu, G. Landwehr, X. F. Zhang and H. Zhang, *J. Appl. Phys.* **74** 2486 (1993).

[14] C. R. Becker, V. Latussek, H. Heinke, M. M. Regnet, F. Goschenhofer, S. Einfeldt, L. He, E. Bangert, M. M. Kraus and G. Landwehr, *Growth and Characterization of Materials for Infrared Detectors*, Editors R. E. Longshore and J. W. Baars, SPIE Proc. Volume 2012 pp. 138-48 (1993).

[15] Y. S. Wu, C. R. Becker, A.Waag, R. N. Bicknell-Tassius and G. Landwehr, *Appl. Phys. Lett.* **60**, 1878 (1992).

[16] Y. S. Wu, C. R. Becker, A. Waag, R. Schmiedl, S. Einfeldt and G. Landwehr, *J. Appl. Phys.* **73**, 7385 (1993).

[17] Y. S.Wu, C. R.Becker, A.Waag, R. N. Bicknell-Tassius and G. Landwehr, *J. Appl. Phys.* **69**, 268 (1991).

[18] M. Möller, R. N. Bicknell-Tassius and G. Landwehr, *J. Appl. Phys.* **72**, 5108 (1992).

[19] D. Fasold, K. Hehl and S. Jetschke, *phys. stat. sol. (a)* **86**, 125 (1984).

[20] E. Bangert, P. Boege, V. Latussek and G. Landwehr, *Semicond. Sci. Technol.* **8**, S99 (1993).

[21] L. R. Ram-Mohan, K. H. Yoo and R. L. Aggarwal, *Phys. Rev. B* **38**, 6151 (1988).

[22] M. H. Weiler, *Semiconductors and Semimetals*, Vol. 16, Editors R. Willardson and A. C. Beer, Academic Press, New York, pp. 119, 1981.

[23] A. Simon, D. Bertho, D. Boiron and C. Jonanin, *Phys. Rev. B* **42**, 5221 (1990).

[24] Y. Kim, A. Ourmazd, M. Bode and R. D. Feldman, *Phys. Rev. Lett.* **63**, 636 (1989).

[25] A. Tardot, A. Hamoudi, N. Magnea, P. Gentile and J. L. Pautrat, *Appl. Phys. Lett.* **62** 2549-50 (1993).

[26] R. D. Feldman, R. F. Austin, C. L. Cesar, M. N. Islam, C. E. Soccolich, Y. Kim and A. Ourmazd, *Long-Wavelength Semiconductor Devices, Materials and Processes*, Editors A. Katz, R. M. Biefeld, R. J. Malik and R. L. Gunshor, Mat. Res. Soc. Symp. Proc. Volume 216, 113 (1991).

Optical properties and interdiffusion of (001) HgTe/Hg$_{1-x}$Cd$_x$Te superlattices

F Goschenhofer, V Latussek, S Einfeldt, M O Möller, C R Becker and G Landwehr

Physikalisches Institut der Universität Würzburg, Am Hubland, 97074 Würzburg, Germany

Abstract. Interdiffusion in HgTe/Hg$_{1-x}$Cd$_x$Te superlattices has been investigated by means of changes in their optical properties. The energy of the lowest inter-band transition, H1→E1, which is calculated using a finite HgTe/Hg$_{1-x}$Cd$_x$Te interface width, is compared with the experimental value in order to ascertain the width and shape of the interface. The results, which can be explained better if interdiffusion is linear rather than nonlinear, are strongly dependent on the sample. Moreover, the observed interdiffusion in the superlattice with the smallest diffusion coefficient is larger than the interdiffusion which occured during growth: the absorption coefficient of as-grown superlattices is independent of time spent at the growth temperature contrary to predictions using experimentally determined interdiffusion results. Apparently, the results of the interdiffusion experiments depend on the thermal history of the sample.

1. Introduction

The optical [1] and electrical [2] properties of Hg based heterostructures depend strongly on the abruptness of their interfaces and consequently on interdiffusion in these interfaces during growth and during subsequent technological processes after growth. Previous diffusion experiments on HgTe/Hg$_{1-x}$Cd$_x$Te superlattices have been primarily based on x-ray diffraction methods [3–5] as well as on chemical mapping [6]. Even though optical absorption depends to a large extent on the interdiffusion of these interfaces as demonstrated by Leopold *et al.* [1], optical absorption has not previously been employed to quantitatively determine diffusion in HgTe/Hg$_{1-x}$Cd$_x$Te superlattices.

The absorption coefficient of HgTe/Hg$_{1-x}$Cd$_x$Te superlattices displays step-like features corresponding to subband transitions which depend on various parameters, among which are period, well and barrier thicknesses, composition of the wells and barriers, valence band offset, strain and the concentration profile of the interfaces. If these parameters with the exception of the interface profile are known with sufficient accuracy, then a theoretical determination of the absorption coefficient should result in the concentration profile of the interfaces. This method has been employed here to determine the temporal dependence of this concentration profile and hence interdiffusion in these interfaces.

2. Growth and parameters

The HgTe/Hg$_{1-x}$Cd$_x$Te superlattices were grown on (001) Cd$_{0.96}$Zn$_{0.04}$Te substrates by molecular beam epitaxy (MBE), RIBER 2300, as has been described in detail elsewhere [7,8]. The substrates were degreased, etched in HCl, loaded into the MBE system and then heat treated at temperatures up to 320°C. The substrate temperature was measured by means of a thermocouple which was in contact with a molybdenum substrate holder and was calibrated at the melting points of indium and tin. The day to day uncertainty in the temperature is < 2°C. Before the superlattice was grown, a 500 Å thick CdTe buffer was grown at 270°C. The superlattices were then grown at 180°C. A polycrystalline CdTe cap layer with a thickness of about 600 Å was grown at 35°C either directly after growth or in one case after several weeks.

The superlattice period as well as the well thickness and hence that of the barrier were determined by means of high resolution x-ray diffraction [7,9]. This is done by taking advantage of the large HgTe structure factor compared to that of CdTe for the (002) Bragg reflection. In general, the investigated superlattices are of good quality as indicated by the full width at half maximum of their (004) Bragg reflection, i.e. as low as 22 arcsec, and the large number of satellites. [7,8] The composition of the initial barrier material was determined to be 0.68 ± 0.02 by means of transmission and reflection measurements on thick test layers of (001) Hg$_{0.32}$Cd$_{0.68}$Te grown under identical conditions. Knowing the well and barrier thicknesses we have been able to confirm this value for the composition of the barriers by annealing several superlattices and then measuring the composition of the resulting alloy.

3. Optical absorption coefficient

Optical transmission and reflection measurements were carried out in the middle and near infrared with a Fourier transform spectrometer, IFS88, from Bruker Instruments Inc. A pyroelectric detector was employed rather than a HgCdTe detector because of its better linearity. The aperature was kept as small as possible for the same reason, i.e. a diameter of 2 to 3 mm. The absorption coefficient was determined by fitting the experimental transmission and reflection spectra to a theoretical description of the multi-layer system using the standard matrix procedure, e.g. Ref. [10]. Minimizing the difference between experimental and theoretical values of merely the transmission at a constant index of refraction resulted in the same absorption coefficient within experimental uncertainty. Therefore, in most cases this procedure was carried out for only the transmission using an appropriate constant refractive index.

The electronic band structure was calculated with an envelope function method [11] which differs formally from two previous methods [12, 13] but combines the essential aspects of both approaches. The bands of both bulk HgTe and CdTe are described by Kane's four-band model (8×8 k · p) including second order far-band contributions, but neglecting the small anisotropy of the valence bands. The effects of strain due to lattice mismatch were also taken into consideration [2]. The numerical values for the band parameters were deduced from measurements on bulk HgTe and Hg$_{1-x}$Cd$_x$Te according to Weiler [14]. The valence band offset between HgTe and CdTe was taken to be 550±50 meV which we have found to be necessary in order to correctly describe subband transition energies and the absorption coefficient [15]. The valence band offset for Hg$_{1-x}$Cd$_x$Te was then assumed to vary linearly with x [16]. The initial x value for the barrier in conjunction with a concentration profile due to subsequent interdiffusion of the interface was integrated into the theory.
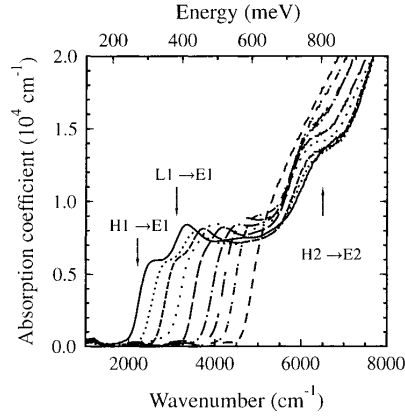
Figure 1. The experimental optical absorption coefficient as a function of wavenumber (cm^{-1}) and energy (eV) at various diffusion times for the superlattice Q424 at 300 K. The diffusion temperature was 180°C.
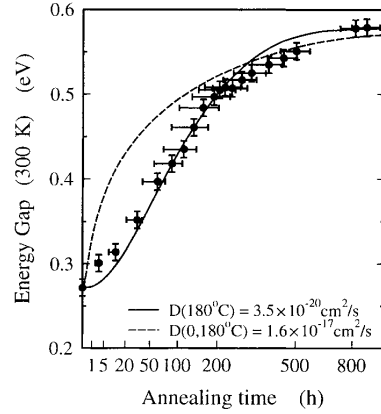
Figure 2. The shift in the E_0 band gap, i.e. H1→E1, of Q424 as a function of diffusion time for a diffusion temperature of 180°C. The solid curve corresponds to a linear fit and the dashed curve to a nonlinear fit.

Diffusion experiments were carried out on the superlattice structures discussed above in vacuum, an Ar atmosphere or oil at 160 and 180°C, i.e. at temperatures similar to those used during growth. After each diffusion step the absorption coefficient was determined and occasionally x-ray diffraction of the sample was measured.

4. Results and discussion

The experimentally determined optical absorption coefficients before and after some of the annealing steps at 180°C for the superlattice Q424 are shown in Fig.1. After the final annealing step, i.e. after 880 hours, the superlattice has become an alloy. Theoretically determined energies of various interband transitions before annealing, which are indicated by arrows, correspond to the observed structure in the absorption coefficient. As shown in Fig.2 the observed shift of the band gap can be much better described by linear than by nonlinear diffusion. Using a Cd dependence similar to that of Tardot et al. [5], nonlinear diffusion can be expressed by

$$D(x, T) = D(0, T) \exp\left(\frac{-0.50\,x\ eV}{kT}\right)$$

where x is the Cd concentration of the barrier. All of the diffusion results in this investigation are listed in Table I and the nonlinear results are shown in Fig.3 together with published results. As can be seen, our results are extremely dependent on sample. They vary from sample to sample by a factor of 50. Some of our nonlinear results are much higher and some much lower than an extrapolation of the published results to 160 and 180°C. The large scatter in our data can at present not be correlated with any growth condition or sample parameter. However, it is worthwhile mentioning that the diffusion in the first four samples in Table I can be

3

TABLE I. The number of periods, the period and layer thicknesses(Å), the linear diffusion coefficient, $D(T)$, and the concentration independent component of the nonlinear coefficient, $D(0, T)$.

	Periods	$\bar{d}_P$	$\bar{d}_w$	d_b	Diffusion	Diffusion coefficient	
		± 0.5	± 1	∓ 1	Temperature	$D(T)$	$D(0, T)$
		Å	Å	Å	°C	$\times 10^{-19}$ cm^2/s	$\times 10^{-16}$ cm^2/s
Q766	100	62.0	23.7	38.3	180	3.0	1.0
					160	1.5	0.5
Q769	100	74.4	31.7	42.7	180	5.0	2.0
					160	2.5	1.5
Q784	100	80.3	30.9	49.4	180	33	6.5
					160	8	1.6
Q785	100	93.0	32.8	60.2	180	16	8.0
					160	8	4.0
Q424	120	110.7	34.0	76.7	180	0.35	0.16

described by a slow initial diffusion and then by a subsequent faster diffusion as has been reported by Arch et al. [4]. The presence of a cap layer was shown to have a relatively small effect on interdiffusion in Q766.

The expected Cd concentration profile for the superlattice Q424 corresponding to an E_0 band gap of 400 meV for both linear and nonlinear diffusion is shown in Fig.4. In addition, the as-grown profile should be dependent on position in the superlattice. In other words, this profile should depend on the length of time spent at the growth temperature, i.e. 180°C. A shift
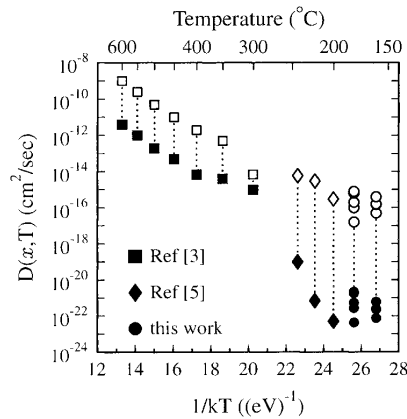
Figure 3. An Arrhenius plot of nonlinear diffusion coefficients in CdTe/HgTe. The upper symbols (empty) represent diffusion in HgTe, D(0,T), and the lower symbols (filled) diffusion in CdTe, D(1,T).
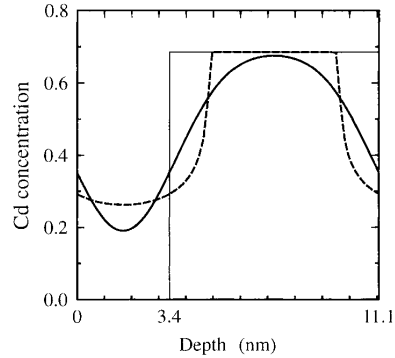
Figure 4. The expected Cd concentration profile for the superlattice Q424 for both linear (solid line) and nonlinear diffusion (dashed line) after an annealing time which corresponds to a E_0 band gap of 400 meV.

4

in the band gap across a superlattice of approximately 6 meV is expected at this temperature for a typical growth time of two hours.

In order to corroborate the expected results of diffusion during growth, Q424 was etched to reduce its thickness and then the absorption coefficient of the resulting superlattice was measured. This was repeated four times until only 80 of the original 120 periods were present. Within experimental error of less than 1 meV, no shift was observed. This means that an upper limit for linear diffusion in Q424 is given by $D(180°C) < 1 \times 10^{-20}$ cm^2/s which is at least a factor of four smaller than the experimental value for this coefficient. The difference between diffusion during growth and after growth is not understood at the present. However, we speculate that diffusion depends on the number of dislocations which are generated due to differences in thermal expansion coefficients of substrate, wells, barriers and cap layer. The low value for diffusion during growth would correspond to an average interface width of approximately two monolayers which is a factor of three narrower than that determined by Kim et al. [6].

In conclusion, we have shown that interdiffusion in HgTe/ $Hg_{1-x}Cd_xTe$ superlattices can be best explained by linear diffusion. The resulting diffusion constant varies by a factor of 50 depending on the sample. Some of the diffusion coefficients are appreciably smaller and some appreciably larger than the literature values. However, the diffusion coefficient for Q424, which is the smallest measured value, is nevertheless larger than that for interdiffusion which occurs during growth by at least a factor of four. We speculate that this is due to the thermal history and differences in thermal coefficients of expansion.

References

[1] Leopold D J, Broerman J G, Peterman D J and Wroge M L 1990 *Appl. Phys. Lett.* **52** 969-71

[2] Simon A, Bertho D, Boiron D and Jonanin C 1990 *Phys. Rev. B* **42** 5221-8

[3] Tang M-F S and Stevenson D A 1987 *Appl. Phys. Lett.* **50** 1272-4

[4] Arch D K, Staudermann J L and Faurie J P 1986 *Appl. Phys. Lett.* **48** 1588-90

[5] Tardot A, Hamoudi A, Magnea N, Gentile P and Pautrat J L 1993 *Appl. Phys. Lett.* **62** 2548-50

[6] Kim Y, Ourmazd A, Bode M and Feldman R D 1989 *Phys. Rev. Lett.* **63** 636-9

[7] Becker C R, He L, Regnet M M, Kraus M M, Wu Y S, Landwehr G, Zhang X F and Zhang H 1993 *J. Appl. Phys.* **74** 2486-93

[8] Becker C R, Latussek V, Heinke H, Regnet M M, Goschenhofer F, Einfeldt S, He L, Bangert E, Kraus M M and Landwehr G 1993 *Growth and Characterization of Materials for Infrared Detectors* R E Longshore and J W Baars, Editors Proc. SPIE 2012 p 138-48

[9] Möller M O, Bicknell-Tassius R N and Landwehr G 1992 *J. Appl. Phys.* **72**, 5108-16

[10] Fasold D, Hehl K and Jetschke S 1984 *phys. stat. sol. (a)* **86**, 125

[11] Bangert E, Boege P, Latussek V and Landwehr G 1993 *Semicond. Sci. Technol.* **8** S99-101

[12] Ram-Moham L R, Yoo K H and Aggarwal R L 1988 *Phys. Rev. B* **38** 6151-9

[13] Johnson N F, Ehrenreich H, Hui P M and Young P M 1990 *Phys. Rev. B* **41** 3655-69

[14] Weiler M H 1981 *Semiconductors and Semimetals* **16** editors Willardson R and Beer A C (New York: Academic) 119-89

[15] von Truchseß M, Latussek V, Sizmann R, Helgesen P, Goschenhofer F, Becker C R, Landwehr G and Batke E submitted to *Phys. Rev. B*

[16] Shih C K and Spicer W E 1987 *Phys. Rev. Lett.* **58** 2594-7

Molecular beam epitaxial growth and characterization of (001) Hg$_{1-x}$Cd$_x$Te-HgTe superlattices

C.R. Becker, V. Latussek, H. Heinke, M.M. Regnet, F.Goschenhofer,
S. Einfeldt, L. He[a] E. Bangert, M.M. Kraus, and G. Landwehr
Physikalisches Institut der Universität Würzburg, Am Hubland, 97074 Würzburg, Germany

ABSTRACT

The molecular beam epitaxially growth of (001) Hg$_{1-x}$Cd$_x$Te-HgTe superlattices has been systematically investigated. The well width as well as the period were determined directly by X-ray diffraction. This was accomplished for the well width by exploiting the high reflectivity from HgTe and the low reflectivity from CdTe for the (002) Bragg reflection. Knowing the well and barrier thicknesses we have been able to set an upper limit on the average composition of the barriers, $\bar{x}_b$, by annealing the superlattice and then measuring the composition of the resulting alloy. $\bar{x}_b$ was shown to decrease exponentially with decreasing barrier width. $\bar{x}_b$ is appreciably smaller in narrow barriers due to the increased significance of interdiffusion in the Hg$_{1-x}$Cd$_x$Te/HgTe interface in narrow barriers.

The experimentally determined optical absorption coefficient for these superlattices is compared with theoretical calculations. The absorption coefficient was determined from transmission and reflection spectra at 300, 77 and 5 K. Using the thickness and composition of the barriers and wells, and an interface width due to interdiffusion, the complex refractive index is calculated and compared with the experimental absorption coefficient. The envelope function method based on an 8×8 second order $\mathbf{k} \cdot \mathbf{p}$ band model was used to calculate the superlattice states. These results, when inserted into Kubo's formula, yield the dynamic conductivity for interband transitions. The experimental and theoretical values for the absorption coefficient using no adjustable parameters are in good agreement for most of the investigated superlattices. Furthermore the agreement for the higher energetic interband transitions is much worse if values for the barrier composition, which are appreciably different than the experimentally determined values, are used.

The infrared photoluminescence was investigated at temperatures from 4.2 to 300 K. Pronounced photoluminescence was observed for all superlattices in this temperature range.

I. INTRODUCTION

Schulman and McGill[1] proposed in 1979 that the CdTe-HgTe superlattice would be a useful material for a number of infrared optoelectronic devices. They predicted that the band gap of the superlattice should be adjustable from 0 to 1.6 eV depending on the CdTe and HgTe layer thicknesses and they suggested that the growth could be carried out by molecular beam epitaxy (MBE). This was first accomplished by Faurie et al. in 1982.[2] Thereafter numerous publications have dealt with the novel electrical and optical properties of these structures, which have been reviewed by Faurie,[3] McGill et al.,[4] Meyer et al.[5] and others.

The CdTe-HgTe superlattice has potential advantages in infrared applications compared to the alloy. For example, better control over the band gap of narrow gap superlattices has been predicted.[6,7] The band gap is controlled primarily by the well thickness and to a lesser extent by the barrier thickness. It increases from approximately 10 to 200 meV when the well width is reduced from 100 to 30 Å. In contrast the band gap of the alloy depends on its composition which has to be progressively better controlled as the band gap goes to zero. The band gap of a superlattice is a smooth, slowly varying function of the layer thicknesses and hence arguably easier to control. However the barrier normally consists of Hg$_{1-x}$Cd$_x$Te and not CdTe because the Hg flux is left on during growth and both Hg and Cd compete for cation sites. The composition of the well and the barrier influences the height of the potential barrier between the two and hence the band gap. Their x values are not readily accessible but should depend primarily on their initial values, i.e. on the growth parameters, and in the case of narrow layers on subsequent interdiffusion. Kim et al.[8] have shown that interdiffusion is two orders of magnitude larger near the surface when compared to a depth of 7000 Å or more. Therefore interdiffusion should depend primarily on how long a particular layer spends near the surface which is constant with the exception of the superlattice periods grown last.

The superlattice period is readily accessible by x-ray diffraction experiments, however the well and barrier thicknesses and their compositions are not so easily determined. Historically well and barrier thicknesses have been inferred

132

from the growth parameters or measured by transmission electron microscopy (TEM).[9] We have been able to determine the well thickness and hence that of the barrier by means of high resolution x-ray diffraction.[10, 11] This is done by taking advantage of the large HgTe structure factor compared to that of CdTe for the (002) Bragg reflection. The well thickness as determined by this method has been corroborated by (TEM) for a superlattice with an extremely short period of 31.4 Å.

The composition of the well and barrier can not be determined directly except possibly by a destructive method such as chemical mapping[8] which utilizes TEM. In this investigation we have estimated the composition of the initial barrier material by means of transmission and reflection measurements on thick test layers of (001) $Hg_{1-x}Cd_xTe$ grown under identical conditions with the exception of the presence of the HgTe wells. Knowing the well and barrier thicknesses we have been able to set an upper limit on the actual composition of the barriers by annealing several superlattices and then measuring the composition of the resulting alloy.

A large number of band structure calculations for the $Hg_{1-x}Cd_xTe$-HgTe superlattice have been published during the last decade.[5, 12–14] Ram-Moham *et al.*[12] employed the envelope function method and developed a transfer matrix procedure to calculate the superlattice states. He accounted for the full 8×8 Kane hamiltonian including all second order terms representing the far-band contributions, but did not apply his results to a calculation of the optical constants. On the other hand N.F. Johnson *et al.*[13] applied a slightly different version of the envelope function method, and deduced optical constants from his superlattice energies and eigenfunctions. But in his approach he used a simplified band model, which omits all the second order far-band contributions, with the exception of a finite heavy hole mass. In order to overcome these shortcomings, we have combined the essential aspects of both approaches.[15] This enables us to calculate the optical constants based on a realistic band structure model, which includes all second order higher band contributions. This should be a sound basis for a realistic comparison between theory and experiment.

II. EXPERIMENTAL AND THEORETICAL DETAILS

A. Growth

Epitaxial growth was carried out in a four chamber RIBER 2300, molecular beam epitaxial (MBE) system which has been modified to permit the growth of Hg based materials. The vacuum in the growth chamber is better than 6×10^{-10} Torr when no Hg has recently been admitted. Three MBE cells were employed, two of which were commerical cells and which contained high purity CdTe and Te. The third cell is a self designed stainless steel cell for Hg which can be refilled without breaking the vacuum. The flux of the latter cell is stable to within ± 1.5 and ± 3 % over a period of 2 and 30 hours, respectively. The CdTe and Te fluxes depend upon how long their respective shutters have been closed and/or open. This is discussed in more detail elsewhere.[11] The steady state values for CdTe, Te and Hg were 3×10^{-7}, 6×10^{-7} and 2.8×10^{-4} Torr, respectively. In this article pressure is loosely referred to as flux. This Hg flux is roughly 2.5 times larger than the minimum flux necessary to maintain epitaxial growth of HgTe.

The $Hg_{1-x}Cd_xTe$-HgTe superlattices were grown on (001) $Cd_{0.96}Zn_{0.04}Te$ and CdTe substrates which had been degreased, chemo-mechanically polished for several minutes in a weak solution of bromine in methanol and then rinsed in methanol. Two substrates which were chemo-mechanically polished by the manufacturer (epi-ready) were merely degreased, i.e. Q424 and Q426. Immediately prior to mounting the $5 \times 10 \times 1$ mm substrates on a molybdenum holder with a solution of graphite in isopropanol and loading into the MBE system, they were rinsed in de-ionized water, briefly dipped in hydrochloric acid and then rinsed in de-ionized water so as to remove all of the original oxide and carbon from the substrate surface.[16] We have found that the newly formed oxide as a result of this previous step, is much more easily evaporated from the surface.[17] This is accomplished by heating the substrates at temperatures up to about $320^\circ C$ while monitoring the substrate surface by reflection high energy electron diffraction (RHEED) as described elsewhere.[18] The substrate temperature was measured with an accuracy of $\pm 2^\circ C$ by means of a thermocouple which was in physical contact with a molybdenum substrate holder. The thermocouple was carefully calibrated at the melting points of indium and tin.

Before the superlattice was grown, a thin CdTe buffer was grown on the (001) $Cd_{0.96}Zn_{0.04}Te$ or CdTe substrate at $270^\circ C$ until the reflection high electron energy diffraction (RHEED) pattern indicated that the surface was smooth by the presence of short streaks. The thickness of this buffer was between 30 and 1000 Å. This surface was characterized by a (2×1) half order reconstruction in the [0$\bar{1}$1] azimuth. We use the convention of refering to the direction of the incident electrons when refering to reconstruction in a particular azimuth. The superlattice was then grown at $180^\circ C$.

B. X-ray diffraction details and theory

We have used a high resolution five crystal x-ray diffractometer to determine accurate values for the well thickness, the average superlattice period and the deviation from this average in the superlattice. The Cu $K\alpha_1$ radiation was resolved by means of the Ge (220) Bragg reflection in a four crystal monochromator. The reasons for a measurable (002) Bragg reflection for the zinc blende structure as opposed to the diamond structure where it is forbidden is discussed by Möller *et al.*.[10] The rather large (002) Bragg reflection in these superlattices is caused primarily by the HgTe well; the structure factor for the (002) Bragg reflection is much larger for HgTe than for CdTe.[10] To our knowledge this behavior, the large difference in the size of the structure factor between HgTe and CdTe, is unique to this system and perhaps to related Hg containing superlattices. This is due to the relatively large size of the Hg atom with its large number of electrons. In fact the structure factor goes to zero for $Hg_{1-x}Cd_xTe$ with an x value of about 0.88. Thus an observable envelope of the superlattice satellites is due to the slit function corresponding to the HgTe layers. From the angular separation of the first order zero points of this envelope, $\Delta\omega_{Z.P.}$, we can calculate the average thickness of the HgTe well, $\bar{t}_w$, with an accuracy of $\geq \pm 3$ Å, which depends on the number of satellites and the position of the first order zero points, $\Delta\omega_{Z.P.}$, relative to the satellites. Similarily the average superlattice period, $\bar{t}_P$, can be determined from the angular separation of the superlattice satellites, $\Delta\omega_P$. From the increased broadening of the higher order satellites, $\delta\omega_{Sat.}$, for the (004) reflection, the deviation of the superlattice period from its average value throughout the structure can be obtained. Here we have used the following equations:[19]

$$\bar{t}_P = \frac{\lambda|\gamma_H|}{\Delta\omega_P \sin(2\theta_B)} \tag{1}$$

$$\frac{\delta t_P}{\bar{t}_P} = \frac{\delta\omega_{Sat.}\,\bar{t}_P \sin(2\theta_B)}{\lambda|\gamma_H|} \tag{2}$$

$$\bar{t}_w = \frac{2\cdot\lambda|\gamma_H|}{\Delta\omega_{Z.P.}\sin(2\theta_B)} \tag{3}$$

where λ is the wavelength of the reflected x-rays, θ_B is the Bragg angle for the substrate, γ_H is $\vec{k}_H \times \vec{n}$, $\vec{k}_H$ is the scattered unit wave vector and $\vec{n}$ is the unit vector normal to the surface.

C. Composition of wells and barriers

In order to determine the composition of our barriers, we have grown alloys with the same CdTe and Hg fluxes and at the same temperature used for the superlattice. In addition we have grown alloys with periodic growth stops of the same duration as that required for the growth of the HgTe well. In other words the growth conditions including the opening and closing of the Te and CdTe shutters were identical, with the exception of no Te flux. We determined the composition of the alloys grown by both of these methods from the E_0[20] and E_1 (L6-L4,5)[21,22] energy gaps by means of transmission and reflection measurements, respectively, to be 0.68 ± 0.02. However one condition, the presence of the HgTe wells, is not the same and interdiffusion in these short period superlattices must be taken into consideration.

In order to set an upper limit on the average barrier composition, $\bar{x}_b$, annealing experiments were carried out on several superlattices at 240 to 250°C for 24 hours. The superlattice was placed in a quartz ampoule together with either a drop of Hg which could not come into contact with the superlattice or with 400 mbar of 99.999% pure Ar gas. In the latter case, the superlattice surface was held in contact with a clean CdTe substrate by means of a weak tantalum spring on a piece of molybdenum.

D. Optical absorption coefficient

1. Experiment

Optical transmission and reflection measurements were carried out in the middle and near infrared with a Fourier transform spectrometer, IFS88, from Bruker Instruments Inc. A deuterated triglycine sulfate detector was employed rather than a liquid nitrogen cooled detector, *e.g.* $Hg_{1-x}Cd_xTe$, because of its better linearity. The aperature was kept as small as possible for the same reason, i.e. a diameter of 2 to 3 mm. The absorpion coefficient was

134

determined by fitting the experimental transmission and reflection spectra to a theoretical description of the multi-layer system using the standard matrix procedure. Minimizing the difference between experimental and theoretical values of merely the transmission at a constant index of refraction resulted in the same absorption coefficient within experimental uncertainty. Therefore, in most cases this procedure was carried out for only the transmission using an appropriate constant refractive index.

2. Theory

The envelope function method of Bangert *et al.*[15] was employed which differs formally from previous ones.[12, 13] It was conceived in such a way as to yield a large number of superlattice energies, wave functions and dipole matrix elements which are needed for the calculation of the optical absorption. The bands of both bulk HgTe and CdTe are described by Kane's four-band model (8×8 $\mathbf{k} \cdot \mathbf{p}$) including second order far-band contributions, but neglecting the small anisotropy of the valence bands. The effects of strain due to lattice mismatch were also taken into consideration.[14] The numerical values for the band parameters (E_g, Δ, γ_1, γ_2, γ_3, F and E_p) were deduced from measurements on bulk HgTe and $Hg_{1-x}Cd_xTe$ by Weiler.[23] The valence band offset between HgTe and CdTe was taken to be 350 meV which is the generally accepted value.[5] The valence band offset for $Hg_{1-x}Cd_xTe$ was then assumed to vary linearly with x.[24] The thickness of the layers, and the superlattice period were determined by means of x-ray diffraction as discussed above. The composition of the barrier was taken to be that of alloys grown under the same conditions , i.e. 0.68 ± 0.02, and not the average x value in the barrier. This value for the alloy was used in conjunction with the interface width due to interdiffusion of the interface according to Kim *et al.*[8] which was integrated into the theory.

The real and imaginary components ($n(\omega)$ and $k(\omega)$) of the complex refractive index are obtained from

$$N^2(\omega) = (n(\omega) + ik(\omega))^2 = \varepsilon_L(\omega) + i\frac{\sigma(\omega)}{\omega\epsilon_0} \tag{4}$$

where $\varepsilon_L(\omega)$ is the lattice contribution and $\sigma(\omega)$ the dynamic conductivity. $\sigma(\omega)$ is determined by making use of Kubo's formula[15] which employes the superlattice energies, wave functions and dipole matrix elements mentioned above. It should be emphasized that no adjustable parameters are included in this theory.

III. RESULTS AND DISCUSSION

A. Photoluminescence measurements

Fourier transform infrared luminescence spectra of some of these superlattices have been published elsewhere.[11, 25] The photoluminescence spectra of almost all of the superlattices in this investigation consist of one nearly symmetric line. The full width at half maximum of this line lies between 16 and 60 meV at 4.2 K and between 52 and 113 meV at 300 K. This attests to the good quality of these superlattices.

B. X-ray diffraction measurements

A smoothed rocking curve of the (002) reflection for the superlattice Q230 and the slit function used for the HgTe well thickness determination are shown in Fig.1 as the full and dotted lines, respectively. The large number of satellites which is typical of most of the investigated superlattices, is an indication of the high structural quality of these superlattices. The period, well and barrier thicknesses of all the superlattices investigated are listed in Table 1. The variation of these periods from their average values, according to Eq. 2, is less than 10 % and in most cases less than 5 %. This is also an indication of the good uniformity of these superlattices. The experimental uncertainty in the period and the HgTe well thickness is ±0.5 and $\geq \pm3$ Å, respectively.

Two of four extremely short period superlattices, Q250a and Q250c, which were grown simultaneously, have been investigated by x-ray diffraction in greater detail.[11] The rocking curve for the (002) Bragg reflection and a simulation of Q250a are shown in Fig.2. The simulation was calculated using a concentration profile across the $Hg_{1-x}Cd_xTe$-HgTe interface with the same width and shape as the interface according to Kim *et al.*[8] If an abrupt interface was employed then the simulated intensities of the satellites were much larger, *e.g.* the second order satellites were one
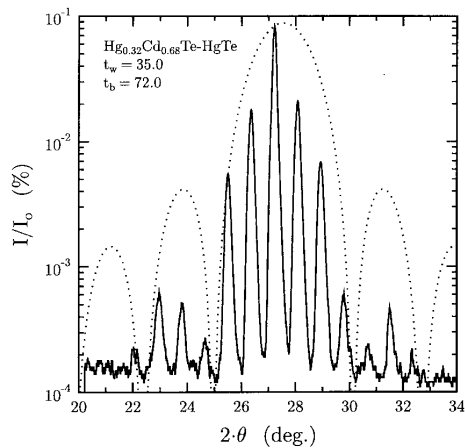
FIG. 1. X-ray rocking curve for the (002) Bragg reflection from the $Hg_{0.32}Cd_{0.68}$Te-HgTe superlattice Q230. The full line represents the experimental data and the dotted line is the envelope of the superlattice satellites which is due to the slit function corresponding to the HgTe layers. The large number of satellites is an indication of the excellent structural quality of the superlattice.
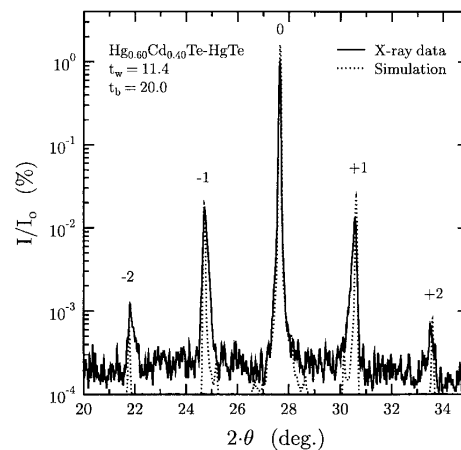
FIG. 2. X-ray rocking curve for the (002) Bragg reflection from the $Hg_{0.60}Cd_{0.40}$Te-HgTe superlattice Q250a. The full line with random noise represents the experimental data and the dotted line is a simulation of the data.

to two orders of magnitude larger. Furthermore, if an interface with approximately twice the width of the published interface was used, then the second order satellites were no longer discernible. Thus according to these simulations, the concentration profile across the $Hg_{1-x}Cd_x$Te-HgTe interface in these superlattices is similar to that of the interface according to Kim *et al.*[8]

The rocking curve of the (004) Bragg reflection for one of the superlattices which was grown on an epi-ready $Cd_{0.96}Zn_{0.04}$Te substrate is shown in Fig. 3. The full width at half maximum (FWHM) is 22 and 19 arc seconds for the main superlattice peak and the substrate, respectively. The value for the superlattice, which is only slightly larger than that of the substrate, compares favorably with the best published values for a $Hg_{1-x}Cd_x$Te- HgTe superlattice, *e.g.* Myers *et al.*,[26] as well as with values for the best GaAs-Al_xGa_{1-x}As superlattices. The (002) rocking curve for this superlattice is displayed in Fig. 4. The negative even order satellites, i.e. -2, -4 and -6, are completely missing due to the slit function which corresponds to the HgTe well thickness. The fact that the +2 and +4 satellites are still present, albeit appreciably weaker, can be explained by a slight difference in the lattice constant of the superlattice and that of the well; the position of the principal superlattice peak is determined by the lattice constant of the superlattice, whereas the position of the slit function is given by the lattice constant of the scattering material, i.e. the well. A simulation of the (002) rocking curve for Q426 using a concentration profile with the same width and shape as the experimentally determined profile mentioned above,[8] resulted in a better fit between the simulated and experimental satellite intensities than a simulation utilizing an abrupt interface. This concentration profile is shown in Fig.5.

C. Composition of wells and barriers

Prior to approximately 1986 the composition of the well and barrier material in $Hg_{1-x}Cd_x$Te-HgTe superlattices was assumed to be HgTe and CdTe, respectively. In 1987 Reno *el at.*[27] determined the x value of a thin layer, i.e.

136
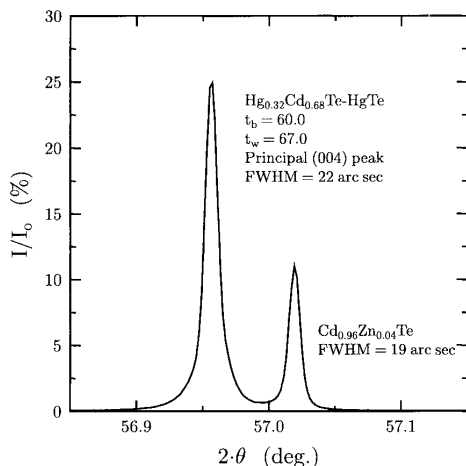
FIG. 3. X-ray rocking curve for the (004) Bragg reflection from the $Hg_{0.32}Cd_{0.68}Te$-HgTe superlattice Q426.
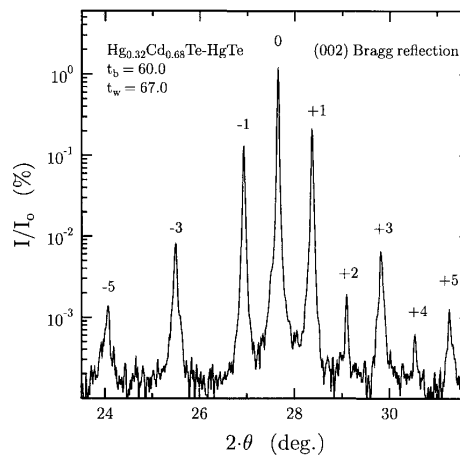
FIG. 4. X-ray rocking curve for the (002) Bragg reflection from the $Hg_{0.32}Cd_{0.68}Te$-HgTe superlattice Q426.

150-170 Å of (001) $Hg_{1-x}Cd_xTe$ barrier material grown at $185^\circ C$ to be 0.85 by x-ray photoelectron spectroscopy. Due to absorption of the photo-emitted electrons, this is the x value for approximately 50 Å of the layer near the surface. Later Schulman et al.[9] determined the x value of a test layer of (001) $Hg_{1-x}Cd_xTe$ grown at $175^\circ C$ to be 0.85. Most of the recent literature either assumes this x value to be correct, independent of the substrate temperature and the other growth parameters, or does not mention how the x value is determined. A recent exception is the work of Monterrat et al.[28] which reports an x value of approximately 0.70 for barrier material in (001) single and multiple quantum wells grown at $180^\circ C$.

As mentioned above, the composition of alloys grown with the same growth parameters as those used for our barrier material was determined to be 0.68 ± 0.02. We found that MBE growth with the same growth conditions as described above but with illumination of the substrate with an Ar ion laser, resulted in an x value of 0.85. Wu et al.[18] have shown that illumination with an Ar ion laser as well as irradiation with the high energy electrons used in their RHEED oberservations, i.e. 10 keV, significantly reduces the desorption time for excess Te from a Te stabilized CdTe surface. Because the x value of $Hg_{1-x}Cd_xTe$ is governed primarily by the substrate temperature and the CdTe to Te flux ratio,[22] an enhanced desorption of Te from $Hg_{1-x}Cd_xTe$ would result in a larger x value. This is consistent with our observations from RHEED oscillations that the growth rate for $Hg_{0.32}Cd_{0.68}Te$ and HgTe decreases with increasing high energy electron intensity, i.e. an electron current of 200 μA results in a 10% reduction in growth rate. A larger x could also be caused by an enhanced Hg desorption, however this does not seem probable; the magnitude of the Hg flux which is approximately 2.5 times larger than that necessary to maintain epitaxial growth does not significantly influence either the x value of $Hg_{1-x}Cd_xTe$ or the growth rate.[22]

In order to determine the composition of the barrier in these superlattices, four superlattices were annealed at $250^\circ C$ for 24 hours in an Ar atmosphere and one in a Hg atmosphere as described above. Both of these methods should be effective in reducing or preventing the diffusion of Hg out of the superlattice near the surface. If Hg does diffuse out of the superlattice, then the x value of the resulting alloy and the calculated value for $\bar{x}_b$ would be upper limits. Diffusion of Hg into the superlattice under an Hg atmosphere is possible, which would lower the x value near the surface.

The x value of one of the resulting alloys was determined from reflection measurements of the E_1 gap to be $0.48 \pm .01$. The corresponding x value from transmission measurements of the E_0 gap is somewhat higher, i.e. 0.52. Furthermore the discrepency between the E_0 and the E_1 gap increases with decreasing superlattice thickness. This is an indication

TABLE I. The number of periods, the period (Å), thickness(Å) and average Cd concentration of both the well and barrier for the investigated superlattices. Both measured values of the Cd concentration for the barriers, $\bar{x}_b$, and empirical values for $\bar{x}_b$ and $\bar{x}_w$, which were calculated by using the Cd concentration profile according to Ref.8, are included. Experimental and theoretical values for the energy gap, i.e. $HH_1 \rightarrow C_1$ for the investigated superlattices, are listed for a number of the superlattices at 5 and 300 K.

	Periods	$\bar{t}_P$	$\bar{t}_w$	$\bar{t}_b$	$\bar{x}_w$	$\bar{x}_b$	$\bar{x}_b$	Energy gap; $HH_1 \rightarrow C_1$ (meV)			
		±0.5	±3	∓3	empirical		experimental	theoretical		experimental	
								5 K	300 K	5 K	300 K
Q250	900	31.4	11.4	20.0	0.04	0.44	0.36 ± 0.05	118 ± 50[a]	216 ± 54[a]	120	200
Q211	100	47.0	16.0	31.0	0.03	0.53	0.50 ± 0.05				
Q178	90	54.1	30.6	23.5	0.02	0.48					
Q218	100	64.9	32.2	32.7	0.02	0.54	0.55 ± 0.05	178 ± 39	260 ± 35	210	300
Q168	180	67.4	29.6	37.8	0.02	0.56		208 ± 41	286 ± 36	155	300
Q247	100	82.5	31.4	51.1	0.02	0.59					
Q215	100	120.8	30.7	90.1	0.02	0.64		251 ± 32	329 ± 29	250	305
Q174	90	121.0	30.3	90.7	0.02	0.64	0.64 ± 0.03	242 ± 32	320 ± 30	210	300
Q167	140	87.0	35.1	51.9	0.01	0.59		177 ± 29	259 ± 26	160	260
Q230	100	107.0	35.0	72.0	0.01	0.62		204 ± 26	285 ± 25	210	280
Q424	120	110.7	34.7	76.0	0.01	0.63		195 ± 27	276 ± 25	180	272
Q214	100	76.0	40.0	36.0	0.01	0.55		125 ± 28	211 ± 25	190	240
Q200	100	77.1	38.4	38.7	0.01	0.56		143 ± 28	228 ± 26	174	245
Q195	100	82.0	38.7	43.3	0.01	0.58		150 ± 26	234 ± 25	160	235
Q163	100	89.0	40.0	49.0	0.01	0.59	0.60 ± 0.03	136 ± 24	220 ± 23		225
Q204	20	96.8	38.9	56.9	0.01	0.61		164 ± 23	247 ± 22	140	220
Q164	80	116.1	43.0	73.1	0.01	0.62		137 ± 18	220 ± 18		211
Q171	90	129.1	43.5	85.6	0.01	0.63					
Q162	100	80.0	47.9	32.1	0.01	0.54		55 ± 24	146 ± 22		176
Q426	110	127.0	67.0	60.0	0.01	0.63		53 ± 10	130 ± 10	27[b]	120
Q165	100	106.0	63.0	43.0	0.01	0.55		25 ± 2	112 ± 12		110

[a]These results for the energy gap were calculated using $x_o = 0.40$ instead of $x_o = 0.68$ which was employed for all of the other energy gaps listed in this table.
[b]This energy gap was determined by means of magnetoabsorption measurements

that diffusion between the CdTe substrate and the $Hg_{1-x}Cd_xTe$ alloy is responsible for this discrepancy. Reflection measurements should be less sensitive to changes in x due to diffusion near the substrate/alloy interface. Therefore x values as determined from reflection measurements of the E_1 gap are used in the following with one exception. The exception is the superlattice which was annealed in an Hg atmosphere and could consequently have a lower x value near the surface. In view of the uncertainity in this case, an average of the two x values (i.e. 0.24 and 0.22 for the E_0 and E_1 gap, respectively) is employed.

If all of the CdTe is in the barrier whose width is 91 ± 3 Å, then $\bar{x}_b$ is 0.64 ± .03. Obviously, this is an upper limit for $\bar{x}_b$ due to the assumption that all of the CdTe is in the barrier. Interdiffusion between the well and the barrier becomes more prominent as the well and barrier become thinner. The $\bar{x}_b$ upper limit for these samples are plotted as a function of the barrier width in Fig.6 and are listed in Table 1. As can be seen, $\bar{x}_b$ is appreciably lower for narrower barriers.

As mentioned above, Kim *et al.*[8] have experimentally determined the concentration profile in a similar superlattice which was also grown at 180°C. By assuming that the width and shape of the interfaces in this investigation are the same (see Fig.5), as suggested by the satellite intensity simulations which were discussed in the section on x-ray diffraction, we have calculated values for $\bar{x}_b$, which are displayed as triangles in Fig.6. The boundaries of the barriers
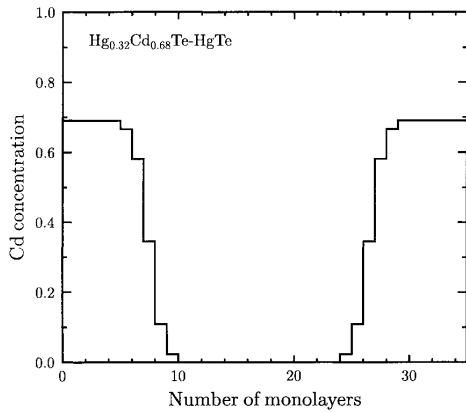
FIG. 5. Cd concentration profile used in the x-ray simulation and in the empirical determination of the average Cd barrier concentration, $\bar{x}_b$, for Q426. The width and shape of the $Hg_{0.32}Cd_{0.68}Te$-HgTe interface is the same as the experimental width and shape according to Ref.8.
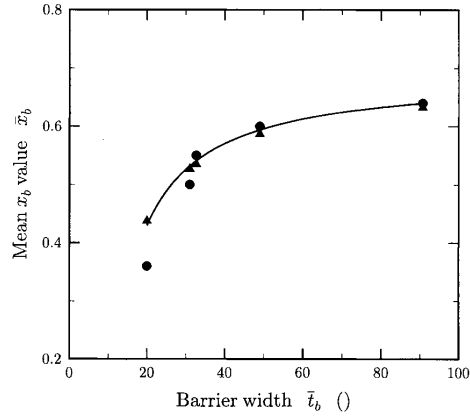
FIG. 6. $\bar{x}_b$ as a function of the barrier width is shown as filled circles. The filled triangles represent values which have been calculated using the Cd concentration profile published in Ref.8. The curve is a least square fit of an exponential function to the calculated data, see Eq. 4.

were consistently chosen to occur at an x value of 0.16 so as to ensure a better fit to the experimental data for the wider barriers. The fit of these calculated values to the experimental data is reasonable with a slightly worse fit for narrow barriers. This is to be expected when the barrier width begins to approach a value which is twice the width of the interface. The calculated values for both $\bar{x}_b$ and $\bar{x}_w$ are listed in Table 1. The following empirical relationship is the result of a fit of an exponential function to the calculated values of $\bar{x}_b$ and the barrier widths:

$$\bar{x}_b = x_o(2 - e^{(6.4/\bar{t}_b)}) \tag{5}$$

where $\bar{t}_b$ is the barrier width in Å and x_o is the Cd concentration of a very thick barrier, i.e. the Cd concentration of alloys grown under the same conditions.

If this model is correct then the Cd concentration of the barrier at a position at least four monolayers removed from the interface is x_o. Therefore the value of x_o, i.e. 0.68 ± 0.02 together with an interdiffusion width or interface width was used in the band structure calculations discussed below. Obviously the diffusion which has taken place at the interface becomes increasingly more significant with decreasing barrier width.

One of the superlattices, Q250b, with the extremely short period of 31.4 Å was annealed at 250^oC for 24 hours under an Hg atmosphere. The x value of the resulting alloy was determined from transmission and reflection measurements to be 0.24 and 0.22, respectively. If all of the CdTe is in the barrier whose width is 20.0 Å then the x value of the barrier is about 0.36. For this narrow well width, i.e. 11.4 Å, however this is not a realistic assumption as suggested by the calculated value for $\bar{x}_w$, i.e. 0.04, which is listed together with values for all of the superlattices in Table 1. Therefore the average x value in the barrier should be somewhat less than 0.36.

Obviously appreciable interdiffusion has taken place in Q250b. The initial barrier composition, $\bar{x}_b$, was 0.68 according to the alloys grown under nearly identical growth conditions. This superlattice consists of 900 periods, each with a width of 31.4 Å, which were subjected to the growth temperature of 180°C for 4 hours. As mentioned above, Kim et al.[8] have shown that interdiffusion is larger near the surface. Their published values for the Hg diffusion constant at 180°C are approximately 1×10^{-17}, 1×10^{-18} and 1×10^{-19} cm^{2}sec^{-1} for the depths of 100, 3500 and 7000 Å respectively. The time spent at a distance of 3500 Å or less from the surface was 30 minutes. Thus to a first approximation, an interdiffusion width for Hg of $2\pi \cdot \sqrt{Dt} \approx 20$ Å can be expected. This is roughly the barrier width and therefore a reduction in the empirical value of $\bar{x}_b$ from 0.68 for a very wide barrier to 0.44 or less for a barrier width
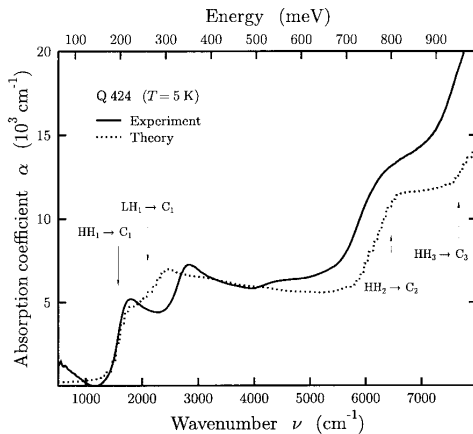
FIG. 7. The experimental and theoretical optical absorption coefficient as a function of wavenumber (cm^{-1}) and energy (eV) for the superlattice Q424 at 5 K. Theoretically determined values of various subband transitions are indicated, e.g. $HH_1 \to C_1$.

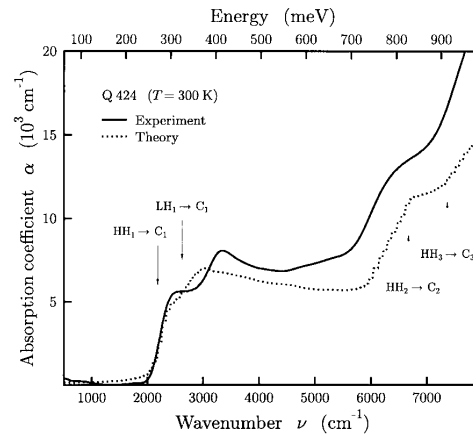FIG. 8. The experimental and theoretical optical absorption coefficient as a function of wavenumber (cm^{-1}) and energy (eV) for the superlattice Q424 at 300 K. Theoretically determined values of various subband transitions are indicated, e.g. $HH_1 \to C_1$.

of 20.0 Å is reasonable. The experimental value for $\bar{x}_b$ of 0.36 ± 0.05 is smaller than the empirical value. Apparently less Cd is incorporated into very narrow barriers. This is corroborated by the theoretical predictions discussed in the next section concerning the maximum Cd concentration, i.e. $x_o = 0.40$ for Q250, in very narrow barriers which is required for reasonable agreement between experimental and theoretical values of the absorption coefficient.

D. Optical absorption coefficient

The experimentally and theoretically determined optical absorption coefficients for the superlattice Q424 at 5 and 300 K are shown in Fig.7 and Fig.8, respectively. Theoretically determined energies of various transitions, which are indicated by arrows, correspond to the observed structure in the absorption coefficient. The energy of the transition from the first heavy hole subband to the first conduction subband ($HH_1 \to C_1$) transition decreases from 272 to 180 meV when the temperature is lowered from 300 to 5 K. The theoretical value for the ($HH_1 \to C_1$) transition is 84 ± 6 meV lower at 5 K and 64 ± 6 meV lower at 77 K for all of the superlattices with the exception of the three with extremely narrow well or barrier widths, i.e. Q250, Q211 and Q178. The temperature dependence of the transition from the first light hole subband to the first conduction subband ($LH_1 \to C_1$) is somewhat smaller and that of the higher order transitions, e.g. $HH_2 \to C_2$, is less regular. These statements concerning the relative temperature dependence of the subband transitions are true for all of the investigated superlattices with the exception stated above. The step in the absorption coefficient between 800 and 900 meV, which is due to $HH_2 \to C_2$ and $HH_3 \to C_3$ in this case, is nearly temperature independent.

A comparison of the experimentally and theoretically determined absorption coefficients is made in Fig.9 for the superlattice Q426 at 300 K. The fit for Q426 as well as for Q424, which is shown in Figs. 7 and 8, is excellent with two exceptions, when one considers the fact that no adjustable parameters were used in the theoretical calculations. The first exception is the discrepency in the minor structure due to the $LH_1 \to C_1$ transition which is sometimes refered to as the interface subband to conduction subband ($I_1 \to C_1$) transition. This discrepency is not understood at the present time. One possible cause of the shift of the experimental peak to higher energies is the Burstein-Moss
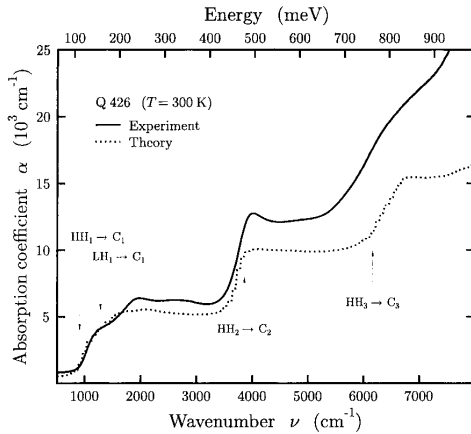
FIG. 9. The experimental and theoretical optical absorption coefficient as a function of wavenumber (cm^{-1}) and energy (eV) for the superlattice Q426 at 300 K. Theoretically determined values of various subband transitions are indicated, e.g. $HH_1 \rightarrow C_1$.
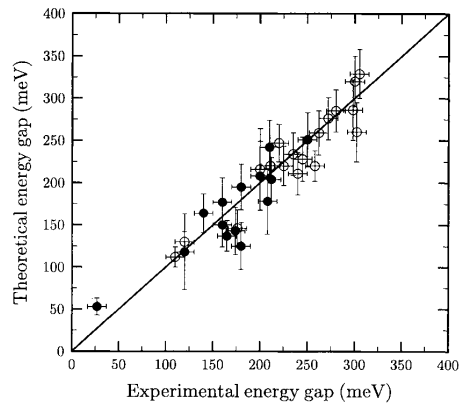

FIG. 10. Experimental and theoretical values of the energy gap, i.e. $HH_1 \rightarrow C_1$. Values for 300 K are indicated by empty circles and those for 5 K by filled circles. The error bars for the theoretically determined energy gap correspond to the experimental uncertainity in the well and barrier thicknesses, i.e. ± 3 Å or about one monolayer.

shift due to filling of either the conduction or valence subband. However according to our calculations, a shift of the Fermi energy from the valence band HH_1 to the conduction band C_1 for Q424, which corresponds to a carrier concentration of $> 2 \times 10^{17}$, can not account for this discrepency. The second exception is the difference in magnitude of the absorption coefficient at higher energies which is only partially due to an increased experimental uncertainity in the absorption coefficient for larger absorption coefficients.

Experimental and theoretical values for the energy gap, i.e the $HH_1 \rightarrow C_1$ transition for these superlattices, are listed in Table 1 and shown in Fig.10. The energy of the $HH_1 \rightarrow C_1$ transition depends on the period, the well thickness and on the x_o value of the barrier in a complicated manner. However the structure in the absorption coefficient between 800 and 900 meV depends only on the x_o value of the barrier. The energy and the shape of this structure in the absorption coefficient is only in good agreement with theory if the x_o value of the barrier is taken to be 0.68 ± 0.02, with the following exception.

Theoretical values for the energy gap and the absorption coefficient for the superlattices with extremely narrow well or barrier widths, i.e. Q250, Q211 and Q178, were in satisfactory agreement with experiment, only if the x_o value of the barrier was assumed to be less than 0.68 ± 0.02, e.g. 0.40 for Q250. Apparently there is less Cd in very narrow barriers than expected if the Cd concentration profile as determined by Kim *et al.*[8] is assumed to be applicable for these barriers.

IV. CONCLUSIONS

Both the well width as well as the period of a number of MBE grown short period (001) $Hg_{1-x}Cd_xTe$-HgTe superlattices were determined directly by x-ray diffraction. The well width was determined by exploiting the high reflectivity from HgTe and the low reflectivity from CdTe for the (002) Bragg reflection. An upper limit for the average composition of the barriers, $\bar{x}_b$, was determined for the barriers. $\bar{x}_b$ was found to decrease exponentially with decreasing barrier width, e.g. $\bar{x}_b \approx 0.64$ and 0.36 for barrier widths of 90.7 and 20.0 Å respectively. This exponential dependence can be explained by assuming that the width and shape of the $Hg_{1-x}Cd_xTe/HgTe$ interface

of all the investigated superlattices are identical to an experimentally determined concentration profile.[8] The relative importance of this interface, i.e. interdiffusion between the barrier and well, increases with deceasing barrier width.

The experimentally determined energy gap at 5 and 300 K for all the investigated superlattices with only several exceptions are in good agreement with theoretical predictions. As mentioned above, this theory does not contain any adjustable parameters. This statement concerning good agreement between experiment and theory is also true for the absorption coefficient. The energy gap which is due to the $HH_1 \rightarrow C_1$ transition for these superlattices depends on the period, the well thickness and on the x_o value of the barrier in a complicated manner. However the structure in the absorption coefficient between 800 and 900 meV depends only on the x_o value of the barrier. The energy and the shape of this structure in the absorption coefficient is only in good agreement with theory if the x_o value of the barrier is taken to be 0.68 ± 0.02 with the exception of superlattices with extremely narrow wells or barriers.

ACKNOWLEDGMENTS

[a] Permanent Address: Shanghai Institute of Technical Physics, Chinese Academy of Sciences, Shanghai, People's Republic of China

[1] J.N.Schulman, and T.C.McGill, Appl. Phys. Lett. **34**, 663 (1979).

[2] J.P.Faurie, A.Million and J.Piaguet, Appl. Phys. Lett. **41**, 713 (1982).

[3] J.P.Faurie, IEEE J. Quantum Electron. **QE-22**, 1656 (1986).

[4] T.C.McGill, G.Y.Wu and S.R.Hetzler, J. Vac. Sci. Technol. A **4**, 2091 (1986).

[5] J.R.Meyer, C.A.Hoffman and F.J.Bartoli, Semicond. Sci. Technol. **5**, S90 (1990) and references therein.

[6] D.L. Smith, T.C.McGill and J.N. Schulman, Appl. Phys. Lett. **43**, 180 (1983).

[7] J. Reno and J.P. Faurie, Appl. Phys. Lett. **49**, 409 (1986).

[8] Y.Kim, A.Ourmazd, M.Bode and R.D.Feldman, Phys. Rev. Lett. **63**, 636 (1989).

[9] J.N.Schulman, O.K.Wu, E.A.Patten, J.W.Han, Y.Lansari, L.S.Kim, J.W.Cook, Jr. and J.F.Schetzina, Appl. Phys. Lett. **53**, 2420 (1988).

[10] M. Möller, R.N. Bicknell-Tassius and G. Landwehr, J. Appl. Phys. **72**, 5108 (1992).

[11] C.R. Becker, L. He, M.M. Regnet, M.M. Kraus, Y.S. Wu, G. Landwehr, X.F. Zhang and H. Zhang, to be published in J. Appl. Phys., Aug. (1993).

[12] L.R. Ram-Moham, K.H. Yoo and R.L. Aggarwal, Phys. Rev. B **38**, 6151 (1988).

[13] N.F. Johnson, H. Ehrenreich, P.M. Hui and P.M. Young, Phys. Rev. B **41**, 3655 (1990).

[14] A. Simon, D. Bertho, D. Boiron and C. Jonanin, Phys. Rev. B **42**, 5221 (1990).

[15] E. Bangert, P. Boege, V. Latussek and G. Landwehr, Semicond. Sci. Technol. **8**, S99 (1993).

[16] Y.S.Wu, C.R.Becker, A.Waag, R.N.Bicknell-Tassius and G. Landwehr, Appl. Phys. Lett. **60**, 1878 (1992).

[17] Y.S. Wu, C.R. Becker, A. Waag, R. Schmiedl, S. Einfeldt and G. Landwehr, J. Appl. Phys. **73**, ... (1993).

[18] Y.S.Wu, C.R.Becker, A.Waag, R.N.Bicknell-Tassius and G. Landwehr, J. Appl. Phys. **69**, 268 (1991).

[19] M.Quillec. *Structural Characterization of Superlattices by x-Ray diffraction.*, Springer Proceedings in Physics (Les Houches, France, 1986), Vol. 13, pp. 121 ff.

[20] G.L. Hansen, J.L. Schmit and T.N. Casselman, J. Appl. Phys. **53**, 7099 (1982).

[21] R.R. Galazka and A. Kisiel, Phys. stat. sol. **34**, 63 (1969).

[22] L. He, C.R Becker, R.N. Bicknell-Tassius, S. Scholl and G. Landwehr, J. Appl. Phys. **73**, 3305 (1993).

[23] M.H. Weiler, *Semiconductors and Semimetals*, Vol. 16, editors R. Willardson and A.C. Beer, Academic Press, New York, pp. 119, 1981.

[24] C.K. Shih and W.E. Spicer, Phys. Rev. Lett. **58**, 2594 (1987).

[25] M.M. Kraus, M.M. Regnet, C.R. Becker, R.N. Bicknell-Tassius and G. Landwehr, J. Appl. Phys. **71**, 5610 (1992).

[26] T.H. Myers, R.W. Yanka, K.A. Harris, A.R. Reisinger, J. Han, S. Hwang, Z. Yang, N.C. Giles, J.W. Cook Jr., J.F.Schetzina, R.W. Green and S. McDevitt, J. Vac. Sci. Technol. A **7**, 300 (1989).

[27] J.Reno, R.Sporken, Y.J.Kim, C.Hsu and J.P.Faurie, Appl. Phys. Lett. **51**, 1545 (1987).

[28] E. Monterrat, L. Ulmer, R.Mallard, N.Magnea and J.L. Pautrat, J. Appl. Phys. **73**, 1774 (1992).

142

The optical absorption coefficient of HgTe–CdTe superlattices—theory and experiment

E Bangert, P Boege, V Latussek and G Landwehr

Physikalisches Institut, Universität Würzburg, 8700 Würzburg, Federal Republic of Germany

Abstract. On the basis of Kane's band model we apply the envelope-function method to calculate the superlattice states. Inserting these results into Kubo's formula the dynamical conductivity for interband transitions is derived. Adding the lattice contribution of the dielectric function we obtain the complex refractive index. Our results are compared with experimentally determined absorption coefficients, measured with Fourier transform spectroscopy on MBE-grown superlattices fabricated on a Riber 2300 system at our institute.

1. Introduction

During the last decade a rather large number of papers concerning the calculation of semiconductor superlattice states have been published [1–3].

Among the various approaches concerning this problem are two extremal ones, namely the tight-binding and the envelope-function method. Ram-Moham et al [2] applied the envelope-function method and deduced a transfer matrix formulation to calculate the superlattice states. He accounted for the full 8×8 Kane Hamiltonian including all second-order terms representing the far-band contributions, but did not utilize his results for a calculation of the optical constants. On the other hand Johnson et al [3] again applied the envelope-function method in a slightly different version, and deduced optical constants from his superlattice energies and state functions. But in his approach he used a simplified band model, which omits all the second-order far-band contributions with the exception of a finite heavy-hole mass. Therefore, we combine the essential aspects of both approaches and calculate the optical constants based on a realistic band structure model, which includes all the second-order higher band contributions. This should be a sound basis for a realistic comparison between the theoretical mode and experiments.

Our envelope-function approach differs formally from previous ones [2, 3]. It was conceived in such a way that it yields a large number of superlattice energies, wavefunctions and dipole matrix elements, which enter the calculation of the optical absorption and dispersion. The bulk bands of both materials are described by Kane's four-band model (8×8 $k \cdot p$ matrices) including second-order far-band contributions, but neglecting the small anisotropy of the valence bands. The numerical values

of the band parameters, E_g, Δ, γ_1, γ_2, γ_3, m^* and E_p, are obtained from Weiler [4], they are deduced from measurements on bulk samples of HgTe and $Hg_{1-x}Cd_xTe$. The layer thicknesses d_1, d_2 ($d_1 + d_2 = a =$ superlattice period) were determined by x-ray diffraction. Since during the growth of the superlattices on which the optical absorption was measured the Hg shutter was always open, the barriers contain Hg. From thin (HgCd)Te films, which were grown under identical conditions, the mercury content was determined from optical measurements to be about 20% ($x = 0.8$). The valence band offset was chosen as 350 meV, which is the generally accepted value [5]. Therefore our calculated superlattice states, and moreover the resulting optical constants, contain no fitting parameters, so that the comparison with experimental results can be considered as a reliable test of the theoretical model.

Since the envelope-function approach has become a standard technique in semiconductor physics, we omit the details of the calculation, but point out the essentials:

(i) according to the '8×8 matrix' form of Kane's model we deal with eight component envelope functions $\Psi = (\varphi_1, \ldots, \varphi_8)$

(ii) as boundary conditions for matching the envelope functions at the interface we apply: (a) $\varphi_i(z)$ continuous, $i = 1 \ldots 8$; (b) $v_z\Psi(z)$ continuous, where v_z is the velocity operator which is in the $k \cdot p$ scheme written as

$$v_z = \frac{1}{\hbar} \frac{\partial H(k_\parallel, k_z)}{\partial k_z}\bigg|_{k_z \to \frac{1}{i}\frac{\partial}{\partial z}}.$$

Condition (b) ensures the probability current conservation (growth is in the z direction).

Figure 1 shows the dispersion of various superlattice

E Bangert *et al*
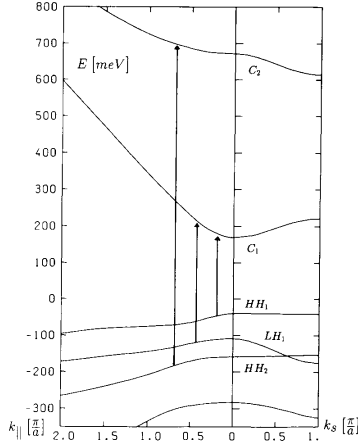
Figure 1. Energy bands of a HgTe (40 Å)/Hg$_{0.2}$Cd$_{0.8}$Te (36 Å) superlattice. Superlattice dispersion $E_i(0, k_s)$ right-hand side, in-plane dispersion $E_i(k_\parallel, 0)$ left-hand side. HH$_i$ means heavy hole bands, LH$_i$ light hole bands, and C$_i$ conduction bands. The energy gaps and the valence band offset are adjusted according to the given temperature ($T = 300$ K) and the indicated Cd content [4]. $E = 0$ corresponds to the bottom of the bulk HgTe conduction band. Arrows indicate the transitions with appreciable contributions to the optical constants.

bands $E_i(k_\parallel, k_s)$. The dispersion in the growth direction (right-hand side) is weak compared with the in-plane dispersion (left-hand side). For $E < 0$ the heavy-hole bands (HH$_i$) dominate the spectrum, one light-hole band—often referred to as the interface state—is found at about -150 meV. All bands are far from parabolic. The dominant transitions contributing to the optical constants are marked by arrows.

For the calculation of the real part $n(\omega)$ and the imaginary part $k(\omega)$ of the complex refractive index $N(\omega)$ we apply the relation

$$N^2(\omega) = (n(\omega) + ik(\omega))^2 = \varepsilon_L(\omega) + i\frac{\sigma(\omega)}{\omega\varepsilon_0}$$

where $\varepsilon_L(\omega)$ is the lattice contribution. The dynamical conductivity $\sigma(\omega)$ is obtained by making use of Kubo's formula

$$\sigma(\omega) = \frac{e^2}{V}\int_0^\infty e^{-i\omega t}\,dt\int_0^\beta d\lambda\,\mathrm{Tr}[\rho v(-i\hbar\lambda)v(t)]$$

$$= \pi\frac{e^2}{V\omega}\sum_{\alpha,\beta}|v_{\alpha\beta}|^2\delta(\hbar\omega + \hbar\omega_{\alpha\beta})(f_\alpha - f_\beta)$$

$$+ i\frac{e^2\hbar}{V}\sum_{\alpha,\beta}|v_{\alpha\beta}|^2\frac{1}{\hbar\omega_{\alpha\beta}}\frac{f_\alpha - f_\beta}{\hbar\omega + \hbar\omega_{\alpha\beta}}$$

Here α, β denote the superlattice states e.g. $|\alpha\rangle = |i, k_\parallel, k_s\rangle$ with energy $\varepsilon_\alpha = \varepsilon_i(k_\parallel, k_s)$ and $\hbar\omega_{\alpha\beta} = \varepsilon_\alpha - \varepsilon_\beta$. f is the Fermi function. The dipole operator for the
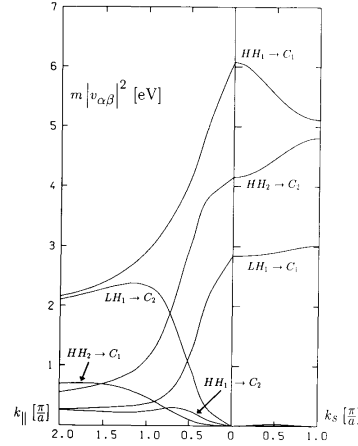
Figure 2. Transition probabilities for the superlattice characterized in figure 1 as a function of $k_\parallel$ and k_s. A strong decrease along $k_\parallel$ for the dominant transitions HH$_i \rightarrow$ C$_i$ and LH$_1 \rightarrow$ C$_1$ is demonstrated. The transition LH$_1 \rightarrow$ C$_2$, which is forbidden at $k = 0$ becomes allowed with increasing in-plane $k_\parallel$ value.

optical transitions is essentially the velocity operator, which is in the $\boldsymbol{k \cdot p}$ scheme written as

$$v = \frac{1}{\hbar}\frac{\partial H_{\mathrm{Kane}}}{\partial k_\parallel}.$$

The matrix elements $v_{\alpha\beta} = \langle i, k_\parallel, k_s|v|j, k_\parallel, k_s\rangle$ depend strongly on $k_\parallel$ but are smooth functions of k_s as can be seen from figure 2 for various transitions. Transitions like LH$_1 \rightarrow$ C$_2$ and HH$_2 \rightarrow$ C$_1$, which are forbidden at $k = 0$ become allowed for finite $k_\parallel$ values. It is important to incorporate these dependences in the calculation of $\sigma(\omega)$. We evaluate Re$(\sigma(\omega))$ and Im$(\sigma(\omega))$ separately. This allows us to obtain both $n(\omega)$ and $k(\omega)$.

In figures 3 and 4 we present our theoretical results by full curves obtained by the procedure described above for two superlattices. The absorption coefficient $\alpha(\omega) = (\omega/c)k(\omega)$ represents all possible interband transitions, but only two steps at 270 meV and 750 meV (figure 3) separated by a plateau are prominent in the absorption. These steps arise from the onset of the HH$_1 \rightarrow$ C$_1$ and HH$_2 \rightarrow$ C$_2$ transitions. A considerable dipole matrix element belongs to the LH$_1 \rightarrow$ C$_1$ transitions which contribute only in the plateau region.

The mean value of $n(\omega)$ is dominated by the lattice dielectric constant $\varepsilon(\omega)$, which is independent of ω in our frequency region and equal to 10 [6]. The variation of $n(\omega)$ due to the considered transitions turns out to be only 0.3.

The experimentally determined absorption spectrum $\alpha(\omega)$ (broken curves in figure 3 and figure 4) were extracted from reflection $R(\omega)$ and transmission $T(\omega)$ measurements of superlattices grown on semi-insulating CdTe substrates by MBE. About 20 superlattices of

144
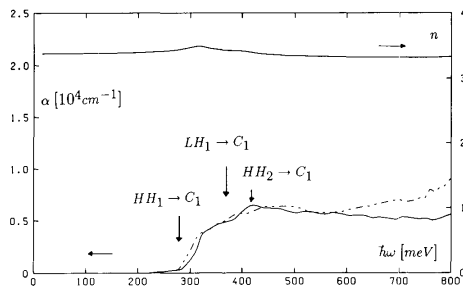
Figure 3. Comparison between theoretical (full curves) and experimental (broken curves) absorption spectra in the photon energy range 0–800 meV for the same superlattice as figure 1. Arrows indicate the onset of the different transitions. The upper full curve represents our calculated refractive index, showing only a weak radiation-frequency dependence.
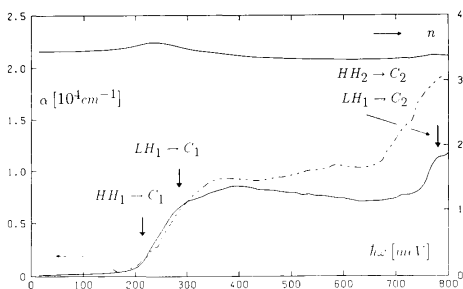
Figure 4. Comparison between theoretical (full curves) and experimental (broken curves) absorption spectra in the photon energy range 0–800 meV for a HgTe (35 Å)/Hg$_{0.2}$Cd$_{0.8}$Te (72 Å) superlattice. Arrows indicate the onset of the different transitions. The second plateau is approaching, but not yet developed.

different well and barrier thicknesses were produced with 100 periods each. Our analysis of the experimental $R(\omega)$ and $T(\omega)$ results accounts for both layers—superlattice and substrate—randomizing the rapid oscillations of R and T due to the thick substrate in accordance with the limited resolution of the Fourier spectrometer (Bruker IFS 88).

Keeping in mind that all input quantities for the theoretical calculation originate from independent measurements, the prominent structures (figure 3) of the experimentally determined absorption data are well reproduced by the theory, so that the interpretation of the observed absorption in terms of transitions between the indicated superlattice states seems very reasonable. The plateau in the interval from 350 to 700 meV can be interpreted as a balance between an increasing number of transitions and decreasing dipole matrix elements for large $k_\parallel$ values. It is interesting to notice that the increase in the absorption at about 750 meV, which is marked as $LH_1 \to C_1$ and $HH_2 \to C_2$, is about 50% due to the $LH_1 \to C_2$ transition, which is forbidden at $k_\parallel = 0$ but becomes allowed and strong at $k_\parallel = (\pi/a)$, as can be deduced from figure 2 and figure 1. In figure 4, data for a superlattice with different well and barrier widths are shown and compared with theory. The agreement is also satisfying: the second plateau is approaching, but not yet developed. It should be mentioned that our theoretical model also allows the description of previous experimental data [5].

Acknowledgment

References

[1] Meyer J R, Hoffman C A and Bartoli F J 1990 *Semicond. Sci. Technol.* **5** 90 and references therein
[2] Ram-Moham L R, Yoo K H and Aggarwal R L 1988 *Phys. Rev.* B **38** 6151
[3] Johnson N F, Ehrenreich H, Hui P M and Young P M 1990 *Phys. Rev.* B **41** 3655
[4] Weiler M H 1981 *Semiconductors and Semimetals* vol 16 eds R Willardson and A C Beer (New York: Academic) p 119
[5] Lansari Y, Han J W, Hwang S, Kim L S, Cook J W Jr, Schetzina J F, Schulman J N and Otsuka N 1989 *J. Vac. Sci. Technol.* B **7** 241
[6] Chang Y C, Cheung J, Chiou A and Khoshnevisan M 1990 *J. Appl. Phys.* **68** 4233

Anhang D

Magnetotransport in Typ-III-Halbleiterheterostrukturen

Quantum transport in n-type and p-type modulation-doped mercury telluride quantum wells

G. Landwehr, J. Gerschütz, S. Oehling, A. Pfeuffer-Jeschke *, V. Latussek, C.R. Becker

Physikalisches Institut der Universität Würzburg, Am Hubland, 97074 Würzburg, Germany

Abstract

Asymmetrically modulation-doped HgTe quantum wells of (0 0 1) orientation were produced by molecular beam epitaxy. N-type doping was achieved with iodine and p-type doping by the incorporation of nitrogen. At 4.2 K the n-type samples have electron mobilities up to 10^5 cm^2/Vs, the maximum Hall mobility of the p-type specimens is around 2×10^4 cm^2/Vs. Very pronounced Shubnikov–de Haas oscillations were observed in both n-type and p-type samples. In the n-type specimens the quantum oscillations persisted up to temperatures of 60 K. The Shubnikov–de Haas oscillations in the p-type samples were highly irregular. Because the data cannot be explained without detailed theoretical calculations of Landau levels for the heterostructure self consistent Hartree calculations were performed using a $8 \times 8 \boldsymbol{k} \cdot \boldsymbol{p}$ model. The magnetic field-dependent density of states was calculated. More regular oscillations are predicted at higher magnetic fields approaching 30 T. © 2000 Elsevier Science B.V. All rights reserved.

PACS: 72.20.M; 73.61.G; 71.20.M

Keywords: HgTe; Quantum wells; Magnetotransport; Band structure

In the past, quantum transport experiments on n-type modulation-doped HgTe heterostructures have been performed primarily on superlattices and multiple quantum wells (MQW). Shubnikov-de Haas (SdH) oscillations and quantum Hall effect have been observed in those samples [1,2]. Quantum transport effects in modulation-doped n-type HgTe single quantum wells (SQW) grown by molecular beam epitaxy were initially reported by Goschenhofer et al. [3]. These samples show very pronounced SdH oscillations in a temperature range between 1.6 and 60 K together with well-pronounced quantum Hall plateaus at low temperatures. Fig. 1 shows the temperature dependence of the magnetoresistance and the Hall effect for one sample with a mobility of 68.2×10^3 cm^2/Vs and a carrier concentration of 5.16×10^{11} cm^{-2}. The existence of SdH oscillations up to 60 K is the consequence of the small effective mass of about $0.02m_0$ [4]. At low temperatures spin splitting is observed for magnetic fields above 2 T. Quantum Hall plateaus at all integer filling factors are observed in this regime.

* Corresponding author. Tel.: +49-931-885869; fax: +49-931-885142.

E-mail address: pfeuffer@physik.uni-wuezburg.de (A. Pfeuffer-Jeschke)

148
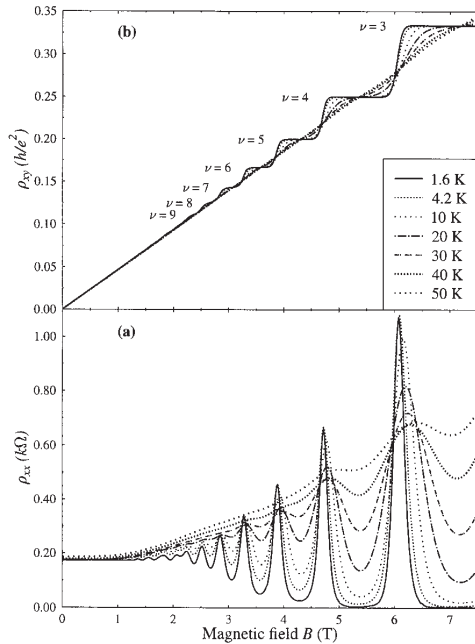
Fig. 1. Temperature dependence of the SdH oscillations (a) and the quantum Hall effect (b) for a n-type HgTe QW.

For specimens with a small carrier concentration of about $1.6 \times 10^{11}\,\mathrm{cm}^{-2}$ the plateau with occupation number of 1 at 25.813 kΩ was achieved at a field strength of about 4 T.

In this article we shall concentrate on p-type modulation-doped HgTe SQWs. Quantum transport experiments on intrinsic p-type HgTe/HgCdTe superlattices and intrinsic p-type HgTe/HgCdTe SQWs have been reported in the literature [5,6]. Whereas the superlattices showed Hall mobilities up to $30 \times 10^3\,\mathrm{cm}^2/\mathrm{Vs}$ the mobility of the SQWs was only about $1 \times 10^3\,\mathrm{cm}^2/\mathrm{Vs}$. SdH oscillations and quantum Hall effect were evident in the SQWs, but the SdH oscillations were not pronounced. A weakly developed Hall plateau at filling factor 2 was observed and a very wide one at filling factor 1 ranging from a magnetic field of 4 T to a magnetic field of 15 T. To our knowledge no quantum transport results have yet been reported on p-type modulation-doped HgTe SQWs.

We have produced asymmetrically modulation-doped (0 0 1) HgTe QWs with $Hg_{0.3}Cd_{0.7}Te$ barriers by molecular beam epitaxy (MBE) in which the overlying CdTe layer was doped with nitrogen. All samples were grown on $Cd_{0.96}Zn_{0.04}Te(0\,0\,1)$ substrates. A $Hg_{0.3}Cd_{0.7}Te$ barrier with thickness of 26 nm was grown on top of a 100 nm thick CdTe buffer. The thicknesses of the subsequently grown HgTe QWs varied from 12 to 20 nm. The upper barrier consisted of a 2 nm $Hg_{0.3}Cd_{0.7}Te$ layer. This QW structure was separated from the doped layer by a spacer. The spacer consisted of a 2 nm thick graded gap transition from HgCdTe to CdTe and a 2.5 nm thick CdTe layer. The CdTe layers with a typical thickness of 12 nm were doped with nitrogen at growth temperatures between 220°C and 230°C. All samples are fully strained as was confirmed by high-resolution X-ray diffraction.

Magnetotransport measurements have been performed up to magnetic fields of 10 T and for temperatures between 1.6 and 4.2 K. All samples showed a high degree of homogeneity as confirmed by measurements in different magnetic field orientations and with redundant contact combinations. The hole densities deduced from the classical Hall effect varied between 4.7×10^{11} and $8.65 \times 10^{11}\,\mathrm{cm}^{-2}$ at 1.6 K and the mobility varied between 14.3×10^3 and $35.8 \times 10^3\,\mathrm{cm}^2/\mathrm{Vs}$. At 1.6 K the samples showed well-pronounced SdH oscillations and the quantum Hall effect was evident, even though the plateaus were not well developed. In contrast to the n-type samples mentioned above the oscillations died out very fast with increasing temperature as a consequence of the large mass of the holes. Fig. 2 shows the magnetoresistance and the Hall effect of a typical sample with a well width of 15 nm, a carrier concentration of $8.65 \times 10^{11}\,\mathrm{cm}^{-2}$ and a Hall mobility of $14.3 \times 10^3\,\mathrm{cm}^2/\mathrm{Vs}$ at 1.6 K. Weakly developed Hall plateaus at filling factors of 10, 7, 5 and 4 can be observed and the SdH oscillations are highly irregular. If one takes the Hall plateaus seriously the sequence of minima in the SdH oscillations cannot be associated with a regular sequence of filling factors. Nevertheless the information about the filling factor is useful in determining a hole concentration which can be compared to that of the Hall effect. For a carrier concentration of $p = 8.65 \times 10^{11}\,\mathrm{cm}^{-2}$ we expect minimia in the SdH oscillations according to the formula $B = hp/ev$ for filling factors of $v = 10, 7, 5$
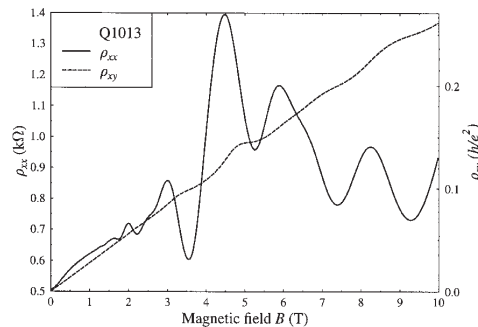
Fig. 2. SdH oscillations and Hall effect of a p-type sample at 1.6 K.

Fig. 3. Self consistently calculated band structure of a HgTe QW with $p = 8.0 \times 10^{11}$ cm^{-2}.

and 4 at magnetic fields of about 3.6, 5.1, 7.1 and 8.9 T respectively. These values coincide quite well with the position of the minima in the magnetoresistance.

Irregular patterns in the SdH oscillations are well known from heterostructures with two or more occupied subbands [7]. In order to understand main features of the data we have performed self-consistent Hartree calculations of the band structure based on a $8 \times 8 \boldsymbol{k} \cdot \boldsymbol{p}$ model. The model includes all second-order terms representing the remote-band contributions, but neglects the intrinsic inversion asymmetry of the material, which is known to be extremely small. The envelope function approximation is used to calculate the subbands of the heterostructure. We have calculated the band structure of a HgTe QW embedded in Hg$_{0.3}$Cd$_{0.7}$Te barriers taking the anisotropy of the in plane band structure (warping) into account. This anisotropy is known to be negligible for the conduction bands but is important for the valence bands, for the band parameters see Ref. [4].

In the following the results are discussed for a 150 Å wide HgTe SQW with a hole density of 8.0×10^{11} cm^{-2}. HgTe QWs of this thickness are in the so-called inverted semiconducting regime, where the conduction band is the first heavy hole subband (H1) and the valence band is the second heavy hole subband (H2). Fig. 3 shows the self consistently calculated band structure. The subband dispersion is shown for $\boldsymbol{k} = (k_x, k_y)$ in $(0, 1)$ and $(1, 1)$ directions. Whereas the H1 subband is nearly axially symmetric, the importance of the axial asymmetry (warping) of

the H2 subband is obvious. Due to the asymmetric doping of the heterostructure the Hartree potential itself is asymmetric which results in a lifting of the spin degeneracy for each subband for a given k-vector. The band structure demonstrates that the QW is an indirect semiconductor because the maximum of the valence band is not located at the center of the Brillouin zone but at a finite $\boldsymbol{k}$. Only one spin component of the H2 subband is occupied with holes above the Fermi energy. The band structure shown in Fig. 3 results in two Fermi contours for the holes. This is also shown in Fig. 4 where lines of constant energy for the occupied subband have been plotted. Only the first quadrant of the Brillouin zone is shown. The grey area is a ring-like region that is occupied by the holes. In contrast to the inner Fermi contour which is nearly a circle the outer one shows clearly the four fold symmetry of the band structure.

Using the Hartree potential from the self consistent band structure calculation we have calculated the Landau level spectrum from 2 up to 30 T. The Landau levels corresponding to the band structure discussed above have been plotted in the lower part of Fig. 5. Again we have taken the four fold symmetry of the QW into account. This results in four sets of Landau levels with the same symmetry. Landau levels with
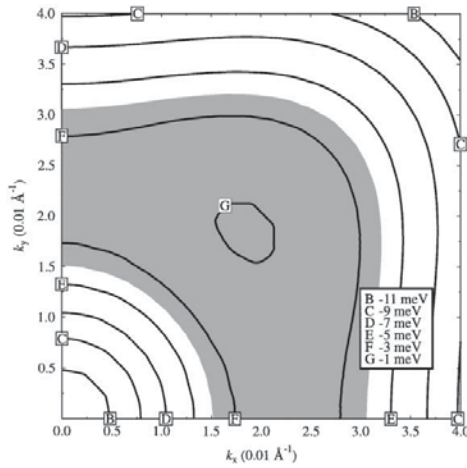
150

Fig. 4. Contour plot of the first valence band with the occupied states (grey area) of the example discussed in the text.
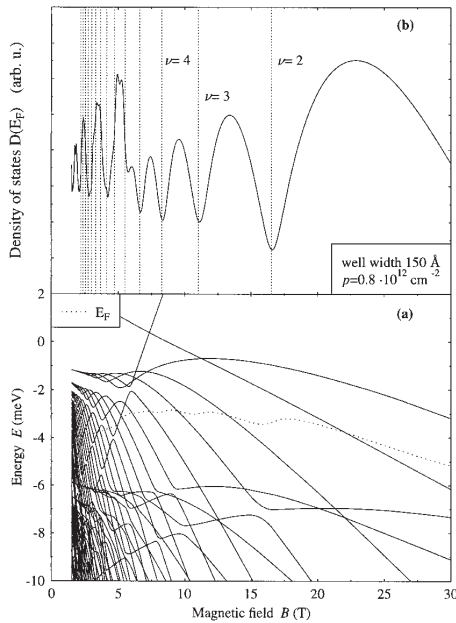

Fig. 5. Landau levels (a) and density of states (b) of a HgTe QW with $p = 8.0 \times 10^{11}$ cm^{-2}.

different symmetry may cross, in contrast to Landau levels with the same symmetry. The anticrossing behaviour is well known from p-type systems where the axial asymmetry of the band structure is important [7]. But due to the complex band structure of the H2 subband this anticrossing behaviour is more pronounced here. It is noteworthy that to our knowledge this is the first Hartree calculation for p-type HgTe QWs and the first calculation of Landau levels in which warping has been taken into account in this system. The Landau level structure is very complicated for small magnetic fields where there is a quasicontinuum. For fields above 7 T we obtain a more regular structure. This can also be seen in the upper part of Fig. 5 where we have plotted the density of states (DOS) at the Fermi energy. Assuming a Gaussian broadening of the Landau levels the DOS has been calculated according to

$$D(E) = \frac{1}{2\pi l_c^2} \sum_n \frac{1}{\sqrt{\pi \Gamma^2}} \exp\left(-\frac{(E - E_n)^2}{\Gamma^2}\right),$$

where $l_c = \sqrt{\hbar/eB}$ is the magnetic length and the sum is over all Landau levels. For the broadening parameter we assumed $\Gamma = \Gamma_0 \sqrt{B/\text{T}}$ with $\Gamma_0 = 0.2$ meV. The oscillations in the DOS below 6 T are highly irregular and the minima in the DOS cannot be associated with integer filling factors (vertical dotted lines in Fig. 5). Above 6 T the oscillations become more regular and the minima can be found at integer filling factors.

In conclusion our calculations have shown that only one subband is occupied in our samples. Due to the fact that the holes are located at finite $\boldsymbol{k}$, irregular oscillations in the DOS arise at lower magnetic fields. More regular SdH oscillations are predicted for higher magnetic fields up to 30 T.

Acknowledgements

References

[1] C.A. Hoffman, J.R. Meyer, F.J. Bartoli, Y. Lansari, J.W. Cook Jr., J.F. Schetzina, Phys. Rev. B 44 (1991) 8376.

[2] C.A. Hoffman, J.R. Meyer, F.J. Bartoli, Semicond. Sci. Technol. 8 (1993) S48.

[3] F. Goschenhofer, J. Gerschütz, A. Pfeuffer-Jeschke, R. Hellmig, C.R. Becker, G. Landwehr, J. Electron. Mater. 27 (1998) 532.

[4] A. Pfeuffer-Jeschke, F. Goschenhofer, S.J. Cheng, V. Latussek, J. Gerschütz, C.R. Becker, R.R. Gerhardts, G. Landwehr, Physica B 256–258 (1998) 486.

[5] K.C. Woo, S. Rafol, J.P. Faurie, Phys. Rev. B 34 (1986) 5996.

[6] K.C. Woo, S. Rafol, J.P. Faurie, Surf. Sci. 196 (1988) 665.

[7] V. Latussek, E. Bangert, G. Landwehr, Ann. Phys. 48 (1991) 394.

MAGNETO-OPTICAL STUDIES OF INVERTED SEMICONDUCTING HgTe/(HgCd)Te SUPERLATTICES GROWN ON CdZnTe AND GaAs SUBSTRATES

M. von TRUCHSESS, A. PFEUFFER-JESCHKE, V. LATUSSEK,
C. R. BECKER, AND E. BATKE

*Physikalisches Institut der Universität Würzburg, Am Hubland,
D-97074 Würzburg, Germany*

We report on far-infrared magneto-optical investigations of inverted semiconducting $HgTe/Hg_{1-x}Cd_xTe$ superlattices. Cyclotron resonances and various interband transitions were observed and compared to the predictions of an 8×8 $k \cdot p$ band structure calculation including an external magnetic field. We will discuss two characteristic transitions that allow us to distinguish an inverted from a semimetallic or normal semiconducting superlattice.

1 Introduction and Experimental Details

Typ-III superlattices composed of the semimetal HgTe and the wide-gap semiconductor $Hg_{1-x}Cd_xTe$ have the unique feature that they can exist either in the normal semiconducting, the semimetallic or the inverted semiconducting regime.[1] Here we present magneto-optical investigations of inverted semiconducting $HgTe/Hg_{1-x}Cd_xTe$ superlattices. Many different transitions that can be classified as cyclotron resonances (CR) and interband transitions (IB) were observed and compared to the predictions of an 8×8 $k \cdot p$ band structure calculation including an external magnetic field B. We found two transitions that are characteristic for an inverted semiconducting superlattice. One is an IB that exhibits a negative magnetic field dispersion at small magnetic fields, the other is a hole cyclotron resonance that can occur only at a magnetic field strength $B > B_C$, where B_C is the critical field for the magnetic field induced

Table 1: Sample parameters for $HgTe/Hg_{1-x}Cd_xTe$ superlattices. d_W and d_B indicate well and barrier width, respectively.

sample	d_W(nm)	d_B(nm)	x	periods	substrate
A	13.8	7.2	0.68	90	(100) $Cd_{0.96}Zn_{0.04}Te$
B	11.9	7.6	0.68	80	(100) GaAs
C	14.0	7.5	0.90	80	(211)B $Cd_{0.96}Zn_{0.04}Te$
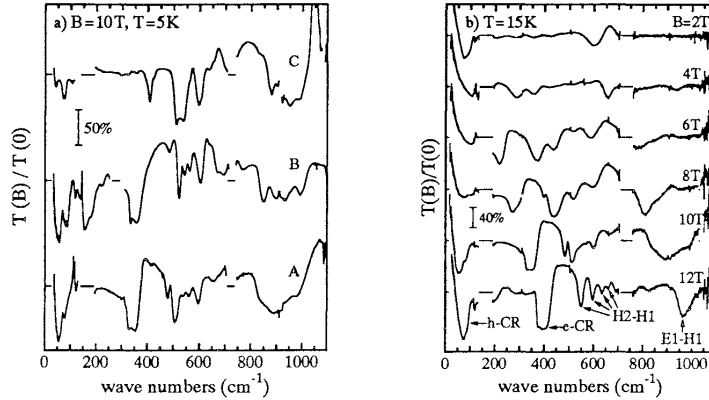
Figure 1: Normalized transmission for a) the samples of Tab. 1 and b) sample A for different magnetic field strengths.

transition from the inverted to the normal semiconducting regime. Our super-lattices were grown by molecular beam epitaxy on different types of substrates.[2] The sample parameters are listed in Tab. 1. Frequency dependent transmission measurements were performed with unpolarized radiation in Faraday geometry with magnetic field up to 12.5 T in the growth direction. Resonances were obtained from the normalized transmission $T(B)/T(0)$.

2 Results and Discussions

In Fig. 1a) we compare transmission spectra for our samples at temperature $T = 5\,K$ and magnetic field strength $B = 10\,T$. Independent of the substrates, we observe for all samples qualitatively similar spectral structures. All samples showed n-type behaviour. For samples A and B the resonance with the rectangular shaped line at about $350\,cm^{-1}$ is an electron CR. Due to the high total electron density this line is saturated, i.e. the CR amplitude is at the theoretical limit of 50% which applies for unpolarized radiation. Because of the smaller total electron density in sample C, the CR line is not saturated. Thus we observe a nearly symmetric line shape at about $400\,cm^{-1}$. Transitions with frequencies above the cyclotron frequency are IB, and those with energies lower than $120\,cm^{-1}$ are hole CR as will be shown below from an analysis of magnetic field dependent measurements for sample A (see Fig. 1b). In Fig. 1b)
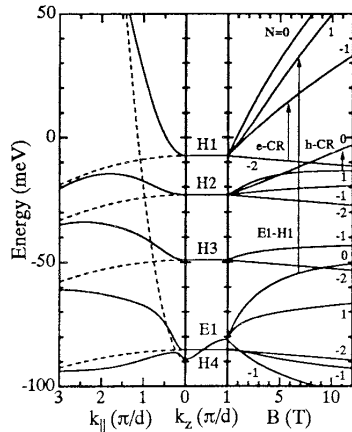
Figure 2: Calculated band structure for sample A at $T = 15$ K.
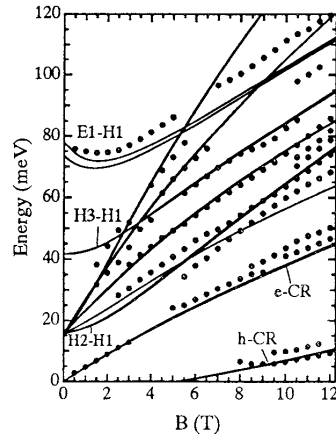
Figure 3: Comparsion between theory and experiment for sample A at $T = 15$ K.

for 12 T electron (e) and hole (h) CR, H2-H1 and E1-H1 IB are marked. All resonances shift with decreasing magnetic field to smaller energies. The h-CR disappears for B < 8T, i.e. can not be separated from the Drude background absorption which induces a frequency dependence of $T(0)$ and increases the normalized transmission in the frequency regime $\bar{\nu} < 100\,\text{cm}^{-1}$. In Fig. 2 we show the calculated band structure for sample A and in Fig. 3 the experimental resonance positions for sample A are compared with the theoretically predicted transition energies. The numerical calculation takes into account the full 8×8 $\mathbf{k} \cdot \mathbf{p}$ Hamiltonian including all second-order terms representing the far-band contributions, an external magnetic field and the effects of strain. The calculation is based on a recently established set of band parameters.[3] The wave vektor $\mathbf{k_z}$ and $\mathbf{k_{||}}$ indicate the dispersion parallel and perpendicular to the growth direction, respectively. The dotted lines show the $\mathbf{k_{||}}$-dispersion if we neglect coupling of the subbands at finite $\mathbf{k_{||}}$. At $\mathbf{k_{||}}=0$ the dispersionless subbands Hj (j $= 1,\ldots,4$) are Γ_8 heavy-hole states, whereas E1 crossing the H4 subband is essentially a mixed Γ_6-Γ_8 light-hole state. Such a band structure is referred to as inverted semiconducting, since H1 forms the conduction band and E1 a valence band. The Fermi energy for our n-type samples lies in the H1 subband. At finite magnetic fields all bands split into Landau-levels,

3

marked with the quantum number $N = -2, -1, \ldots$. For the sake of clarity only the Landau-levels with lowest quantum numbers are shown. All H_j states have a $N = -2$ Landau-level that decreases linearly with increasing magnetic field, whereas for the E1 subband the lowest quantum number is $N = -1$. Some important transitions are indicated by arrows and appropriatly labeled, e.g. the e-CR of the H1 subband $(N = -2 \rightarrow N = -1)$ and the transition $(N=1 \rightarrow N=0)$ of the H2 subband, which we interprete as a h-CR. However, at sufficently high magnetic field strengths the $N=0$ state of the H2 subband becomes a conduction band state and the transition might be classified as an IB. In n-type samples the h-CR can only be observed when the final state $(N=0)$ is not occupied. This occurs for magnetic fields larger than $B_C=7.8\,\mathrm{T}$, which is the critical magnetic field where the H2 $N = 0$ state crosses the H1 $N = -2$ state. At $B=B_C$ the magnetic field induced transition from the inverted to the normal semiconducting regime occurs. The E1-H1 IB exhibits a negative magnetic field dispersion at small magnetic fields, since the E1 $N=0$ energy increases faster with magnetic field than the H1 $N = 1$ energy, as is observed (see Fig. 3). At higher magnetic fields, E1 $N=0$ is essentially independent of B such that the transition energy is dominated by the magnetic field dependence of the H1 $N = 1$ state. In the limit of vanishing magnetic fields, only the H2-H1 IB can be nearly linearly extrapolated to the H2-H1 subband separation. In conclusion, CR and IB were investigated from magneto-optical measurements on inverted semiconducting $HgTe/Hg_{1-x}Cd_xTe$ superlattices. Good agreement between the experiment and a $\mathbf{k \cdot p}$ band structure calculation was obtained. Two characteristic transitions for the inverted semiconducting regime were discussed.

Acknowledgements

References

1. N. F. Johnson, P. M Hui, and H. Ehrenreich, *Phys. Rev. Lett.* **61**, 1993 (1988).
2. C. R. Becker, L. He, M. M. Regnet, M. M. Kraus, Y. S. Wu, G. Landwehr, X. F. Zhang, and H. Zang, *J. Appl. Phys.* **74**, 2486 (1993).
3. M. von Truchsess, V. Latussek, R. Sizmann, P. Helgesen, F. Goschenhofer, C. R. Becker, G. Landwehr, and E. Batke, *Phys. Rev.* B **51**, 17618 (1995).

156

Spectroscopy of interface states in HgTe/Hg$_{1-x}$Cd$_x$Te superlattices

M. von Truchsess*, A. Pfeuffer-Jeschke, V. Latussek, C.R. Becker, E. Batke

Physikalisches Institut der Universität Würzburg, Am Hubland, D-97074 Würzburg, Germany

Abstract

Information on interface states in HgTe/Hg$_{1-x}$Cd$_x$Te superlattices has been obtained via studies of interband transitions in an external magnetic field. Interband transitions can exhibit novel characteristic features if interface states are involved. For example, the magnetic field dispersion can be negative at sufficiently small magnetic field strengths if the initial state is an interface state. We discuss in detail the influences of the magnetic field strength, the well and barrier thicknesses, and the temperature on the properties of interband transitions involving interface states. © 1998 Elsevier Science B.V. All rights reserved.

In superlattices composed of the wide gap semiconductor CdTe and the semimetal HgTe, so called interface states can be formed that have a maximum in their probability density at the heterointerfaces and evanesce in the wells and barriers [1]. Such states are a unique feature of type III superlattices, and they owe their existence essentially to the sign reversal of the effective mass of the lighter carriers when the heterointerface is crossed. Despite their uniqueness no experimental evidence has been provided till now for the presence of interface states. In this article we shall demonstrate that interface states can lead to new features for interband transitions in a magnetic field, e.g., the magnetic field dispersion can be negative at sufficiently small magnetic field strengths if the inital state is an interface state. This is somewhat surprising, since both the initial and final state properties determine the interband transitions. However, this opens an experimental opportunity to investigate the properties of interface states in type III superlattices via interband absorption. A detailed investigation is performed to clarify the influence of interface states on interband transitions in a magnetic field. We shall demonstrate that the presence of negative dispersion in interband absorption experiments in type III heterostructures is direct proof that the initial state is an interface state.

* Corresponding author. Tel.: + 49 931 888 5896; fax: + 49 931 888 5143; e-mail: truchs@physik.uni-wuerzburg.de.

Our sample is a HgTe (13.8 nm)–$Hg_{0.32}Cd_{0.68}Te$ (7.2 nm) superlattice of 90 periods grown at a temperature of 180°C on a (1 0 0) $Cd_{0.96}Zn_{0.04}Te$ substrate by molecular beam epitaxy [2]. Interband transitions with a magnetic field B applied in the growth direction were studied with a rapid-scan Fourier transform spectrometer from liquid helium temperature up to room temperature. The corresponding resonances for unpolarized radiation incident perpendicular to the layers were obtained by means of normalized transmission spectra $T(B)/T(0)$.

In Fig. 1 the normalized transmission $T(B)/T(0)$ for 5 K is shown for different magnetic field strengths B. Various transitions between the Landau-levels of different minibands are resolved. With one exception all interband transitions shift nearly linearly with increasing magnetic field strengths to higher energies. The positions of the exceptional transition, which are indicated by arrows for some field strengths, exhibit a negative magnetic field dispersion in the low magnetic field regime, i.e. $B \leqslant 2$ T. At higher fields the transition monotoni-

cally increases in energy with increasing B similar to all other transitions.

In Fig. 2 we show the calculated electronic band structure for our superlattice, where k_z and $k_\parallel$ denote the wave vector parallel and perpendicular to the growth direction, respectively. The calculation includes the complete 8×8 $k \cdot p$ Hamiltonian taking into account the Γ_6, Γ_8, and Γ_7 bulk bands, all second order terms from the far band contributions, the strain in the layers, and an external magnetic field within an axial approximation. Details of the calculation are given elsewhere [3]. Each envelope function at the miniband edge, i.e. $k_\parallel = k_z = 0$, has eight components arising from the eight bulk Bloch functions, one of which has the lowest number of nodes x, where $j = x + 1$. The miniband is then labeled Hj, Lj or Ej ($j = 1, 2, 3, ...$), corresponding to this component of the envelope function associated with the Γ_8 (heavy hole), Γ_8 (light hole), or Γ_6 (electron) bulk bands, respectively. Our superlattice is in the inverted semiconducting
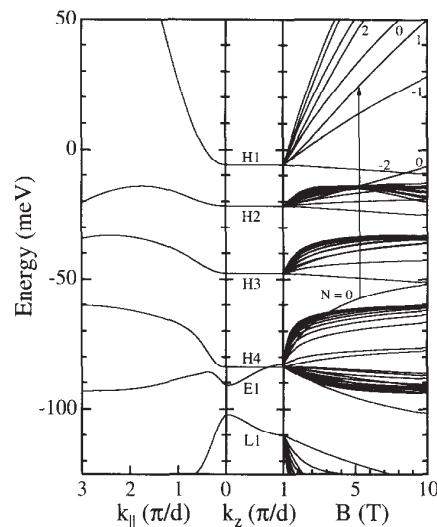

Fig. 1. Normalized transmission $T(B)/T(0)$ for a HgTe (13.8 nm)/$Hg_{0.32}Cd_{0.68}Te$ (7.2 nm) superlattice shown for equal increments of the magnetic field strength B ($\Delta B = 0.2$ T) at liquid helium temperature. The arrows indicate positions of the interband transition with a negative magnetic field dispersion.

Fig. 2. Calculated band structure for the superlattice whose normalized transmission spectra are shown in Fig. 1. $k_\parallel$ and k_z are wave vectors in the superlattice plane and in the growth direction, respectively. Both are given in units of π/d, where d is the superlattice period. The Landau-levels are shown for $k_z = \pi/d$. The arrow indicates the interband transition with negative magnetic field dispersion.

regime, i.e., the E1 miniband is a valence band and the H1 miniband forms the lowest conduction band. The valence bands H2, H3, H4, and E1 show electron-like $E(k_\parallel)$-dispersion at the miniband edges, whereas the dispersion of the L1 and all lower minibands are hole-like. The E1 and H4 minibands are degenerate at $k_z = 0.8 \, \pi/d$, where d is the superlattice period.

In an external magnetic field, the motion perpendicular to the growth direction quantizes, resulting in Landau-levels labeled with the Landau quantum numbers $N \geqslant -2$ [4]. Without loss of generality the Landau-levels are plotted for the upper miniband edges at $k_z = \pi/d$. There is qualitatively no difference in the Landau-level dispersions at the lower and upper miniband edges, except for very small magnetic fields $B \leqslant 0.2$ T. This is due to the anti-crossing of the E1 and H4 $k_\parallel$-dispersions which occurs only at the lower miniband edge. The interband transitions visible in Fig. 1 are transitions between Landau-levels from the E1 and H2 to the H1 miniband. Note that the H2–H1 transitions are symmetry forbidden only for $B = 0$. From all possible transitions, the E1($N = 0$) – H1($N = 1$) transition has the highest oscillator strength in the magnetic field regime shown. Since the $N = 0$ Landau-level of the E1 miniband shows a stronger magnetic field dispersion than the $N = 1$ state of the H1 miniband, a negative magnetic field dispersion for the transition energy is observed at sufficiently small fields. At higher fields the dispersion of the H1($N = 1$) Landau-level dominates and the transition energy increases monotonically with increasing B.

In Fig. 3 the magnitude of the envelope functions squared is shown for the E1($N = 0$) and H1($N = 1$) Landau-levels at different magnetic field strengths. At $B = 0$ the initial state is clearly an interface state, whereas the final state is a normal quantum well state with a maximum in the probability density at the center of the well. With increasing magnetic field strength the minibands begin to mix. At finite values of B the initial state is strongly influenced by contributions of the H4 miniband such that the probability density near the center of the well is enhanced. Thus, at finite values of B one might call the initial state a quasi interface state. With increasing B, the H1 ($N = 1$) state is mixed with L and
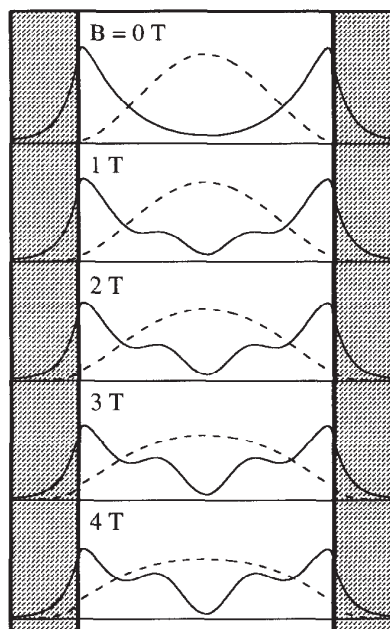

Fig. 3. Calculated magnitude of the envelope functions squared for one period of a HgTe (13.8 nm)/Hg$_{0.32}$Cd$_{0.68}$Te (7.2 nm) superlattice at $k_z = \pi/d$. Solid (dashed) lines indicate the probability density for the $N = 0$ ($N = 1$) Landau-level of the E1 (H1) miniband. The shaded area represents the Hg$_{0.32}$Cd$_{0.68}$Te barrier material.

E states in such a way that the probability density becomes nearly constant across the well.

It needs to be demonstrated whether a negative magnetic field dispersion occurs only if the initial state of an interband transition is an interface state. The necessary conditions for the occurance of a negative magnetic field dispersion in interband absorption are: (1) the effective mass at the miniband edge of the initial state must be lower than that of the final state; (2) both bandedge masses must have the same sign. At a fixed temperature one can tune the effective masses by varying the thicknesses of the wells and barriers. However, if the barrier thickness is large enough for a fixed well thickness, only the widths of the Ej and Lj minibands are slightly affected, and the Hj states, which are essentially quantum well states, show no dispersion in the growth direction. Thus a good

estimate of the effective mass is obtained if a calculation for a single HgTe quantum well versus well thickness is performed.

Fig. 4a and Fig. 4b show calculated subband energies and effective masses at the subband edges, respectively, for a single HgTe quantum well sandwiched between thick $Hg_{0.32}Cd_{0.68}Te$ barriers for a temperature of 5 K. For the sake of simplicity the influence of strain is neglected. The zero in energy in Fig. 4a is assigned to the top of the HgTe bulk valence band edge. For a thin well the conduction band is formed by the E1 subband and the valence band by the H1 subband. This band structure is representative for the normal semiconducting regime. Upon increasing the well width, the E1 subband energy shifts downwards crossing sucessively the Hj subbands. The band structure is then that of an inverted semiconductor. With increasing well thickness, the E1 and L1 subband edges approach each other. Whenever the E1 state crosses a Hj

Fig. 4. (a) Calculated subband energies and (b) subband edge masses vs. well thickness for a HgTe quantum well embedded in $Hg_{0.32}Cd_{0.68}Te$ barriers at liquid helium temperatures. The influence of strain is neglected.

state with odd j (1, 3, 5, ...), the masses undergo a sign reversal. Note that for certain well thicknesses, the E1 effective mass diverges. This is the case, for example at 8.8, 11.6, and 17 nm. At these thicknesses the E1 mass becomes infinite due to the fact that the in plane dispersion at the edges becomes flat. Consequently, for small magnetic fields the Landau-level dispersion is dominated by the Zeeman spin-splitting with a huge effective Landè g-factor of 185 and 330 for a thicknesses of 8.8 and 11.6 nm, respectively.

For a well thickness close to 10 and 12.3 nm the H1 and the E1 masses are equal and both are electron-like. For well thickness from 10 to 11 nm, 12.3 to 16.9 nm and larger than 17 nm, the condition for the observation of a negative magnetic field dispersion in the E1–H1 interband absoption is fullfilled for many transitions between Landau-levels. However, a negative dispersion can also occur for the $E1(N = 0) - H1(N = 1)$ transition for well thicknesses which are larger than 10 nm and at which the E1 mass diverges. This is due to the fact that the Zeeman spin-splitting of the $E1(N = 0)$ results in a magnetic field dispersion exceeding that of the $H1(N = 1)$ Landau-level. For negative energies (see Fig. 4a) the E1 state is an interface state. Thus, if one observes an interband transition with negative magnetic field dispersion at low magnetic field strengths the inital state is always an interface state. At higher magnetic fields the magnetic field dispersion of the transition energy is always dominated by the dispersion of the final state.

The subband energies and effective masses at the subband edges are also strongly influenced by temperature. Increasing the temperature would shift the E1 subband energy up such that the quantum well might become a normal semiconductor. For example the temperature induced transition would occur for our superlattice at about 286 K. At a slightly higher temperature ($T = 301$ K) the E1 state is no longer an interface state.

In summary, we have investigated whether the influence of interface states in $HgTe/Hg_{1-x}Cd_xTe$ superlattices can lead to characteristic features of interband transitions in a magnetic field. It has been shown that an interband transition can exhibit a negative magnetic field dispersion at sufficiently small magnetic field strength if the
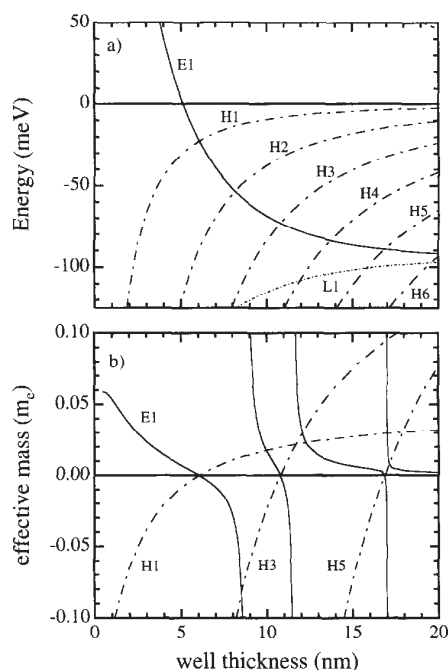
160

initial state is an interface state. For well thicknesses larger than 10 nm there will be at least one interband transition with such a dispersion. The envelope function of the lighter carriers is strongly influenced by the well and barrier thicknesses, the temperature and the magnetic field strength. Due to the temperature dependent Γ_6–Γ_8 band mixing one can transform an interface state to a normal quantum well state by increasing the temperature. Our experiment provides the first experimental evidence for the presence of interface states in $HgTe/Hg_{1-x}Cd_xTe$ superlattices. It was demonstrated, that via interband absorption the properties of interface can be studied.

References

[1] J.N. Schulman, Y.-C. Chang, Phys. Rev. B 33 (1986) 2594.
[2] C.R. Becker, L. He, M.M. Regnet, M.M. Kraus, Y.S. Wu, G. Landwehr, X.F. Zhang, H. Zhang, J. Appl. Phys. 74 (1993) 2486.
[3] A. Pfeuffer-Jeschke, Ph.D. Thesis, Würzburg, 1998.
[4] L.R. Ram-Mohan, K.H. Yoo, R.L. Aggarwal, Phys. Rev. B 38 (1988) 6151.

MBE growth and characterization of HgTe based quantum wells and superlattices

C.R. Becker*, X.C. Zhang, K. Ortner, A. Pfeuffer-Jeschke,
V. Latussek, V. Daumer, G. Landwehr, L.W. Molenkamp

Physikalisches Institut der Universität Würzburg, Am Hubland, D-97074 Würzburg, Germany

Abstract

The MBE growth of type III HgTe/Hg$_{1-x}$Cd$_x$Te heterostructures will be discussed. Spin–orbit (s–o) coupling is particularly large in HgTe based quantum wells; the observed value of 17 meV is at least two to three times larger than values reported in the literature for III–V heterostructures or any other system. Rashba spin–orbit splitting in n type modulation doped quantum wells (QWs) has been investigated as a function of the 2DEG density and compared with self-consistent Hartree calculations based on an $8 \times 8\, \boldsymbol{k} \cdot \boldsymbol{p}$ model. Furthermore the presence of two periodic SdH oscillations in p type QWs with an inverted band structure has been observed and is the first direct evidence that these heterostructures are indirect semiconductors.
© 2003 Elsevier B.V. All rights reserved.

1. Introduction

The Hg$_{1-x}$Cd$_x$Te alloy has been one of the most commercially exploited alloys in recent decades. Recent applications require increasingly complex heterostructures [1]. In addition, physics based on spin in semiconductor heterostructures have recently aroused much interest, not only from the fundamental point of view, but also due to an increased interest in devices which are based on the spin of the electron rather than its charge [2]. It is well known that the bulk inversion asymmetry (BIA) of the crystal structure, e.g., zinc blende, can remove the spin degeneracy of electrons even in the absence of a magnetic field [3,4]. Zero magnetic field spin–orbit (s–o) splitting can also be a consequence of structure inversion asymmetry (SIA) known as Rashba s–o splitting [5,6] such as that found in inversion layers or asymmetric quantum wells (QWs) with an asymmetric confinement potential [7]. The Rashba effect usually dominates in 2D structures [8] and in particular, the influ-

ence of BIA has been shown to be negligible in the HgTe based narrow-gap heterostructures discussed here [9].

The Rashba effect has been investigated by means of experiments involving Shubnikov-de Haas oscillations and self-consistent Hartree calculations based on the band structure via an $8 \times 8\, \boldsymbol{k} \cdot \boldsymbol{p}$ Kane model [10]. The band structure and hence the optical and transport properties of type III heterostructures are largely determined by that of the quantum well. The validity of the band structure and consequently the input parameters, e.g., valence band offset, has been demonstrated by means of absorption experiments on HgTe/Hg$_{0.3}$Cd$_{0.7}$Te superlattices [11].

2. Experimental and theoretical details

Fully strained HgTe/Hg$_{0.3}$Cd$_{0.7}$Te heterostructures were grown by molecular beam epitaxy (MBE) on Cd$_{0.96}$Zn$_{0.04}$Te(001) substrates at a temperature of 180 °C; growth details can be found in [11,12]. n type QWs have been modulation doped either symmetrically or asymmetrically using CdI$_2$. The Hg$_{0.3}$Cd$_{0.7}$Te barriers are composed of a 5–10 nm thick spacer and a 9 nm thick doped layer. A Hg$_{0.3}$Cd$_{0.7}$Te

* Corresponding author. Tel.: +49-931-888-5794;
fax: +49-931-888-5142.
E-mail address: becker@physik.uni-wuerzburg.de (C.R. Becker).

cap layer of ≥ 5.5 nm thickness was subsequently grown. In addition, p type modulation doped HgTe/Hg$_{0.3}$Cd$_{0.7}$Te have been grown using either plasma activated nitrogen or arsenic as the dopant [13,14]. The HgTe width was determined via a dynamic simulation of the $(0\,0\,2)$ and $(0\,0\,4)$ Bragg reflections [11]. The other thicknesses were estimated from the corresponding growth rates. After growth, a standard Hall bar was fabricated by means of a wet chemical etch, then a 200 nm thick Al$_2$O$_3$ film, which serves as an insulating layer, was deposited by electron beam evaporation. Finally Al was evaporated to form a gate electrode. Ohmic indium contacts were fabricated by thermal bonding. The samples were measured in either a He^4 or He^3 cryostat with standard lock-in techniques using a current of 1 μA at temperatures down to 0.4 K and magnetic fields up to 14 T. The mobilities at zero gate voltage and 1.6 K are 1.3×10^5 and 3.5×10^5 cm^2/(Vs) for two n type specimens with well widths of 12 and 21 nm, respectively. The highest observed mobility for a p type HgTe/Hg$_{0.3}$Cd$_{0.7}$Te QW is 1.0×10^5 cm^2/(Vs).

In order to interpret the experimental transport data, self-consistent Hartree based on an $8 \times 8\,\boldsymbol{k} \cdot \boldsymbol{p}$ band structure model including all second order terms in the conduction and valence band blocks of the 8×8 Hamiltonian have been carried out [15,10].

3. Results and discussion

3.1. Rashba s–o splitting

As expected from their high electron mobilities, all n type, modulation doped QWs show very pronounced SdH oscillations and well developed quantum Hall plateaus [10]. The results of a Fourier transformation of the complex SdH oscillations for the symmetrically modulation doped sample Q1605 with a well width of 21 nm are shown in Fig. 1. At a gate voltage, V_g, of 0.2 V, the QW potential is nearly symmetric and only two frequencies, which correspond to the H1 and E2 subbands, are resolved and no splitting of the H1 subband can be observed. For either more positive or more negative gate voltages, a large splitting of the H1 subband is apparent. Besides the main peaks; E2, H1+ and H1−; harmonics can be observed. The largest Hall mobility was 6.0×10^5 cm^2/(Vs) at a gate voltage of 2.0 V; to our knowledge this is the highest value that has been observed for HgTe QWs.

According to self-consistent band structure calculations the first two conduction subbands are H1 and E2, and the valence band is the H2 subband. This is a consequence of the inverted band structure of QWs with a large well width [10]. No splitting of the H1 and E2 subbands for the symmetric case was predicted and none was observed. However in the asymmetric case, a small spin splitting of the E2 subband at finite $k_\parallel$ is predicted as well as a substantially larger splitting of the H1 subband. It should be mentioned here that the two spin split branches of the H1 subband cannot be des-
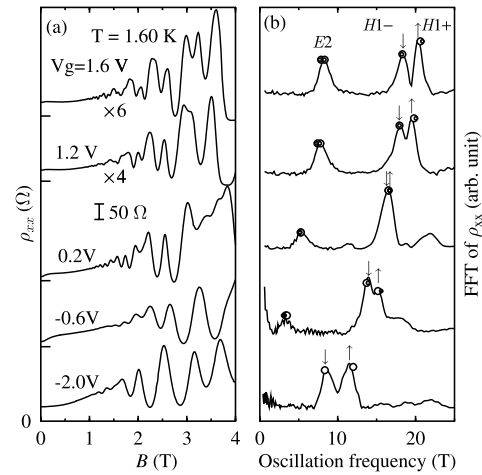

Fig. 1. SdH oscillations in $\rho_{xx}(B)$ (a) and the corresponding fast Fourier transformations (FFT) (b) for a n type symmetrically modulation doped HgTe QW (Q1605) at 1.6 K and various gate voltages. In (b) the up and down arrows represent the two spin states of the H1 subband. The circles represent the results of theoretical calculations for the population of H1 and E2 subbands.

ignated as spin-up and spin-down because their eigenstates are not linearly polarized and do not carry a net magnetic moment [16]. The degeneracy of the H2 valence subband is also removed and one spin component has a larger maximum at finite $k_\parallel$, i.e., here we are dealing with an indirect semiconductor [14].

As can be seen in Fig. 2, the experimental values and the theoretical calculations of the difference in population, Δn_{H1}, between the two spin states of the H1 subband are in good agreement. The calculated carrier densities in both the H1 and E2 subbands at various gate voltages also agree with the experimental values. It should be emphasized that the occupation of the E2 subband depends mainly on the well width and not on the details of the self-consistently calculated Hartree potential.

Winkler [16] has demonstrated that spin splitting for the heavy hole like state $|\Gamma_8, \pm 3/2\rangle$ should be proportional to $k_\parallel^3$ for small $k_\parallel$ values. The spin split heavy hole subband dispersion can be expressed as

$$E_\pm(k_\parallel) = \frac{\hbar^2 k_\parallel^2}{2m^*} \pm \beta k_\parallel^3 \qquad (1)$$

where β is the spin–orbit coupling constant between the Γ_8 and Γ_6 bands. Indeed, the numerical results for ΔE_{H1} shown in Fig. 3 can be described by a cubic dependence on $k_\parallel$ at small values of $k_\parallel$. In contrast, spin splitting for the electron like state $|\Gamma_6, \pm 1/2\rangle$ and the light hole like state $|\Gamma_8, \pm 1/2\rangle$, should be a linear function of $k_\parallel$. This is in good agreement with the self-consistently calculated ΔE_{E2} versus $k_\parallel$ behavior at small values of $k_\parallel$ as shown in Fig. 3.
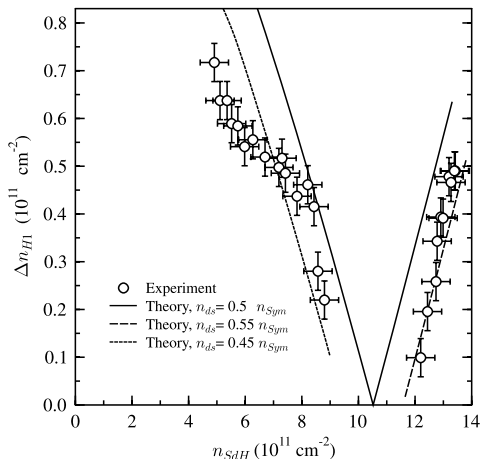
Fig. 2. Experimental (circles) and calculated (lines) population differences Δn_{H1} in the two spin states of the H1 subband as a function of the total charge carrier density, n_{SdH}. The n_{ds} parameter is the depleted charge density in the doped layer on the substrate side. n_{sym} is the carrier density when the QW potential is symmetric. This corresponds to the point when $\Delta n_{H1} = 0$. n_{ds} is employed as an input parameter in the self-consistent Hartree calculations.

3.2. p Type modulation doped QWs

Experimental results shown in Fig. 4 for a p type asymmetrically modulation doped QW, Q1441, with an inverted band structure displays pronounced and complex SdH scillations, which begin below 0.3 T, and well developed quantum Hall plateaus. This QW also has a large mobility, i.e. $\mu = 1.0 \times 10^5$ cm^2/(Vs). Noteworthy is also the large change in the magneto-resistance for magnetic fields up to 0.2 T. If dρ_{xx}/dB is plotted versus $1/B$, two periods can eas-
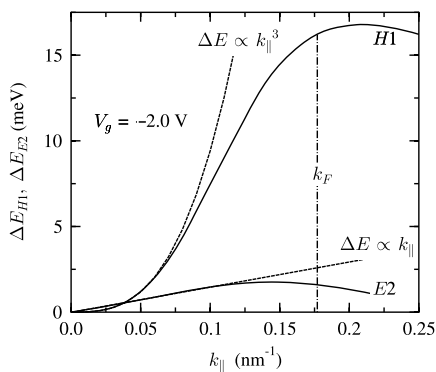
Fig. 3. The calculated spin splitting energy of the H1 and E2 subbands (solid curves), ΔE_{H1} and ΔE_{E2}, vs. in-plane wave vector $k_\parallel$ for sample Q1605 at $V_g = -2.0$ V. The position of the Fermi wave vector k_F is denoted by the dotted-dashed line. The two dashed lines demonstrate that ΔE_{H1} and ΔE_{E2} are proportional to $k_\parallel^3$ and $k_\parallel$, respectively, at small $k_\parallel$.
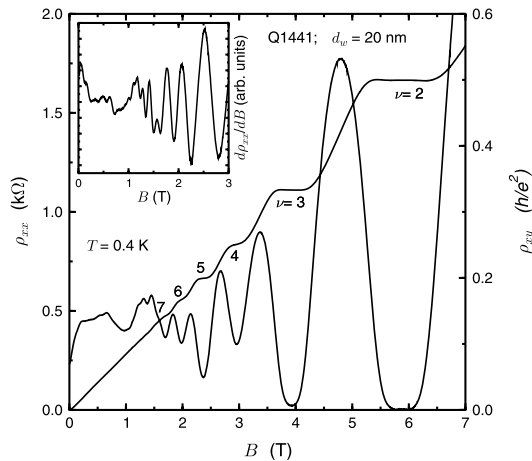
Fig. 4. The quantum Hall effect and SdH oscillations for a p type asymmetrically modulation doped QW, Q1441, with $d_w = 20$ nm at a temperature of 0.4 K. $p = 2.9 \times 10^{11}$ cm^{-2} and $\mu = 1.0 \times 10^5$ cm^2/(Vs) at 0.4 K. dρ_{xx}/dB at low B is displayed in the inset.

ily be distinguished, which are due to the indirect band gap.

A FFT of the SdH oscillations for various hole concentrations in a gated p type QW results in two frequencies cor-
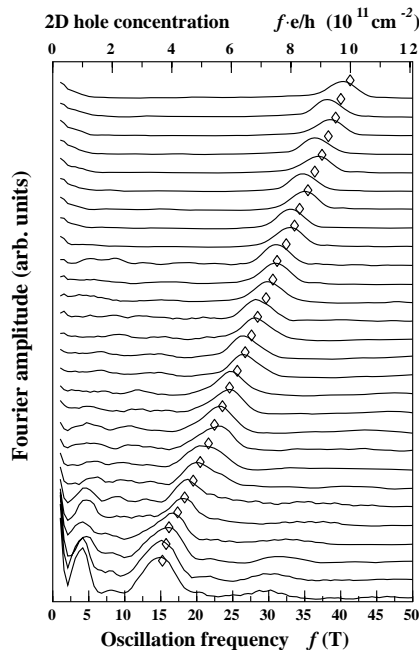

Fig. 5. FFT of SdH oscillations for the gated Hall bar from Q1645 with $d_w = 15$ nm at 0.45 K. The diamonds represent the total hole density from the Hall coefficient. The peak at the frequency p_1 vanishes when the hole concentration exceeds 5×10^{11} cm^{-2}.

responding to the concentrations p_1 and p_2, see Fig. 5. The total hole concentration, p_2, is in good agreement with the Hall concentration at low magnetic fields [14]. $p_2/p_1 = 4$, within experimental uncertainties, for $p_2 < 5 \times 10^{11}$ cm^{-2}. p_2 can be increased up to 1.1×10^{12} cm^{-2}, however, above 5×10^{11} cm^{-2} the peak corresponding to p_1 disappears as shown in Fig. 5, in good agreement with theoretical calculations.

The valance band of HgTe QWs with an inverted band structure has a maximum at finite $k_\parallel$ [14]. Therefore, at hole concentrations of less than about 5×10^{11} cm^{-2} a contour plot of the intersection of the Fermi energy with that of the first valence subband, H2, results in four equivalent unconnected areas. For $p_2 > 5 \times 10^{11}$ cm^{-2} the Fermi contour resembles a single distorted ring [14]. The experimental results are in good agreement with the theoretical prediction of four equivalent valleys.

4. Conclusions

Magneto-transport studies have been performed on n and p type modulation doped HgTe single QWs with inverted band structure. Rashba spin splitting in n type QWs with an inverted band structure has been investigated at different electron concentrations via a gate voltage. A large Rashba spin splitting has been observed, which is due to the heavy hole nature of the first conduction subband, H1.

SdH oscillations of p type QWs display two periods, however, they have been shown to be due to their indirect band gap and the resulting multiple valleys, and not due to Rashba spin–orbit splitting. Both n and p modulation doped HgTe QWs, have high mobilities of up to 6.0×10^5 and 1.0×10^5 cm^2/(Vs), respectively.

References

[1] R.D. Rajaval, D.M. Jamba, J.E. Jensen, J.A. Wilson, J.L. Johnson, E.A. Patten, K. Kosai, P. Goetz, S.M. Johnson, J. Cryst. Growth 184–185 (1998) 1272.
[2] S. Datta, B. Das, Appl. Phys. Lett. 56 (1990) 665.
[3] G. Dresselhaus, Phys. Rev. 100 (1955) 580.
[4] C. Kittel, Quantum Theory of Solids, Wiley, New York, 1963.
[5] E.I. Rashba, Fiz. Tverd. Tela 2 (1960) 1224;
E.I. Rashba, Sov. Phys. Solid State 2 (1960) 1109.
[6] Y.A. Bychkov, E.I. Rashba, J. Phys. C 17 (1984) 6039.
[7] P. Pfeffer, W. Zawadzki, Phys. Rev. B 59 (1999) R5312.
[8] U. Rössler, F. Malcher, G. Lommer, in: G. Landwehr (Ed.), Springer Series in Solid-State Sciences, vol. 87, Springer-Verlag, Berlin, 1989, p. 376.
[9] M.H. Weiler, in: R. Willardson, A.C. Beer (Eds.), Semiconductors and Semimetals, vol. 16, Academic Press, New York, 1981, p. 119.
[10] X.C. Zhang, A. Pfeuffer-Jeschke, K. Ortner, V. Hock, H. Buhmann, C.R. Becker, G. Landwehr, Phys. Rev. B 63 (2001) 245305.
[11] C.R. Becker, V. Latussek, A. Pfeuffer-Jeschke, G. Landwehr, L.W. Molenkamp, Phys. Rev. B 62 (2000) 10353;
C.R. Becker, V. Latussek, G. Landwehr, L.W. Molenkamp, Phys. Rev. B 68 (2003) 035202.
[12] F. Goschenhofer, J. Gerschütz, A. Pfeuffer-Jeschke, R. Hellmig, C.R. Becker, G. Landwehr, J. Electron. Mater. 27 (1998) 532.
[13] K. Ortner, X.C. Zhang, S. Oehling, J. Gerschütz, A. Pfeuffer-Jeschke, V. Hock, C.R. Becket, G. Landwehr, L.W. Molenkamp, Appl. Phys. Lett. 79 (2001) 3980.
[14] K. Ortner, X.C. Zhang, A. Pfeuffer-Jeschke, C.R. Becker, G. Landwehr, L.W. Molenkamp, Phys. Rev. B 66 (2002) 075322.
[15] A. Pfeuffer-Jeschke, Doctoral thesis, Physikalisches Institut der Universität Würzburg, 2000.
[16] R. Winkler, Phys. Rev. B 62 (2000) 4245.

164

MBE growth and characterization of Hg based compounds and heterostructures

C.R. Becker*, X.C. Zhang, K. Ortner, J. Schmidt, A. Pfeuffer-Jeschke, V. Latussek, Y.S. Gui, V. Daumer, J. Liu, H. Buhmann, G. Landwehr, L.W. Molenkamp

Physikalisches Institut der Universität Würzburg, Am Hubland, 97074 Wurzburg, Germany

Abstract

The MBE growth of $Hg_{1-x}Cd_xTe$ alloys and type III $HgTe/Hg_{1-x}Cd_xTe$ heterostructures has been discussed, including similarities and differences between the (0 0 1) and (1 1 2)B orientations. Furthermore the MBE growth of HgTe based quantum wells (QWs) with the incorporation of Mn are additional topics. An investigation of the optical properties of type III superlattices with a normal band structure has lead to information about band structure of these heterostructures as well as information about the interface and the semimetallic QW. For example, by means of the full 8×8 Kane Hamiltonian in the envelope function approximation, it has been demonstrated that the energy separation between the H1–E1 and L1–E1 intersubband transition energies is primarily determined by the valence band offset, Λ, between HgTe and CdTe. This has led to unambiguous values for the offset and its temperature dependence, i.e. $\Lambda(T) = 570 \pm 60$ meV and $d\Lambda/dT = -0.40 \pm 0.04$T meV/K. Furthermore the energy gap of HgTe at room temperature has also been determined. Magneto-transport measurements of n-type QWs show very pronounced Shubnikov-de Haas (SdH) oscillations and well developed quantum Hall plateaus for temperatures up to approximately 60 K. A large Rashba spin–orbit splitting of the first conduction subband, H1, has been observed in $HgTe/Hg_{1-x}Cd_xTe$ QWs with an inverted band structure. Self-consistent Hartree calculations of the band structure based on the above model allows us to quantitatively describe the experimental results and demonstrates that the heavy hole nature of the H1 subband greatly influences the spatial distribution of electrons in the QW and thus enhances the Rashba spin splitting, i.e. $\Delta E_{H1} = \beta k_{\parallel}^3$. Furthermore, the presence of two periodic SdH oscillations in p-type QWs with an inverted band structure has been observed and is the first direct evidence that these heterostructures are indirect semiconductors. The influence of Mn in the upper barrier on the 2D electrons in the well has been investigated as a function of their separation. With spacer thicknesses of 10 and 15 nm, no appreciable change is observed, however, a reduction of the spacer thickness to 5 nm results in an increase in the maximum population difference between the two Rashba spin split H1 subbands by a factor of approximately two. © 2002 Elsevier Science B.V. All rights reserved.

Keywords: Molecular beam epitaxy growth; HgTe; $Hg_{1-x}Cd_xTe$; Superlattices; Quantum wells; Valence band offset; Band structure; Rashba spin splitting; Indirect band gap

1. Introduction

The $Hg_{1-x}Cd_xTe$ alloy has been one of the most commercially exploited alloys in recent decades. Both bulk samples and epitaxial layers over the entire composition range can be produced. Due to applications requiring increasingly complex heterostructures [1], molecular beam epitaxy (MBE) is now one of the more important growth techniques. The MBE growth and the dependence of the composition and surface structure on crystal orientation will be discussed. The topics include surface structure, incorporation of Hg and Cd, n and p

type doping, modulation doping of both n and p type quantum wells (QWs), etc.

The band structure and hence the optical and electrical properties of type III heterostructures are largely determined by that of the QW. For example the band gap of HgTe and its temperature dependence directly influences the temperature dependence of the superlattice (SL) subbands and thus the temperature dependence of the intersubband transition energies [2]. The magnitude of the negative band gap of HgTe at room temperature is subject to large experimental uncertainties due to difficulties in the conventional magneto-optical method at temperatures above 100 K [3]. Another such property is the deformation potential of HgTe relative to that of CdTe which has only recently been experimentally

---

*Corresponding author.
E-mail address: becker@physik.uni-wuerzburg.de (C.R. Becker).

determined by means of an optical absorption investigation of HgTe/Hg$_{0.32}$Cd$_{0.68}$Te SLs under hydrostatic pressure [4]. Furthermore, it has been shown that the valence band offset is to a good approximation primarily responsible for the energy difference between the first heavy hole, H1, and the first light hole, L1, subband of a HgTe/Hg$_{1-x}$Cd$_x$Te SL with normal band structure [2]. This energy difference is nearly independent of other SL parameters, and consequently leads to a precise determination of the valence band offset, Λ, between HgTe and CdTe.

The band structure and consequently the optical properties depend on the band structure of the QWs and barriers, i.e. HgTe and Hg$_{1-x}$Cd$_x$Te, their widths, and the potential energy differences between these two components. The latter depends in turn on their composition, the valence band offset as well as the shape and width of the Cd concentration profile across the interfaces. A profile described by an error function similar to an experimental profile according to Kim et al. [5] is assumed and leads to a consistent description of the experimental results. Finally, the width of this interface, d_t, has been shown to be a convenient variable for the study of interdiffusion in these SLs [6].

If the HgTe layer is less than 6 nm thick then the heterostructure is a normal semiconductor, however, if the thickness is greater than 6 nm then the band structure is inverted, i.e. the Γ_6 and Γ_8 bands exchange places and the energy gap is negative. Magneto-transport experiments have been conducted on both n and p type modulation doped HgTe/Hg$_{1-x}$Cd$_x$Te QWs with an inverted band structure. An analysis of Shubnikov-de Haas (SdH) oscillations in gate controlled n type QWs reveals a large Rashba spin–orbit splitting [7,8]. This is due to the heavy hole character of the first conduction subband. In a p-type QW two periodic SdH oscillations are observed which are caused by the indirect band structure [9].

2. Experimental details

The epitaxial alloys and heterostructures were grown in a Riber 2300 MBE system as has been described elsewhere [2,10]. After the growth of a thin CdTe buffer layer, the alloys and heterostructures were grown on (0 0 1) and (1 1 2)B oriented Cd$_{0.96}$Zn$_{0.04}$Te substrates at 180 °C. The (0 0 1) QWs were modulation doped symmetrically, on both sides of the QW, and asymmetrically, on one side only, with either iodine or arsenic for n and p type structures, respectively. The Hg$_{0.3}$Cd$_{0.7}$Te barriers are comprised of a 50 Å thick spacer and a 90 Å thick doped layer.

Asymmetric HgTe/Hg$_{0.3}$Cd$_{0.7}$Te(0 0 1) modulation doped n type QWs, were grown with Mn in the upper barrier. Mn is separated from the HgTe layer by means of a Hg$_{0.3}$Cd$_{0.7}$Te spacer, which was varied between 5

and 15 nm. Then a Hg$_{0.3}$Cd$_{0.7}$Te cap was grown, thereby maintaining the same total thickness of all layers above the HgTe layer, i.e. 34 nm.

The composition of the barrier material [11] has been determined by means of transmission measurements on thick test layers of Hg$_{1-x}$Cd$_x$Te grown under identical conditions. SL periods and HgTe(0 0 1) layer widths have been determined via a dynamic simulation of the (0 0 2) and (0 0 4) Bragg reflections measured in a six crystal X-ray diffractometer [2]. A simulation of (1 1 2)B oriented heterostructures is more complicated and the results less accurate [12,13].

After growth of the QWs, standard Hall bars were fabricated by means of a wet chemical etch, then a 200 nm thick Al$_2$O$_3$ film, which serves as an insulating layer, was deposited by electron beam evaporation. Finally Al was evaporated to form a gate electrode.

Optical transmission measurements were carried out in the middle and near infrared with a Fourier transform spectrometer, Bruker IFS88. A LiTaO$_3$ detector was usually employed rather than a liquid nitrogen cooled detector e.g. Hg$_{1-x}$Cd$_x$Te, because of its better linearity. The aperture was kept as small as possible for the same reason, i.e. a diameter of 2–3 mm. The absorption coefficient, α, was determined by fitting the experimental transmission spectra to a theoretical description of the multi-layer system using standard matrix procedures [14].

3. Theoretical details

A large number of **k·p** band structure calculations using the envelope function approximation for the HgTe/Hg$_{1-x}$Cd$_x$Te SL have been published during the last decade [15–18]. A brief review of these and other investigations pertinent to the results presented here can be found in Ref. [2].

The bands of both bulk HgTe and CdTe are described by Kane's four-band model (8×8 **k·p**) including second-order remote band contributions. The envelope function method has been used to calculate the band structure of the HgTe/CdTe SL. The results of the axial approximation are not exact, however, they give a good approximation, within 1 or 2 meV, for the subband energies at $k_\parallel = 0$ as well as for an average of the subband dispersion over all $k_\parallel$ directions. Consequently all absorption coefficient calculations and most intersubband transition energy calculations were carried out using an adapted Hamiltonian in the axial approximation, in order to reduce the calculation time.

The effects of strain due to lattice mismatch were also taken into consideration. The lattice mismatch between HgTe and its environment is less than 0.1% which results in a shift in intersubband transition energies of less than 3 meV and can therefore be neglected. In contrast to the [0 0 1] direction [17], the strain tensor

for the [1 1 2] direction has a shear strain component. This results in a piezoelectric field in the growth direction [19]. We have calculated the strain for a free standing, strained (1 1 2)B SL and a fully strained (1 1 2)B SL on a $Cd_{0.96}Zn_{0.04}Te$ substrate. From these results the piezoelectric field has been calculated to be less than 5 mV/100 Å whose influence on intersubband transition energies is less than 1 meV and can therefore be neglected in the calculations.

A revised set of values for the band parameters ($\Delta = 1.0$ eV, $\gamma_1 = 4.1$, $\gamma_2 = 0.5$, $\gamma_3 = 1.3$, $F = 0$ and $E_p = 18.8$ eV) deduced from measurements on bulk HgTe and $Hg_{1-x}Cd_xTe$ by Weiler [20] were employed which nevertheless reproduce the same bulk band structure:

$$m_{hh}^*(1 1 2) = \left(\gamma_1 - 2\gamma_2 - \frac{3}{2}(\gamma_3 - \gamma_2) \right)^{-1} m_0$$
$$= 0.53 m_0 \tag{1}$$

and

$$m_{hh}^*(0 0 1) = (\gamma_1 - 2\gamma_2)^{-1} m_0 = 0.32 \quad \text{at 5 K.} \tag{2}$$

The energy gaps of HgTe and $Hg_{1-x}Cd_xTe$ were taken from the empirical $E_g(x, T)$ relationship according to Laurenti et al. [11] with the exception of HgTe at temperatures greater than 5 K as discussed below. The valence band offset between HgTe and $Hg_{1-x}Cd_xTe$ is employed as an adjustable variable and is assumed to vary linearly with x for $Hg_{1-x}Cd_xTe$, i.e. $x\Lambda$ [21]. An interface width, d_t, which results during growth or from interdiffusion of the two types of layers was integrated into the theory. The concentration profile across the interface is described by an error function similar to an experimental profile according to Kim et al. [5].

Self-consistent Hartree calculations of modulation doped $HgTe/Hg_{1-x}Cd_xTe$ QWs have been carried out using Kane's four-band model (8×8 $\mathbf{k \cdot p}$) described above in order to quantitatively describe the observed Rashba spin–orbit splitting, see Ref. [8] for details.

4. Results and discussion

4.1. Growth and characterization of $Hg_{1-x}Cd_xTe$

The growth of undoped $Hg_{0.80}Cd_{0.20}Te(1 1 2)B$ has been investigated with regard to the mobility μ and the surface structure [22]. The mobility has a maximum value of approximately 3×10^5 cm^2 V^{-1} s^{-1} for a Hg/Te flux ratio of between 150 and 180. In contrast the void density has a maximum value of 6×10^5 cm^{-2} at low ratios and falls rapidly to a nearly constant value of 2×10^3 cm^{-2} for ratios $\geqslant 200$. At a ratio of 180 the void density is approximately 4×10^3 cm^{-2}. In order to obtain maximum mobilities, a Hg/Te flux ratio of 180 was employed for the n-type layers in this investigation.

Hence these samples have slightly higher void densities than the minimum values.

The optimum Hg/Te flux ratio for the (1 1 2)B orientation is about half of the optimum value for $Hg_{0.80}Cd_{0.20}Te(0 0 1)$ according to He et al. [23]. The latter value was chosen with regard to mobility and density of hillocks. Obviously the incorporation of Hg is more efficient in the (1 1 2)B alloys. This is also the case for Cd; the Cd/Te flux ratio necessary to grow an (1 1 2)B alloy with $x = 0.20 \pm 0.01$ at 180 °C is approximately 20–30% smaller than the ratio needed for the same composition in the (0 0 1) orientation [10]; and a (1 1 2)B alloy grown with only the CdTe and Hg sources results in $x = 0.95 \pm 0.02$, but a (0 0 1) alloy grown under the same conditions has a composition given by $x = 0.68 \pm 0.02$ [2].

The n and p type doping of $Hg_{1-x}Cd_xTe$ has been investigated using iodine in the form of CdI_2, and either arsenic as Cd_3As_2 or plasma activated nitrogen, respectively. n Type doping has been successful for the (0 0 1) and (1 1 2)B orientations [10,22] over the entire composition range with the exception of large Cd concentrations in the (1 1 2)B orientation. Producing p type alloys is more difficult and to our knowledge in situ doping has never been consistently successful. There is one exception; CdTe can be p type doped with plasma activated nitrogen up to concentrations of approximately 10^{18} cm^{-3}, however, at high charge carrier concentrations the crystalline quality is adversely effected. Normally p type doping of the alloy with As requires an ex situ anneal in Hg vapor at high temperatures. Nevertheless p type conductivity has been achieved in HgTe QWs by means of in situ doping and activation of Cd_3As_2 in a CdTe layer [24].

A low resolution atomic force microscope (AFM) image of an $Hg_{0.80}Cd_{0.20}Te(1 1 2)B$ epitaxial layer is shown in Fig. 1. Long parallel ridges and trenches are observed whose height difference is approximately 30 Å. These ridges and trenches are parallel to the edges of the sample, i.e. the {1 1 0} surface. The (1 1 2)B surface can be thought of as an (1 1 1)B surface with a high ledge density [25]. If the height of the individual steps is the distance between nearest neighbors, i.e. between cation and anion, then the distance between steps is 11.2 Å. Experimentally, a pattern in the reflection of high energy electron diffraction is observed whose period in real space is 11.1 ± 0.3 Å, which is in very good agreement with the above step width. These microscopic edges are parallel to the [1 1 0] direction and consequently parallel to the ridges and trenches shown in Fig. 1. Apparently preferential growth along these ledges result in these trenches and ridges.

The $Hg_{0.80}Cd_{0.20}Te(0 0 1)$ surface [22], is radically different. Nearly elliptically shaped mounds with a height of approximately 300 Å are observed which are similar to the mounds observed on the HgTe(0 0 1)
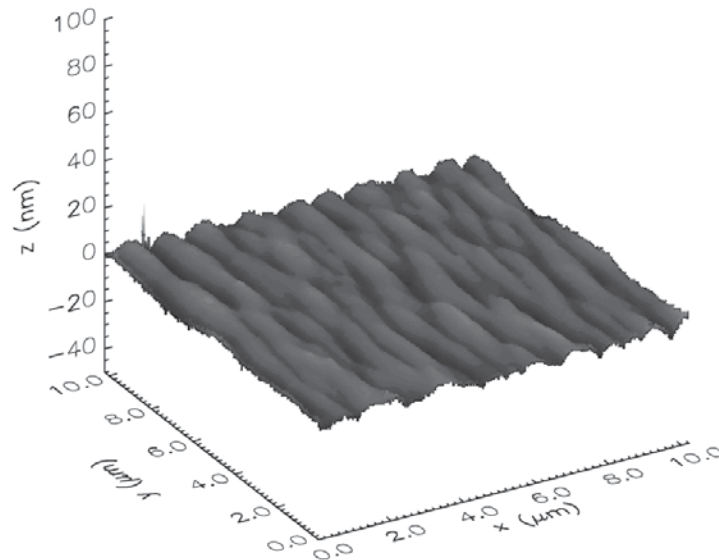
Fig. 1. A low resolution AFM image of a $Hg_{0.80}Cd_{0.20}Te(1\,1\,2)B$ epitaxial layer.

surface by Oehling et al. [26] with a scanning tunnel microscope. The latter mounds consist of a series of terraces whose height is that of one monolayer, i.e. 3.2 ± 0.3 Å, and width is approximately 500 Å. A high resolution AFM image of an $Hg_{0.80}Cd_{0.20}Te(1\,1\,2)B$ surface demonstrates that these long ridges also consist of terraces whose height difference is one monolayer and average width is approximately 180 Å [22].

4.2. Optical absorption; intersubband transitions in SLs

The experimental and theoretical absorption spectra for a $(1\,1\,2)B$ $HgTe/Hg_{0.05}Cd_{0.95}Te$ SL at 5 K are shown in Fig. 2. Three distinctive steps are observed which we have assigned to the H1–E1, L1–E1 and H2–E2 intersubband transitions. H, L and E are the heavy hole, light hole and electron subbands, respectively. In contrast, Yang et al. [27] attributed the first two steps at lower energies in a similar SL to the H1–E1 and H2–E2 transitions, and the weak shoulder near 240 meV to L1–E1. A correct assignment requires agreement between the calculated transition probabilities and the observed absorption coefficient spectrum as well as between the calculated and experimental frequencies. That this is the case here, is demonstrated in Fig. 2. The relative heights of the three steps are in good agreement with experiment, even though their absolute magnitudes are underestimated due to the neglect of Coulomb interaction between electron and hole [28]. The energies of the H1–E1 and L1–E1 transitions are in good agreement whereas agreement is only fair at higher energies, e.g. for H2–E2, as expected for a perturbation

theory. The weak shoulder near 240 meV is due to the H2–E1 transition which is allowed only for $\mathbf{k}>0$. For these reasons and others which will become apparent below, we shall concentrate on the H1–E1 and L1–E1 transitions.
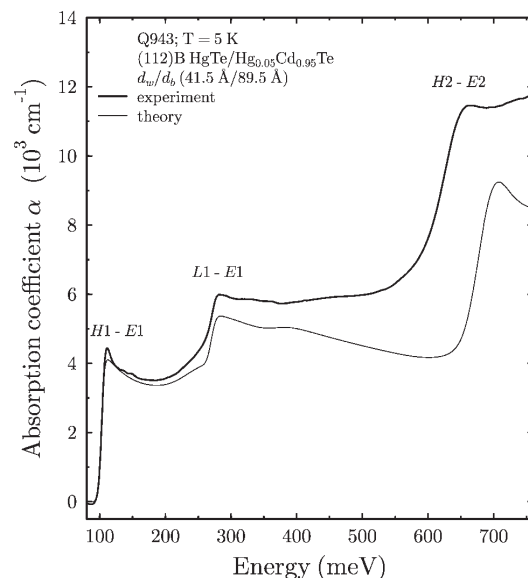

Fig. 2. The experimental and theoretical absorption coefficients of the $(1\,1\,2)B$ $HgTe/Hg_{0.05}Cd_{0.95}Te$ SL Q943 at 5 K.
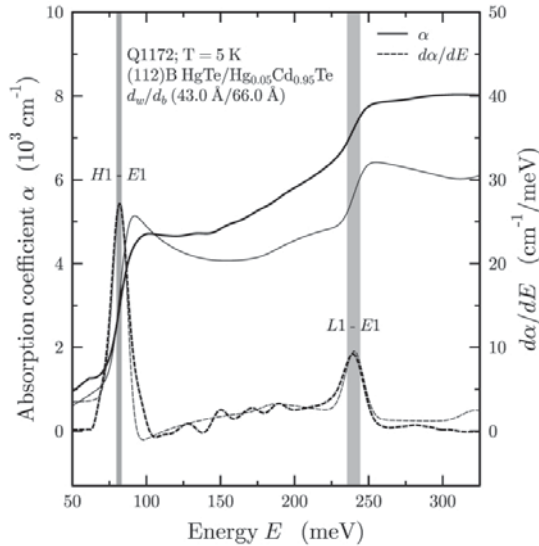
Fig. 3. The experimental (thick line) and theoretical (thin line) absorption coefficients, their first derivatives (thick and thin dashed lines, respectively) for the (1 1 2)B HgTe/Hg$_{0.05}$Cd$_{0.95}$Te SL Q1172 at 5 K. The intersubband transition energies are indicated by vertical lines and their dispersion for $\mathbf{q} \| \mathbf{z}$, the miniband width, by the width of these vertical lines

A determination of the experimental intersubband transition energies is not trivial, due largely to a lack of knowledge about the position of a particular band gap relative to the frequency of photoluminescence peaks [27,29,30], or that of the absorption edges [31]. The method employed by Becker et al. [2] is to determine the position of the absorption edge and then its position relative to the intersubband transition energy itself. This can be accomplished by calculating the transition energies as well as the corresponding absorption coefficient. Finally, by fitting the theoretical and experimental absorption coefficients, one can determine the experimental intersubband transition energies relative to their absorption edges.

The absorption edges have been determined by two different methods. In the first method, the absorption edge is defined as the energy at the maximum value of the first derivative of the absorption coefficient. In the second method the absorption edge is determined from the temperature dependence of the transmission according to

$$\frac{\Delta T}{T} = \frac{T_2}{T_1} - 1 \approx d\Delta\alpha \qquad (3)$$

where T and d are the transmission and sample thickness, respectively. Hence a good approximation of $\Delta\alpha$ can be obtained merely from a ratio of transmission spectra at slightly different temperatures [2] without the compli-

cations and uncertainties in calculating the absorption spectrum of the SL in a multi-layer structure [14]. The absorption edges according to both of these methods coincide with the H1–E1 and L1–E1 intersubband transition energies to within ± 2 meV for all investigated SLs with one exception in which a systematic discrepency of 4 meV for L1–E1 is observed [2].

Good agreement between experimental and theoretical values of the absorption edges, i.e. dα/dE, is demonstrated for a (1 1 2)B oriented SL in Fig. 3. The full width at half maximum, FWHM, of dα/dE for the H1–E1 and L1–E1 intersubband transitions is approximately 13 and 16 meV, respectively, and thus sufficiently narrow to allow a determination of these energies with a precision of ± 2 meV or better. The absorption edges for Q943 shown in Fig. 2 are even sharper with corresponding FWHMs of 8.5 and 12 meV.

The H1–E1 and L1–E1 intersubband transition energies at 5 K for all of the investigated (1 1 2)B SLs are plotted vs. QW width, d_w, in Fig. 4. Also shown is the energy difference between these two intersubband transitions, i.e. $E_{H1}-E_{L1} = E_{L1-E1} - E_{H1-E1}$. The strong inverse dependence of both transitions on d_w is obvious, whereas $E_{H1}-E_{L1}$ is nearly independent of d_w. The latter energy difference depends nearly linearly on the valence band offset, Λ. Hence a determination of Λ is possible which is not influenced by uncertainties in d_w. The three sets of lines in Fig. 4 are theoretical results for a series
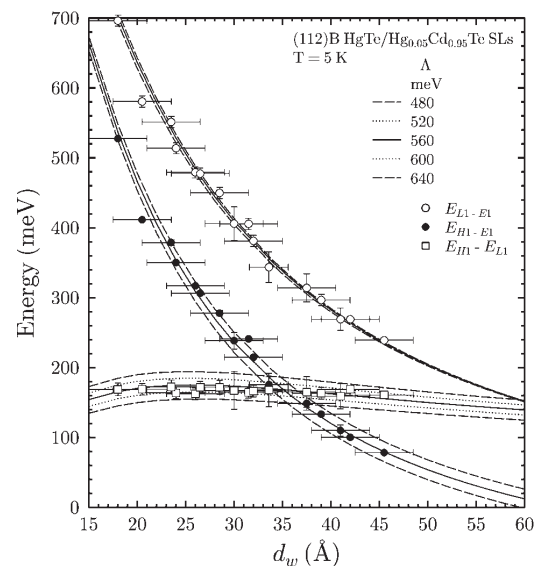

Fig. 4. The experimental values for E_{H1-E1} (filled circles), E_{L1-E1} (empty circles) and the energy difference, $E_{H1}-E_{L1}$ (empty squares), for all (1 1 2)B SLs together with theoretical results at 5 K (lines) are plotted vs. d_w. Calculated results using $d_t = 24$ Å for possible values of Λ are shown. d_t is the interface width.
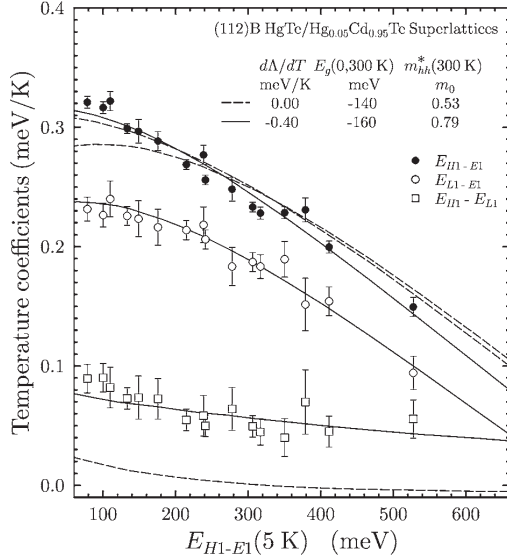
Fig. 5. Linear temperature coefficients for E_{H1-E1} (filled circles), E_{L1-E1} (empty circles) as well as $E_{H1}-E_{L1}$ (empty squares) are plotted vs. E_{H1-E1} at 5 K for all (1 1 2)B SLs. Calculated results for $d\Lambda/dT =$ 0.00 meV/K and E_g(HgTe, 300 K) $= -140$ meV are reproduced as dashed lines, and the results when $d\Lambda/dT = -0.40$ meV/K, E_g(HgTe, 300 K) $= -160$ meV and in addition m_{hh}^* is temperature dependent, i.e. $m_{hh}^* = 0.79 m_0$ at 300 K, as solid lines.

of Λ values. By means of an error analysis involving all relevant bulk and SL parameters together with their uncertainties, the valence band offset between HgTe and CdTe has been determined to be $\Lambda = 570 \pm 60$ meV for both the (0 0 1) and (1 1 2)B orientations [2]. A detailed comparison of this value and literature values can be found in Ref. [2].

Experimental values of $E_{H1}-E_{L1}$ display a significant temperature dependence [2]. Therefore according to the conclusions presented above, Λ is also temperature dependent. Linear temperature coefficients have been calculated for the three pertinent energies using the SL parameters determined below. The calculated results are obviously in excellent agreement with the experimental values according to Ref. [2]. Because the temperature dependence of $E_{H1}-E_{L1}$ is linear within experimental

uncertainties, the authors concluded that this is also the case for Λ.

The temperature dependence has been determined using a procedure which relies only on experimentally determined energies and not on d_w or other SL parameters. This is illustrated in Fig. 5 where the temperature coefficients for E_{H1-E1}, E_{L1-E1} and $E_{H1}-E_{L1}$ are plotted vs. E_{H1-E1} (5 K) for the (1 1 2)B SLs. The dashed lines are results of the theory when Λ is assumed to be temperature independent and the energy gap of HgTe at room temperature, E_g(0, 300 K), is taken to be -140 meV [32]. Even though the temperature dependence of the H1–E1 transition can be reproduced, this is clearly not the case for either L1–E1 or the energy separation between these two transitions, $E_{H1}-E_{L1}$. Consequently the results of previous investigations, which are based merely on the H1–E1 transition can be misleading. For example the conclusion of von Truchsess et al. [33] that Λ is temperature independent, is obviously incorrect.

It has been demonstrated that the temperature dependence of the L1–E1 intersubband transition is determined by the temperature dependence of both the HgTe band gap and Λ. A least square fit to the experimental values of L1–E1, shown as a solid line in Fig. 5, results in E_g(0, 300 K) $= -160 \pm 2$ meV and $d\Lambda/dT = -0.40 \pm 0.04$ meV/K [2], which are listed in Table 1. This value for E_g(0, 300 K) differs appreciably from literature values of -140 and -120 meV [11,32], which clearly lie outside of the experimental uncertainties in this investigation. However, these two values are not experimental values: they have been determined by extrapolating experimental results for $T < 100$ K up to room temperature.

On the basis of X-ray photoemission spectroscopy, and ultra violet spectroscopy (UPS) Sporken et al. [34] concluded that the valence band offset between CdTe and HgTe was independent of temperature between 50 K and room temperature with an uncertainty of ± 0.25 meV/K. However the valence band offset was not determined at $\mathbf{k} = 0$: their UPS samples were sputtered and they employed the He I and He II emission lines whose energies correspond to a position in the Brillouin zone far removed from $\mathbf{k} = 0$ [35].

The results for E_{H1-E1} and $E_{H1}-E_{L1}$ using $d\Lambda/dT = -0.40$ meV/K and E_g(0, 300) $= -160$ meV are in good

Table 1
Experimentally determined values together with their uncertainties for E_g(0, 300 K), Λ_0, Λ(300 K), $d\Lambda/dT$ and m_{hh}^*(300 K), for the (1 1 2)B and (0 0 1) orientations

	E_g(0, 300 K) meV	Λ_0 meV	Λ(300 K) meV	$d\Lambda/dT$ meV/K	m_{hh}^*(5 K)[a] m_0	m_{hh}^*(300 K) m_0
(1 1 2)B	-160 ± 2	572 ± 60	452 ± 60	-0.40 ± 0.04	0.53	0.79 ± 0.04
(0 0 1)	-157 ± 4	566 ± 60	458 ± 60	-0.41 ± 0.10	0.32	0.40 ± 0.11

The valence band offset is given by $\Lambda(T) = \Lambda_0 + (d\Lambda/dT)T$.
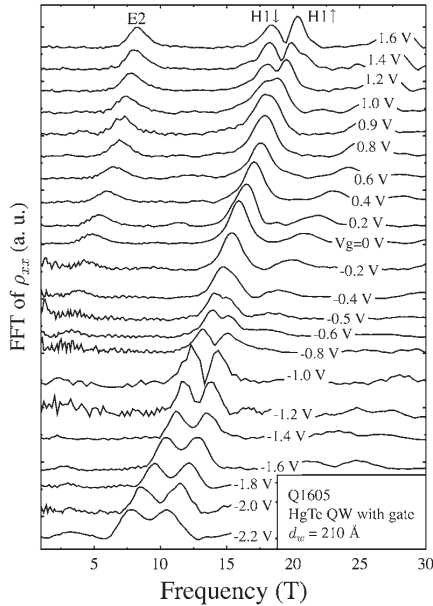[a] After Ref. [20].

Fig. 6. FFT of SdH oscillations in $\rho_{xx}(B)$ for a n type symmetrically modulation doped HgTe QW (Q1605) measured at 1.6 K and various gate voltages. The up and down arrows represent the two spin states of the H1 subband.

agreement with experiment at lower values of E_{H1-E1} (5 K) as previously reported [36], however, at higher energies this is not the case [2]. Better agreement with experiment over the entire energy range can only be achieved by assuming that the heavy hole effective mass is also temperature dependent. A least square fit to the experimental values of E_{H1-E1}, which is shown as a solid line in Fig. 5 results in $m_{hh}^{*}(1\,1\,2) = 0.79 \pm 0.04 m_0$ at 300 K [2], see Table 1.

The experimental temperature dependence of E_{L1-E1} and E_{H1-E1}, as well as that of $E_{H1}-E_{L1}$ cannot be explained unless Λ and m_{hh}^{*} are temperature dependent. Within experimental error the results for the (0 0 1) and the (1 1 2)B orientations are equivalent [2] as can be seen in Table 1, with the exception of the heavy hole effective mass as expected according to Eq. (1) and Eq. (2).

4.3. Magneto-transport; n type modulation doped QWs

As expected from their high electron mobility, all n type, modulation doped QWs show very pronounced SdH oscillations and well developed quantum Hall plateaus [8]. The results of a Fourier transformation of the complex SdH oscillations for the symmetrically modulation doped sample Q1605 with a well width of 21 nm are shown in Fig. 6. At a gate voltage, V_g, of

0.2 V, when the QW potential is nearly symmetric only two frequencies, which correspond to the H1 and E2 subbands, are resolved and no splitting of the H1 subband can be observed. For either more positive or more negative gate voltages, a large splitting of the H1 subband is apparent. Besides the main peaks labelled by E2, H1+ and H1−, peaks due to the sums of the E2 and H1 peaks can be observed. The largest Hall mobility was 6×10^5 cm^2 V^{-1} s^{-1} at a gate voltage of 2.0 V; to our knowledge this is the highest value that has been observed for HgTe QWs.

According to self-consistent band structure calculations the first two conduction subbands are H1 and E2, and the valence band is the H2 subband. This is a consequence of the inverted band structure of QWs with a large well width. No splitting of the H1 and E2 subbands for the symmetric case was predicted and none was observed [8]. However, in the asymmetric case, a small spin splitting of the E2 subband at finite $k_\parallel$ is predicted as well as a substantially larger splitting of the H1 subband. It should be mentioned here that the two spin split branches of the H1 subband cannot be designated as spin-up and spin-down because their eigenstates are not linearly polarized and do not carry a net magnetic moment [37]. The H1 and E2 subbands which are a mixture of states with different symmetries contain an equal contribution of up and down spinor components at finite $k_\parallel$. The degeneracy of the H2 valence subband is also removed and one spin component has a larger maximum at finite $k_\parallel$, i.e. here we are dealing with an indirect semiconductor.

The experimental values and the theoretical calculations of the difference in population, Δn_{H1}, between the two spin states of the H1 subband have been compared. The total carrier density, n_{SdH}, has been employed in the calculations rather than the carrier density in only the H1 subband, n_{H1}, because the electric field $\langle E \rangle$ is, to a good approximation, proportional to n_{SdH}.

The calculated carrier densities in both the H1 and E2 subbands at various gate voltages agree with the experimental values for a well width, d_w, of 21 ± 2 nm. A simulation of the X-ray diffraction results in 22 ± 2 nm, in agreement with the above value. It should be emphasized that the occupation of the E2 subband depends mainly on the well width and not on the details of the self-consistently calculated Hartree potential. Furthermore the well width and hence the calculated carrier densities for two additional QWs, an asymmetric and a symmetric QW, have been corroborated by simulations of the corresponding X-ray diffraction results.

Finally Rashba spin–orbit splitting has also been observed and described quantitatively for a number of QWs in which only one conduction subband is occupied. No abnormal temperature and B dependence has been observed [38], ruling out magneto-intersubband scattering [39].
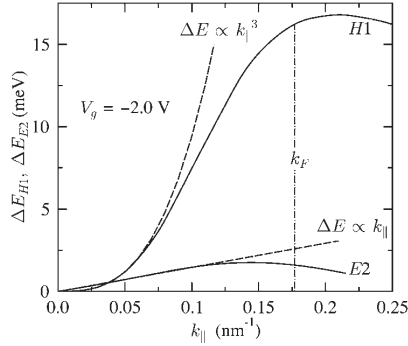
Fig. 7. The calculated spin splitting energy of the H1 and E2 subbands (solid curves), ΔE_{H1} and ΔE_{E2}, versus in-plane wave vector $k_{\|}$ for sample Q1605. The position of the Fermi wave vector k_F is denoted by the dotted-dashed line. The two dashed lines demonstrate the proportionality to $k_{\|}^3$ and $k_{\|}$, respectively, at small $k_{\|}$ values.

Winkler [37] has demonstrated that spin splitting for the heavy hole like state $|\Gamma_8, \pm 3/2\rangle$ should be proportional to $k_{\|}^3$ for small $k_{\|}$ values. The spin split heavy hole subband dispersion can be expressed as

$$E_{\pm}(k_{\|}) = \frac{h^2 k_{\|}^2}{2m^*} \pm \beta k_{\|}^3 \qquad (4)$$

where β is the spin–orbit coupling constant between the Γ_8 and Γ_6 bands. In contrast, spin splitting for the electron like state $|\Gamma_6, \pm 1/2\rangle$ and the light hole like state $|\Gamma_8, \pm 1/2\rangle$, should be a linear function of $k_{\|}$. This is in good agreement with the self-consistently calculated ΔE_{H1} and ΔE_{E2} vs. $k_{\|}$ behavior shown in Fig. 7; the H1 conduction subband in a type III HgTe QW with an inverted band structure is principally a heavy hole state, and the E2 subband is an admixture of the light hole and electron state.

4.4. Magneto-transport; p type modulation doped QWs

Experimental results shown in Fig. 8 for a p type asymmetrically modulation doped QW, Q1441, with an inverted band structures display pronounced and complex SdH oscillations, which begin below $0.3T$, and well developed quantum Hall plateaus. This QW also has a large mobility, i.e. $\mu = 1.0 \times 10^5$ cm^2 V^{-1} s^{-1}. If dρ_{xx}/dB is plotted vs. $1/B$, two periods can easily be distinguished, which are due to the indirect band gap. A Fast Fourier transformation (FFT) of the SdH oscillations for various hole concentrations in this gated p type QW results in two frequencies corresponding to the concentrations p_1 and p_2. The total hole concentration, p_2, is in good agreement with the Hall concentration at low magnetic fields. $p_2/p_1 = 4$, within experimental uncertainties, for $p_2 < 5 \times 10^{11}$ cm^{-2} [9]. p_2 can be increased up to 1.1×10^{12} cm^{-2}, however, above

5×10^{11} cm^{-2} the peak corresponding to p_1 disappears, in good agreement with theoretical calculations discussed below.

At hole concentrations of less than approximately 5×10^{11} cm^{-2} a contour plot of the intersection of the Fermi energy with that of the first valence subband, H2, results in four equivalent unconnected areas. For $p_2 > 5 \times 10^{11}$ cm^{-2} the Fermi contour resembles a single distorted ring [40]. The experimental results are in good agreement with the theoretical prediction of four equivalent valleys.

4.5. Magneto-transport; n type modulation doped QWs with Mn

QWs with Mn in the upper barrier with different spacer thickness between the HgTe and $Hg_{0.3}Cd_{0.68}Mn_{0.02}Te$ layers have different transport properties; when the spacer is reduced from 15 to 10 nm both the carrier concentration and mobility remain the same within experimental uncertainties or decrease slightly, however, a further reduction to 5 nm causes a significant reduction in these values.

As expected from their high mobilities, well developed SdH oscillations have been observed. Fourier analysis of these spectra reveal two spin split components of the H1 subband as well as the sum frequencies. The population difference between the two spin split components decreases with more positive gate voltages. This is caused by a reduction in the structure inversion asymmetry due to a larger electron concentration and hence a higher Fermi energy. The relative population difference $\Delta n_{H1}/n_{sym}$, where $n_{sym} = n_{H1}$ when $\Delta n_{H1} = 0$, is plotted in Fig. 9 vs. the normalized charge carrier concentration, $(n_{sym} - n_{H1}/n_{sym})$, in order to facilitate a suitable comparison of the QWs with spacer thicknesses of 5, 10 and 15 nm.
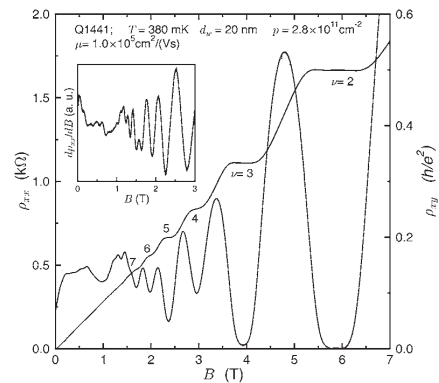

Fig. 8. ρ_{xx} and ρ_{xy} vs. B for a p type asymmetrically modulation doped QW with an inverted band structure at 380 mK. dρ_{xx}/dB is plotted vs. B in the inset.
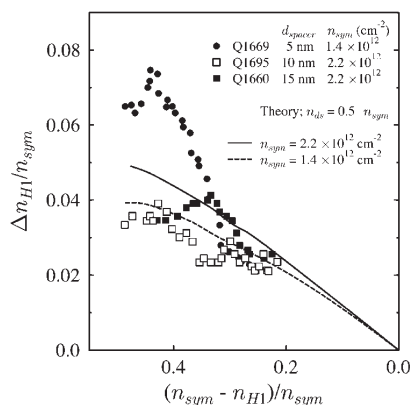
Fig. 9. The relative difference in population of the H1$-$ and H1$+$ subbands as a function of normalized charge carrier concentration for QWs with spacer thicknesses of 5, 10 and 15 nm.

As can be seen in Fig. 9, theoretical calculations are in good agreement with experiment for the two QWs with thicker spacers. In contrast self-consistent Hartree calculations for the case of a 5 nm spacer, which do not take Mn into account, under estimate the experimental population difference by a factor of approximately 2.

If this enhanced population difference were due to *giant* Zeeman splitting, then it should be strongly temperature dependent [41] contrary to experimental results which show no change between 380 mK and 4.2 K. Therefore we infer that Mn increases the asymmetry of the QW structure and thus enhances Rashba spin–orbit splitting.

In addition to this desired influence of Mn, decreasing the spacer thickness reduces both the 2D electron concentration and the electron mobility. Nevertheless, electron mobilities of 0.6, 0.8 and 1.1×10^5 cm^2 V^{-1} s^{-1} have been achieved when Mn is separated from the well by 5, 10 and 15 nm thick spacers, respectively.

5. Conclusions

Selected aspects of MBE growth of Hg$_{1-x}$Cd$_x$Te and HgTe/Hg$_{1-x}$Cd$_x$Te heterostructures have been discussed.

By means of an optical investigation of HgTe/Hg$_{1-x}$Cd$_x$Te SLs with a normal band structure combined with calculations based on an $(8 \times 8$ **k·p**$)$ model, it has been demonstrated that the energy separation between the H1–E1 and L1–E1 intersubband transition energies is primarily determined by the valence band offset, Λ, between HgTe and CdTe. This has led to unambiguous values for the offset and its temperature dependence, i.e. $\Lambda(T) = 570 \pm 60$ meV and $d\Lambda/dT = -0.40$ meV/K. Furthermore the energy gap of HgTe at room temperature has also been determined to be -160 meV.

Magneto-transport studies have been performed on both n and p type modulation doped HgTe single QWs with inverted band structure. Rashba spin splitting in n type QWs with an inverted band structure has been investigated at different electron concentrations via a gate voltage. A large Rashba spin splitting has been observed, which is due to the heavy hole nature of the first conduction subband, H1. SdH oscillations of p type QWs display two periods, which have been shown to be due to their indirect band gap and the resulting multiple valleys, and not due to Rashba spin–orbit splitting. Both n and p modulation doped HgTe QWs, have high mobilities of up to 6×10^5 and 1.0×10^5 cm^2 V^{-1} s^{-1}, respectively.

The results of magneto-transport experiments on HgTe QWs with Mn in the upper barrier are in good agreement with self-consistent Hartree calculations when the Mn is separated from the 2D electrons by spacers of 10 and 15 nm. However, the observed population difference of the two spin split states for a QW with a 5 nm spacer is larger than theoretical predictions by at least a factor of two. We conclude that Mn increases the asymmetry of the QW.

References

[1] R.D. Rajaval, D.M. Jamba, J.E. Jensen, J.A. Wilson, J.L. Johnson, E.A. Patten, K. Kosai, P. Goetz, S.M. Johnson, J. Cryst. Growth 184/185 (1998) 1272.

[2] C.R. Becker, V. Latussek, A. Pfeuffer-Jeschke, G. Landwehr, L.W. Molenkamp, Phys. Rev. B 62 (2000) 10353.

[3] M. Dobrowolska, A. Mycielski, W. Dobrowolski, Solid State Commun. 27 (1978) 1233.

[4] V. Latussek, C.R. Becker, G. Landwehr, R. Bini, L. Ulivi, unpublished.

[5] Y. Kim, A. Ourmazd, M. Bode, R.D. Feldman, Phys. Rev. Lett. 63 (1989) 636.

[6] C.R. Becker, V. Latussek, W. Spahn, F. Goschenhofer, S. Oehling, G. Landwehr, in: R.E. Longshore, J.W. Baars (Eds.), Growth and Characterization of Materials for Infrared Detectors, SPIE Proc., vol. 2554, 1995, p. 6.

[7] Y.A. Bychkov, E.I. Rashba, J. Phys. C 17 (1984) 6039.

[8] X.C. Zhang, A. Pfeuffer-Jeschke, K. Ortner, V. Hock, H. Buhmann, C.R. Becker, G. Landwehr, Phys. Rev. B 63 (2001) 245305.

[9] K. Ortner, X.C. Zhang, A. Pfeuffer-Jeschke, C.R. Becker, G. Landwehr, L.W. Molenkamp, Phys. Rev. B, in press.

[10] F. Goschenhofer, J. Gerschütz, A. Pfeuffer-Jeschke, R. Hellmig, C.R. Becker, G. Landwehr, J. Electron. Mater. 27 (1998) 532.

[11] J.P. Laurenti, J. Camassel, A. Bouhemadou, B. Toulouse, R. Legros, A. Lusson, J. Appl. Phys. 67 (1990) 6454.

[12] M. Li, C.R. Becker, R. Gall, W. Faschinger, G. Landwehr, Appl. Phys. Lett. 71 (1997) 1822.

[13] M. Li, R. Gall, C.R. Becker, T. Gerhard, W. Faschinger, G. Landwehr, J. Appl. Phys. 82 (1997) 4860.

[14] D. Fasold, K. Heil, S. Jetschke, Phys. Stat. Sol. A 86 (1984) 125.

[15] L.R. Ram-Mohan, K.H. Yoo, R.L. Aggarwal, Phys. Rev. B 38 (1988) 6151.

[16] N.F. Johnson, H. Ehrenreich, P.M. Hui, P.M. Young, Phys. Rev. B 41 (1990) 3655.

[17] A. Simon, D. Bertho, D. Boiron, C. Jouanin, Phys. Rev. B 42 (1990) 5221.

[18] J.R. Meyer, C.A. Hoffman, F.J. Bartoli, Semicond. Sci. Technol. 5 (1990) S90.

[19] L. De Caro, L. Tapfer, Phys. Rev. B 51 (1995) 4374.

[20] M.H. Weiler, in: R. Willardson, A.C. Beer (Eds.), Semiconductors and Semimetals, 16, Academic Press, New York, 1981, p. 119.

[21] C.K. Shih, W.E. Spicer, Phys. Rev. Lett. 58 (1987) 2594.

[22] J. Schmidt, K. Ortner, J.E. Jensen, C.R. Becker, J. Appl. Phys. 91 (2002) 451.

[23] L. He, C.R. Becker, R.N. Bicknell-Tassius, S. Scholl, G. Landwehr, J. Appl. Phys. 73 (1993) 3305.

[24] K. Ortner, X.C. Zhang, S. Oehling, J. Gerschütz, A. Pfeuffer-Jeschke, V. Hock, C.R. Becker, G. Landwehr, L.W. Molenkamp, J. Appl. Phys. 79 (2001) 3980.

[25] M.A. Berding, A. Sher, J. Electron. Mater. 28 (1999) 799.

[26] S. Oehling, M. Ehinger, T. Gerhard, C.R. Becker, G. Landwehr, M. Schneider, D. Eich, H. Neureiter, R. Fink, M. Sokolowski, E. Umbach, Appl. Phys. Lett. 73 (1998) 3205.

[27] Z. Yang, Z. Yu, Y. Lansari, S. Hwang, J.W. Cook, J.F. Schetzina, Phys. Rev. B 49 (1994) 8096.

[28] C. Tanguy, Phys. Rev. Lett. 75 (1995) 4090, and references therein.

[29] K.A. Harris, R.W. Yanka, L.M. Mohnkern, A.R. Riesinger, T.H. Myers, Z. Yang, Z. Yu, S. Hwang, J.F. Schetzina, J. Vac. Sci. Technol. B 10 (1992) 1574.

[30] J.R. Meyer, A.R. Reisinger, K.A. Harris, R.W. Yanka, L.M. Mohnkern, L.R. Ram-Mohan, J. Cryst. Growth 138 (1994) 981.

[31] C.L. Cesar, M.N. Islam, R.D. Feldman, R.F. Austin, D.S. Chemla, L.C. West, A.E. DeGiovanni, Appl. Phys. Lett. 56 (1990) 283.

[32] G.L. Hansen, J.L. Schmit, T.N. Casselman, J. Appl. Phys. 53 (1982) 7099.

[33] M. von Truchsess, V. Latussek, C.R. Becker, E. Batke, J. Cryst. Growth 159 (1996) 1128.

[34] R. Sporken, S. Sivananthan, J.P. Faurie, D.H. Ehlers, J. Fraxedas, L. Ley, J.J. Pireaux, R. Caudano, J. Vac. Sci. Technol. A 7 (1989) 427.

[35] D. Eich, K. Ortner, U. Groh, Z.N. Chen, C.R. Becker, G. Landwehr, R. Fink, E. Umbach, Phys. Stat. Sol. A 173 (1999) 261.

[36] C.R. Becker, V. Latussek, M. Li, A. Pfeuffer-Jeschke, G. Landwehr, J. Electron. Mater. 28 (1999) 826.

[37] R. Winkler, Phys. Rev. B 62 (2000) 4245.

[38] X.C. Zhang, A. Pfeuffer-Jeschke, K. Ortner, C.R. Becker, G. Landwehr, Phys. Rev. B 65 (2002).

[39] T.H. Sander, S.N. Holmes, J.J. Harris, D.K. Maude, J.C. Portal, Phys. Rev. B 58 (1998) 13856.

[40] G. Landwehr, J. Gerschütz, S. Oehling, A. Pfeuffer-Jeschke, V. Latussek, C.R. Becker, Physica E 6 (2000) 713.

[41] D. Keller, D.R. Yakovlev, B. König, W. Ossau, Th. Gruber, A. Waag, L.W. Molenkamp, Phys. Rev. B 65 (2002).

Optical and electrical properties of type III HgTe/Hg$_{1-x}$Cd$_x$Te heterostructures

C. R. Becker , X. C. Zhang, K. Ortner, V. Latussek and A. Pfeuffer-Jeschke

Physikalisches Institut der Universität Würzburg, Am Hubland, 97074 Würzburg, Germany

ABSTRACT

By means of an optical investigation involving the envelope function approximation using the full 8 × 8 Kane Hamiltonian, it has been demonstrated that the valence band is primarily responsible for the separation between the $H1 - E1$ and $L1 - E1$ intersubband transition energies of semiconducting HgTe/Hg$_{1-x}$Cd$_x$Te superlattices with a normal band structure. This results in an unequivocal determination of the valence band offset between HgTe and CdTe, Λ, which is 570 ± 60 meV at 5 K for both the (001) and the (112)B orientations. In order to correctly predict the temperature dependence of both intersubband transition energies, the following is required: Λ is also temperature dependent according to $d\Lambda/dT = -0.40 \pm 0.04$ meV/K; the heavy hole effective mass has a significant temperature dependence; and the energy gap E_g(HgTe, 300 K)$= -160 \pm 5$ meV which is appreciably lower than the extrapolated values found in the literature.

Both n and p type modulation doped HgTe/Hg$_{1-x}$Cd$_x$Te quantum wells, QW, have been investigated. Magneto-transport measurements of n type QWs show very pronounced Shubnikov-de Haas, SdH, oscillations and well developed quantum Hall plateaus for temperatures up to approximately 60 K. The SdH oscillations for asymmetric n type modulation doped structures display spin splitting at zero magnetic field, whereas this is not the case for similar symmetric structures. This effect increases with increasing quantum well width and preliminary calculations qualitatively agree with these results which we tentatively ascribe to Rashba spin splitting.

1. INTRODUCTION

The optical properties and the band structure of type III superlattices, SLs, are largely determined by that of the quantum well. Consequently, an investigation of the optical and electrical properties of type III superlattices can lead to information about properties of the zero gap or semimetallic material used in the quantum well. Two examples are the band gap of HgTe at room temperature and the valence band offset between HgTe and CdTe, Λ.[1] The magnitude of the negative band gap of HgTe at room temperature is subject to large experimental uncertainties due to difficulties in the conventional magneto-optical method at temperatures above 100 K.[2] Hence the most commonly accepted values for this important parameter are the results of extrapolation. Furthermore, it will be shown that Λ is to a good approximation primarily responsible for the energy difference between the first heavy hole, $H1$, and the first light hole, $L1$, subband of a HgTe/Hg$_{1-x}$Cd$_x$Te superlattice with normal band structure. This energy difference is nearly independent of other superlattice parameters, and consequently leads to a precise determination of Λ.

To our knowledge quantum transport effects in HgTe quantum wells were first reported by Goschenhofer et al.[3] Modulation doped quantum well structures allow free charge carriers to be physically separated from the corresponding ionized donors or acceptors. As is well known, this results in large carrier mobilities. In addition these mobilities are further enhanced by the extremely low electron effective mass in type III HgTe/Hg$_{1-x}$Cd$_x$Te QWs. Both n and p type modulation doped QWs have been studied and examples of the results will be presented.

2. EXPERIMENTAL AND THEORETICAL DETAILS

The heterotructures were grown in a Riber 2300 molecular beam epitaxial, MBE, system which has been modified to permit the growth of Hg based materials as has been described elsewhere.[4] After the growth of a thin CdTe buffer layer, the HgTe/Hg$_{1-x}$Cd$_x$Te superlattices and single quantum wells were grown on (001) and (112)B oriented Cd$_{0.96}$Zn$_{0.04}$Te and CdTe substrates at 180°C with the exception of three (112)B SLs at 188°C. The (001) QWs were modulation doped symmetrically, on both sides of the quantum well, and asymmetrically, on one side only, with either iodine or arsenic for n and p type structures, respectively. The Hg$_{1-x}$Cd$_x$Te barriers are comprised of a 50 Å thick spacer and a 90 Å thick doped layer. The composition of the barrier material[5] has been determined by means of transmission measurements on thick test layers of Hg$_{1-x}$Cd$_x$Te grown under identical conditions At a growth temperature of 180°C, $x = 0.68 \pm 0.02$ and $x = 0.95 \pm 0.02$ for the (001) and (112)B orientations, respectively. The

superlattice period and the HgTe width of (001) SLs have been determined via a dynamic simulation of the (002) and (004) Bragg reflections measured in a five crystal x-ray diffractometer.[1] X-ray diffraction in (112)B oriented heterostructures is more complicated and the results less accurate. Shear strain results in a monoclinic distortion which must be taken into account before the data can be correctly simulated.[6,7] The HgTe thicknesses in quantum well structures have been infered from growth rates which were determined for SLs.

The absorption coefficient was determined by fitting the experimental transmission spectra to a multi-layer system using standard matrix procedures.[8] It can be easily shown that a transmission spectrum divided by a spectrum at a slightly different temperature, is proportional to the corresponding change in the absorption coefficient; $\Delta T/T$ = $(T_2/T_1$ -1) $\approx$ $d\Delta\alpha$, where T and d are the transmission and sample thickness, respectively. Hence a good approximation of $\Delta\alpha$ can be obtained merely from a ratio of the transmission spectra without the complications and uncertainties in calculating the absorption spectrum of the SL in a multi-layer structure.[1]

The bands of both bulk HgTe and CdTe are described by Kane's four-band model (8×8 $\mathbf{k} \cdot \mathbf{p}$) including second order remote band contributions. The absorption coefficient was calculated from the complex dielectric constant by means of the Kubo formula.[9] The details of these calculations are described elsewhere.[1]

The effects of strain due to lattice mismatch are less then 3 meV and can be neglected. In contrast to the [001] direction,[10] the strain tensor for the [112] direction has a shear component. This results in a piezoelectric field in the growth direction,[11] whose influence on the intersubband energies is less than 1 meV and can also be neglected. The energy gaps of HgTe and $Hg_{1-x}Cd_xTe$ were taken from the empirical $E_g(x,T)$ relationship according to Laurenti et al.[5] with the exception of HgTe at 300 K as discussed below. The valence band offset between HgTe and CdTe is employed as an adjustable variable and is assumed to vary linearly with x for $Hg_{1-x}Cd_xTe$, i.e $x\Lambda$.[12] An interface width, d_t, which results during growth or from interdiffusion was integrated into the theory. The resulting concentration profile is described by an error function similar to an experimental profile according to Kim et al.[13]

3. RESULTS AND DISCUSSION

### 3.1. Optical properties of (112)B and (001) HgTe/$Hg_{1-x}Cd_x$Te superlattices

The absorption spectra for a (112)B HgTe/$Hg_{0.05}Cd_{0.95}$Te SL at 5 K are shown in Fig. 1. Three distinctive steps are observed which we have assigned to the $H1 - E1$, $L1 - E1$ and $H2 - E2$ intersubband transitions. H, L and E are the heavy hole, light hole and electron subbands, respectively. In contrast, Yang et al.[14] attributed the first two steps at lower energies in a similar SL to the $H1 - E1$ and $H2 - E2$ transitions, and the weak shoulder near 190 meV to $L1 - E1$. A correct assignment requires agreement between the calculated transition probabilities and the observed absorption coefficient spectrum as well as between the calculated and experimental frequencies. That this is the case here, is demonstrated in Fig. 1 where the experimental and theoretical absorption coefficients are plotted versus energy. The relative heights of the three steps are in good agreement with experiment, even though their absolute magnitudes are underestimated due to the neglect of Coulomb interaction between electron and hole.[15] The energies of the $H1 - E1$ and $L1 - E1$ transitions are in good agreement whereas agreement is only fair at higher energies, e.g. for $H2 - E2$, as expected for a perturbation theory. The weak shoulder near 190 meV is due to the $H2 - E1$ transition which is allowed only for $\mathbf{k} > 0$. For these reasons and others which will become apparent below, we shall concentrate on the $H1 - E1$ and $L1 - E1$ transitions.

The intersubband transition energies have been determined from the absorption edges which coincide to within $\leq \pm 2$ meV for all samples except one.[1] The absorption edge is defined as the energy at the maximum value of the first derivative of the absorption coefficient. The experimental and theoretically calculated α and its derivative are shown in Fig. 1. The shape and width of the experimental α and $d\alpha/dE$ of Q1172 were simulated by assuming a Gaussian distribution of quantum well widths with $\Gamma = 1.6$ Å.[16] The energies of the $H1-E1$ and $L1-E1$ transitions at 5 K for all of the investigated (112)B SLs are plotted versus quantum well width, d_w, in Fig. 2. Also shown is the energy difference between these two intersubband transitions, i.e. $E_{H1} - E_{L1} = E_{L1-E1} - E_{H1-E1}$. Obviously both transitions have a strong inverse dependence on d_w, whereas $E_{H1} - E_{L1}$ is nearly independent of d_w. On the other hand, $E_{H1} - E_{L1}$ depends nearly linearly on the valence band offset, Λ. Hence a determination of Λ is possible which is not influenced by uncertainties in d_w. The five sets of lines in Fig. 2 are the results of the theory for these intersubband energies for a series of Λ values assuming $d_t = 24$ Å and $x_w = 0.0$, x_w is the Cd concentration in the well. Furthermore, it has been demonstrated that Λ is nearly independent of all other SL parameters such as d_t and x_w. Nevertheless, taking this weak dependence into consideration results in a range of possible values at 5 K expressed as $\Lambda = 570 \pm 26$ meV.
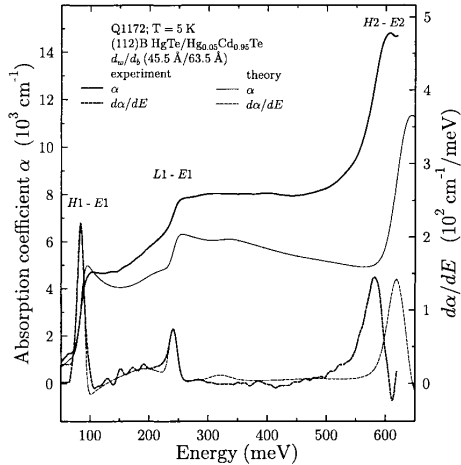
Figure 1. The experimental (thick line) and theoretical (thin line) absorption coefficients, their first derivatives (thick and thin dashed lines, respectively) for the (112)B HgTe/Hg$_{0.05}$Cd$_{0.95}$Te SL Q1172 at 5 K.
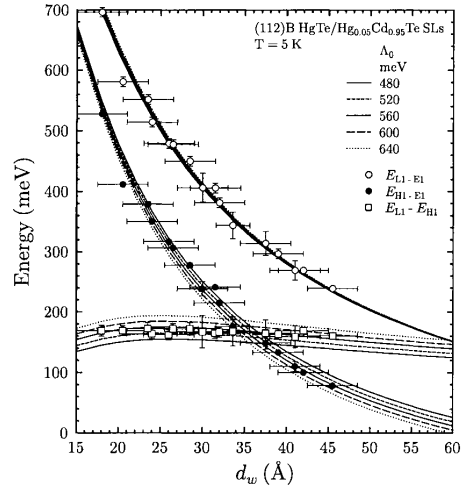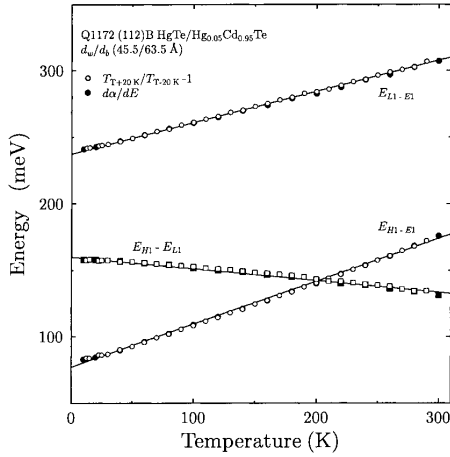
Figure 2. The experimental values for E_{H1-E1} (filled circles), E_{L1-E1} (empty circles) and $E_{H1} - E_{L1}$ (empty squares) for all (112)B SLs together with theoretical results at 5 K (lines) for possible values of Λ.

E_{H1-E1} and E_{L1-E1} for Q1172 are shown as a function of temperature in Fig. 3. Values determined from the transmission ratio are indicated by empty circles and those from $d\alpha/dE$ by filled circles. The energies from these two methods are nearly equal: most of the latter symbols are obscured by the former. As can be seen there is less scatter in the data from the transmission ratio method. Experimental values of $E_{H1} - E_{L1}$, which are plotted versus temperature as empty and filled squares, display a significant temperature dependence. Therefore according to the conclusions presented above, Λ is also temperature dependent. Linear temperature coefficients have been calculated for these three energies using the SL parameters determined below, and are displayed in Fig. 3 as three lines. Obviously, the calculated results are in excellent agreement with the experimental values. Because the temperature dependence of $E_{H1} - E_{L1}$ is linear within experimental uncertainties, we propose that this is also the case for Λ: $\Lambda(T) = \Lambda_0 + d\Lambda/dT \cdot T$.

In order to determine the magnitude of this temperature dependence, we have employed a procedure which relies only on experimentally determined energies and not on d_w or other SL parameters. This is illustrated in Fig. 4 where the temperature coefficients for E_{H1-E1}, E_{L1-E1} and $E_{H1} - E_{L1}$ are plotted versus $E_{H1-E1}(5\ K)$ for the (112)B SLs. The dashed lines are results of the theory when Λ is assumed to be temperature independent and the energy gap of HgTe at room temperature, $E_g(0,300\ K)$, is taken to be -140 meV.[17] Even though the temperature dependence of E_{H1-E1} can be reproduced, this is clearly not the case for either E_{L1-E1} or the energy separation between these two transitions, $E_{H1} - E_{L1}$. It has been demonstrated that the temperature coefficient of E_{L1-E1} is a function of the temperature dependence of both the HgTe band gap and Λ. In addition, the temperature coefficient of E_{H1-E1} is a function of the temperature dependence of these two parameters as well as the heavy hole effective mass, m^*_{hh}. A least square fit of the experimental data results in $E_g(0,300\ K) = -160 \pm 2$ meV, $d\Lambda/dT = -0.40 \pm 0.04$ meV/K, and $m^*_{hh}(112) = 0.79 \pm 0.04\,m_0$ at 300 K, which is shown as solid lines in Fig. 4. $m^*_{hh}(112) = 0.53\,m_0$ at 5 K according to Weiler et al.[18] has been employed.

The more symmetric (001) surface has a number of advantages but also distinct disadvantages. For example, the more symmetric Hamiltonian does not lead to a monoclinic distortion or a piezoelectric effect as is the case for (112).[6,7] As mentioned above, values for the well and barrier widths via x-ray diffraction are more accurate, however, the Cd concentration in the barriers is appreciably lower, 0.68 instead of 0.95. This has two important consequences.

Figure 3. The experimental E_{H1-E1}, E_{L1-E1} as well as $E_{H1} - E_{L1}$ are plotted as a function of temperature. Values determined from $d\alpha/dE$ are represented by filled symbols and those from the transmission ratio by empty symbols. The lines are due to theoretical results.
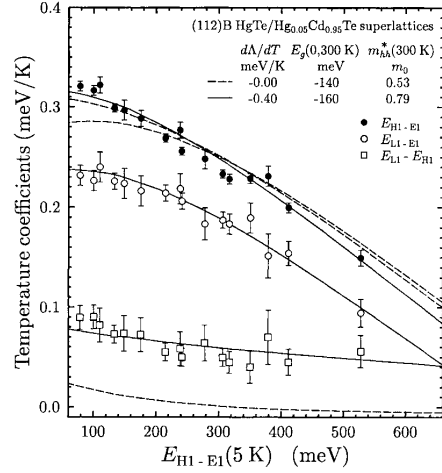
Figure 4. Linear temperature coefficients for E_{H1-E1} (filled circles), E_{L1-E1} (empty circles) as well as $E_{H1} - E_{L1}$ (empty squares) are plotted versus E_{H1-E1} at 5 K for all (112)B SLs. Calculated results are represented by dashed and solid lines.

First of all, due to the lower energy barrier the usefull experimental data are limited to a smaller energy range. Secondly, the absorption edges are at least a factor of 2.5 broader, apparently due to greater alloy fluctuations in the barriers.[16] The results for this orientation are given by $\Lambda = 564 \pm 27$ meV at 5 K, $d\Lambda/dT = -0.41 \pm 0.10$ meV/K, $E_g(0,300$ K$)= -157 \pm 4$ meV and $m^*_{hh}(001) = 0.40 \pm 0.11\,m_0$ at 300 K. $m^*_{hh}(001) = 0.40\,m_0$ at 5 K has been employed.[18]

3.2. $E_g(0,300$ K$)$, $\Lambda(T)$ and $m^*_{hh}(T)$

The valence band offset between HgTe and CdTe has been the subject of a long standing controversy, which has been reviewed by, for example, Meyer et al.[19] In early magneto-optical experiments on semiconducting superlattices, both a small offset of 40 meV and a larger value of approximately 350 meV were deduced.[20,21] X-ray and ultraviolet photoelectron spectroscopy, XPS and UPS, have provided a consistent value of approximately 350 meV at 300 K.[22,23,12] Johnson, Hui and Ehrenreich[24] resolved the apparent controversy demonstrating that both small and large values could explain the magneto-optical results of Guldner et al.[20] Values for Λ up to 800 meV have been subsequently reported for magneto-optical experiments.[25] Recently a magneto-optical investigation of the electron effective mass at the conduction band edge together with the energy of all four observed intersubband transitions for a (001) SL by von Truchsess et al.[26] resulted in a value of 550 ± 50 meV at 4.2 K. The UPS study of Eich et al.,[27] which was carried out at $k \approx 0$ in contrast to all previous XPS and UPS studies, reports a value of 530 ± 30 meV at 300 K.

In the present investigation we have demonstrated that $\Lambda = 570 \pm 30$ meV at 5 K for both the (001) and the (112)B orientations. Consideration of the experimental uncertainties in the parameters for the bulk constituents[18] as well as the uncertainties in the superlattice parameters discussed above, result in $\Lambda = 570 \pm 60$ meV at 5 K, and $\Lambda = 450 \pm 60$ meV at 300 K for (001) and (112)B. The temperature dependence of both $H1 - E1$ and $L1 - E1$ intersubband transitions can only be explained, if $E_g(0,300$ K$)= -160 \pm 5$ meV and if both Λ and m^*_{hh} have a significant temperature dependence. Even though there is no a priori reason that Λ and its temperature coefficient must be equivalent for these two orientations, within experimental error, this is the case. The extrapolated values for $E_g(0,300$ K$)$[5,17] of -120 and -140 meV, respectively are significantly larger than the experimentally determined value in this investigation, i.e. $E_g(0,300$ K$)= -160 \pm 5$ meV.

3.3. Magneto-transport results for n and p type modulation doped HgTe QWs

All n type samples show very pronounced SdH oscillations and well developed quantum Hall plateaus. Typical results for different temperatures are shown in Fig. 5. The SdH oscillations can persist up to 60 K. The SdH peaks are symmetric and the position of the extrema remain almost constant over the entire temperature range, which suggests that the carrier concentration is nearly constant up to 60 K. Furthermore $\rho_{xy}(B)$ is symmetric with respect to the classsical free electron result, $\rho_{xy} = B/(en)$. The mobility, μ, which is inversely proportional to the resistence at zero magnetic field, is 6.82×10^4 cm^2/Vs at 1.6 K and shows a slight increase with increasing temperature up to 25 K, as expected from screening of the impurities in the barrier. Above 25 K μ decreases exponentially, consistent with scattering dominated by LO phonons.[28]
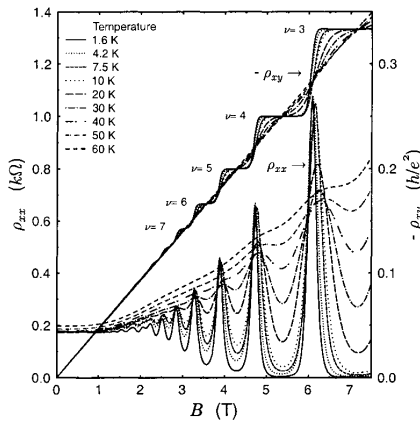
Figure 5. The SdH oscillations in ρ_{xx} and the quantum Hall effect in ρ_{xy} for a n type modulation doped HgTe QW, Q1099, are plotted versus B at various temperatures.
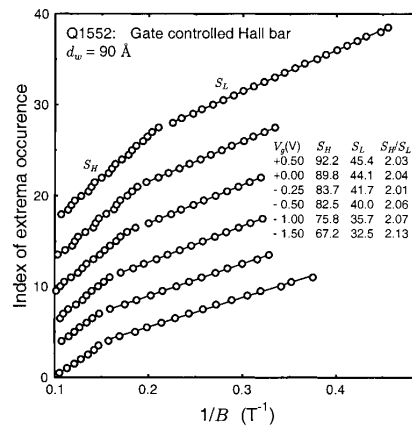

Figure 6. The index of extrema occurence is plotted versus $1/B$ for various gate voltages, V_g. An offset has been added in the y direction for clarity. The slopes at high and low magnetic fields, S_H and S_L, are tabulated.

Lifting of the spin degeneracy in the absence of a magnetic field has aroused much interest in narrow gap heterojunctions, HJs, due to a large spin orbit interaction, e.g. In$_{1-x}$Ga$_x$As/In$_{1-x}$Al$_x$As HJs,[29] Hg$_{1-x}$Cd$_x$Te,[30] and intrinsic HgTe single quantum wells.[31] Two mechanisms are believed to be responsible for this zero field spin splitting. One is due to the k^3 term in the Hamilton as a result of the inversion asymmetry of the zinc blende structure, the other is due to the "macroscopic" asymmetry of the heterojunction potential, i.e. Rashba spin splitting, which can give rise to a beating pattern in SdH oscillations at low magnetic fields. In narrow gap sytems the former effect is believed to be negligible compared to the latter.[32] In order to study this effect, experiments were preformed on a gate controlled Hall bar. ρ_{xx} and ρ_{xy} for a 90 Å thick QW change systematically with applied gate voltage; the carrier density can be varied by 46%. In Fig. 6 the plot of the index of extrema occurence in SdH oscillations versus $1/B$ displays two linear regions. The slope at low magnetic fields gives the population of one spin state, n_-, and the high field slope the total carrier concentration n. Thus $S_H/S_L = 1 + n_+/n_-$ reflects the relative populations, n_+ and n_-, in both spin states. S_H/S_L is nearly equal to 2 as shown in Fig. 6, suggesting only a small zero field spin splitting effect in this QW. Nevertheless spin splitting does indeed become larger when the QW potential becomes more asymmetric at larger negative gate voltages which are not shown here.

In contrast to the previous sample, zero field spin splitting is much larger in wider QWs. In Fig. 7 are shown the SdH oscillations and their Fourier transformation for an asymmetric and a symmetric 200 Å thick HgTe quantum well. Of the two occupied subbands, E_2 is degenerate in both samples, however, the H_1 subband is spin split in the former sample but degenerate in the latter, as can be easily demonstrated from the carrier densities deduced from SdH oscillations, n_{SdH}, and the Hall coefficient, n_{Hall}; equality of these densities is fulfilled if the multiplication
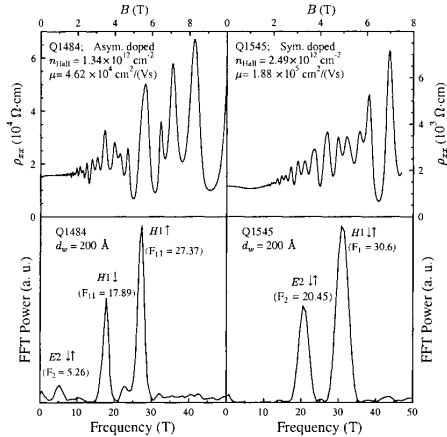
Figure 7. SdH oscillations and the fast Fourier transformation, FFT, of an asymmetrically and a symmetrically n modulation doped HgTe QW at 1.6 K. $(2F_2 + F_{1\downarrow} + F_{1\uparrow})e/h \approx n_{\text{Hall}}$ for the asymmetrical QW and $(2F_2 + 2F_1)e/h \approx n_{\text{Hall}}$ for the symmetric QW.
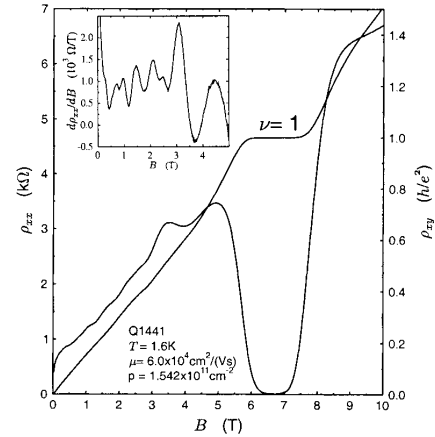
Figure 8. SdH oscillations and QHE for an As doped p type HgTe QW. The $\nu = 1$ plateau is very pronounced, and in the low magnetic field regime complex SdH oscillations are present, as shown in the insert.

factors for the $F_{1\uparrow}$ and $F_{1\downarrow}$ peaks are 1 for the asymmetric sample and that for the F_1 peak is 2 for the symmetric sample. We ascribe this to a clear manifestation of Rashba spin splitting in wide quantum wells. Apparently Rashba spin splitting increases with increasing quantum well widths. Currently a theoretical model is being developed in order to explain this behavior quantitatively.

In Fig. 8 SdH oscillations and the QHE for an As modulation doped HgTe QW are shown. The irregular SdH oscillations at low magnetic fields can be seen more clearly in the plot of $d\rho_{xx}/dB$ versus B shown in the insert. Detailed band structure calculations are needed to explain this irregular behavior. The $\nu = 1$ plateau is very pronounced and $\rho_{xx}(\nu = 1)$ agrees with the expected value within the accuracy of our measurement system, i.e. 0.04%. To our knowledge this is the best developed manifestation of the QHE in p type HgTe heterostructures.

4. CONCLUSIONS

Intersubband transitions and their dependence on temperature in semiconducting $HgTe/Hg_{1-x}Cd_xTe$ superlattices with normal band structure have been investigated for a large number of superlattices. It has been demonstrated that the valence band offset between HgTe and CdTe, Λ, is primarily responsible for the separation between the $H1 - E1$ and $L1 - E1$ transition energies of $HgTe/Hg_{1-x}Cd_xTe$ superlattices with normal band structure. This leads to $\Lambda = 570 \pm 60$ meV at 5 K for both the (001) and the (112)B orientations. This uncertainty in Λ is due to uncertainties in the $\mathbf{k} \cdot \mathbf{p}$ band parameters of the bulk constituents as well as due to a weak dependence on d_t and x_w and uncertainties in their values.

An explanation of the temperature dependence for both of these intersubband transition energies leads to the following unambiguous conclusions. Λ is temperature dependent as described by the linear temperature coefficient of -0.40 ± 0.04 meV/K for both orientations. Thus $\Lambda = 450 \pm 60$ meV at 300 K. Secondly, the energy gap of HgTe at 300 K is given by $E_g(0,300 \text{ K}) = -160 \pm 5$ meV. This value is appreciably lower than the extrapolated values found in the literature. Finally the anisotropic heavy hole effective mass for HgTe was shown to have a significant temperature dependence.

Quantum transport studies have been performed on both n and p type modulation doped HgTe single QWs. The focus has been mainly on Rashba spin splitting in n type samples, which displays a clear quantum well width dependence. SdH oscillations of p type QWs at low magnetic fields are irregular. In both n and p modulation doped HgTe QWs, well developed quantum Hall plateaus have been observed. Therefore the HgTe QW is an excellent new system in which to study localization in the quantum Hall regime.

REFERENCES

1. C. R. Becker, V. Latussek, A. Pfeuffer-Jeschke, G. Landwehr and L. W. Molenkamp, Phys. Rev. B, in press.
2. M. Dobrowolska, A. Mycielski and W. Dobrowolski, Solid State Commun. **27**, 1233 (1978).
3. F. Goschenhofer, J. Gerschütz, A. Pfeuffer-Jeschke, R. Hellmig, C. R. Becker and G. Landwehr, J. Elec. Mat. **27**, 532(1998).
4. C. R. Becker, V. Latussek, W. Spahn, F. Goschenhofer, S. Oehling and G. Landwehr, *Growth and Characterization of Materials for Infrared Detectors*, Editors R. E. Longshore and J. W. Baars, SPIE Proc. Volume 2554 p. 6 (1995).
5. J. P. Laurenti, J. Camassel, A. Bouhemadou, B. Toulouse, R. Legros and A. Lusson, J. Appl. Phys. **67**, 6454 (1990).
6. M. Li, C. R. Becker, R. Gall, W. Faschinger and G. Landwehr, Appl. Phys. Lett. **71**, 1822 (1997).
7. M. Li, R. Gall, C. R. Becker, T. Gerhard, W. Faschinger and G. Landwehr, J. Appl. Phys. **82**, 4860 (1997).
8. D. Fasold, K. Heil and S. Jetschke, phys. stat. sol. (a) **86**, 125 (1984).
9. E. Bangert, P. Boege, V. Latussek and G. Landwehr, Semicond. Sci. Technol. **8**, S99 (1993).
10. A. Simon, D. Bertho, D. Boiron and C. Jouanin, Phys. Rev. B **42**, 5221 (1990).
11. Liberato De Caro and Leander Tapfer, Phys. Rev. B **51**, 4374 (1995).
12. C. K. Shih and W. E. Spicer, Phys. Rev. Lett. **58**, 2594 (1987).
13. Y. Kim, A. Ourmazd, M. Bode and R. D. Feldman, Phys. Rev. Lett. **63**, 636 (1989).
14. Z. Yang, Z. Yu, Y. Lansari, S. Hwang, J. W. Cook, Jr. and J. F. Schetzina, Phys. Rev. B **49**, 8096 (1994).
15. Christian Tanguy, Phys. Rev. Lett. **75**, 4090 (1995); and references therein.
16. C. R. Becker, A. Pfeuffer-Jeschke, M. Li, K. Ortner, V. Daumer, S. Oehling, W. Tang and G. Landwehr, J. Cryst. Growth **184/185**, 1185 (1998).
17. G. L. Hansen, J. L. Schmit and T. N. Casselman, J. Appl. Phys. **53**, 7099 (1982).
18. M.H. Weiler, *Semiconductors and Semimetals*, edited by R. Willardson and A.C. Beer (Academic Press, New York, 1981), Vol. 16, p. 119.
19. J. R. Meyer, C. A. Hoffman, T. H. Myers and N. C. Giles, in *Handbuch on Semiconductors*, edited by T. S. Moss, Vol. 3 edited by S. Mahajan (North-Holland, Amsterdam, London, New York and Tokyo, 1994), p. 535.
20. Y. Guldner, G. Bastard, J. P. Vieren, M. Voos, J. P. Faurie and A. Million, Phys. Rev. Lett. **51**, 907 (1983); J. M. Berroir, Y. Guldner, J. P. Vieren, M. Voos and J. P. Faurie, Phys. Rev. B **34**, 891 (1986).
21. J. N. Schulman, O. K. Wu, E. A. Patten, Jeong W. Han, Y. Lansari, L. S. Kim, J. W. Cook, Jr. and J. F. Schetzina, Appl. Phys. Lett. **53**, 2420 (1988).
22. Steven P. Kowalezyk, J. T. Cheung, E. A. Kraut and R. W. Grant, Phys. Rev. Lett. **56**, 1605 (1986).
23. R. Sporken, S. Sivananthan, J. P. Faurie, D. H. Ehlers, J. Fraxedas, L. Ley, J. J. Pireaux and R. Caudano, J. Vac. Sci. Technol. A **7**, 427 (1989).
24. N. F. Johnson, P. M. Hui and H. Ehrenreich, Phys. Rev. Lett. **61**, 1993 (1988).
25. K. H. Yoo, R. L. Aggarwal, L. R. Ram-Mohan and O. K. Wu, J. Vac. Sci. Technol. A **8**, 1194 (1990).
26. M. von Truchsess, V. Latussek, F. Goschenhofer, C. R. Becker, G. Landwehr, E. Batke, R. Sizmann and P. Helgesen, Phys. Rev. B **51**, 17618 (1995).
27. D. Eich, K. Ortner, U. Groh, Z. N. Chen, C. R. Becker, G. Landwehr, R. Fink and E. Umbach, phys. stat. sol. (a) **173**, 261 (1999).
28. B. J. F. Lin, D. C. Tsui, M. A. Paalanen, and A. C. Gossard, Appl. Phys. Lett. **45**, 695 (1984).
29. J. Nitta, T. Akazaki, and H. Takayanagi, Phys. Rev. Lett. **78**, 1335 (1997).
30. R. Wollrab, R. Sizmann, F. Koch, J. Ziegler and H. Maier, Semicond. Sci. Technol. **4**, 491 (1989).
31. Schultz, M., F. Heinrichs, U. Merkt, T. Colin, T. Skauli and S. Løvold, Semicond. Sci. Technol. **11**, 1168 (1996).
32. E. A. De Andrada e Silva, G. C. la Rocca and F. Bassani, Phys. Rev. B **50**, 8523 (1994).

ELSEVIER

Growth and studies of $Hg_{1-x}Cd_xTe$ based low dimensional structures

C.R. Becker*, K. Ortner, X.C. Zhang, A. Pfeuffer-Jeschke, V. Latussek, Y.S. Gui[1],
V. Daumer, H. Buhmann, G. Landwehr, L.W. Molenkamp

Physikalisches Institut der Universität Würzburg, Am Hubland, Würzburg 97074, Germany

Abstract

The band structure of HgTe quantum wells (QWs) has been determined from absorption experiments on superlattices in conjunction with calculations based on an 8×8 $\boldsymbol{k} \cdot \boldsymbol{p}$ model. The band structure combined with self-consistent Hartree calculations has enabled transport results to be quantitatively explained.

Rashba spin–orbit, (SO) splitting has been investigated in n-type modulation doped HgTe QWs by means of Shubnikov–de Haas oscillations (SdH) in gated Hall bars. The heavy hole nature of the H1 conduction subband in QWs with an inverted band structure greatly enhances the Rashba SO splitting, with values up to 17 meV.

By analyzing the SdH oscillations of a magnetic two-dimensional electron gas (2DEG) in modulation-doped n-type $Hg_{1-x}Mn_xTe$ QWs, we have been able to separate the gate voltage-dependent Rashba SO splitting from the temperature-dependent giant Zeeman splitting, which are of comparable magnitudes. In addition, hot electrons and Mn ions in a magnetic 2DEG have been investigated as a function of current.

Nano-scale structures of lower dimensions are planned and experiments on sub-micrometer magneto-transport structures have resulted in the first evidence for ballistic transport in quasi-1D HgTe QW structures.

1. Introduction

Interesting new physics has resulted from the study of a two-dimensional electron gas (2DEG) which is subjected to additional interactions. For example, the Rashba spin–orbit (SO) interaction [1] has been the subject of numerous investigations of III–V heterostructures [2–4]. The Rashba SO coupling is particularly strong in narrow-gap HgTe quantum wells (QWs) with an inverted band structure [5], i.e., when the well width $d_w > 6$ nm. The recently introduced magnetic 2DEG [6] in which magnetic ions (usually Mn ions) are exchange coupled to the 2DEG is another example.

In order to correctly interpret the results of magneto-transport experiments, knowledge of the corresponding band structure is necessary. This knowledge has been determined from an investigation

---

* Corresponding author.

E-mail address: becker@physik.uni-wuerzburg.de (C.R. Becker).

[1] Present address: Shanghai Institute of Physics, Chinese Academy of Sciences, Shanghai 200082, China.

of intersubband transitions in $HgTe/Hg_{1-x}Cd_xTe$ superlattices with an inverted band structure [7].

Schultz et al. [8] investigated Rashba SO splitting in a gated, undoped HgTe/CdTe(1 1 2)B QW with $d_w = 11$ nm. They observed a large Rashba SO splitting (R), which they interpreted via a two-band model which presumes that SO splitting is linearly dependent on $k_\parallel$. However, the first conduction subband for an HgTe QW with an inverted band structure has heavy hole character [5,9]. And using an analytical model, Rashba [10] in a pioneering investigation and, more recently, Winkler [11] have demonstrated that Δ_R is proportional to $k_\parallel^3$ instead of $k_\parallel$ at small values of $k_\parallel$ for heavy holes. This has been corroborated by means of numerical, self-consistent Hartree calculations based on an 8×8 $\boldsymbol{k} \cdot \boldsymbol{p}$ band structure model [5,12].

Here we shall present magneto-resistance and Hall measurements on n-type modulation-doped QWs with an inverted band structure. The asymmetry of the QW potential was varied by means of a top electric gate, and the resulting Rashba SO splitting has been quantitatively explained via detailed self-consistent subband calculations based on the envelope function method.

A magnetic 2DEG has been produced by incorporating Mn in these narrow-gap heterostructures. In these structures Gui et al. [13] have probed the interplay of Rashba, Zeeman and Landau effects, whose level splittings are of comparable magnitude; the observed beating patterns in Shubnikov-de Haas (SdH) oscillations show the effects of a combination of Rashba SO interaction and sp–d exchange interaction, which have been separated via gate voltage and temperature-dependent experiments, respectively. The 2D electrons are coupled to the local moments of magnetic ions via a ferromagnetic sp–d exchange interaction, resulting in spin splitting energies, ΔE_S, of tens of meV, which are comparable to or larger than the Landau level splitting, $\hbar\omega_c$, and finally, as discussed above, the Rashba SO interaction is of a similar magnitude in type III heterostructures [5].

2. Experimental and theoretical details

Epitaxial growth of the superlattices (SLs) and fully strained QWs was carried out in a Riber 2300, molecular beam epitaxial chamber (MBE) [7,14] on $Cd_{0.96}Zn_{0.04}Te$ substrates at 180°C. The QWs were modulation doped using CdI_2 as a doping material. After growth, a standard Hall bar was fabricated by means of a wet chemical etch, then a 250 nm thick Al_2O_3 film, which serves as an insulating layer, was deposited by electron beam evaporation. Finally Al was evaporated to form a gate electrode. Ohmic indium contacts were fabricated by thermal bonding.

Optical transmission measurements were carried out in the middle infrared regime with a Fourier transform spectrometer, Bruker IFS88. The experimental absorption coefficients are compared with results based on an 8×8 $\boldsymbol{k} \cdot \boldsymbol{p}$ model [7].

Numerous $\boldsymbol{k} \cdot \boldsymbol{p}$ band structure calculations using the envelope function approximation for the $HgTe/Hg_{0.3}Cd_{0.7}Te$ SL have been published [15–18]. In this investigation, the bands of both bulk HgTe and CdTe are described by Kane's four-band model (8×8 $\boldsymbol{k} \cdot \boldsymbol{p}$) including all second-order remote band contributions [7].

The QWs were measured in an He^4 cryostat with standard lock-in techniques using a current of 1 μA at temperatures between 0.4 and 4.2 K and magnetic fields up to 14 T. Mobilities up to 3.5 and 6.0×10^5 cm^2/(V s) have been achieved for the $HgTe/Hg_{0.3}Cd_{0.7}Te$ QWs at 1.6 K without and with a gate voltage, respectively. In contrast, the mobility of $Hg_{0.98}Mn_{0.02}Te/Hg_{0.3}Cd_{0.7}Te$ QWs was appreciably lower with values up to 1.0×10^5 cm^2/(V s) at 4.2 K for zero gate voltage. The experimental magneto-transport results have been quantitatively described by means of self-consistent Hartree calculations based on the 8×8 $\boldsymbol{k} \cdot \boldsymbol{p}$ model discussed above [12,19].

3. Results and discussion

3.1. Optical properties and band structure

Transmission spectra of an (1 1 2)B oriented SL are shown in Fig. 1 at several temperatures. Numerous distinctive steps are visible and with decreasing temperature, sharp minima at the absorption edges can be observed. The three broad steps at 300 K have been assigned to the H2–E2, H3–E3 and H4–E4 intersubband transitions. H, L and E are the heavy hole, light hole and electron subbands, respectively. In the inverted band regime, the valence subbands and the
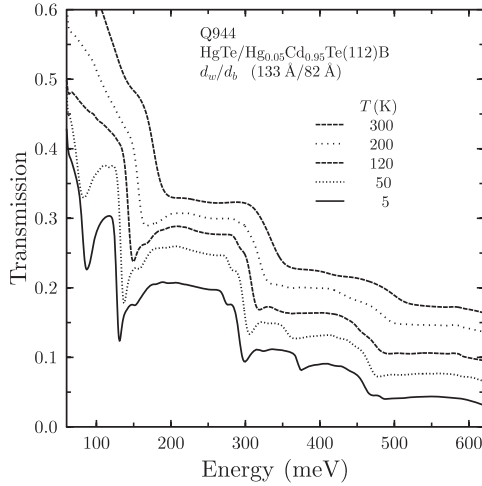
Fig. 1. The transmission spectra of a HgTe/Hg$_{0.05}$Cd$_{0.95}$Te (1 1 2)B superlattice, Q944, at several temperatures. The spectra are shifted along the vertical axis for clarity.
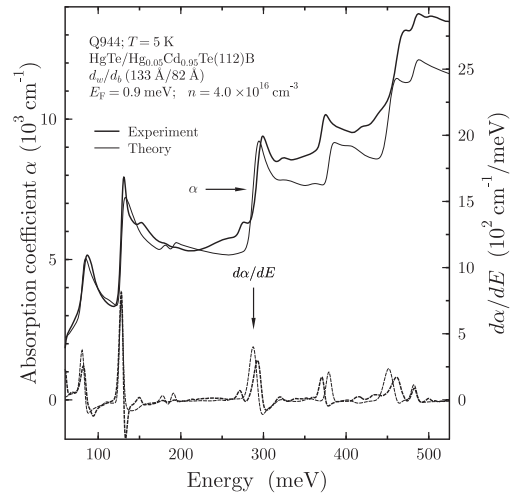

Fig. 2. The experimental (thick line) and theoretical (thin line) absorption coefficients, and their first derivative (thick and thin dashed lines, respectively) for a HgTe/Hg$_{0.05}$Cd$_{0.95}$Te (1 1 2)B SL, Q944, at 5 K.

conduction subbands at low energies are mixed to varying degrees at finite k, however, for the sake of brevity we shall continue to use these designations. With decreasing temperature fine structure becomes readily discernable.

The calculated absorption coefficient spectrum of an (1 1 2)B oriented SL, which is shown in Fig. 2, is in good agreement with the experimental spectrum. The relative heights of the corresponding steps are in good agreement with the experiment, even though the absolute magnitude of the absorption coefficient, α, is underestimated due to the neglect of Coulomb interaction between electron and hole [20]. The maxima at the absorption edges are slightly more pronounced than that predicted by our 8×8 $k \cdot p$ model, nevertheless agreement with experiment is reasonable.

3.2. Rashba effect in QWs with an inverted band structure

The symmetrically modulation doped sample Q1605 with a well width of 21 nm displays very pronounced SdH oscillations in magnetic fields between 0.7 and 14 T at a temperature of 1.6 K. Fourier analysis of the complex SdH oscillations shows that at higher gate voltages three subbands are occupied, see

Fig. 3(b). No splitting of the H1 subband can be observed when the QW potential is symmetric, i.e., $V_g \approx$ 0.2 V. For either more positive or more negative gate voltages, a splitting of the H1 subband is apparent. Well developed quantum Hall plateaus, not shown here, indicate the excellent quality of the sample [5]. The largest Hall mobility was 6.0×10^5 cm^2/V s at a gate voltage of 2.0 V; to our knowledge this is the highest value that has been observed for HgTe QWs.

The results of self-consistent band structure calculations for sample Q1605 are shown in Fig. 4. Using the usual subband notation, H1 and E2 are conduction bands, and H2 is the first valence band. This is a consequence of the inverted band structure of QWs with a large well width. In agreement with experiment, a small SO splitting is predicted for E2 and a much larger value for H1. Using the calculated band structure, the carrier densities in the H1+, H1− and E2 subbands have been calculated at various gate voltages. The results are in good agreement with self-consistent Hartree calculations [5]. The degeneracy of the H2 valence subband is also removed and one spin component has a maximum at finite $k_\parallel$, i.e., this is a semiconductor with an indirect band gap [21].
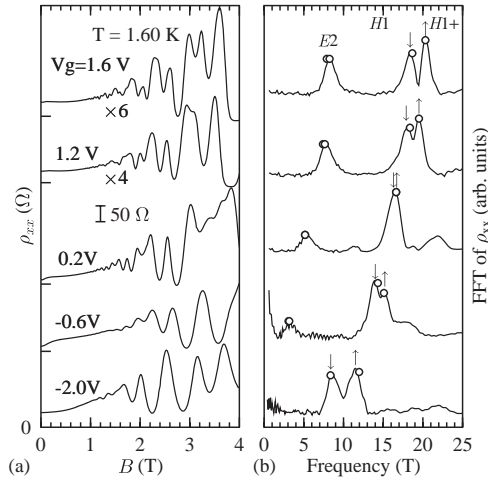
Fig. 3. SdH oscillations in $\rho_{xx}(B)$ (a) and the corresponding fast Fourier transformations (FFT) (b) for an n-type symmetrically modulation-doped HgTe QW Q1605 at 1.6 K and various gate voltages. (a) The two uppermost curves have been multiplied by a factor of 6 and 4. (b) The up and down arrows represent the two spin states of the H1 subband. The circles represent the results of theoretical calculations for the population of H1 and E2 subbands.
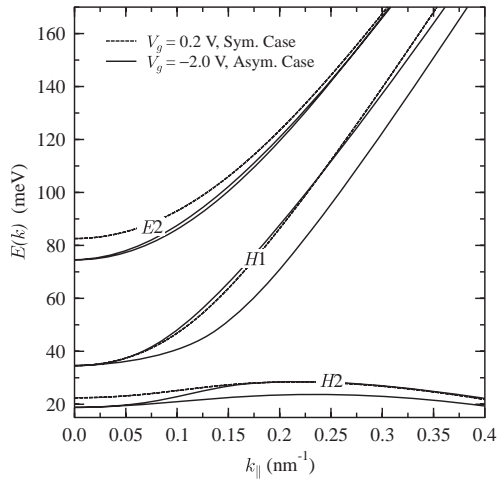

Fig. 5. Experimental (circles) and calculated (lines) population differences Δn_{H1} in the two spin states of the H1 subband as a function of the total charge carrier density, n_{SdH}. The n_{ds} parameter is the depleted charge density in the doped layer on the substrate side.

Fig. 4. Self-consistently calculated subband dispersion $E(k)$ of the HgTe QW Q1605 at $V_g = -2.0$ V (solid lines) and $V_g = 0.2$ V (dashed lines), which represent the asymmetric and the symmetric cases, respectively.
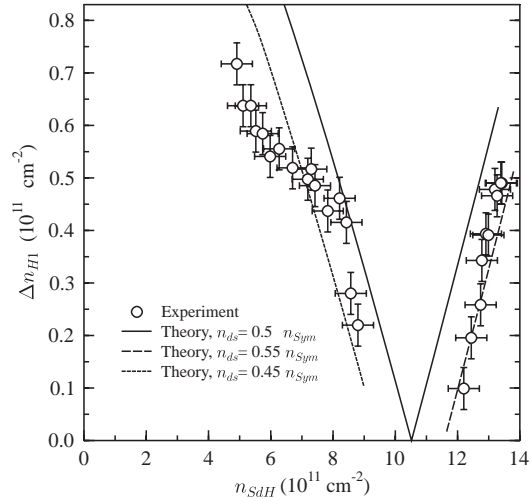
The data for HgTe/Hg$_{0.3}$Cd$_{0.7}$Te QWs clearly demonstrate that Rashba SO splitting is caused by an asymmetrical potential. Because only one H1 peak is resolved for the symmetric case, Zeeman spin splitting can be excluded. Furthermore, experiments in tilted magnetic fields allow us to distinguish between Zeeman and Rashba splitting. In a 2DEG, Zeeman splitting depends on the total magnetic field. SdH experiments carried out in tilted magnetic fields have shown that the peaks in the Fourier transform spectra depend only on the normal component of the magnetic field thus excluding Zeeman splitting.

The gate voltage has been introduced as a variable in the numerical simulation by employing the sheet carrier density inside the QW as an input parameter. The experimental population differences between the two SO split states of the H1 subband for all gate voltages are shown in Fig. 5 as circles and the theoretical values as lines. If we assume that the top gate voltage does not influence the status of the doped layer on the substrate side, then the depleted charge density on the substrate side, denoted by n_{ds}, should remain constant and be exactly one half of the carrier density n_{sym} over the entire gate voltage range. n_{sym} is the

186

carrier density when the potential of the QW is symmetric. However, better agreement with experiment is achieved if n_{ds} is assumed to be 10% smaller for a negative gate voltage, and 10% larger for a positive voltage. If the former value for n_{ds} is valid then the latter is physically meaningful.

As pointed out by Pfeffer and Zawadzki [22] and Hu et al. [23], the detailed distribution of the electric field in the QW is always unknown and it is not clear to what extent one can rely on the field distribution obtained by fitting the measured total electron concentration based on self-consistent subband structure calculations, as has been done here. Nevertheless, our experimental results can be satisfactorily reproduced.

Rashba SO splitting for type I and III heterostructures has been described using a one band model and a modified two band model [23,8]. Both models result in a linear dependence on $k_\parallel$; $E^\pm(k_\parallel) = E_0 + \hbar^2 k_\parallel^2/2m^* \pm \alpha k_\parallel$. But it is well known that these models are not applicable for narrow-gap heterostructures. Self-consistent calculations [11,24] as well as analytical model calculations [25] for normal electronic subbands in type I narrow-gap systems have shown that the SO splitting is linear only for small $k_\parallel$ due to band nonparabolicity.

Fig. 6 displays the SO splitting energies of the H1 and E2 subbands, ΔE_{H1} and ΔE_{E2}, as a function of $k_\parallel$ for the calculated inverted band structure shown in Fig. 4. The ΔE_{H1} versus $k_\parallel$ plot starts with a nearly zero slope at $k_\parallel = 0$, increases nonlinearly and then finally begins to decrease for increasing $k_\parallel$ due to band mixing, i.e., nonparabolicity effects. SO splitting reaches a maximum value slightly above the Fermi wave vector. This is another unique feature of the inverted band structure and one more consequence of the heavy hole character of the envelope function for the first conduction subband. ΔE_{H1} can be described very well at small values of $k_\parallel$ by a $k_\parallel^3$ dispersion [10,11] as indicated by the upper dashed line in Fig. 6. On the other hand, the SO splitting of the E2 subband displays a linear behavior at small values of $k_\parallel$, as shown by the lower dashed line in Fig. 6.

Consistent with the above discussion, Rashba [10] and Winkler [11] have shown that SO splitting should be proportional to $k_\parallel^3$ for the heavy hole like state $|\Gamma_8, \pm\frac{3}{2}\rangle$, but for the electron like state $|\Gamma_6, \pm\frac{1}{2}\rangle$ and the light hole like state $|\Gamma_8, \pm\frac{1}{2}\rangle$, SO splitting should be
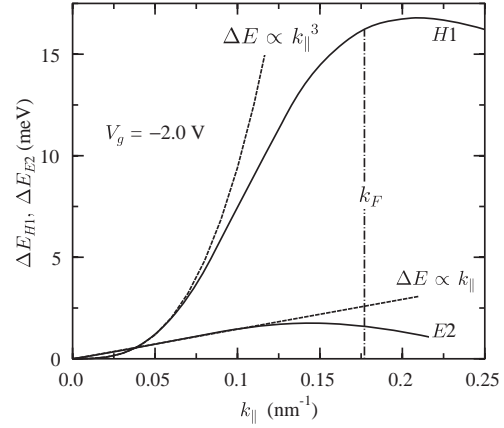

Fig. 6. The calculated SO splitting energy of the H1 and E2 subbands (solid curves), ΔE_{H1} and ΔE_{E2}, versus in-plane wave vector $k_\parallel$ for sample Q1605 at $V_g = -2.0$ V. The position of the Fermi wave vector k_F is denoted by the dotted-dashed line. The two dashed lines demonstrate that ΔE_{H1} and ΔE_{E2} are proportional to $k_\parallel^3$ and $k_\parallel$, respectively, at small $k_\parallel$.

a linear function of $k_\parallel$. This is in good agreement with the self-consistently calculated ΔE_{H1} and ΔE_{E2} versus $k_\parallel$ behavior shown in Fig. 6. The SO split heavy hole subband dispersion can be expressed as $\Delta E(k_\parallel) = \beta k_\parallel^3$ where β is the SO coupling constant between the Γ_8 and Γ_6 bands. Analogous to α for a linear dependence, β can only correctly describe the SO splitting at small values of $k_\parallel$. At larger values, for example, only a rough estimate of the SO splitting can be expected at the Fermi wave vector for a given gate voltage and obviously β cannot describe the SO splitting for all $k_\parallel$.

3.3. Magnetic 2DEG: Rashba and Zeeman effects

In the magnetic 2DEG in a $Hg_{1-x}Mn_xTe/Hg_{0.3}Cd_{0.7}Te$ QW, a giant Zeeman spin splitting is also expected. As visible in Fig. 7 the occupancy of the H1− and H1+ subbands does not change with temperature; the asymmetry of the QW structure does not change and hence no change in the Rashba SO splitting is observed. Beating patterns are clearly visible in the SdH oscillations because of the existence of two closely spaced frequency components with similar amplitudes due to level splitting. In this case these nodes in the beating patterns depend on the temperature as can
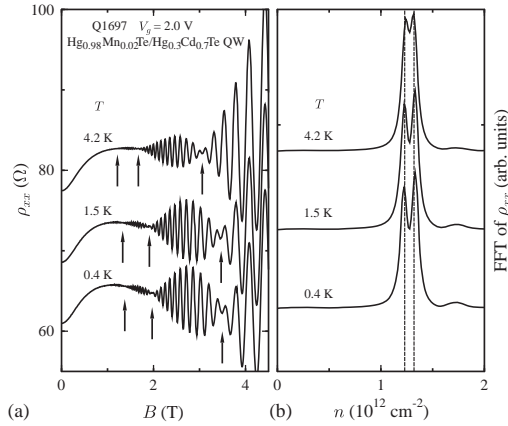
Fig. 7. (a) SdH oscillations in $\rho_{xx}(B)$ (b) and the corresponding fast Fourier transformations (FFT) for an n-type modulation-doped $Hg_{0.98}Mn_{0.02}Te$ QW, Q1697, at $V_g = 2.0$ V and various temperatures. All curves have been shifted vertically for clarity. Arrows in (a) indicate a dependence of the node positions on temperature, whereas the absence of an increase in either n_{H1} or Δn_{H1} with increasing temperature is visible in (b).

Fig. 8. The difference in total splitting energies between two temperatures, i.e., $\delta(1.4\ \mathrm{K}) - \delta(T)$ for temperatures $T = 2.0, 2.5, 3.0, 4.0, 5.0, 6.0, 7.0, 8.0, 10.0, 12.0, 14.0, 16.0, 20.0, 23.0, 26.0$ and 31.0 K from bottom to top, for an n-type modulation-doped $Hg_{0.94}Mn_{0.06}Te$ QW, Q1715. The experimental values are shown as symbols and those from Eq. (1) as lines.

be seen in Fig. 7. This behavior is characteristic of a change in Zeeman spin splitting rather than Rashba SO splitting, which has been shown to depend on the structure inversion asymmetry, i.e., the gate voltage.

In order to analyze the experimental results for $Hg_{1-x}Mn_xTe$ QWs, we take advantage of the fact that a splitting of the Landau levels leads to a modulation of the SdH amplitude A according to $A \propto \cos(\pi v)$ where $v = \delta/(\hbar\omega_c)$, $\hbar\omega_c$ is the Landau level separation energy and δ is the energy splitting of each Landau level [2]. Nodes in the beating pattern in the SdH oscillations will occur for half-integer values of v; ± 0.5, ± 1.5, etc.; when A is zero. Three nodes were observed in the SdH oscillations of Q1697 at higher charge carrier concentrations, and fewer nodes at lower concentrations.

The large temperature induced shift of the observed nodes in Q1697, shown in Fig. 7, is caused by the strong sp–d exchange interaction between the conduction electrons and the Mn ion spins, as discussed by Gui et al. [26] for bulk $Hg_{1-x}Mn_xTe$. The temperature dependence stems from the reduction in magnetization of the Mn ions with increasing temperature. The effective g^* factor in dilute magnetic semiconductors
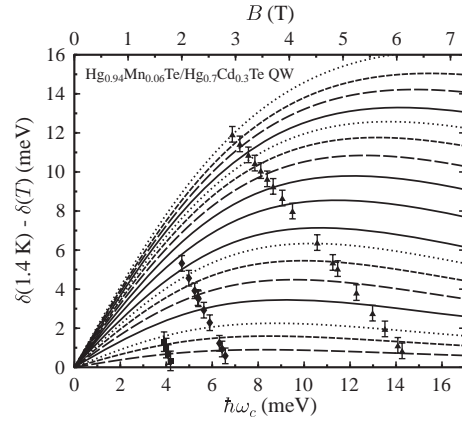
can be expressed phenomenologically as [6,27]

$$g^* = g_0 - \frac{(\Delta E)_{\max}}{\mu_B B} B_{5/2}\left[\frac{5 g_{Mn}\mu_B B}{2 k_B (T + T_0)}\right], \qquad (1)$$

where $g_{Mn} = -2$, $B_{5/2}(x)$ is the Brillouin function for a spin of $S = \frac{5}{2}$, which has been empirically modified by using a rescaled temperature, $T + T_0$, in order to account for antiferromagnetic spin–spin interaction, and $(\Delta E)_{\max}$ is the saturated spin splitting energy caused by the sp–d exchange interaction. g_0 is the g factor for an HgTe QW without the presence of Mn [28], i.e., $g_0 = -20$.

As is visible in Fig. 8, a least-squares fit of Eq. (1) for a $Hg_{1-x}Mn_xTe$ QW at the corresponding temperatures is in good agreement with the experimental results for the difference in total level splitting, i.e., $\delta(1.4\ \mathrm{K}) - \delta(T)$ [13]. In addition it has been demonstrated that the magnitude of the Rashba SO splitting energy is greater than that of Zeeman and Landau level splitting for magnetic fields up to 4–5 T [13].

The observed beating pattern in the SdH oscillations has also been investigated as a function of current [29]. The electron concentration does not change, i.e., the asymmetry of the QW is invariant, see Fig. 9. Therefore, the observed shift of the nodes in the beating pattern is a consequence of a change in the giant
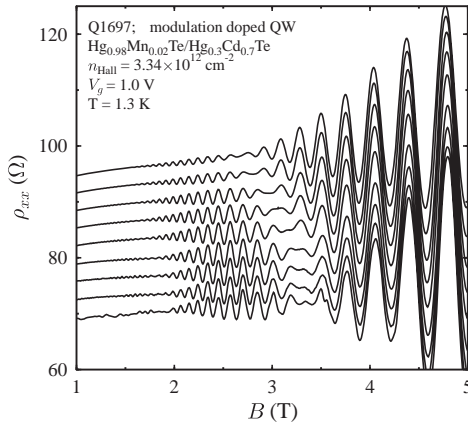
188

Fig. 9. SdH oscillations in $\rho_{xx}(B)$ for an n-type modulation-doped Hg$_{0.98}$Mn$_{0.02}$Te QW, Q1697, at $V_g = 1.0$ V. The curves from bottom to top correspond to currents of 1, 10, 20, 50, 75, 100, 150, 200 and 300 μA, and all curves have been shifted vertically for clarity.

Zeeman splitting due to an increase in the manganese temperature, and not a result of Rashba SO splitting. The Mn temperature has been determined by using Eq. (1) after determining the corresponding parameters via an experiment with variable lattice temperature, see Fig. 8. The temperature of the hot electrons has been obtained from an analysis of the amplitudes of the fast Fourier transformation of the SdH oscillations via $X/\sinh(X)$ where $X = f(m^*, B)$.

The electrons lose some of their kinetic energy to the Mn ions via spin-flip scattering and to the lattice. As expected the lattice temperature does not increase due to the large heat capacity of the lattice. In contrast the temperature of the Mn ion system increases, albeit much slower than that of the electrons, linearly with current up to approximately 20 K above the lattice temperature [29].

4. Conclusions

The optical properties of HgTe/Hg$_{1-x}$Cd$_x$Te heterostructures have been investigated in the inverted band structure regime. It has been demonstrated that the optical properties and the corresponding band structure are in good agreement with theory as is the case in the normal band structure regime.

With this knowledge, we have investigated Rashba SO splitting in HgTe QWs with an inverted band structure by means of gate controlled Hall devices. SO splitting of the H1 subband shows a large gate voltage dependence. In contrast, SO splitting of the E2 subband is experimentally unresolved. Band structure calculations based on the 8×8 $\bm{k} \cdot \bm{p}$ Kane model were performed which are in very good agreement with experiment. It has been shown that the heavy hole character of the H1 conduction subband determines the electron density distribution in the QW and enhances the Rashba SO splitting at large electron densities. These are unique properties of the conduction subband of type III inverted heterostructures. An analytical model with $\beta k_\parallel^3$ dispersion can be employed to describe the SO splitting of the H1 conduction subband at small values of the in-plane wave vector $k_\parallel$ rather than the $\alpha k_\parallel$ model commonly used for type I QWs. In addition, the relative magnitude of Rashba SO splitting in the H1 and E2 subbands has also been shown to be a consequence of the heavy hole character of the H1 subband and the light particle nature of the E2 subband which is an admixture of the light hole and electron states.

The relative magnitudes of the Rashba, Zeeman and Landau effects of a magnetic 2DEG in modulation-doped n-type Hg$_{1-x}$Mn$_x$Te/Hg$_{0.3}$Cd$_{0.7}$Te QWs have been investigated. Giant Zeeman and Rashba SO splitting have been separated by analyzing the temperature and gate voltage dependence, respectively, of the node positions and beating patterns in SdH oscillations. It has been experimentally demonstrated that Rashba SO splitting is larger than or comparable to the sp–d exchange interaction induced giant Zeeman splitting in this magnetic 2DEG even at moderately high magnetic fields. The Mn temperature has also been investigated as a function of current. Values of 20 K above the lattice temperature have been observed.

References

[1] E.I. Rashba, Fiz. Tverd. Tela 2 (1960) 1224 [Sov. Phys. Solid State 2 (1960) 1109];
Yu.A. Bychkov, E.I. Rashba, Pis'ma Zh. Eksp. Teor. Fiz. 39 (1984) 66 [JETP Lett. 39 (1984) 78].

[2] B. Das, D.C. Miller, S. Datta, R. Reifenberger, W.P. Hong, P.K. Bhattacharya, J. Singh, M. Jaffe, Phys. Rev. B 39 (1989) 1411.

[3] B. Das, S. Datta, R. Reifenberger, Phys. Rev. B 41 (1990) 8278.

[4] G. Engels, J. Lange, Th. Schäpers, H. Lüth, Phys. Rev. B 55 (1997) R1958.

[5] X.C. Zhang, A. Pfeuffer-Jeschke, K. Ortner, V. Hock, H. Buhmann, C.R. Becker, G. Landwehr, Phys. Rev. B 63 (2001) 245305.

[6] I.P. Smorchkova, N. Samarth, J.M. Kikkawa, D.D. Awschalom, Phys. Rev. Lett. 78 (1997) 3571.

[7] C.R. Becker, V. Latussek, G. Landwehr, L.W. Molenkamp, Phys. Rev. B 68 (2003) 035202.

[8] M. Schultz, F. Heinrichs, U. Merkt, T. Colin, T. Skauli, S. Løvold, Semicond. Sci. Technol. 11 (1996) 1168.

[9] N.F. Johnson, P.M. Hui, H. Ehrenreich, Phys. Rev. Lett. 61 (1988) 1993.

[10] E.I. Rashba, Sheka, Fiz. Tverd. Tela 2 (1959) 162 [Sov. Phys. Solid State 1 (1959) 368].

[11] R. Winkler, Phys. Rev. B 62 (2000) 4245.

[12] A. Pfeuffer-Jeschke, Doctoral Thesis, Physikalisches Institut der Universität Würzburg, 2000.

[13] Y.S. Gui, C.R. Becker, J. Liu, V. Daumer, H. Buhmann, L.W. Molenkamp, cond-mat/026355, 2002.

[14] F. Goschenhofer, J. Gerschütz, A. Pfeuffer-Jeschke, R. Hellmig, C.R. Becker, G. Landwehr, J. Electron. Mater. 27 (1998) 532.

[15] L.R. Ram-Mohan, K.H. Yoo, R.L. Aggarwal, Phys. Rev. B 38 (1988) 6151.

[16] N.F. Johnson, H. Ehrenreich, P.M. Hui, P.M. Young, Phys. Rev. B 41 (1990) 3655.

[17] A. Simon, D. Bertho, D. Boiron, C. Jouanin, Phys. Rev. B 42 (1990) 5221.

[18] J.R. Meyer, C.A. Hoffman, F.J. Bartoli, Semicond. Sci. Technol. 5 (1990) S90.

[19] G. Landwehr, J. Gerschütz, S. Oehling, A. Pfeuffer-Jeschke, V. Latussek, C.R. Becker, Physica E 6 (2000) 713.

[20] C. Tanguy, Phys. Rev. Lett. 75 (1995) 4090, and references therein.

[21] K. Ortner, X.C. Zhang, A. Pfeuffer-Jeschke, C.R. Becker, G. Landwehr, L.W. Molenkamp, Phys. Rev. B 66 (2002) 075322.

[22] P. Pfeffer, W. Zawadzki, Phys. Rev. B 52 (1995) R14332.

[23] C.M. Hu, J. Nitta, T. Akazaki, H. Takayamgi, Phys. Rev. B 60 (1999) 7736.

[24] R. Winkler, U. Rössler, Phys. Rev. B 48 (1993) 8918.

[25] E.A. de Andrada e Silva, G.C. la Rocca, F. Bassani, Phys. Rev. B 55 (1997) 16293.

[26] Y.S. Gui, J. Liu, K. Ortner, V. Daumer, C.R. Becker, H. Buhmann, L.W. Molenkamp, Appl. Phys. Lett. 79 (2001) 1321.

[27] N.B. Brandt, V.V. Moshchalkov, Adv. Phys. 33 (1984) 193;
J.K. Furdyna, J. Appl. Phys. 64 (1988) R29.

[28] X.C. Zhang, K. Ortner, A. Pfeuffer-Jeschke, C.R. Becker, G. Landwehr, R. Winkler, unpublished.

[29] Y.S. Gui, C.R. Becker, J. Liu, M. König, V. Daumer, H. Buhmann, L.W. Molenkamp, unpublished.

190

Cyclotron masses of asymmetrically doped HgTe quantum wells

A. Pfeuffer-Jeschke [a,*], F. Goschenhofer [a], S.J. Cheng [b], V. Latussek [a],
J. Gerschütz [a], C.R. Becker [a], R.R. Gerhardts [b], G. Landwehr [a]

[a] Physikalisches Institut der Universität Würzburg, Am Hubland, 97074 Würzburg, Germany
[b] Max-Planck-Institut für Festkörperforschung, Heisenbergstr. 1, 70569 Stuttgart, Germany

Abstract

We report on experimental and theoretical investigations of the cyclotron mass in six n-type modulation doped HgTe single quantum wells. Magnetotransport measurements at low temperatures resulted in well pronounced Shubnikov–de Haas oscillations and quantum Hall plateaus. The cyclotron mass was determined from the temperature dependence of the Shubnikov–de Haas oscillations at low magnetic fields. Theoretical calculations of the semi-classical cyclotron mass are based on a 8×8 $\mathbf{k} \cdot \mathbf{p}$ model. The influence of the induced free carriers is included in a self-consistent Hartree calculation. © 1998 Elsevier Science B.V. All rights reserved.

Keywords: HgTe; Quantum wells; Magnetotransport; Band structure

Type-III heterostructures composed of the semimetal HgTe and the wide-gap semiconductor $Hg_xCd_{1-x}Te$ have been widely investigated by optical and transport methods during the past two decades. Magnetotransport investigations were mainly performed on superlattices. Shubnikov–de Haas (SdH) oscillations and quantum Hall effect have been observed in those samples [1]. Studies of quantum wells (QW) have focused on optical and magnetooptical experiments [2]. To our knowledge quantum transport effects in modulation doped n-type HgTe QWs were first reported by Goschenhofer et al. [3].

In this paper we discuss the latter results in the light of band structure calculations for six asymmetrically doped n-type HgTe QWs, grown by mo-

lecular beam epitaxy. CdTe doped with iodine is separated from the HgTe quantum well by a spacer. The spacer consists of an undoped CdTe layer and a $Hg_{0.3}Cd_{0.7}Te$ barrier. Finally a $Hg_{0.3}Cd_{0.7}Te$ barrier was grown on top of the HgTe quantum well. From the growth rates we deduce a QW thickness of 45 Å where the relative error is at least 10%. By adjusting the thickness of the spacer and doped layer the density of the two-dimensional (2D) electron gas could be varied. Hall effect measurements were done in a temperature range between 1.6 and 60 K. All samples show well pronounced quantum Hall plateaus and SdH oscillations. The effective cyclotron mass was extracted from the temperature dependence of the SdH oscillations. In order to compare these experimental results with theoretical predictions we performed self-consistent Hartree calculations based on an 8×8 $\mathbf{k} \cdot \mathbf{p}$ band structure model for different electron densities. From the band structure we de-

* Corresponding author. Fax: +49-931-8885142; e-mail: pfeuffer@physik.uni-wuerzburg.de

duced the semi-classical cyclotron mass, which is compared with the experimentally determined mass.

Fig. 1 shows the magnetoresistance and the Hall effect for sample Q1099 at 1.6 K. SdH oscillations are visible for fields as low as 1 T. Well pronounced quantum Hall plateaus are observed. The Hall mobility of this sample is 68.2×10^3 cm^2/V s. From the period of the SdH oscillations at high fields a 2D carrier concentration of 5.16×10^{11} cm^{-2} was determined. This value coincides well with the 2D carrier concentration obtained from the Hall coefficient. The SdH peak near 2 T clearly shows evidence for spin splitting, while peaks below 2 T are spin degenerate. The maxima above 2 T are completely spin split, as evidenced by the Hall effect which displays quantum Hall plateaus at all integer filling factors.

The inverse of the magnetic field strengths of the minima in ρ_{xx} versus their index of occurence is shown in Fig. 2. Two straight lines corresponding to the spin degenerate and the spin split regions are evident. The slope of the curve in the high field section is slightly lower than twice the slope of the curve in the low field section, i.e. $s_h/s_l = 1.95 \pm 0.02$. This is probably the consequence of a small zero-field spin splitting of the first subband due to the asymmetrically doped structure. This asymmetry results in a lack of inversion sym-
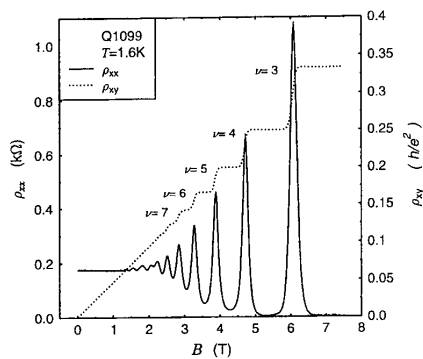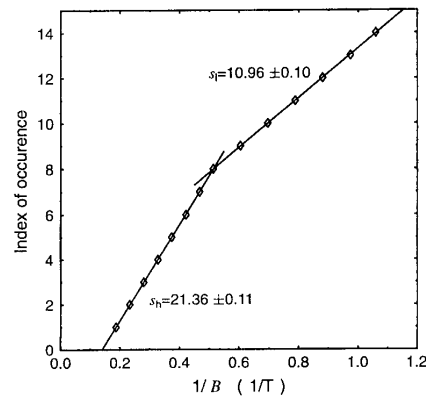

Fig. 2. Plot of the inverse magnetic field strenghts of the minima in ρ_{xx} versus their index of occurence.

metry and, under the influence of the spin–orbit interaction, a lifting of the Kramers degeneracy of the two spins for $k \neq 0$. Stormer et al. [4] have shown that for similar hole systems, the slope s_h of the high field component yields the total 2D carrier density in the system according to $n = (e/h)s_h = 5.16 \times 10^{11}$ cm^{-2}. The period of the low field section can then be translated into the density $n_1 = (e/h)s_l = 2.65 \times 10^{11}$ cm^{-2} of one spin component, leaving $n_2 = n - n_1 = 2.51 \times 10^{11}$ cm^{-2} carriers for the second spin component.

The cyclotron mass m^* of the electrons may be derived from the temperature dependence of the SdH amplitudes, $A(T,B)$, at low magnetic field. We have used the well known formula [5]:

$$\frac{A(T_1,B)}{A(T_2,B)} = \frac{T_1 \sinh(\beta T_2 m^*/m_0 B)}{T_2 \sinh(\beta T_1 m^*/m_0 B)},$$

where $\beta = 2\pi^2 k_B m_0/\hbar e$ is a constant, to fit the ratio of SdH amplitudes for various temperatures T_1 and T_2 below 10 K at a fixed magnetic field. This procedure has been repeated for several maxima at low magnetic field.

The masses obtained from the fit to the experimental results of all six quantum well structures are summarized in Table 1. Some samples could only be studied under illumination with a red light

Fig. 1. SdH and quantum-Hall effect of sample Q1099 at 1.6 K.

Table 1
Experimental results for six different HgTe quantum wells. (LED: measured under illumination.)

Sample	n_{SdH} (10^{11} cm^{-2})	n_{Hall} (10^{11} cm^{-2})	μ_{Hall} (10^3 cm^2/V s)	m^* ($10^{-2}m_0$)
Q1099	5.16 ± 0.03	5.14 ± 0.15	68.2 ± 2.0	2.5 ± 0.2
Q1100	4.06 ± 0.12	3.82 ± 0.11	11.1 ± 0.3	2.5 ± 0.2
Q1102	10.0 ± 0.1	10.1 ± 0.3	43.4 ± 0.1	3.4 ± 0.2
Q1138 (LED)	2.20 ± 0.07	2.15 ± 0.06	51.1 ± 1.5	2.0 ± 0.3
Q1140 (LED)	1.88 ± 0.06	1.87 ± 0.06	50.0 ± 1.5	1.9 ± 0.3
Q1141 (LED)	2.37 ± 0.07	2.29 ± 0.07	40.9 ± 1.2	2.3 ± 0.3

emitting diode. This is probably due to the relatively thick spacer in these samples. The cyclotron mass obviously increases with the increasing density of the electrons due to the nonparabolic band structure of the QWs.

The band structure calculations are based on Kane's 8×8 $\mathbf{k} \cdot \mathbf{p}$ model including all second-order terms representing the remote-band contributions. We have neglected the intrinsic inversion asymmetry of the HgTe and Hg$_x$Cd$_{1-x}$Te, which is known to be extremely small. The envelope function approximation is used to calculate the subbands of the heterostructure, see e.g. [6]. We have calculated the band structure of a HgTe QW embedded in Hg$_{0.3}$Cd$_{0.7}$Te barriers. The influence of the induced free carriers has been included in a self-consistent Hartree calculation. For the solution of the Poisson equation we assumed that all free carriers come from the doped CdTe layer. We have determined that the anisotropy of the in-plane band structure (warping) can be ignored for the first electron subband. Therefore the Hartree calculations have been done within the axial approximation, whereby the in-plane band structure does not depend on the direction in the (k_x,k_y) plane. All calculations are based on a set of band parameters for HgTe according to Truchsess et al. [7]. For the solution of the Poisson equation we assumed $\epsilon = 21$ [8].

In the following the results for a 45 Å wide HgTe QW with a carrier density of 5.16×10^{11} cm^{-2} (sample Q1099) are discussed. The self-consistently calculated density is slightly asymmetrical as a consequence of the inversion asymmetry of the structure. In Fig. 3 the band structure is shown. E1 is the first electron and H1 the first hole subband, E_F the Fermi energy. For $k \neq 0$ the spin

degeneracy is lifted. The spin splitting at the Fermi wave vector k_F is about 2 meV. This effect is rather small, since the influence of the asymmetric Hartree potential is small compared to the confinement. The occupation of the two spin components of E1 is given by $n_1 = 2.64 \times 10^{11}$ cm^{-2} and $n_2 = 2.52 \times 10^{11}$ cm^{-2} in very good agreement with the experimental values. It is also obvious that the (isotropic) band structure is highly nonparabolic. This is a consequence of the small gap of 55 meV. Given the band structure we can calculate the semiclassical cyclotron mass at the Fermi energy according to

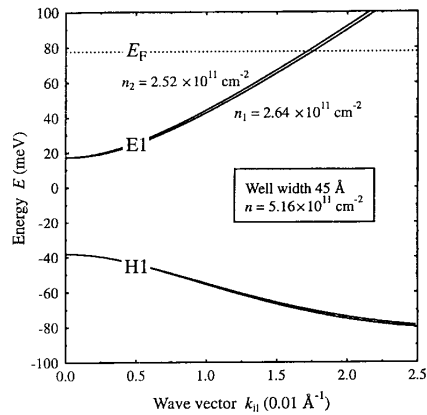$$\frac{1}{m^*} = \frac{1}{\hbar^2 k_\parallel} \frac{\partial E}{\partial k_\parallel} (k_F).$$

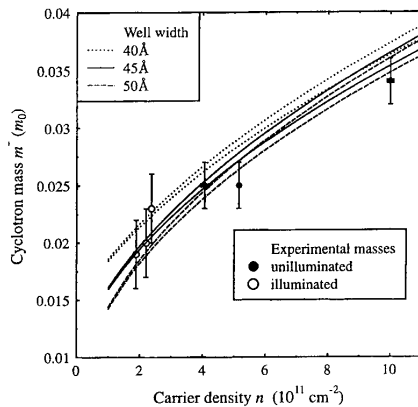Fig. 3. Band structur calculated in the axial approximation.

sities. The general dependence of the experimental cyclotron mass is well described by the theory. A better description of the experimental values is given with the smaller mass and thicker QW width. In summary, the experimental values are in good agreement with theoretical values within the experimental error and the uncertainty of the well thickness.

Fig. 4. Comparison between experimental deduced and theoretical calculated cyclotron masses.

From the two spin split components of the E1 subband we get two masses that differ by a few percent.

In Fig. 4 the calculated masses (lines) as a function of the carrier density are shown. In view of the uncertainty of the sample thickness the cyclotron masses are calculated for well widths of 40, 45 and 50 Å. The circles represent the experimental values. The theoretical as well as the experimental masses obviously increase with increasing electron density as a consequence of the highly nonparabolic band structure. The difference between the heavier and the lighter spin component of one structure increases with increasing density, because the structure becomes more asymmetric at higher den-

References

[1] C.A. Hoffmann, J.R. Meyer, F.J. Bartoli, Semicond. Sci. Technol. 8 (1993) S48.

[2] M. Schultz, U. Merkt, A. Sonntag, U. Rössler, R. Winkler, T. Colling, P. Helgesen, T. Skauli, S. Lovold, Phys. Rev. B 57 (1998) 14772.

[3] F. Goschenhofer, J. Gerschütz, A. Pfeuffer-Jeschke, R. Hellmig, C.R. Becker, G. Landwehr, J. Electron. Mater. 27 (1998) 532.

[4] H.L. Stormer, Z. Schlesinger, A. Chang, D.C. Tsui, A.C. Gossard, W. Wiegemann, Phys. Rev. Lett. 51 (1983) 126.

[5] T. Ando, A.B. Fowler, F. Stern, Rev. Mod. Phys. 54 (1982) 437.

[6] L.R. Ram-Mohan, K.H. Yoo, R.L. Aggarwal, Phys. Rev. B 38 (1988) 6151.

[7] M. von Truchsess, V. Latussek, R. Sizmann, P. Helgesen, F. Goschenhofer, C.R. Becker, G. Landwehr, E. Batke, Phys. Rev. B 51 (1995) 17618.

[8] Landolt-Börnstein, O. Madelung (Ed.), vol. III/22a, Springer, Berlin, 1987.

Anhang E

Kollektive Anregungen in GaAs/Ga$_{1-x}$Al$_x$As Heterostrukturen

COLLECTIVE INTERSUBBAND EXCITATIONS IN A p-DOPED GaAs/AlGaAs MULTIPLE QUANTUM WELL

C. Schüller, J. Kraus and V. Latussek

Physikalisches Institut der Universität Würzburg, W-8700 Würzburg, FRG

J. K. Ebeling

Abt. Optoelektronik der Universität Ulm, W-7900 Ulm, FRG

We report on Raman spectroscopic investigations of collective spin–density (SDW) and charge–density waves (CDW) in the two–dimensional hole gas of a p–modulation doped $GaAs/Al_xGa_{1-x}As$ multiple quantum–well (MQW) structure and on the consequence of Landau damping of these excitations.

From the existence of collective SDW with energies lower than the border of the single–particle continuum we derive that exchange and correlation effects are of considerable strength in such hole gases.

1. Introduction

In a number of recent publications[1,2] the importance of exchange and correlation in the quasi–two–dimensional electron gas of $GaAs/Al_xGa_{1-x}As$ quantum–wells was impressively demonstrated by Raman investigations on intersubband transitions. In inelastic light scattering investigations these transitions are observed due to fluctuations either of the charge density or of the densities of two spin populations. The type of transition observed depends on the relative orientation of the polarization of incident and scattered light (parallel or orthogonal). In the past the spin density excitation spectrum was identified with unscreened single–particle excitations (SPE) – the bare intersubband transition energies – neglecting the influence of exchange[3-7] while charge density waves are known all along to be subject to direct Coulomb interaction. Pinczuk et al.[2] recently observed both CDW as well as SDW as excitations of collective character with energies different from the spectrum of the SPE.

The situation for n–doped samples with only one subband occupied is sketched in Fig. 1 for small inplane wave vector q (in the following q means the transferred inplane wave vector, while the notation k corresponds to the total inplane wave vector in the Brillouin zone). The energies of the SDW are shifted from SPE to lower energies by the exchange Coulomb interaction[8,9], whereas the CDW has energy shifts due to direct as well as exchange terms[3,5,8,9,11,12]. With in-

creasing transfer q the excitation energies of both CDW and SDW overlap the continuum of single–particle excitations. This causes the decay of CDW as well as SDW into uncorrelated intersubband electron–hole pairs (Landau damping)[1,2,13]. An increase of the linewidths with growing inplane wave vector transfer is observed. These results show that not only CDWs but also SDWs of the electron gas of n–doped samples are subject to Landau-damping and demonstrate the collective character of
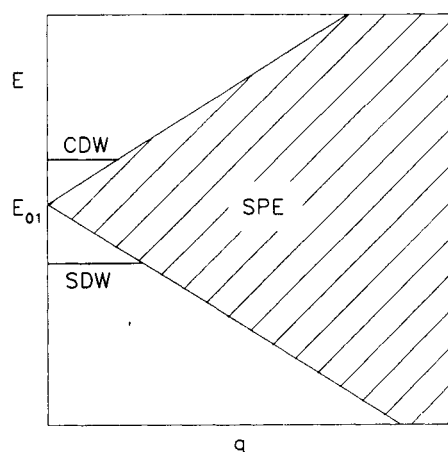
Fig. 1. Schematic dispersion of intersubband excitations of collective (SDW, CDW) and single particle character (SPE) in a n–doped quantum well.

both. Simultaneously the Landau damping of the collective CDWs and SDWs also modifies the line shape of the single–particle continuum[2]. The measurement of both E_{01} (the energy of the SPE for $q = 0$) and the energies of the SDW and CDW allowed Pinczuk et al.[2] a direct determination of Coulomb interactions for intersubband transitions in the conduction band of $GaAs/Al_xGa_{1-x}As$ samples. They found for carrier concentrations $n \leq 3 \times 10^{11}cm^{-2}$ the ratio of the strength of the exchange and direct Coulomb interaction to be greater for about a factor 2 than predicted by an estimate based on local–spin–density functional theory[9]. Contrary to wide–spread belief, exchange and direct terms were found to be of comparable strength.

Because of the complicated valence band structure of two–dimensional semiconductor systems the situation in p–doped quantum–wells is rather different from that of n–doped structures, concerning the single–particle continuum. As a consequence of the extreme non–parabolicity of the hole subbands there exists for every intersubband transition a broad continuum of SPE even for inplane wave vector transfer $q = 0$, whose width increases for a given well dimension with the carrier density n_s of the 2D hole gas. Because of the small subband spacings in the valence band (compared to the conduction band), for a sufficient well width ($L \geq 200$ Å) and doping ($n_s \geq 10^{12}cm^{-2}$), neighbouring continua overlap and the SPE–spectrum is continuous at any value of q - lowest energies excepted only (Fig. 6). So even for $q = 0$ there exist no pure intersubband SDW or CDW in contrast to n–doped wells. The collective excitations of the hole gas are Landau damped in nearly any case. As our sample is just of this type described, the intersubband transitions are observed as broad lines with maxima at positions which only slightly differ in the polarized and depolarized spectra - intersubband excitations of low energy excepted.
Previous investigations of Pinczuk et al. on p–doped multiple quantum wells with $L \approx 100$Å, displayed in Ref. 10, show a disappearence of collective effects in the Raman spectra of hole intersubband transitions in the case of high doping in contrast to the expectations of theory. Landau damping could again contribute to this effect.

2. Experiments and Results

The p–doped sample which we investigated is of a type which was studied theoretically by U. Ekenberg[14]. Our multiple quantum–well (MQW) structure of 40 periods was grown by molecular beam epitaxy. The $Al_xGa_{1-x}As$ barriers ($x = 0.45$) are 500Å thick with the center 300Å doped with Be acceptors. The GaAs well widths and 2D densities are $L = 300$Å and $n_s = 1.6 \times 10^{12}cm^{-2}$. Two subbands (named h_0 and h_1 in our notation) are occupied with holes. They are nearly degenerate at $k = 0$ as a consequence of the two interacting 2D hole gases in each well (see Fig. 2 or Ref. 14).
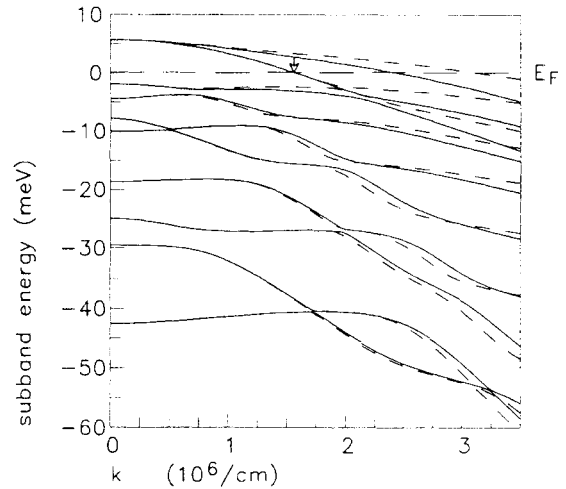

Fig. 2. Calculated valence subband dispersion of the investigated p– doped MQW ($L = 300$Å). The arrow indicates the vertical transition ($q = 0$) of lowest energy possible, which corresponds to the low energy boundary of the continuum at $q = 0$ in Fig. 6. The full lines indicate energies for k–vectors in [100]–direction, the dashed lines such for k–vectors in [110]–direction.

In an effective mass Hartree calculation[15] we selfconsistently calculated the valence subband structure of our sample. Fig. 2 shows the result. The Fermi energy is set to zero.
Fig. 2 shows that the dispersion of the valence subbands is drastically different from the nearly parabolic behavior as found for electrons in the conduction subband system.

The Raman experiments were done in backscattering geometry at $T = 2K$ using a tunable dye–laser operating in the range of 1.6 – 1.8 eV. The q–dependent measurements were performed by rotating the sample relative to the incident and scattered beam. The value of the transferred inplane wave vector q was varied from 0 to $1.6 \times 10^5/cm$.
We observed maxima in the scattering spectrum which show a strong increase in intensity, if the energy of the incident laser photons is nearly in resonance with a transition of the type $h_n \rightarrow c_{n'}$, with $\Delta n = n' - n = 0, \pm 2$, which is dipole–allowed for a square well potential; very weak resonances are found for $\Delta n \neq 0, \pm 2$ (see e.g. the inset of Fig. 4). We identify the excitations in the scattering spectrum as Raman transitions $h_{0/1} \rightarrow h_n$ by comparing the measured peak energies as well as the energies of their resonant excitation with calculated subband spacings at $k = 0$. Transitions $h_{0/1} \rightarrow h_n$ were investigated up to n=6 (Tab. 1 in Ref. 16).
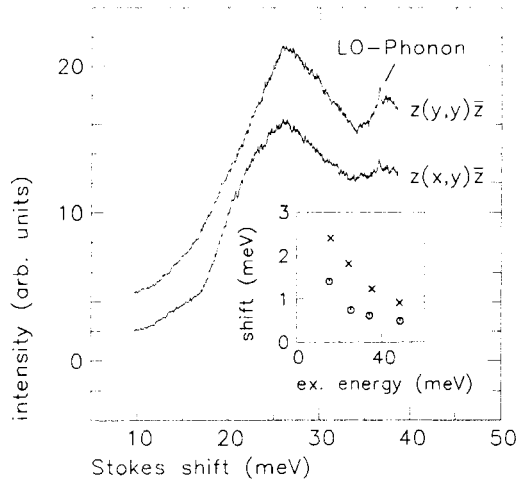
Fig. 3. Raman spectra of the hole intersubband transition $h_{0/1} \to h_4$. The inset shows the differences of the peak positions in the polarized and depolarized spectra of transitions $h_{0/1} \to h_n$ for $n = 3, 4, 5, 6$ (circles) versus excitation energy compared to results of a calculation (crosses).

In Fig. 3 typical Raman spectra of a transition $h_{0/1} \to h_4$ are shown for polarized and depolarized scattering geometry. We mainly assign the broad features to result from single-particle transitions, while the differences between the positions of the peaks in polarized and depolarized spectra due to collective effects are found to be small. A comparison of this energy difference for all transitions $h_{0/1} \to h_n$ with $n = 3, 4, 5, 6$ shows that the observed collective shift depends on the excitation energy: If the transition energy decreases, the shift between the peaks in depolarized and polarized spectra increases. This increase in the 'collective shift' can be explained with growing collective effects. The behavior of the 'collective shift' can be explained with a simple calculation based on the work of Allen, Tsui and Vinter[17] assuming two occupied initial states and one unoccupied final state (at $k = 0$) for the transition $h_{0/1} \to h_n$, neglecting all other states. In this model only direct Coulomb interaction is considered, while exchange and correlation effects as well as effects due to the nonparabolic subband dispersion are neglected. The inset of Fig. 3 shows the results if we take into account the self consistently calculated subband energies and wave functions.

The discrepancy between calculated and measured data could be due to Landau damping: The collective excitations (these are in our simple approach just the charge density excitations) decay even for $q = 0$ into electron–hole pairs and loose their collective character. This means a decreasing energy renormalization of the shift caused by collective effects.

The experimental setup and results described so far are typical for $h_{0/1} \to h_n$ transitions with excitation energies in the midst of the SPE-continuum. The situation for transitions with energies close to the low energy border of this continuum is distinctly different. Because of the attractive character of the exchange interaction, SDWs are expected to have lower energies than the subband separation. For this reason the occurance of nearly pure SDWs with energies close to or even slightly below the border of the single-particle continuum is possible (Fig. 4). In fact two Raman lines of this energy range, displayed in Fig. 4, extremely well fullfill the selection rules of spin density excitations (the polarization of incident and scattered light must be orthogonal). Furthermore the linewidth, especially for the excitation of lower energy in Fig.4 ($\approx$ 1 meV) is much smaller than the linewidth observed for transitions of higher excitation energies (e.g. $\approx$ 10 meV for the excitation $h_{0/1} \to h_4$ displayed in Fig. 3) which indicates, that the probability of decay into SPE is reduced. The SDW measured at 2.5 meV (Fig. 4) can be attached to a transition between the two lowest hole subbands at an inplane wavevector of about $k \approx 1.5 \times 10^6/cm$ (close to the Fermi wave vector k_F, see Fig. 2). The identification as an excitation of the quantum–well is confirmed by the resonance behavior, displayed in the inset of Fig. 4: The energetic position of the first resonance maximum at about 1.612 eV is very close to the calculated $h_1 \to c_3$ subband spacing ($\Delta n = 2$) at $k \approx 1.5 \times 10^6/cm$. The peak energy of the second, much weaker maximum at about 1.658 eV correspond well to the calculated $h_1 \to c_4$ transition ($\Delta n \neq 0, \pm 2$) at the same wave vector. For simplicity
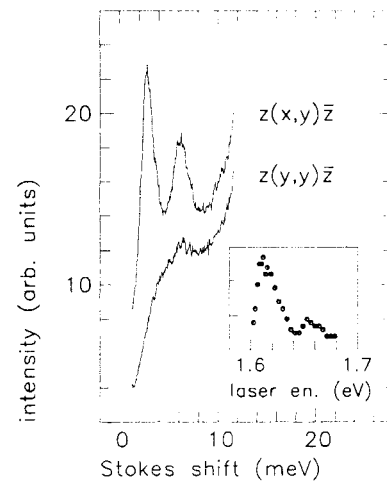

Fig. 4. Polarized and depolarized Raman spectrum of hole intersubband transitions of low excitation energy. The inset shows the resonance behavior (intensity versus laser energy) of the line at 2.5 meV.
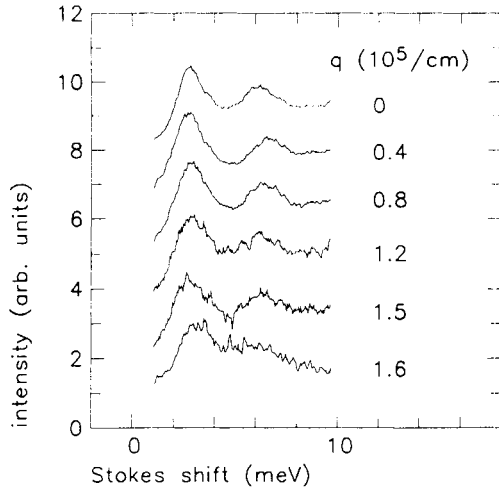
Fig. 5. Depolarized Raman spectra of two hole inter-
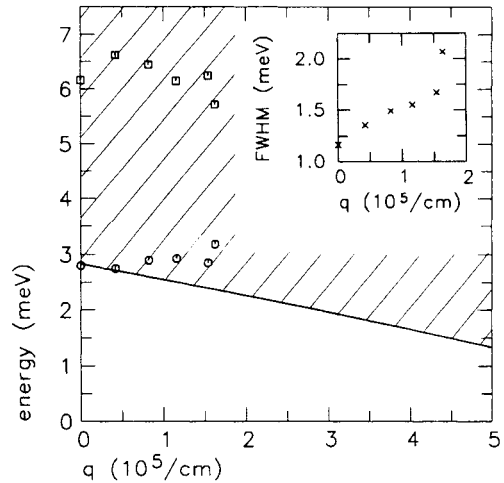subband excitations for several values of the scattering
wave vector q.

Fig. 6. The continuum of SPE as resulting from the
subband structure and Fermi level displayed in Fig. 2
and the peak positions of the excitations of Fig. 5. The
inset shows the q-dependence of the halfwidth of the
2.5 meV transition.

we use the notation h_1 for the whole dispersion curve of
the heavy hole subband, knowing that this is justified
for $k = 0$ only. The resonances of the second SDW at
6.3 meV (Fig. 4) are less intense and seem to be only
slightly shifted. The type of intersubband transition
which results in this SDW is not clear until now.

As displayed in Fig. 5 we have varied the value
of the wave vector transfer q || [100] from 0 up to
$1.6 \times 10^5/cm$ to probe whether there is some effect of
Landau damping resulting from the energy decrease of
the lower border of the single–particle continuum (Fig.
6), where the most striking effects are expected for the
SDW of lowest excitation energy at 2.5 meV. The inset
of Fig. 6 indeed shows an increase of its linewidth with
increasing q, corresponding to a decrease of lifetime.
We also measured some flat dispersion of both SDW
with respect to the scattering wave vector, but we are
not able to explain the behavior because of the com-
plicated structure of the valence subband system.

3. Conclusions

We have investigated intersubband excitations
of spin density and charge density type and effects of
their decay into SPE in a p–doped MQW structure. In
n–doped samples this spectrum of SPE broadens with
increasing inplane wave vector q starting with discrete
transition energies at $q = 0$. As a consequence the de-
cay rate of SDW and CDW into SPE can be tuned by q.
In our p–doped sample the continuum of SPE spreads
over the complete energy range of intersubband transi-

tions even for $q = 0$, lowest energies excepted only. So
the probability of decay into SPE is different for SDW
and CDW of high and low excitation energy. High lying
transitions are observed as broad lines with collective
effects obviously reduced by Landau damping. Two
low lying excitations – identified as nearly pure SDW
by selection rules – are found as well defined lines of a
width which increases with growing wave vector trans-
fer q.

References

[1.] D. Gammon, B. V. Shanabrook, J. C. Ryan, and
     D. S. Katzer, Phys. Rev. B 41, 12311 (1990)

[2.] A. Pinczuk, S. Schmitt-Rink, G. Danan, J. P.
     Valladares, L. N. Pfeiffer, and K. West, Phys.
     Rev. Lett. 63, 1633 (1989)

[3.] G. Abstreiter, R. Merlin, and A. Pinczuk, IEEE
     J. Quantum Electron. 22, 1771 (1986)

[4.] K. Bajema, R. Merlin, F. Y. Yuang, S. C. Hong,
     J. Singh, and P. K. Bhattacharya, Phys. Rev. B
     36, 1300 (1987)

[5.] E. Burstein, A. Pinczuk, and D. L. Mills, Surf.
     Sci. 98, 451 (1980)

[6.]   D. Y. Oberli, D. R. Wake, M. V. Klein, J. Klem, T. Henderson, and H. Morkoc, Phys. Rev. Lett. **59**, 696 (1987)

[7.]   A. Pinczuk, and J. M. Worlock, Surf. Sci. **113**, 69 (1982)

[8.]   T. Ando, A. B. Fowler, and F. Stern, Rev. Mod. Phys. **54**, 437 (1982)

[9.]   T. Ando and S. Katayama, J. Phys. Soc. Jpn. **54**, 1615 (1985)

[10.] T. Ando, J. Phys. Soc. Jpn. **54**, 1528 (1985)

[11.] G. Eliasson, P. Hawrylak, and J. J. Quinn, Phys. Rev. B **35**, 5569 (1987)

[12.] A. C. Tselis, and J. J. Quinn, Phys. Rev. B **29**, 3318 (1984)

[13.] Hong Yu, and J. C. Hermanson, Phys. Rev. B **43**, 4340 (1991)

[14.] U. Ekenberg, Phys. Rev. B **38**, 12664 (1988)

[15.] V. Latussek, E. Bangert, and G. Landwehr, to appear in Ann. Phys. (Leipzig)

[16.] M. Dahl, P. Ils, J. Kraus, B. Müller, G. Schaack, C. Schüller, J. K. Ebeling, and G. Weimann, Superlatt. and Microstruc. **9**, 77 (1991)

[17.] S. J. Allen Jr., D. C. Tsui, and B. Vinter, Solid State Com. **20**, 425 (1976)

INTERSUBBAND PLASMON-PHONON MODES OF A QUASI TWO-DIMENSIONAL ELECTRON GAS IN GaAs

T. FRIEDRICH, M. RÖSCH, V. LATUSSEK, E. BATKE

Physikalisches Institut der Universität Würzburg, D-97074 Würzburg, Germany

K. KÖHLER, P. GANSER

Fraunhofer-Institut für Angewandte Festkörperphysik, D-79108 Freiburg, Germany

The coupling of longitudinal-optical bulk phonons to grating induced intersubband resonances was investigated for electrons in a GaAs quantum well by far-infrared transmission and reflection spectroscopy. The density dependence of the mode frequencies is in good agreement with predictions for a well embedded in two semi-infinite half spaces of the barrier material. A strong asymmetry of the line shapes was observed that arises from influences of the grating coupler.

1 Introduction and Experimental Details

In polar semiconductor structures a coupling of the intersubband resonance to longitudinal-optical (LO) bulk and interface phonons was predicted.[1,2] The mixing of intersubband and LO phonon excitations has previously been investigated by inelastic light scattering for heterostructures based on GaAs.[3] No verification has been provided so far by infrared spectroscopy. Here we present the first comprehensive investigation of intersubband plasmon-phonon modes for electrons in a GaAs quantum well by transmission and reflection spectroscopy in the infrared.

Our GaAs heterostructure was grown by molecular-beam epitaxy on top of a 1 μm buffer on a semiinsulating GaAs substrate and embodied a 20 nm wide GaAs quantum well, embedded between 59 nm thick barriers of δ-doped short period AlAs-GaAs superlattices. Electrons were localized in the well and in an electron inversion layer at the barrier-buffer interface. A thin metal layer of NiCr serves as a front gate to vary the electron density N_s via field effect. Using magnetocapacity and cyclotron resonance measurements, N_s was determined to be about $6 \times 10^{11} \text{cm}^{-2}$ in the quantum well and $3 \times 10^{11} \text{cm}^{-2}$ in the inversion layer at zero gate voltage V_g. The density in the quantum well varied nearly linearly with V_g, and complete depletion was achieved at -0.6 V. The electron concentration of the inversion layer was essentially constant up to -0.4 V, with a threshold voltage of $V_{th} = -2.5$ V. The electric field component to excite the intersubband resonance was provided by a Ag grating coupler of period $a = 6\,\mu$m. Intersubband resonances were obtained from normalized transmission $T(V_g)/T(V_{th})$ and reflection spectra $R(V_g)/R(V_{th})$ at a temperature of 10 K.
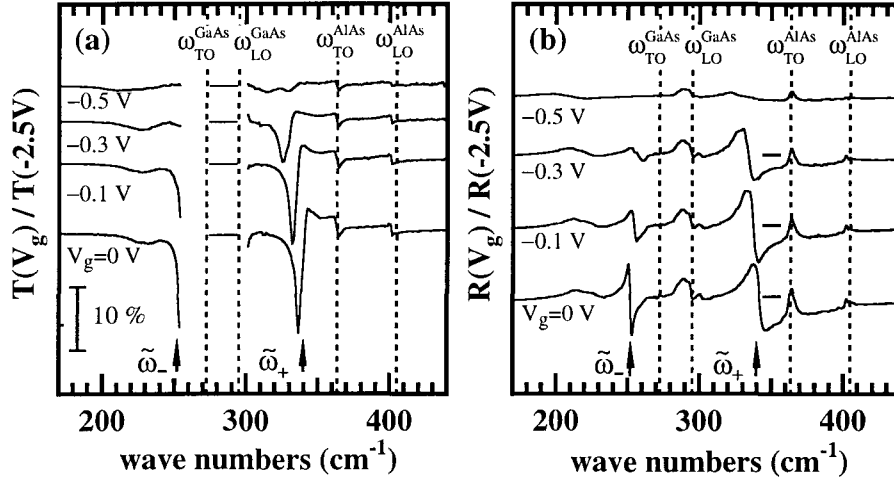
Figure 1: Normalized (a) transmission and (b) reflection spectra for different gate voltages. $\tilde{\omega}_+$ and $\tilde{\omega}_-$ denote the coupled intersubband plasmon-LO bulk phonon modes of the well.

2 Results and Discussion

Figure 1 displays normalized spectra for different gate voltages. All resonant structures are evidently induced by the grating coupler, since for an electric field polarized parallel to the grating stripes as well as for a sample without grating no resonances could be detected. In Fig. 1, the frequencies of the LO and TO bulk phonons of GaAs and AlAs are marked by vertical dashed lines. In transmission, the frequency band from about 250 to $300\,\mathrm{cm}^{-1}$ is blocked due to strong absorption in the reststrahlen regime of the substrate. Note that minima in the normalized transmission spectra correspond to maxima in reflection.

We consider here only the resonances marked $\tilde{\omega}_+$ and $\tilde{\omega}_-$ that show a strong N_s dependence in position and in integrated strength in the regime $-0.5\,\mathrm{V} \leq V_g \leq 0\,\mathrm{V}$. These resonances are associated with the GaAs quantum well and represent the upper (+) and lower (−) modes of the intersubband transition from the ground to the first excited subband coupled to the LO phonon of GaAs. The other resonances which do not change significantly in this gate voltage regime are associated with the electron inversion layer. This we conclude from self-consistent calculations of the intersubband optical transition frequencies which for $V_g = 0\,\mathrm{V}$ predict resonances at about $215\,\mathrm{cm}^{-1}$, $300\,\mathrm{cm}^{-1}$, and $330\,\mathrm{cm}^{-1}$.
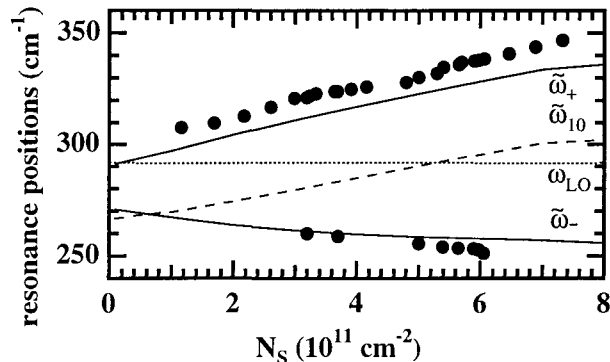
2

Figure 2: Calculated density dependence of the coupled plasmon-phonon modes $\tilde{\omega}_\pm$ (solid lines), ω_{LO} (dotted line), and $\tilde{\omega}_{10}$ (dashed line). Filled circles indicate experimental data.

In Fig. 2, the resonance positions for the $\tilde{\omega}_\pm$ modes are summarized versus the electron density N_s in the quantum well. For a quantum well with subband separation ω_{10}, the intersubband optical transition energy reads[4]

$$\tilde{\omega}_{10}^2 = \omega_{10}^2(1 + \gamma_{10}) \ , \tag{1}$$

where γ_{10} indicates the collective shift associated with depolarization and final state corrections. Due to coupling to the LO phonon of GaAs, the intersubband resonance Eq. (1) splits into the modes[2]

$$\tilde{\omega}_\pm^2 = \frac{1}{2}\left[(\omega_{LO}^2 + \tilde{\omega}_{10}^2) \pm \sqrt{(\omega_{LO}^2 + \tilde{\omega}_{10}^2)^2 - 4\tilde{\omega}_{10}^2(\omega_{LO}^2 + \gamma_{10}\omega_{TO}^2)}\right] \ . \tag{2}$$

In Fig. 2, the solid lines give the calculated frequencies $\tilde{\omega}_\pm$. The N_s dependence of the subband separation ω_{10} and the intersubband optical transition frequencies $\tilde{\omega}_{10}$ (dashed line) were calculated self-consistently for a GaAs well embedded in two semi-infinite AlAs barriers.[4]

The resonant structures observed in Fig. 1 at ω_{LO}^{GaAs} and ω_{TO}^{AlAs} we tentatively attribute to coupling of the intersubband resonance to interface phonons. Interface phonons can exist in the reststrahlen regimes of the well and barrier material. For a GaAs well embedded in two halfspaces of AlAs there is a total of four interface modes, which have an electric field distribution that is symmetric or antisymmetric with respect to the well center. Only the antisymmetric interface phonons couple to the intersubband transition. In the long wavelength limit, the antisymmetric interface phonon frequencies approach the bulk LO frequency of the well and the bulk TO frequency of the barrier material.

3

A striking feature of the coupled modes is their form which exhibits a strong asymmetry. We attribute this line shape to an optical effect which is induced by the grating coupler and has some similarities to the influence of a highly conducting gate in the vicinity of the well. For a metal layer of thickness d with a Drude conductivity $\sigma_g(\omega) = \sigma_g'(\omega) - i\sigma_g''(\omega) = \sigma_0/(1 + i\omega\tau)$, where $\sigma_0 = n_e de^2\tau/m_e$, the normalized transmission and reflection are given by

$$\frac{T(N_s)}{T(0)} = 1 - \frac{2}{\sigma_0}[\sigma_{2D}'(\omega) + \omega\tau\sigma_{2D}''(\omega)] , \tag{3}$$

$$\frac{R(N_s)}{R(0)} = 1 + \frac{4\epsilon_0 c}{\sigma_0^2}\left\{\sigma_{2D}'(\omega)[1 - \omega^2\tau^2] + 2\omega\tau\sigma_{2D}''(\omega)\right\} . \tag{4}$$

Here, the high-frequency conductivity $\sigma_{2D}(\omega) = \sigma_{2D}'(\omega) - i\sigma_{2D}''(\omega)$, describing the absorption of the quasi two-dimensional electron gas, is assumed to be much smaller than $\sigma_g(\omega)$. For the intersubband transition one might set $\sigma_{2D}(\omega) = (N_s e^2 f_{10}/m^*)[-i\omega/(\tilde{\omega}_{10}^2 - \omega^2 - 2i\omega/\tau_{2D})]$,[4] where f_{10} is the oscillator strength and τ_{2D} a phenomenological relaxation time. Depending on the magnitude of $\omega\tau$, there is a mixing of the real and imaginary parts of the high-frequency conductivity $\sigma_{2D}(\omega)$, which induces an asymmetry of the line shapes. We believe that also the grating coupler induces a mixing of $\sigma_{2D}'(\omega)$ and $\sigma_{2D}''(\omega)$.

In conclusion, we studied the coupling of the intersubband plasmon in a GaAs quantum well to the LO bulk phonons with infrared transmission and reflection measurements using the grating coupler technique. The resonance positions can be excellently described in the framework of a self-consistent-field theory. The asymmetric line shape of the coupled intersubband plasmon-LO bulk phonon resonance is explained by a grating coupler induced mixing of the real and imaginary parts of the high-frequency conductivity.

Acknowledgments

References

1. G. H. Kawamoto, J. J. Quinn, and W. L. Bloss, *Phys. Rev.* B **23**, 1875 (1981).
2. L. Wendler and R. Pechstedt, *Phys. Status Solidi* B **141**, 129 (1987).
3. A. Pinczuk and J. M. Worlock, *Surf. Sci.* **113**, 69 (1982).
4. T. Ando, A. B. Fowler, and F. Stern, *Rev. Mod. Phys.* **54**, 437 (1982).

Literaturverzeichnis

[1] Die weiterführende Literatur ist in den abgedruckten Publikationen enthalten.

[2] A. Pfeuffer-Jeschke, Dissertation, Physikalisches Institut der Univerität Würzburg, (2000)

[3] E. G. Novik, A. Pfeuffer-Jeschke, T. Jungwirth, V. Latussek, H. Buhmann, C. R. Becker, G. Landwehr and L. W. Molenkamp, Phys. Rev. B **72**, im Druck

[4] C. R. Becker, V. Latussek, G. Landwehr, R. Bini and L. Ulivi, J. Electr. Mater. im Druck

[5] L. C. Andreani, A. Pasquarello und F. Bassani, Phys. Rev. B **36**, 5887 (1987)

[6] R. Winkler und U. Rössler, Phys. Rev. B **48**, 8918 (1993)

[7] J. Stoer, *Einführung in die Numerische Mathematik I* (Springer, Berlin, 1983)

[8] J. Stoer, R. Bulirsch, *Einführung in die Numerische Mathematik II* (Springer, Berlin, 1990)

[9] B. T. Smith, J. M. Boyle, B. S. Garbow, Y. Ikeba, V. C. Klema, C. B. Moler, in *Matrix Eigensystem Routines – EISPACK Guide*, herausgegeben von G. Goos and J. Hartmann, Lecture Notes in Computer Science Vol. 6 (Springer, Berlin, 1974)

[10] J. N. Schulman and C. L. Anderson, Appl. Phys. Lett. **48**, 1684 (1986)

[11] M. A. Reed, R. J. Koestner, and M. W. Goodwin, Appl. Phys. Lett. **49**, 1293 (1986)

[12] *Handbook of Mathematical Functions*, herausgegeben von M. Abramowitz und I. A. Stegun (Dover Publications, New York, 1970)

[13] Courant, Hilbert, *Methoden der Mathematischen Physik*, (Springer, Berlin, 1993)

[14] W. H. Press, S. A. Teukolsky, W. T. Vetterling, and B. P. Flannery, *Numerical Recipes in Fortran: the art of scientific computing*, (Cambridge University Press, Cambridge, 1992)

Lebenslauf

Persönliche Daten:		Volker Latussek
		geboren am 23. Januar 1964 in Hamm (Westfalen)
Schule:	1970 – 1974	Volksschule St. Josef, Lippstadt (Westfalen)
	1974 – 1980	Ostendorf–Gymnasium, Lippstadt
	1980 – 1983	Ernst Barlach–Gymnasium, Dinslaken (Niederrhein), Allgemeine Hochschulreife
Studium:	1983 – 1989	Diplomstudiengang Physik an der Bayerischen Julius–Maximilians–Universität Würzburg, Diplom
		Thema der Diplomarbeit: 'Landau–Zustände im p–Typ–Inversionskanal von Ge–Bikristallen', (Theorie)
Beruf:	1990 – 1999	Wissenschaftlicher Mitarbeiter am Lehrstuhl für Experimentelle Physik III von Prof. Dr. G. Landwehr
	1990 – 1993	Stipendiat des Graduiertenkollegs 'Mikrostrukturierte Halbleiter'
	seit 4/1999	Geschäftsführer des Physikalischen Instituts
	9.11.2004	Ernennung unter Berufung in das Beamtenverhältnis auf Lebenszeit zum Akademischen Rat

Würzburg, 24. Dezember 2004

Volker Latussek